Solar Energy Conversion by Photoelectrochemical Processes

Ibrahim Abdallah Ismail Hassan

A thesis submitted for the degree of Doctor of Philosophy

Department of Chemistry

University of Bath

Bath, UK

May 2011

To

My beloved country

Egypt

Summary

This thesis reports on experimental work in the field of photo-electrochemistry and focusing on the photo-electrochemical water splitting process. This process is important as a part in the solar energy harvesting process, mimicking the natural photosynthesis process, to produce hydrogen which can be used as a carrier of clean energy in the fuel cells.

In chapters 1 and 2 the literature background for water splitting and semiconductor electrochemistry are summarised. Chapter 3 describes all key techniques for electrochemistry, surface analysis and spectrometry, and conditions employed for experimental methods.

The first main results chapter is chapter 4 with information about the formation and investigation of photo-electrochemically active WO_3 films. Thin, nanostructured, WO_3 films are grown onto conducting FTO substrates and shown to act as photo-catalyst for water splitting under positive potential bias. The time dependence of photo-currents is studied by impedance, light pulse, and light modulation techniques, and the time constants for photo-doping and electron transport are dissected. Clear evidence for trapping of diffusing electrons is obtained from intensity modulated photocurrent spectroscopy.

Chapters 5 to 8 focus on iron oxide films and their preparation. In chapter 5 the layer-by-layer assembly method is employed to form films from hematite nanoparticles and phytate binder molecules. Photo-electrochemical responses are observed as a function of film thickness and applied potential. A model based on differing electron and hole mobility in conjunction with recombination is applied to explain the photo-transient responses.

In chapter 6 hematite films are formed in a chemical vapour deposition (CVD) growth process from a ferrocene precursor. Films are formed in variable thickness on FTO (fluorine-doped tin oxide) and ITO (tin-doped indium oxide) substrates. Photo-electrochemical experiments are conducted and the effect of thickness and

illumination direction discussed in the context of a water splitting process in a mesoporous Fe_2O_3 film. In contrast to the thin mesoporous films investigated in chapter 5, here thicker and denser films are studied. The photo-catalytic efficiency is improved by a factor of 4 due to higher density and potential gradient effects.

In chapter 7 the spray-pyrolysis formation of photo-electrochemically active films is introduced in order to introduce dopants and to affect morphology and structure of deposits. Here, addition of tetramethoxysilane (TMS) in varying amounts to iron oxide precursor systems for spray pyrolysis is investigated and the dramatic effect on the photo-electrochemical water splitting current in aqueous 1 M NaOH is discussed.

In chapter 8 a solid solution iron oxide similar to the perovskite family of materials $SrTi_{1-x}Fe_xO_{3-y}$ (STF) is studied. In this chapter a spray pyrolysis approach to prepare STF films on ITO substrates is employed. In preliminary data, the nanostructured films show good photo-activity with IPCEs of up to 11%.

Acknowledgements

'I do thank GOD for all gifts given to me'

Firstly, I would love to thank my supervisors, Professor Laurie M. Peter and Dr. Frank Marken, for their supervision and kind help during the different stages of my PhD work and for help with the digital simulation work in chapters 5 and 6.

I would also like to thank colleagues and friends who I started with and I got some help from and for being good company throughout my PhD study, especially Jonathan Scragg, James Jennings, Halina Dunn, Alberto Fattori, Claire Thompson, Diego Colombara, Mohamed Aziz, Moustafa Kenawy, Robeen Gaber, and Robert Archer and to Charlie Cummings for junction experiments work in chapter 5.

Many thanks go to various members of staff at the University of Bath who have provided me with invaluable help, including Dr. Mary Mahon and Dr. Gabriele Kociok-Köhn in the Department of Chemistry for XRD measurements and Mr. Hugh Perrott and Dr. John M. Mitchels in the Department of Physics for SEM and EDX measurements. Many thanks also to Mr. Paul Frith, Mechanical Engineering, who helped me with building the photoelectrochemical cell. Thanks should also go to Prof. Kieran Molloy and Dr. Steven Richards for helping with preparing Fe_2O_3 by CVD method

I would like also to thank Dr. Upul Wijayantha, Loughborough University, for helping and teaching how to prepare nanostructured WO_3 films.

My deepest thank goes to my family back in Egypt, who supported me very much and especially to my father who passed away during this work.

Finally, I would like to express my deepest thanks to the Egyptian Government for funding.

Ibrahim Hassan

May 2011

Work done in collaboration with others

All of the work presented in this thesis was carried out by the author apart from the following exceptions:

- The sample of WO_3 described in Chapter 4 was fabricated in cooperation with Dr. Upul Wijayantha, Loughborough University, Loughborough, UK.

- The junction experiments in Chapter 5 have been carried out by Charles Y. Cummings, and Dr. Frank Marken, Department of Chemistry, University of Bath.

- The Fe_2O_3 films in Chapter 6 formed by CVD method have been prepared in cooperation with Prof. Kieran Molloy and Dr. Steven Richards, Department of Chemistry, University of Bath.

- The digital simulation work in Chapters 5 and 6 has been carried out by Dr. Frank Marken.

List of abbreviations

AC	Alternative Current
AFM	Atomic Force Microscopy
AACVD	Aerosol-Aassisted Chemical Vapour Deposition
APCVD	Atomic Pressure Chemical Vapour Deposition
ATO	Antimony-doped Tin Oxide
B_{FWHH}	Peak width at full width half hieght
C_B	Conduction band
CE	Counter Electrode
CIS	Copper Indium diselenide
CVD	Chemical Vapour Deposition
DC	Direct Current
DSSC	Dye Sensitised Solar Cell
EDX / EDS	Energy Dispersive X-ray Spectroscopy
EE	Electrode-Electrolyte illumination
EIS	Electrochemical Impedance Spectroscopy
EPFL	École Polytechnique Fédérale de Lausanne
FTO	Fluorine-doped Tin Oxide
IPCE	Incident Photon to Current Efficiency
ITO	Indium-doped Tin Oxide
kWh	Kilo Watt hour
LBL	Layer-by-layer assembly
LED	Light Emitting Diode
MJ	Mega Joule
RHE	Reversible Hydrogen Electrode
SE	Substrate-Electrolyte illumination
SEM	Scanning Electron Microscopy
STF	Strontium Titanate Ferrate
STP	Standard conditions for Temperature and Pressure
TW	Terawatt
V_B	Valence band
WE	Working Electrode
XRD	X-ray Diffraction
Re(Z) / Z`	Real part of impedance
Im(Z) / Z``	Imaginary part of impedance
j	Complex number = imaginary number = $\sqrt{-1}$
UoG	University of Guelph, Canada
UV	Ultra-Violet

List of symbols

Symbol	Quantity	Units
A / A	Area/Absorption	cm^2/a.u
c	Speed of light	ms^{-1}
C	capacitance	F
C_{SC}	Space Charge Capacitance	F
D_n	Diffusion Coefficient	m^2cm^{-1}
D_e	Electron Diffusion Coefficient	m^2cm^{-1}
D_h	Hole Diffusion Coefficient	m^2cm^{-1}
d / x	Film thickness	μm
d	Space between lattice planes	μm
e^-	electron	C
eV	Electron Volt	J
E_C	Conduction band energy/potential	eV/V
E_V	Valence band energy/potential	eV/V
E_{fb}	Flat Band Energy/potential	eV/V
Eg	Band gap	eV
E_F	Fermi level potential	cm^2s^{-1}
E_{redox}	electrolyte potential	V
E	Electrode potential/Photon energy	V/eV
E_{fb}	Flat-band potential	V
E_0	Standard reduction potential	V
F	Faraday constant	$Cmol^{-1}$
ΔG	Free energy	$kJmol^{-1}$
h^+	hole	-
h	Planck's constant	J.s/eV.s
I	Current	mA
I	Incident light intensity	$Js^{-1}cm^{-2}eV^{-1}$
I_0	Transmitted light intensity	$Js^{-1}cm^{-2}eV^{-1}$
J	Current density	$mAcm^{-2}$
k	Boltzmann constant	JK^{-1}
K	Scherrer constant	-
k_c	apparent chemical rate constant for oxygen evolution	
L_n	Diffusion length	m
N	The ionised donor dopant concentration	-
n	an integer	-
q	Electronic charge	C
R	gas constant / Resistant	$JmolK^{-1}$ /Ω
T	Transmittance	-
Z	Impedance	Ω
|Z|	Impedance amplitude	Ω
ε_0	Vacuum permittivity	Fm^{-1}
ε	Dielectric constant of the semiconductor	-
hv	Photon energy	eV
f / υ	frequency	s^{-1} / Hz
η	Overpotential	V
η_{H2}	Hydrogen overpotential	V

η_{O2}	Oxygen overpotential	V
α	Absorption coefficient	cm^{-1}
θ	angle of X ray incidence and reflection	degree
θ	Phase shift	degree
λ	Wavelength	nm
ω	radial frequency	rad s^{-1}

Table of Contents

Chapter 1

Introduction to Solar Energy Technologies and Water Splitting Processes

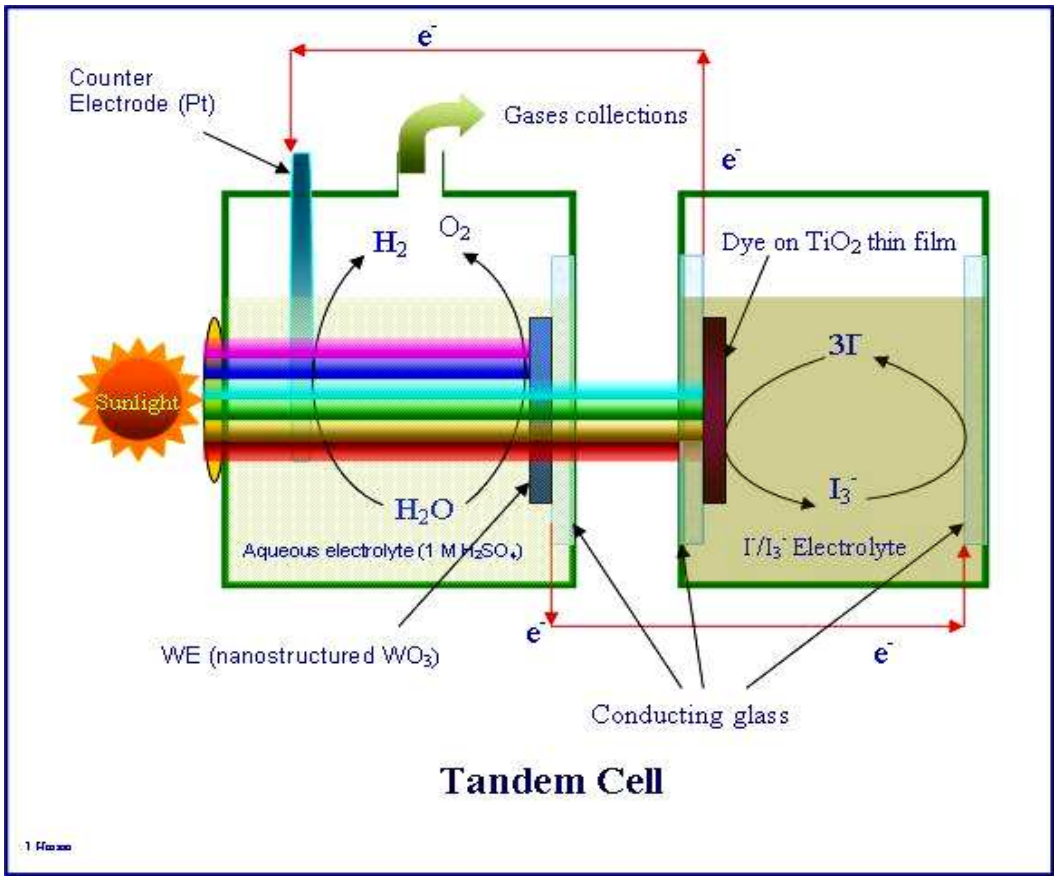

Abstract. In this chapter the literature concerning solar water splitting technologies and research is introduced. The importance of hydrogen generation driven by solar energy is explained and possible technical solutions discussed. The application of transition metal oxide thin film electrodes in this technology is introduced and areas of interest in this study are highlighted.

Content

1.1. The Importance of Searching for Sustainable Energy Sources

Fossil fuels, which are coal, oil, and natural gas, are currently considered the main source of energy because they are the cheapest, most conveniently accessible, and most reliable form of energy for both electricity production and transport fuels such as petrol and its products[1]. When fossil fuels are burned, one of the most significant emitted gases is CO_2, a "green-house" gas that traps heat in the Earth's atmosphere and which contributes to global warming[2]. It is estimated that, the global surface temperature has increased about 0.5^o C since 1970. Moreover, nitrogen oxides, carbon monoxide, and incompletely burned hydrocarbons are produced causing atmospheric pollution[2].

It was estimated[3] that by the year 2050 between 10-30 TW (Terawatt) (1 TW = 1 × 10^{12} W) per year of carbon-free energy will be required globally, as it is expected that the world's population grows to approximately 10-11 billion people. To put this into context, the current global population is 6 billion and the current annual energy consumption is 13 TW per year[4]. Because of that and because fossil fuels are polluting and a finite resource, a renewable and clean energy source is desirable. The main sources of carbon-free renewable energy today are solar energy, wind energy, biomass and timber, wave and tidal energy, hydro-energy, and geothermal energy [5].

Solar power, as an example of sustainable energy, could potentially provide a huge part of the required tens of terawatts of energy. It is estimated that, the energy sent from the sun to the earth is 3x10^{24}J per year, which is about 10000 times the current yearly worldwide energy consumption [6]. In other word; the energy sent to the earth by the sun in one hour is more than that energy consumed by the whole globe in a year [7]. Some of these large amounts of energy should be captured and directed to be used in place of fossil fuels. It is estimated that if a small fraction of the earth's surface was covered by solar cells with a realistic 10 % efficiency, that will provide the whole world with the needed energy [8]. The problem of realizing this vision is currently the high cost of the solar cells in comparison with the cheaper fossil fuels. It was reported in 2003 that[5] the current cost of solar cells are $ 0.3-0.5 / kWh and this is required to be minimized to about $ 0.2 / kWh to provide a cheap renewable energy for the future [6].

Solar energy could potentially be used to provide both (i) direct electrical power output and (ii) stored energy for example in the form of hydrogen. There are many governments and industrial companies interested in investing considerable amounts of money into the development of new renewable energy sources including solar technologies. Water splitting and hydrogen production is one of the most promising targets for renewable energy research. Hydrogen offers one of the best ways to harvest the solar energy into a chemically active form, which can be readily used as a carrier of energy. In this study, one part of the photo-electrochemical hydrogen production (the photo-anode) is investigated.

1.2. Historical Development of Solar Technologies

Although ancient Egyptians considered the sun as a main source of life until they considered it as a God thousands of years ago[9], the real practical considering of using the solar energy to produce power first captured the imagination of the scientific community in 1839, when the French scientist Edmund Becquerel found that a photo-voltage could be produced from the action of light on an electrode[10]. Few successful attempts then were reported to produce electrical power from solar energy until 1947, when the highest efficiency achieved was at just 1% by Telkes[11] employing thermoelectric junctions. Then in 1954 the real development of photovoltaic solar cells began when Chapin et al. [12] found that 6% solar conversion efficiency was obtained by using a semiconductor p-n junction in a single-crystal of silicon. The disadvantage of silicon is the relatively poor light absorption (indirect band gap), which means that unsophisticated cells must be at least 250 μm thick to absorb all the active wavelengths in sunlight with reasonable efficiency.

In 1972 an n-type semiconductor TiO_2 electrode connected to a platinum black electrode through an external load was proposed. Fujishima and Honda[14] were the first to raise the concept of using a photoelectrochemical device for solar energy conversion and storage [13]. Although, in their experiment it was a pH difference on both sides of the membrane, which contributed to the potential difference leading to water splitting, they proposed that water can be split without applying any potential bias by using only solar energy.

In 1980 the first thin-film solar cells were developed based on the cuprous sulphide/ cadmium sulphide (p-Cu_2S/n-CdS) heterojunction. Other thin film solar cells based on amorphous silicon (a-Si:H) dominate the market place, but cadmium telluride (CdTe) and chalcogenides such-as copper indium diselenide (CIS) are offering real competition in the photo-voltaics (PV) market[9]. Materials based on III-V semiconductors, such as gallium arsenide, offer relatively high efficiencies but are costly to produce and are yet to prove more cost effective than silicon based PV devices. It was suggested by Bauer[14] that chalcogenide film thickness of around a micron can replace a traditional silicon solar cell which has a typical thickness of 300 μm., and that decreases the whole cost of energy production.

Nowadays, the inorganic solid-state junction devices are in competition with new technologies such as nanocrystalline conducting polymers and with organic photo-electrochemical devices. The main difference[9] between photoelectrochemical devices and classical solid state junction devices is in the contact media with the semiconductor. This is replaced in organic photoelectrochemical cells by either electrolyte, gel, or organic solvent. A chemisorbed ruthenium dye has been used with n-TiO_2 in the dye sensitised solar cell (DSSC) or "Grätzel cell". This showed very promising photoelectrochemical characteristics for devices for the direct production of electricity from light [15].

Since 1980 many papers have been published concerning of investigation of semiconductors for photoelectrolysis of water. The development of nanocrystalline semiconductor systems and huge financial investment has increased the search for suitable cells for photo-electrochemical water splitting. In 1983[11] it was proposed that a tandem cell could be used, which consists of a series of solar cells (explained in more detail below). The 'brute force' approach is to set up four silicon PV cells in series and pass the electricity which is produced directly into a commercial water electrolyser. However, the water splitting efficiency was only just 7 %. By using III/V semiconductors much higher efficiencies of 12-20 % for water splitting have been produced, but these are expensive materials and not easily manufactured into devices for commercial purposes. In 1999 Grätzel[16] has reported a much cheaper improved tandem cell which can split water directly into oxygen and hydrogen.

Now in the year 2011 there are hundreds of papers published annually concerning photo-electrochemical water splitting. Yet the tandem device efficiency for water splitting is still not high enough to be applicable in an industrial scale to produce cheap hydrogen fuel.

1.3. Hydrogen Fuel as Energy Carrier

In 1788 Lavoisier [7] has introduced the term "hydrogen" (H_2) based on the Greek words "hydro" for "water" and "gene" for "born of"'. Hydrogen is one of two components, with oxygen, in water as it was experimentally proven by the British scientist Henry Cavendish (1731-1810). He was the first to produce water from the elements hydrogen and oxygen. Hydrogen is considered as the lightest gas in the universe[7] with the lowest density 0.08988 g dm^{-3} at STP (standard conditions for temperature and pressure). Liquid hydrogen has the lowest liquid density with about 0.07 g cm^{-3}, while gasoline density, for example, is 0.75 g cm^{-3}. Hydrogen is considered as the most abundant element in the universe with about 90% by weight.

In fact hydrogen is not an energy source, but it is an energy carrier[7 p: 10]. Grimes mentioned in his book[7, p: 13] that hydrogen is considered as an ideal energy carrier, and it can replace fossil fuels in the future for several reasons [7]:

1- Hydrogen can be a renewable energy because it can be produced from water and sunlight.
2- Hydrogen can store about 120 MJ energy per kilogram of hydrogen and it can release 142 MJ per kilogram on combustion. Gasoline, for comparison, stores just about 45 MJ per kilogram of fuel. In a comparison to methane, hydrogen releases about 2.45 times more energy than methane does.
3- It is possible that hydrogen can be produced from electricity through many ways such as electrolysis of water in high efficiency.
4- Hydrogen can be converted into electricity in the fuel cells as a result of reaction with oxygen or with clean air.
5- Hydrogen can be stored easily in gaseous, liquid, or metal hydride form.
6- It can be transported over large distances through pipelines or via tankers.

7- Hydrogen is flexible in conversion into other forms of energy in more ways and more efficiently than any other fuel.

8- Hydrogen is a very clean carrier of energy as its production, storage, transportation and use do not produce significant amounts of pollutants, toxic gases, or products harmful on the environment.

1.4. Photoelectrochemical Water Splitting Processes

Water can be split into its main components, hydrogen and oxygen, by using solar energy through a photoelectrochemical process. Photo-electrolysis of water at semiconductor electrodes has important practical applications and is now extensively studied[17]. In a photoelectrochemical system, both excited electrons in the conduction band (CB; e^-_{CB}) and holes in the valence band (VB; h^+_{VB}) are participating in the water splitting process at anode and cathode:

Anodic Oxidation:

$$2H_2O + 4h^+_{VB} \rightarrow 4H^+ + O_2 \quad (1.4)$$

Cathodic Reduction:

$$4H^+ + 4\, e^-_{CB} \rightarrow 2H_2 \quad (1.5)$$

Overall photo-electrochemical reaction:

$$4h\nu + 2H_2O \rightarrow O_2 + H_2 \quad (1.6)$$

Water photolysis and production of hydrogen and oxygen is a subject of continued interest, and challenges are in particular in the development of novel catalysts [18]. In fact, although the potential needed for water splitting is 1.23 V, energy losses due to overpotentials are part of this process. The reaction of hydrogen evolution on the counter electrode is very fast for example on platinum catalysts and therefore needs little overpotential (η_{H2}). However, the oxygen evolution reaction is kinetically slow and therefore needs a high overpotential (η_{O2}) as shown in Figure 1.1. The additional energy for overpotential losses can be obtained by using light with more than 1.23 eV energy. For continuous water splitting to occur, the current due to hydrogen evolution (I_{H2}) must be equal to that due to water oxidation and production of oxygen ($I_{H2} = I_{O2}$).

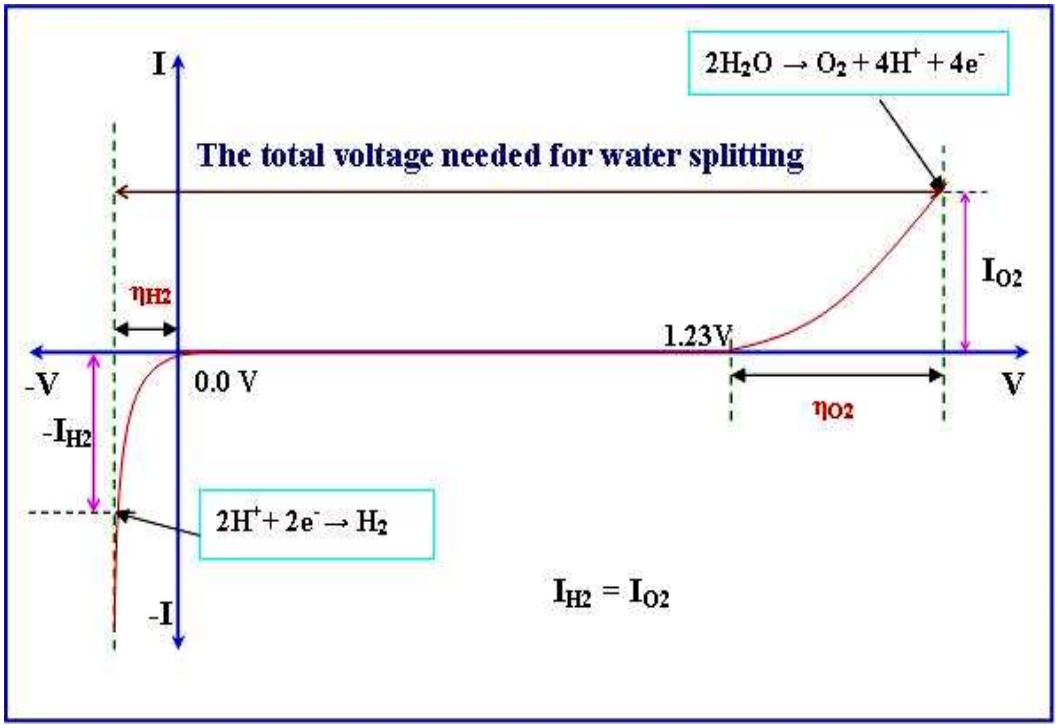

Figure 1.1. Diagram explaining the current – voltage characteristics during water splitting, the overpotential needed for water splitting, and the corresponding photon energy (or semiconductor band gap).

Many studies suggested that metal oxides, such as WO_3, Nb_2O_5, V_2O_5, Ta_2O_5, TiO_2, $Ir(OH)_3$, and CeO_2 have good light absorption and electrocatalytic properties and may therefore be suitable as photoelectrodes for water splitting[18]. Redox-dependent changes of colour due to the electrochromic properties can also modify the light absorption range from UV to VIS and contribute to the water splitting activity. Good electrical properties and stability in water represent the main requirements that must be fulfilled in this application.

It was found that[18] the splitting of water requires a high potential to produce oxygen on most of the metal electrodes surfaces. Without illumination, it was found that oxygen evolution occurs at WO_3 electrode at potentials more than 2.0 V vs normal hydrogen electrode (NHE) at pH 0. This means that WO_3 has an overpotential of ~0.8 V[19]. In AM 1 sunlight, oxygen evolution at the same electrode starts at 0.6 V vs NHE suggesting a shift of 1.4 V[19]. A similar result was reported by Augustynski [19].

Mixed oxides provide a wide range of potential catalysts. By using $ZnGa_2O_4$ and $ZnGa_2O_4$–ZnO precusors, a solid-solution of GaN and ZnO $(Ga_{1\_x}Zn_x)$ $(N_{1\_x}O_x)$ was prepared as a visible-light-driven photo-catalyst for water splitting. It was found that the photo-catalytic activity of the catalyst is dependent on both the Zn/Ga ratio of the starting materials and the nitridation time. Both factors affect the crystallinity and atomic composition of the final $(Ga_{1-x}Zn_x)$ $(N_{1-x}O_x)$ material. It was also revealed that the addition of ZnO promotes crystallization of the catalyst and it controls the zinc concentration, thereby improving activity. By adjusting these two preparation parameters, it was possible to obtain a material with optimal crystallinity and atomic composition for overall water splitting under visible light conditions ($\lambda > 400$ nm) [20].

Certain oxynitrides[21], such as TaON, $LaTiO_2N$ and the $(Ga_{1-x}Zn_x)(N_{1-x}O_x)$ solid solutions, are promising as stable photocatalysts for water splitting under visible-light irradiation. These oxynitrides showed high photocatalytic activity for water oxidation in the presence of an appropriate electron acceptor. Y. Gao et al.[22] characterised green SiC powders by XRD and UV/Vis diffuse reflectance, and studied the photocatalytic splitting of water. The results showed that green SiC powder can absorb visible light and split water with the formation of hydrogen under visible light irradiation. The activity is affected significantly by the initial pH of solutions and the types of added reagents. The addition of OH^- or S^{2-} led to a remarkable increase in the activity.

The Tandem Cell is mainly consisting of two photosystems connected in series as shown in Figure 1.2. The front (or the top) photosystem is a solar cell consists of a counter electrode (Pt) and a working electrode which could be based for example on a thin film nanocrystalline WO_3[23] or Fe_2O_3[24] which absorbs the ultraviolet and blue parts of the high-energy light spectrum. This photosystem produces positive potential which is more than enough for water oxidation but is not energetic enough for immediate hydrogen production. The longer wavelength of the low-energy light in the green and red region passes through the front cell and is absorbed by a Grätzel cell, which is a dye sensitised titanium dioxide solar cell in iodide/tri-iodide electrolyte producing electrical potential under all light conditions. The two electrodes are connected and together they produce the potential required to split water. The advantage of this type of tandem cell is that it is made from widely available and

cheap materials[25]. The tandem cell concept was further developed by Grätzel (EPFL) and Augustynski (UoG)[17]. Further development of the tandem cell has been reported by the company Hydrogen Solar for the core components and coating technologies[26].

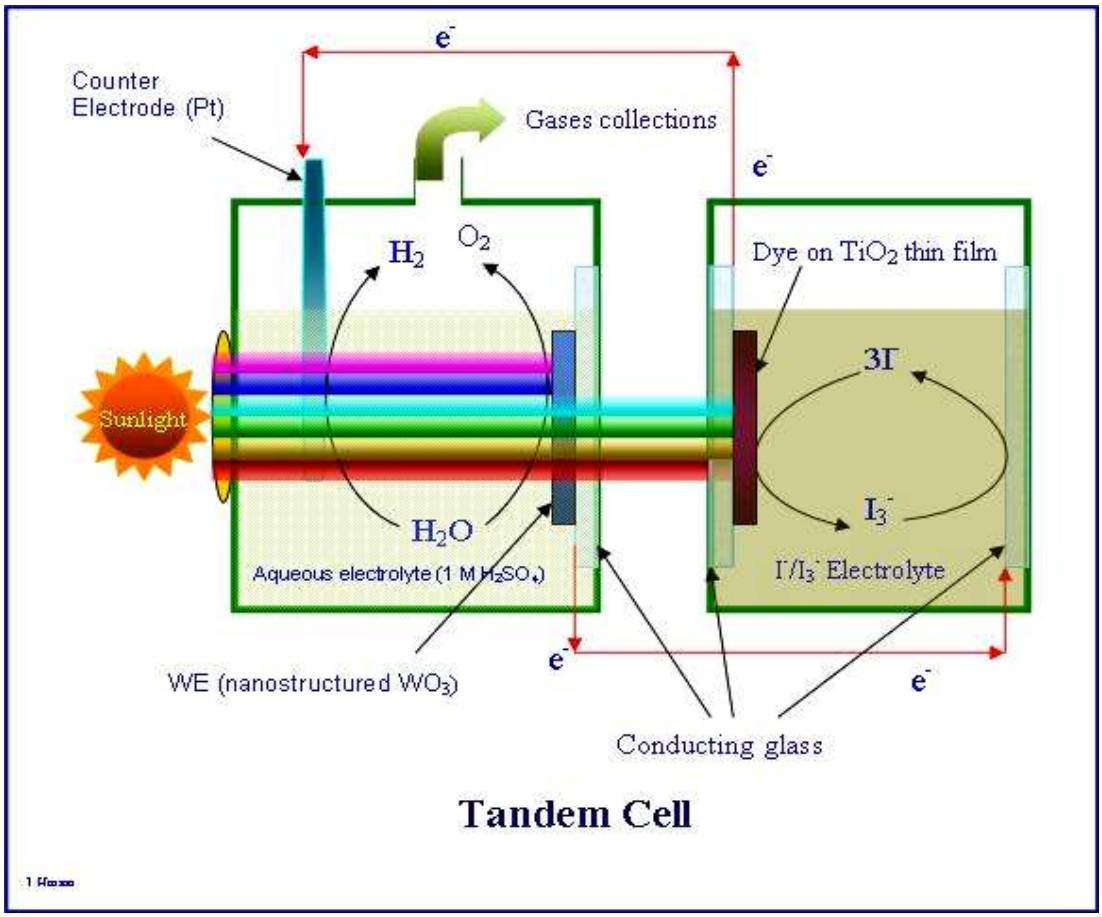

Figure 1.2. A diagrammatic representation of a tandem cell device with hydrogen and oxygen evolution driven in a two stages light absorption process.

When the ultraviolet and blue parts of the light have been absorbed by the electrode in the front photosystem (see Figure 1.2), an excitation of valance band electrons occurs and a charge carrier pair, a hole (h^+) and an electron, are produced. The holes migrate into the electrode/electrolyte interface, which is full of reduced species (OH^-) and oxidation of water occurs into oxygen as it is shown in equation 1.4. The electrons produced in the conduction band (CB) of the front electrode are not energetic enough for hydrogen production and they transfer into the second photosystem which promotes electrons into the dye which then be injected into the CB of the TiO_2 as it shown in Figure 1.3.

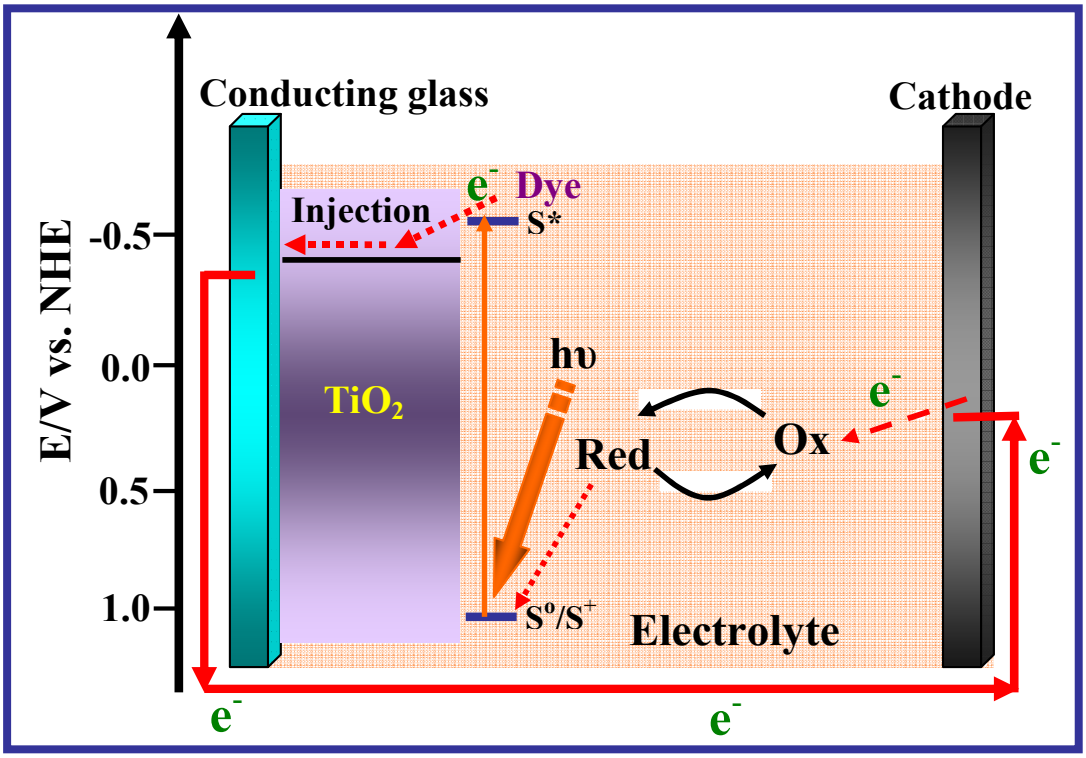

Figure 1.3 Schematic of operation of the dye-sensitised electrochemical photovoltaic cell.

The total produced electrons are collected on the platinum electrode in the front photosystem and the total potential is able to reduce hydrogen on the cathode (Pt):

$$4H^+ + 4e^- \rightarrow 2H_2 \qquad (1.7)$$

The overall photoelectrochemical water splitting process which is taken place in tandem cell can be compared to the biological 'Z-scheme' for photosynthesis (see Figure 1.4a and b).

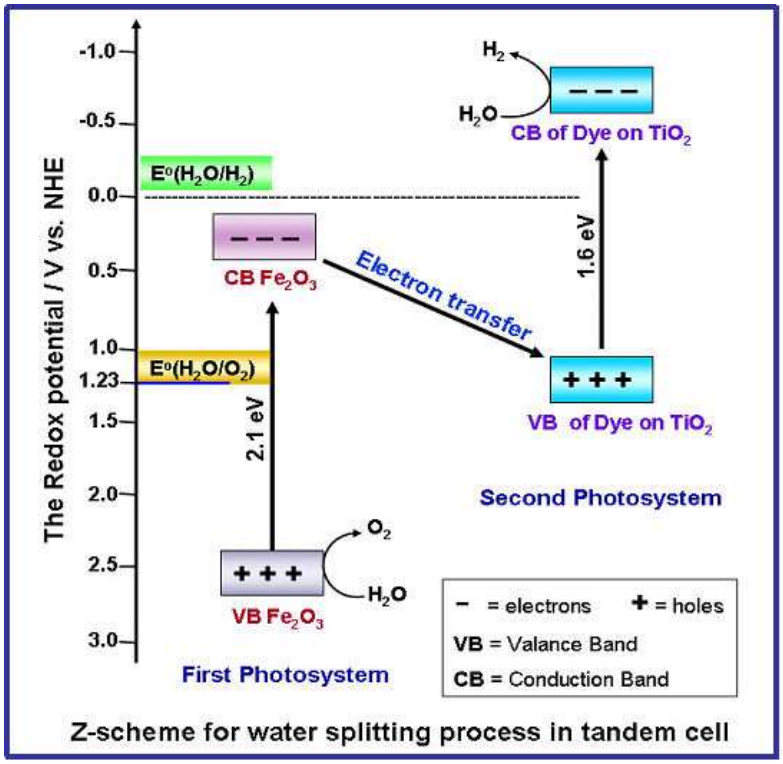

Figure 1.4a. The Z-scheme of photocatalytic water decomposition by a tandem cell.

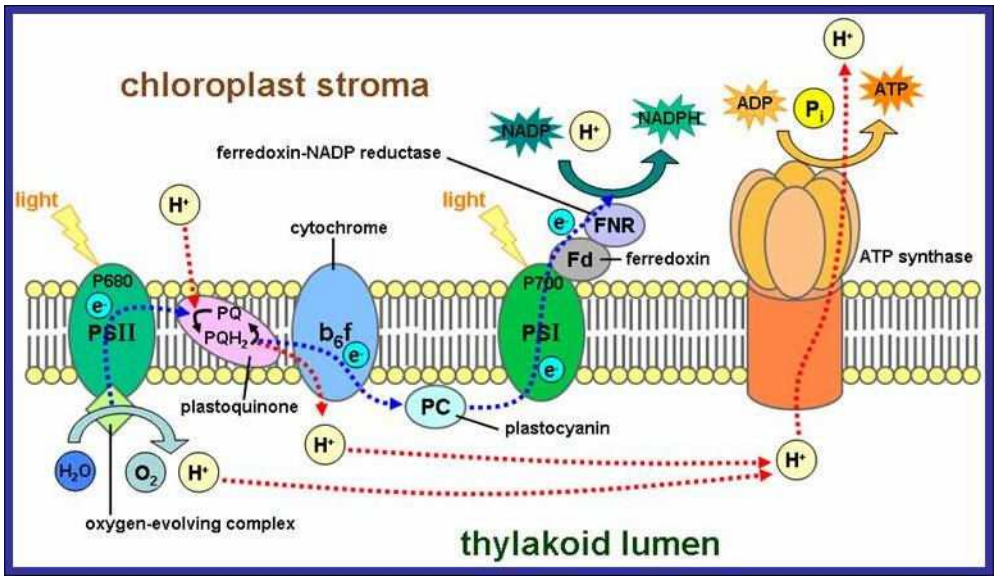

Figure 1.4b. Biological 'Z-scheme' shows light-dependent reactions of photosynthesis at the thylakoid membrane

One of the most important advantages of the tandem cell is that efficiency can be increased by absorption over the whole light spectrum and by connecting the two "photosystem" in parrallel as shown in Figure 1.5. In 2001 it was reported that the overall tandem cell efficiency was only 4.5 % leading to a concerted investigation of

the photosystems efficiencies and stability in order to make this device a cost effective way of producing chemical energy on an industrial scale.

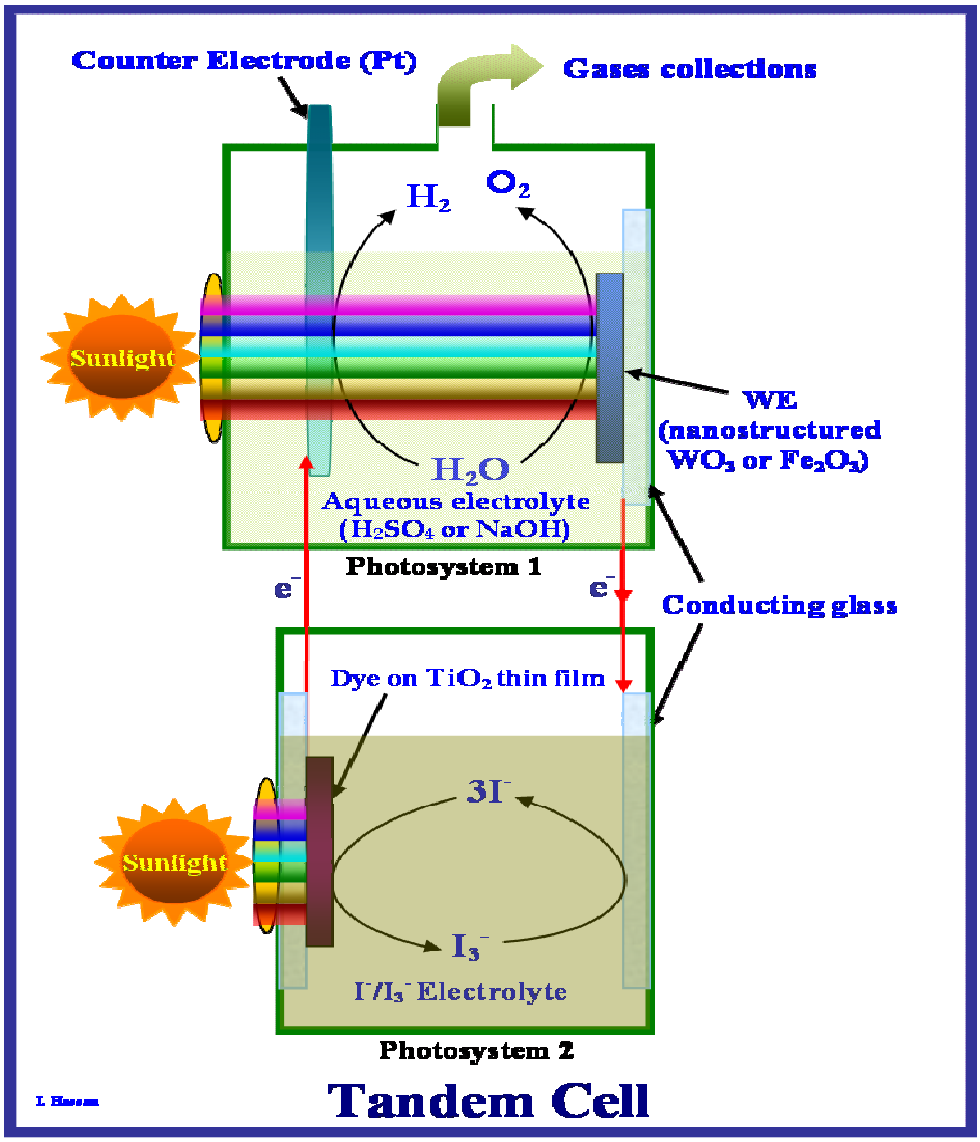

Figure 1.5. A diagrammatic representation of a tandem cell device with hydrogen and oxygen evolution driven in a one stage light absorption process.

1.5. The Contribution Made by this Study

In this study transition metal oxide films are investigated as anodic photo-electrochemical systems for oxygen evolution. First mesoporous WO_3 films are investigated and then different types of nanostructured Fe_2O_3 films are studied. The main aims of the work are to **(i)** develop experimental methods for the quantitative understanding of processes during photoelectrochemical oxygen evolution and **(ii)** a

better understanding of the effects introduced by the type of transition metal oxide, its morphology, and the film architecture.

1.6. References

(1) Casper, J. K., *Fossil Fuels and Pollution: The Future of Air Quality*, Facts On File, New York, **2010**.

(2) Barker, T.; Ekins, P.; Johnstone, N., *Global Warming and Energy Demand,* 2nd ed., the Taylor & Francis e-Library, New York, **2005.**

(3) Hoffert, M. I.; Caldeira, K.; Jain, A. K.; Haites, E. F.; Harveyk, L. D. D.; Potter, S. D.; Schlesinger, M. E.; Schneider, S. H.; Watts, R. G.; Wigley, T. M. L.; Wuebbles, D. J., *Nature*, **1998,** *395,* 881.

(4) Nozik, A. J., *NCPV and Solar Program Review Meeting,* NCPV/CD-520-33586 Page 422**, 2003**, 1-5.

(5) Archer, M. D.; Hill, R.; *Clean Electricity from Photovoltaic*, Imperial College Press, London , UK 1st ed., **2001**.

(6) Grimes, C. A.; Varghese, O. K.; Ranjan, S., *Light, Water, Hydrogen: The Solar Generation of Hydrogen by Water Photoelectrolysis*, Springer Science + Business Media, LLC, New York, **1988**.

(7) Yerga, R. M. N.; Galvan, M. C. A.; del Valle, F.; de la Mano, J. A. V.; Fierro, J. L. G., *ChemSusChem*, **2009**, *2*, 471 – 485.

(8) Grätzel, M., *Nature*, **2001,** *414*, 338.

(9) Redford, D. B.; *Akhenaten: The Heretic King,* Princeton University Press, New Jersy, USA, **1987**.

(10) Fahrenbruch, A. L.; Bube, R. H., *Fundamentals of Solar Cells, : Photovoltaic Solar Energy Conversion*, Academic Press Inc, San Diego,USA, **1983**.

(11) Telkes, Maria, *J. App. Phys.*, **1947,***18*, 1116.

(12) Chapin, D. M.; Fuller, C.S.; Pearson, G.L., *J. Appl. Phys.*, **1954,** *25*, 676.

(13) Fujishima, A.; Honda, K., *Nature*, **1972,** *37*, 238.

(14) Bauer, G. H., *App. Surf. Sci. Part B*, **1993,** *70*, 650.

(15) O'Regan, B.; Grätzel, M., *Nature*, **1991,** *353*, 737.

(16) Grätzel, M., *Cattech*, **1999,** *3*, 3.

(17) Alexandru, E.; Anca D.; Joop S. *Thin Solid Films,* **2007,** *515,* 6371–6374.

(18) Hodes G.; Cahen D., Manassen J. Nature **1976**, 260, 312.

(19) Ulmann, M. S.; Augustynski, J. J. *appl. Phys. Chem*. **1983**, *54*, 6061.

(20) Sun, X.; Maeda, K.; Faucheur, M.; Teramura, K.; Domen, K., *Applied Catalysis A: General,* **2007,** *327,* 114–121.

(21) Maeda, K.; Teramura, K.; Lu, D.; Saito, N.; Inoue, Y.; Domen, K., *Angew. Chem. Int. Ed.,* **2006**, *45*, 7806-7809.

(22) Gao, Y.; Wang, Y.; Wang, Y., *React. Kinet. Catal. Lett.* **2007,** *91*, (1), 13−19.

(23) Santato, C.; Ulmann, M.; Augustynski, J., *J. Phys. Chem. B*, **2001**, *105,* 936.

(24) Khan, S., Akikusa, J., *J. Phys. Chem. B.,* **1999,** *103,* 7184.

(25) http://www.hydrogensolar.com/basics.html, Jan. **2011**.

Chapter 2

Introduction to the Theory of Photoelectrochemical Processes at Semiconductor Electrodes

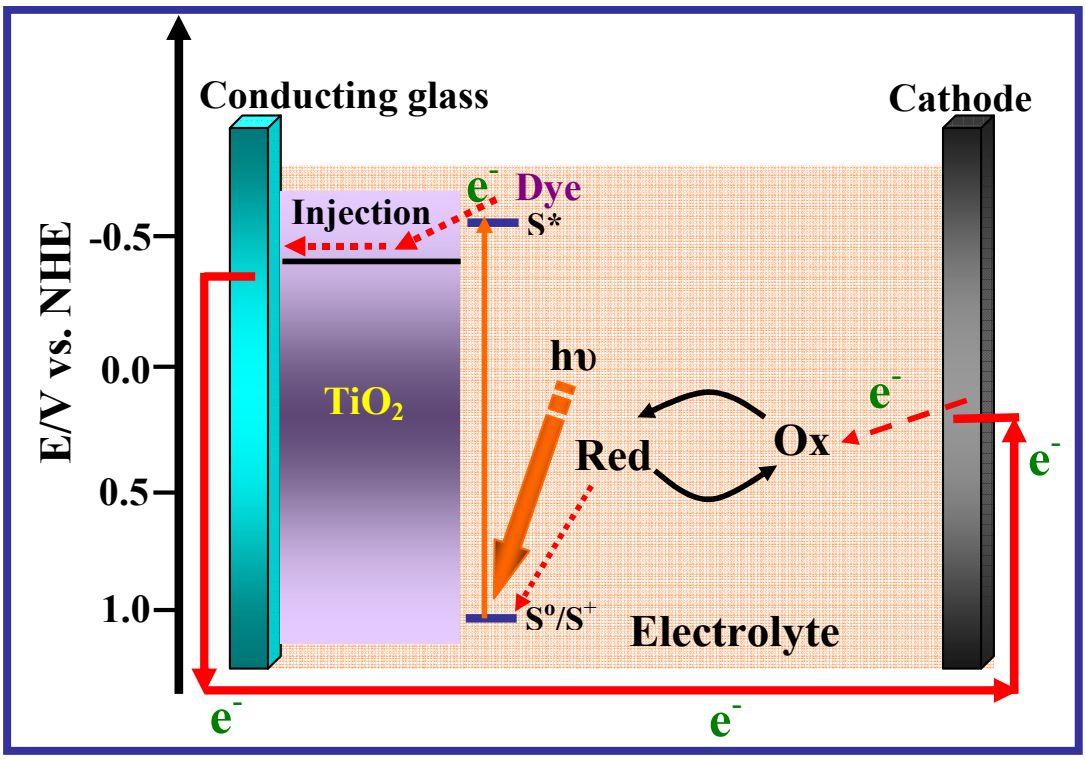

Abstract. In this chapter the fundamental description of semiconductor properties and of the processes at semiconductor | aqueous electrolyte junctions are reviewed. The effects introduced by photo-excitation and the obstacles for efficient energy harvesting via charge transfer at the interface are investigated.

Content

2.1. Introduction to Semiconductor Properties

Accumulation of isolated atoms into interacting structures causes formation of filled and vacant orbitals. In a solid these orbitals are very close in energy so that they form a continuous band of energy levels. The filled "bonding orbitals" form the valence band and the vacant "anti-bonding orbitals" form the conduction band. The energy gap between these bands, here called band gap (E_g), gives the Boltzmann distribution factor for the system. In wide band-gap structures, the valence band (VB, with uppermost energy E_{VB}) is almost filled, and the conduction band (CB, with lowest energy E_{CB}) is almost vacant. The size of the band gap strongly affects the optical properties of solids. If the band gap is large, the valence band is full with electrons and the conduction band is empty, and the material doesn't conduct electricity and is called electrical insulator. If the band gap is intermediate, conduction can be achieved by small thermal promotion or photo-excitation of electrons from the valence band into the conduction band. These materials called semiconductors. Very low band gaps result in degenerate semiconductors. Finally, if the valence and conduction bands overlap into a continuous band, the material is called electrical conductors[1]. Figure 2.1 shows the energy bands in solids, and the energy gaps between the bands. In semiconductors with intermediate energy band gap, the presence of a small percentage of dopant atoms can strongly increase conductivity.

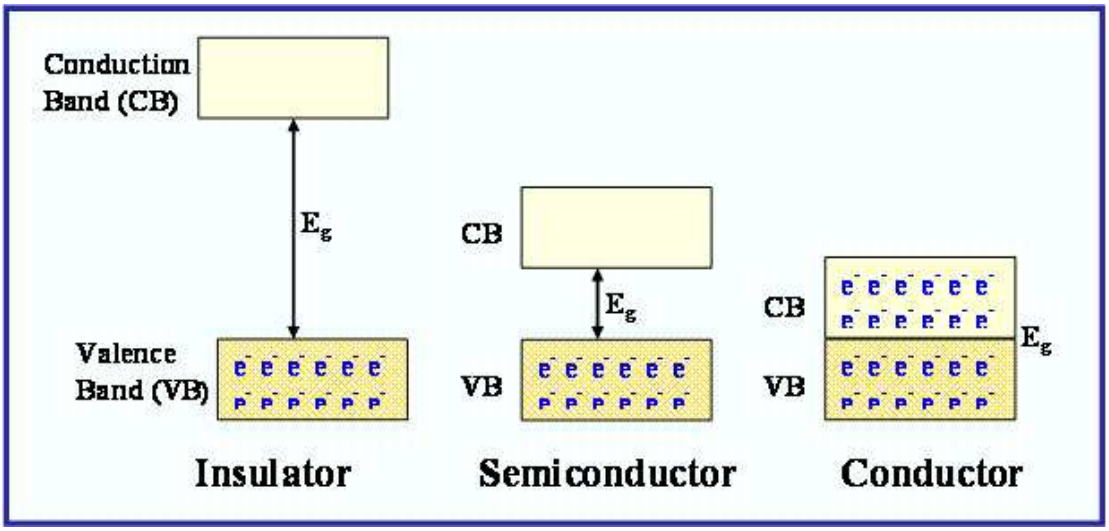

Figure 2.1. The energy bands and the band gap between valence and conduction band in solids.

It was estimated that[2] the band gap values in semiconductors range typically between 0.3 and 3.8 eV. If the semiconductor has a band gap more than 1 eV at standard pressure and temperature, it is only very minimally conducting electricity. However if

the semiconductor has a band gap less than 1 eV, its conductivity in the pure state will be appreciable at 300 K. For excitation of the semiconductor, the activation energy must be greater or equal to the band gap energy[3]. If an excitation of a valence band electron occurs, then charge carrier conduction becomes possible. The excited electrons leave holes behind them in the valance band, which can also move resulting in an additional increases the conductivity. Figure 2.2 shows the 'electron-hole pair' formation process and the photoelectrochemical reactions on the interface of a semiconductor (n- and p-types) and the electrolyte, which will be explained in more detail later in this chapter.

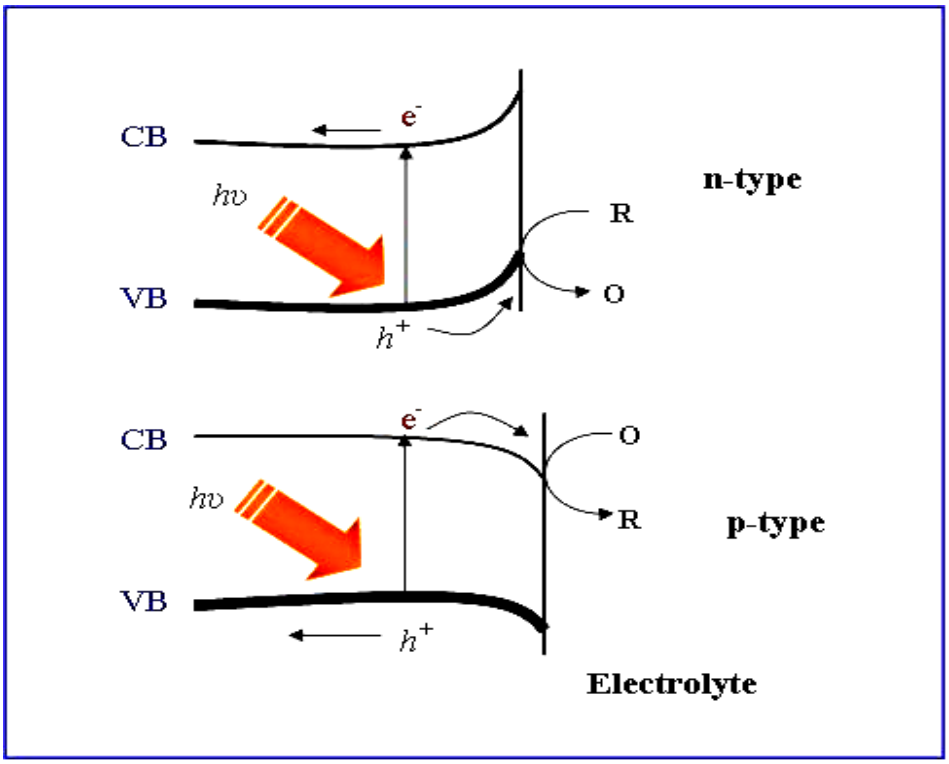

Figure 2.2. The photoelectrochemical process at the semiconductor/electrolyte junction for an n-type surface with positive polarization and for a p-type surface with negative polarization.

At 0 K semiconductor materials have a completely electron-filled valence band separated by only a small energy gap (~1 eV or less) from an empty conduction band. At this low temperature, there is no electrical conduction because the electrons are unable to change their energy states in a small applied electric fields[4]. By increasing the temperature, the electrical conduction increases due to the excitation of some electrons by the thermal activation energy. This characteristic, a positive thermal

coefficient, is opposite to the effect of temperature in metals where heating causes loss of electrical conductivity.

Most of the early fundamental and technological semiconductor development has been carried out with silicon and germanium[4]. Electronically related materials were discovered for "III-V semiconductors". An intensive study of these semiconductors has resulted in many new electronic devices which composed of a trivalent atom with a pentavalent atom such as in GaAs, GaP, InSb, InAs, and InP.

2.2. Doping of Semiconductors

Doping processes of semiconductors refers to the introduction of defects and impurities into an extremely pure (intrinsic) semiconductor in order to change its optical and electrical properties[5]. Impurities can be classified into two categories: donors and acceptors. Donors are elements which donate "excess electrons" to the conduction band. Acceptors are elements accepting electrons and thereby creating hole in the valence band[5]. The addition of small and controlled amounts of certain impurities can affect strongly the electrical properties of semiconductors[4], and this is vital in the development of devices based on semiconductors. The choice of the impurities is dependent upon the type of semiconductor. Lightly and moderately doped semiconductors are referred to as extrinsic. A semiconductor which is doped to such high levels that it acts more like a conductor than a semiconductor is called degenerate[5].

There are two main types of semiconductors depending on the doping element (impurity). The first type is called n-type, which arises for example from doping of a tetravalent semiconductor with a pentavalent element (donor). In this case the semiconductor is dominated by donors and there will be sufficient electrons to take up the four covalent bonds to all its neighbours, and the fifth electron will be left free[4]. In this type of semiconductors, which is dominated by electrons, the electrons are termed 'majority carriers' and the holes are called 'minority carriers'. ZnO and TiO_2 are examples of materials that are always found n-type due to oxygen vacancies.

The second type of doped semiconductors is called p-type, which means for example doping of a tetravalent semiconductor with a trivalent element (acceptor). In this case the semiconductor is dominated by acceptors and there will be a shortage of one electron to complete bonding to the tetravalent neighbours. This electron can be borrowed with very little energy (~ 10^{-2} eV) from a neighbouring atom leaving a hole in the valence band. This behaviour generates holes in the semiconductor [4]. Cu_2O and NiO_2 are examples of semiconductors that are always found to be p-type [6] due to defects.

2.3. Direct and Indirect Semiconductors

Semiconductors are distinguished according to the energy difference between the valence and the conduction band, which called the band gap E_g. More accurately, the band gap is the minimum energy difference between the top of the valence band and the bottom of the conduction band. However, the top of the valence band and the bottom of the conduction band are not usually at the same value of the electron momentum. Therefore, a transition of the electron from valence to conduction band can be associated with a "forbidden" change in momentum. There are two different classes of semiconductors:

Direct Semiconductors: here the top of the valence band and the bottom of the conduction band occur at the same value of electron momentum, as it is shown in Figure 2.3.

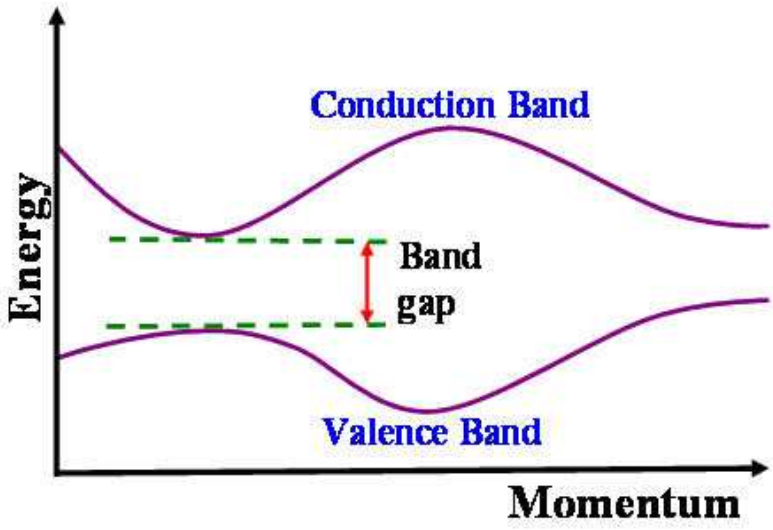

Figure 2.3. Schematic diagram showing the band gap for a semiconductor as a function of electron momentum. A "direct transition" is possible in this direct semiconductor due to the match in momentum.

Indirect Semiconductors: here the maximum energy of the valence band occurs at a different value of electron momentum to the minimum energy of the conduction band, as it is shown in Figure 2.4**.** An optical transition of the electron from valence to conduction band is therefore associated with a "forbidden" change in momentum. These transitions are weak.

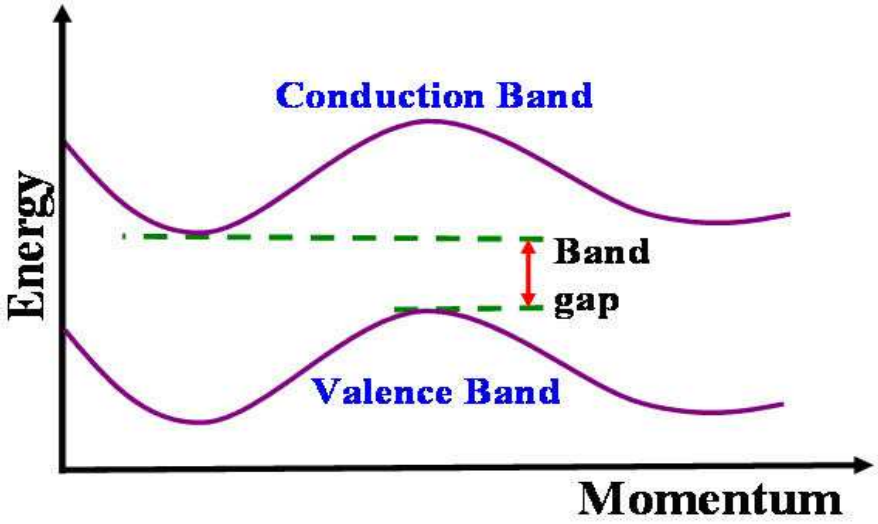

Figure 2.4. Schematic diagram showing the band gap for a semiconductor as a function of electron momentum. An "indirect transition" is required in this indirect semiconductor due to mismatch of momentum.

A pair of electrons-holes can be produced by photons when they hit the semiconductor with energy equal or more than the band gap. This process is quite

easy (with high extinction coefficient) in direct semiconductors because the excited electron doesn't need to change momentum to move from valence to conduction band. However, in case of indirect semiconductor the electron must undergo a change in its momentum for a photon of energy of the band gap to produce an electron-hole pair. This can happen but it requires that electron to not only interact with the light photon to get the excitation energy, but also with the lattice vibrations called phonons to either lose or gain momentum. This slows down the indirect processes (low extinction coefficient). Gallium arsenide is an example for direct semiconductors, which are used to manufacture optical devices such as LEDs and lasers. Silicon is a famous example for indirect semiconductors, as are WO_3 and Fe_2O_3.

2.4. Recombination Centres and Trapping Sites in Semiconductors

Semiconductors have defect sites in the crystal lattice such as dislocations, vacancies, or impurities. Particle boundaries between crystallites can also be considered as potential trapping sites. The trapping sites can capture charge carriers (holes/electrons) from the valence and conduction band so that they recombine and therefore these sites called recombination centres. This recombination affects detrimentally the photocurrent until the trapping sites be filled then the photocurrent can increase. Figure 2.5 shows a schematic drawing of the trapping sites in the WO_3 lattice affecting the rate of electron transport.

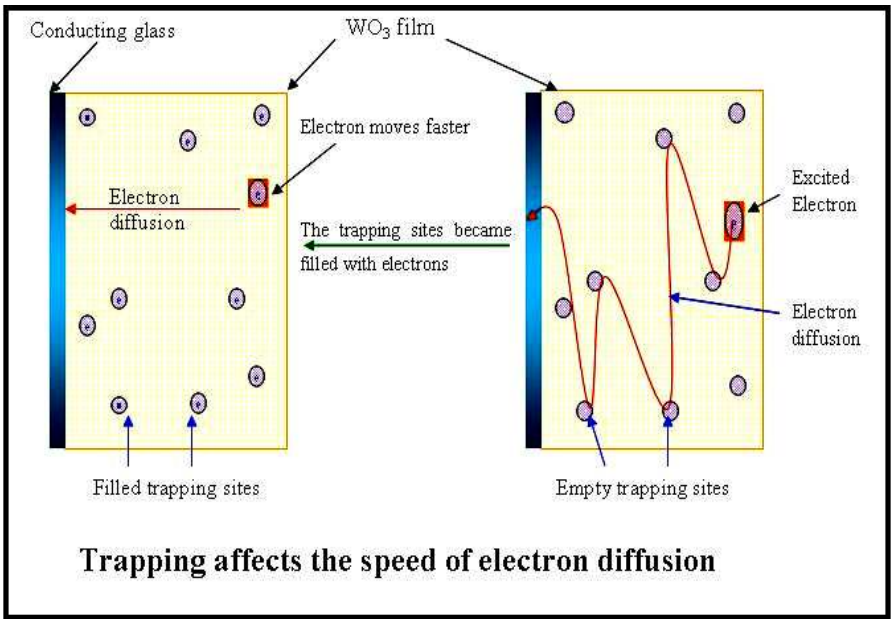

Figure 2.5. Schematic drawing of the effect of trapping processes on the electron diffusion in a WO_3 semiconductor film.

2.5. The Semiconductor | Electrolyte Junction

The formation of a semiconductor-electrolyte junction controls most of the processes accompanied with photoelectrochemical reactions in photoelectrochemical cells. When a semiconductor is immersed in an electrolyte, electrical current flows across the junction until equilibrium between the potential (the Fermi level) of the semiconductor and that of the redox couple in the electrolyte is reached. In the semiconductor, the Fermi level potential represents the chemical potential of electrons. In the electrolyte the redox potential of the redox couples (as expressed in the Nernst equation) represents the electrochemical potential of electrons or the Fermi level of the electrolyte [7, 8]. The equilibrium can be reached when the semiconductor Fermi level (E_F) equals the redox potential of the electrolyte (E_{redox}). In the intrinsic (un-doped) semiconductor, the Fermi level locates in about half distance between the valence and the conduction band, while in extrinsic (doped) semiconductor, the Fermi level locates either close to the valence or conduction band according to the dopants type. If the extrinsic semiconductor is n-type, its Fermi level is usually above the Fermi level of the electrolyte, so equilibrium occurs via transfer of electrons from the semiconductor to the electrolyte. While if the semiconductor is p-type, its Fermi level will be lower than that of the electrolyte, and the electrons transfer from the electrolyte to the semiconductor. At the equilibrium, a positive charge area known as the space-charge or depletion layer, since the region is depleted of majority charge carriers ‘‘the electrons’’, distributes on each side of the junction, which differs from the bulk charge distribution in the semiconductor. Consequently, the valence and conduction band edges are bent upwards and a potential barrier is established against further electron transfer from the semiconductor into the electrolyte through the junction. On the electrolyte side of the junction the electrical double layer, which may be envisaged as the compact (Helmholtz) layer, is formed followed by a diffusion (Gouy-Chapman) layer as it is shown in Figure 2.6.

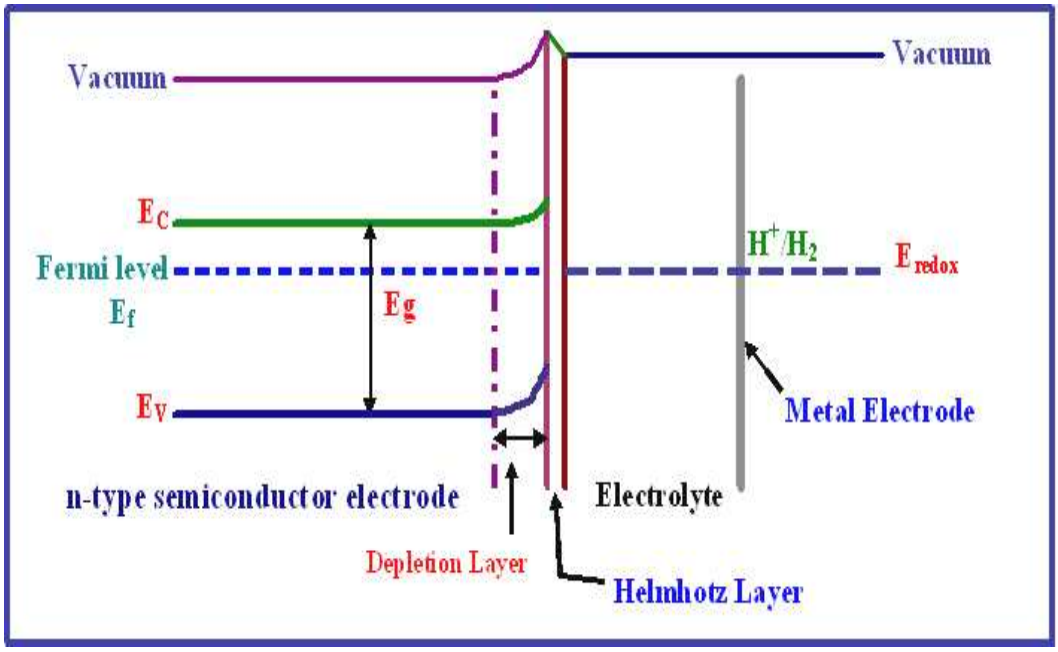

Figure 2.6. Schematic drawing of the semiconductor (n-type)/electrolyte interface. In the semiconductor (left) side E_g is the band gap between valence (E_V) and conduction (E_C) band potential. The depletion layer is the space charge layer. In the electrolyte (right) side H^+/H_2 is the redox couple in the electrolyte and the Helmholtz layer (compact layer) is followed by Gouy-Chapman (diffusion layer).

2.6. The Flat Band Potential

The flat band potential E_{fb} is a very useful quantity in photo-electrochemistry as it defines the transition between depletion and accumulation effects and thereby is associated with the energy of the band edge of a given semiconductor material. The semiconductor is subjected to an applied voltage, which increases the potential applied across the semiconductor-electrolyte junction. Under depletion conditions there are only few charge carriers at the interface whereas under accumulation conditions the concentration of charge carriers rises and the interfacial capacitance increases. This effect can be used experimentally to measure the flat band potential. Using the Mott-Schottky equation (eq. 2.1) the flat band potential of the semiconductor can be determined.

$$\frac{1}{(C_{SC})^2} = \frac{2\,(\Delta\Phi_{SC}\,RT\,/\,F)}{\varepsilon_o\,\varepsilon\,N} \qquad (2.1)$$

In this expression, $\Delta\Phi_{SC} = E\text{-}E_{fb}$ is the voltage drop in the space-charge layer, R is the gas constant, F the Faraday constant, ε the dielectric constant of the semiconductor, ε_o the permittivity of the vacuum and N is the ionised donor dopant concentration. A plot of the square of the reciprocal capacity (C_{SC}, measured) against the applied voltage gives a straight line and this is extrapolated to $1/(C_{SC})^2 = 0$ to derive the flat band potential E_{fb} as it is shown in Figure 2.7.

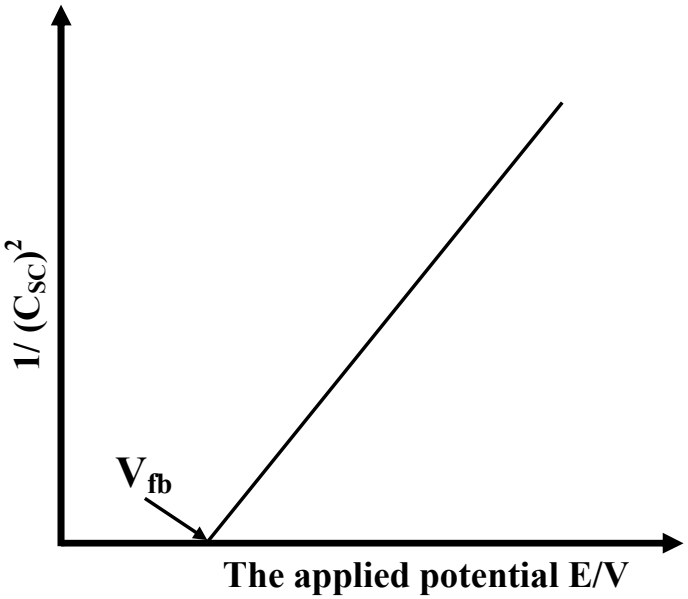

Figure 2.7. Calculation of the flat band (V_{fb}) through the relationship between the applied potentials and the square of the reciprocal capacity.

Flat band potentials have been determined for many materials[9] and based on this the valence and conduction band positioins have been estimated. A selection of values is shown in Figure 2.8. In aqueous solution the band potentials of most oxide semiconductors shift by 0.059 V per pH unit. This is a consequence of protons in the electrolyte solution acting as potential balancing ions at the interface.

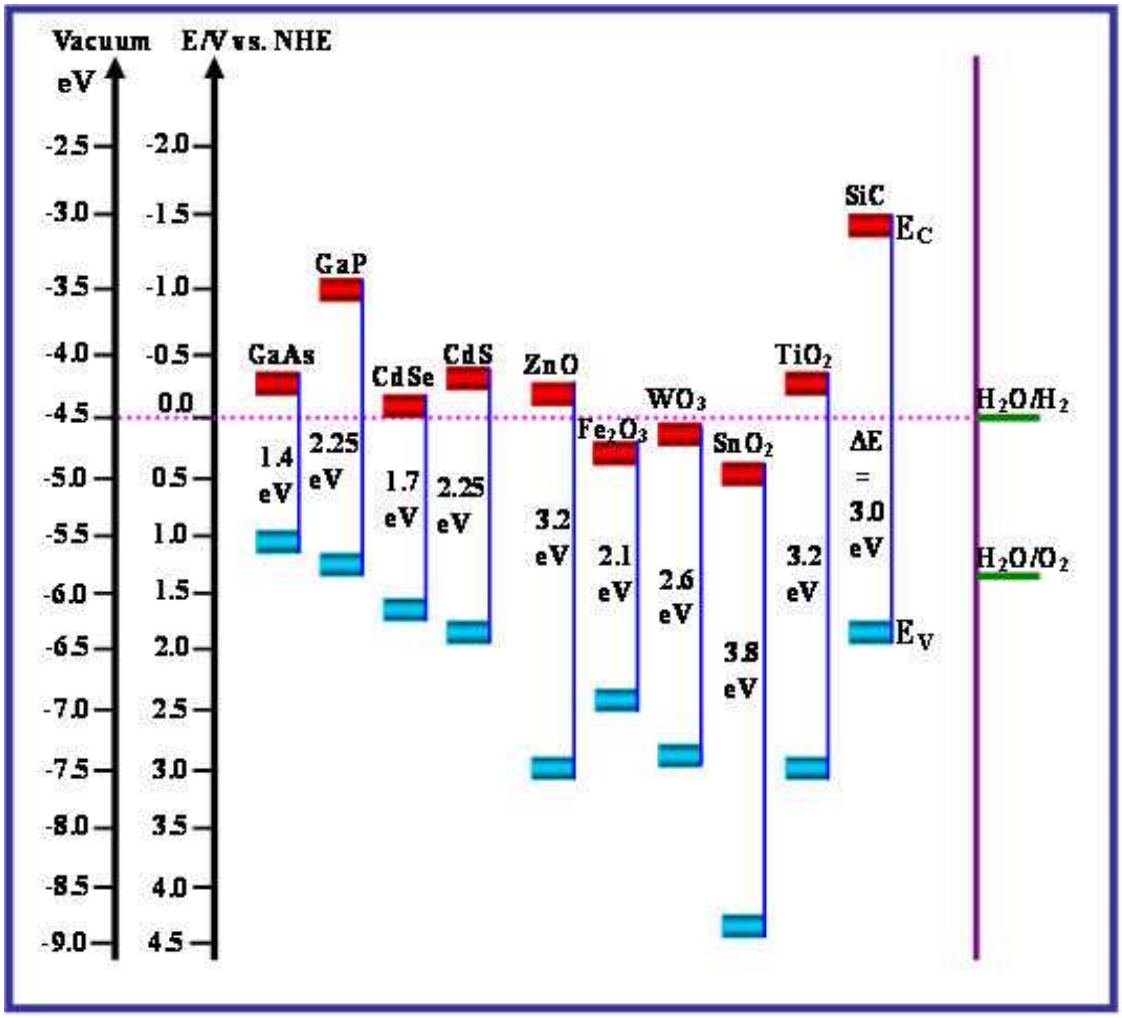

Figure 2.8. Band positions for some semiconductors in contact with an aqueous electrolyte at pH = 1.

2.7. Photoelectrochemical Processes and Photocorrosion Reactions

Photo-electrochemical processes are based on production of interfacial electron-hole pairs by the action of light. The semiconductor plays the main role as a working electrode in contact to the electrolyte. Generally the photo-generation of holes and electrons in semiconductor materials are characterized by the strong oxidation and reduction potentials for the photo-generated holes and electrons, respectively. Sometimes it happens that these holes and electrons can oxidize or reduce the semiconductor itself causing electrode decomposition or corrosion, which is one of the most troublesome problems in photo-electrochemical reactions[10]. It was found that metal oxide semiconductors are relatively stable to photocorrosion in aqueous solution but they have a considerable band gap. Attempts to minimise the band gap of the metal oxide semiconductor to increase their photoactivity and limit

photocorrosion have been reported. For example, to overcome the large band gap of TiO_2 (3.2 eV) a dye has been used to cover the TiO_2 film surface. The dye absorbs the light and consequently an electron excitation occurs from the dye HOMO (highest occupied molecular orbital) to the dye LUMO (lowest unoccupied molecular orbital) which inject the electrons into the conduction band of TiO_2[11] as it shown in Figure 2.9. Crucially, in this process no high energy hole is generated.

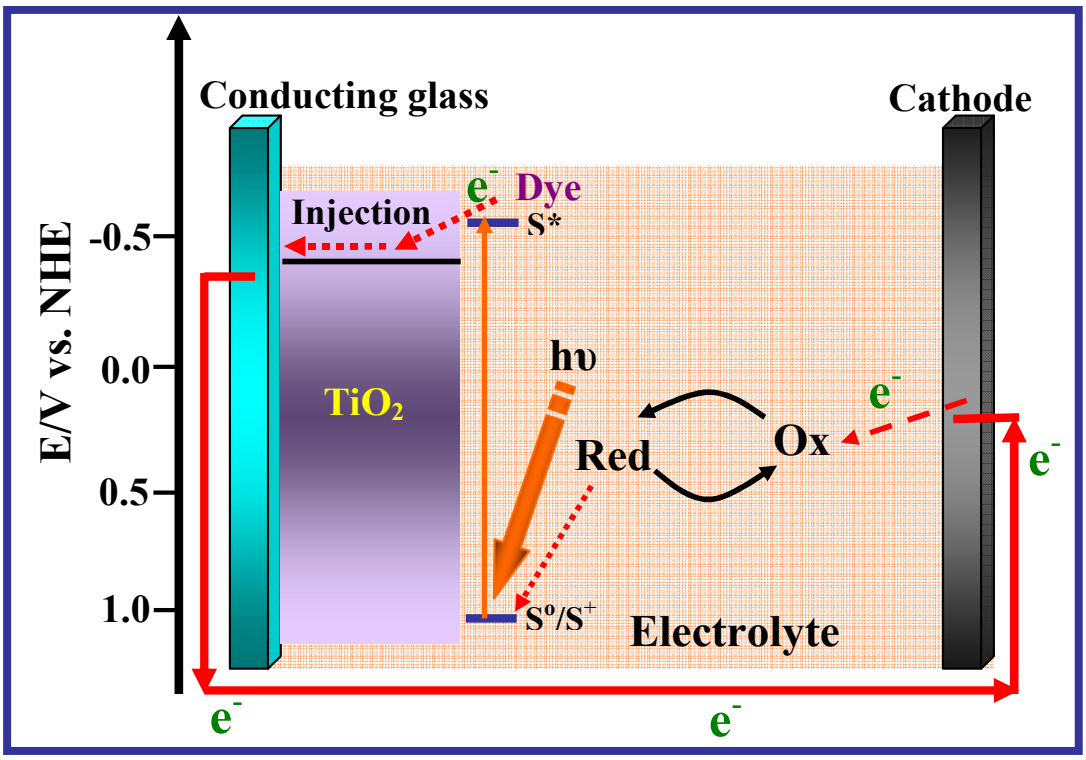

Figure 2.9. Schematic of operation of the dye-sensitised electrochemical photovoltaic cell.

2.8. Catalysis of Oxygen Evolution at Semiconductor Surfaces

The formation of electron – hole pairs at the semiconductor | electrolyte interface is followed by the extraction of the electron and the reaction of the hole. Photocatalytic reaction of water to oxygen during photo-elelectrochemical water splitting at semiconductor surfaces has received considerable attention as a new type of clean energy supply with minimal environmental impact [12]. However, the formation of O_2 from H_2O is a complex multi-step process and associated with large overpotentials on most electrode surfaces. Good catalyst surfaces are desirable for maximum energy harvesting. Photocatalytic oxygen evolution has been studied for example on α-Fe_2O_3

electrodes [13]. It was found that there are several important factors affecting the oxygen evolution reaction rate such as electrolyte anion, Fe^{3+} ion concentration, pH value, Fe^{3+} / Fe^{2+} equilibrium concentration and incident light wavelength (λ). It was found that the oxygen evolution stopped at Fe^{3+} / Fe^{2+} concentration ratio of 3: 7 – 4: 6. It was also found that the evolution rate dramatically decreased at longer wavelength incident light (> 400 nm). Increasing the pH value increases the oxygen evolution. During illumination and oxygen evolution, α-Fe_2O_3 films also peeled off the substrate and dissolved in the electrolyte [13].

In recent studies on catalysts the work by Nocera et al.[14] has attracted considerable attention. Cobalt phosphate [15], nickel borate [16], and cobalt borate [17] are the latest materials with high promise [18]. Previously catalysts based on ruthenium oxide[19] and molecular ruthenium complexes[20] have been investigated. Grätzel and coworkers[21] developed highly promising oxygen evolving photo-electrodes based on Fe_2O_3[22] coated with cobalt oxide or with iridium oxide [23]. The study of both photo-catalytic films and catalyst coatings on semiconductor films is in rapid development and new improved systems are becoming now available [24]. The use of Fe_2O_3 has also been proposed for the hydrogen evolution process [25].

2.9. Overall Mechanism of Photoelectrochemical Oxygen Evolution at Semiconductor Surfaces

The oxygen evolution process is a complex multi-step process with important applications in energy harvesting technologies and in natural photosynthesis [26]. Catalysis is at the heart of both hydrogen and oxygen evolution. A schematic diagram for the case of platinum catalyst particles is shown in Figure 2.10.

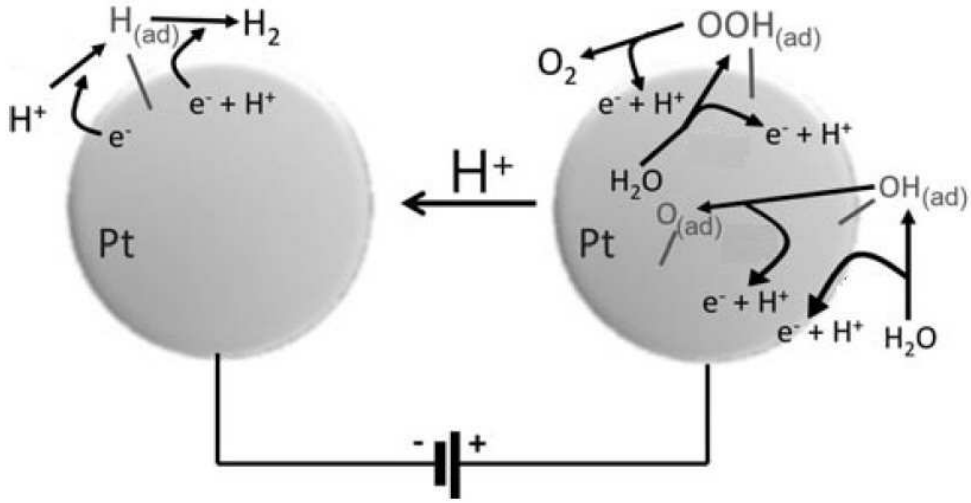

Figure 2.10. Schematic drawing of the energised formation of hydrogen and oxygen from water with two platinum catalyst particles indicating possible reaction intermediates [26].

The hydrogen evolution process proceeds via adsorbed intermediates and requires a surface bond formation process (see Figure 2.11.). The energy barrier for bond formation is strongly catalyst dependent and has to be considered as a contribution to the "thermochemical overpotential". Good catalysts have the ability to bind both protons and hydrogen in a balanced fashion to minimise the overpotential.

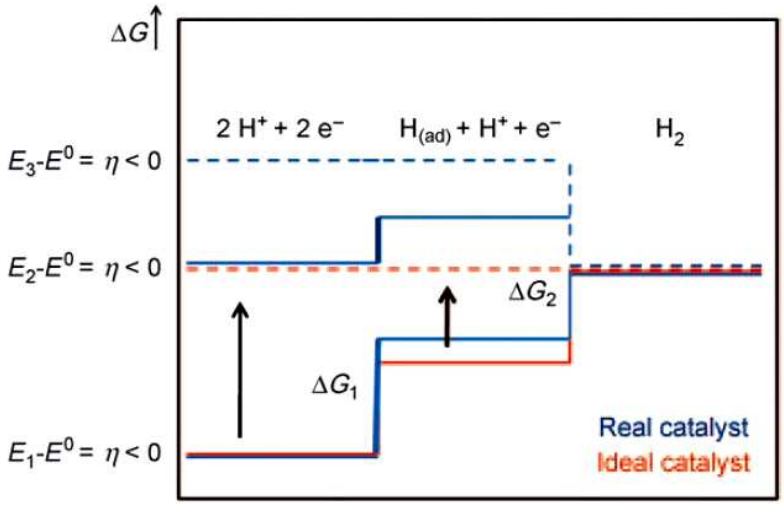

Figure 2.11. Diagrammatic representation of the reaction coordinate for the hydrogen evolution reaction and the corresponding Gibbs energy profiles for three applied potentials E_1, E_2, and E_3 [26].

The formation of oxygen requires at least four reaction steps and surface bond species may be associated with each of these (see Figure 2.12.). In the energy profile for this reaction the presence of additional overpotential is likely to arise during the bond formation step.

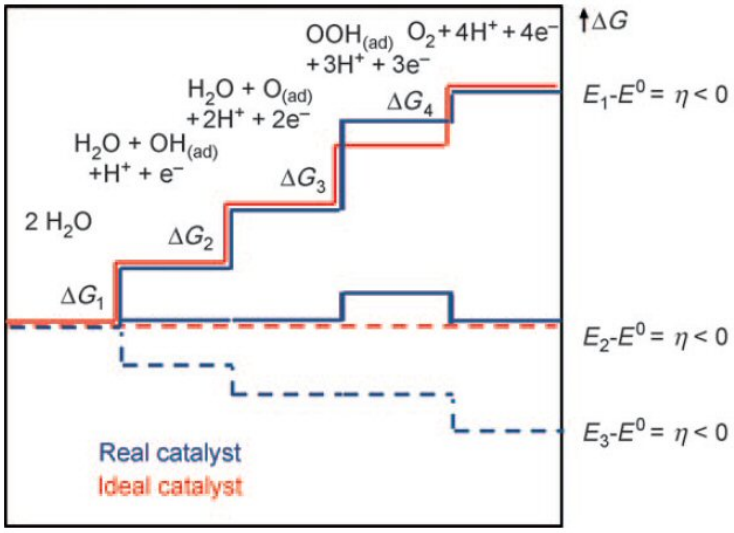

Figure 2.12. Diagrammatic representation of the reaction coordinate for the oxygen evolution reaction and the corresponding Gibbs energy profiles for three applied potentials E_1, E_2, and E_3 [26].

In nature, oxygenic photosynthesis has evolved and the problem of oxygen evolution was overcome in a highly developed redox cycle as introduced by Kok [27]. Figure 2.13 shows the photo-activated cycle where four photons provide energy and the four Mn centers contribute to binding of water and release of oxygen in a rate of typically one O_2 per 2 ms.

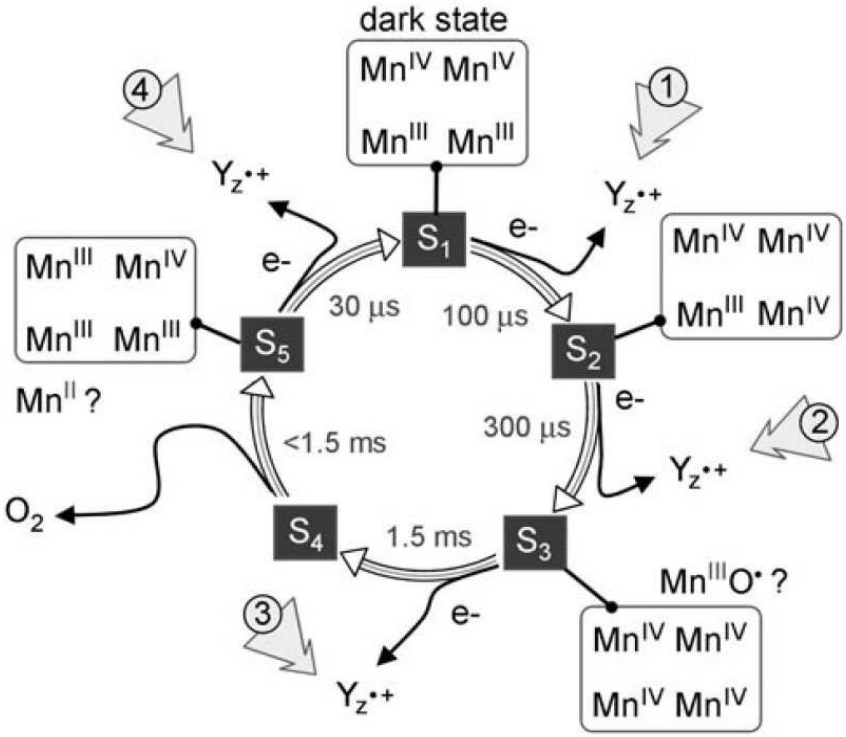

Figure 2.13. The Kok cycle[26] for the photosynthetic oxygen formation at a manganese cubane reaction centre. Yz is redox active Tyrosine.

The complexity of the natural oxygen evolution suggests that synthetic catalysts may still be far less developed and further improvements are likely especially when based on bio-mimetic systems.

2.10. Introduction to Photoelectrochemical Cells

Broadly, there are three types of photoelectrochemical cells [28,29] distinguished based on their mode of operation.

(A) Regenerative photoelectrochemical cells. Regenerative photoelectrochemical cells convert the light into electrical energy without any net chemical change. The incident photons of light generate electron-hole pairs. The electrons move to the conduction band and then to the external circuit. The holes are driven to the surface where they are scavenged by the reduced molecule (R), which exists in the redox pair in the electrolyte, and oxidise it ($h^+ + R \rightarrow O$). The electrons which re-entered the cell from the external circuit re-reduce the oxidised form ($e^- + O \rightarrow R$), for example n-type CdS in Na_2S_x (polysulfide) electrolyte, as shown in Figure 2.14.

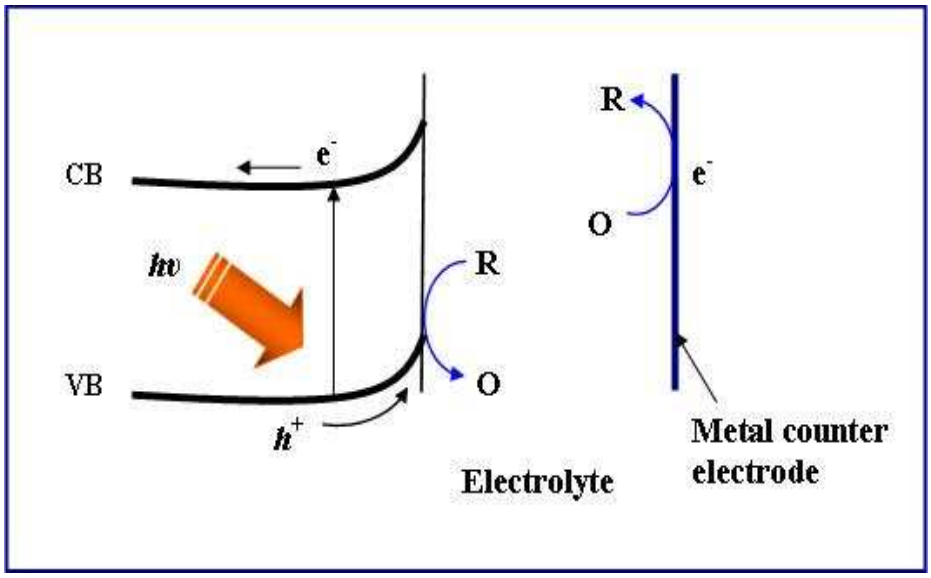

Figure 2.14: Schematic of the photoelectrochemical reactions on the regenerative photoelectrochemical cells.

(B) Photoelectrolysis cells. This type of cell is based on the photoelectrosynthetic process in which optical energy is converted into chemical free energy. Similar reactions to those in the regenerative cells occur except that there are two redox systems. One system is reacting with the positive holes at the surface of the semiconductor electrode and the second system is reacting with the negative charges (electrons) which enter from the counter electrode. Water splitting by sunlight is an example for this type of photoelectrolysis cells. Water is oxidised to oxygen at the semiconductor photoanode and reduced to hydrogen at the cathode (see Figure 2.15).

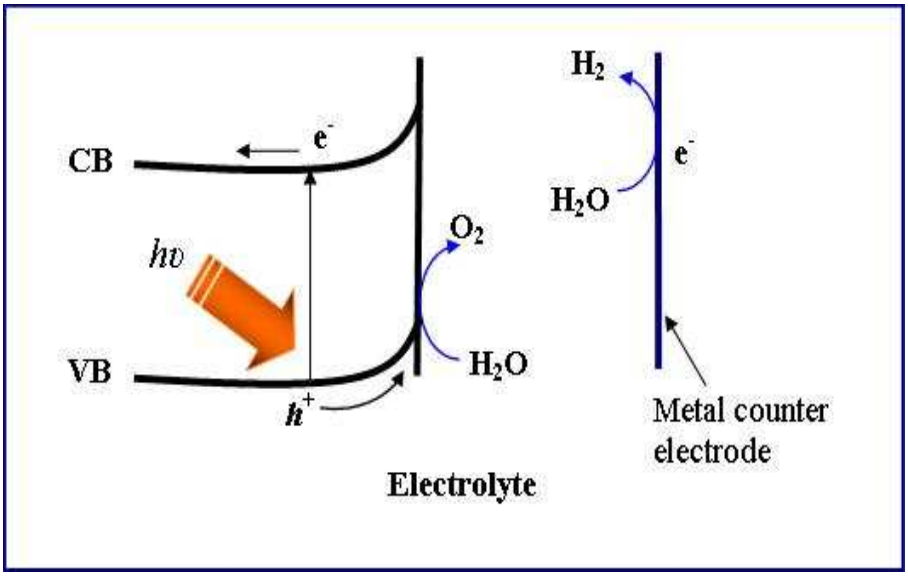

Figure 2.15: Schematic of the photoelectrochemical reactions on the photoelectrolysis cells

(C) Photocatalytic cells. This type of cell is a photosynthetic cell in which the net electrolyte reaction exhibits a negative free energy (spontaneous) change and the optical energy provides merely the activation energy for chemical reactions, see Figure 2.16.

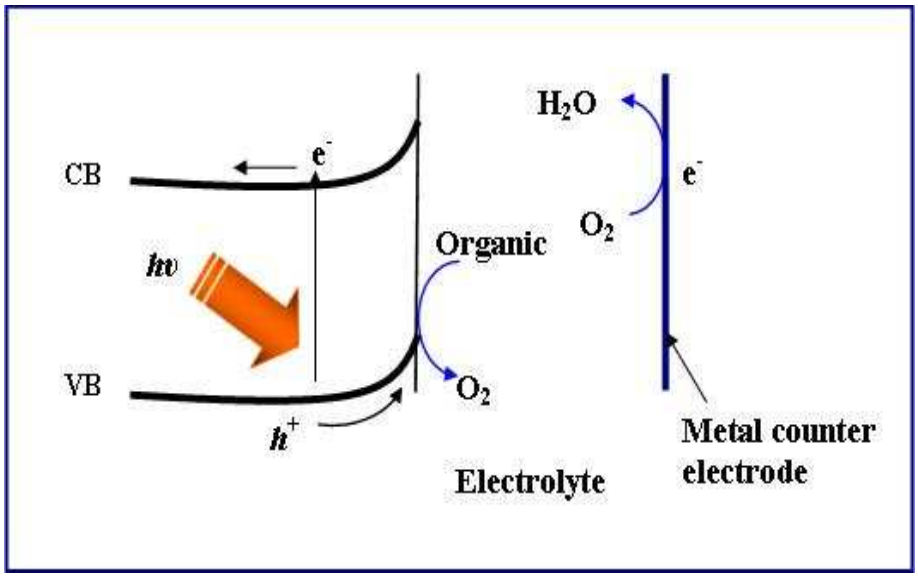

Figure 2.16: Schematic of the photoelectrochemical reactions on the photocatalytic cells

The type of cell of interest in this study is the photo-electrolysis cell where light energy is harvested in the form of a chemical energy carrier such as hydrogen. The formation of oxygen is necessary with an applied potential as low as possible to avoid energy losses. Photoelectrochemical processes will be studied as a function of potential and at various types of semiconductor electrode surfaces. Insight into the mechanism is obtained from photo-electrochemical measurements.

2.11. References

(1) Bard, A. J.; Faulkner, L. R., *Electrochemical Methods Fundamentals and Applications*, John Wiley & Sons, New York, **2001**.

(2) Linsebigler, A. L.; Lu, G. Q.; Yates, J. T., *Chemical Reviews,* **1995,** *95*, 735.

(3) Rosenberg, H. M., The Solid Sstate; an Introduction to the Physics of Crystals for Students of Physics, Materials Science, and Engineering, 2nd ed., J. W. Arrowsmith Ltd, Bristol, UK, **1978**.

(4) Woodyard, J. R., U.S. Patent 2,530,110 filed, **1944**, granted **1950.**

(5) Morrison, R., Electrochemistry at Semiconductor and Oxidized Metal Electrodes, Plenum Press, New York, **1980**.

(6) Alkire, R. C.; Gerischer, H.; Kolb, D. M.; Tobias, C. W., *Advances in Electrochemical Science and Engineering*, WILEY-VCH Verlag GmbH, D-69469 Weinheim, Germany, **1997**, *5*.

(7) Gerischer, H., J. Electroanal. Chem. Interfacial Electrochem., **1975,** 58, 263.

(8) Savenije, T.; Warman, J.; Goosens, A., *Chem. Phys. Lett.*, **1998,** *278*, 148.

(9) Nozik, A., *Photoeffects at Semiconductor-Electrolyte Interfaces*, American Chemical Society, Washington, D. C. **1981**.

(10) Grätzel, M., *Nature*, **2001,** *414,* 338.

(11) Nozik, A. J., *Phil. Trans. R. Soc. Lond. A,* **1980,** *295*, 453-470.

(12) Li, D.; Zheng, J., Li, Z.; Fan, X., Liu, L.; Zou, Z., *International Journal of Photoenergy,* **2007,** 1-7

(13) Ohmori, T.; Takahashi, H.; Mametsuka, H.; Suzuki, E., *Phys. Chem. Chem. Phys.*, **2000**, *2*, 3519-3522.

(14) McAlpin, J. G.; Gregory, J.; Surendranath, Y.; Dinca, M.; Stich, T. A.; Stoian, S. A.; Casey, W. H.; Nocera, D. G.; Britt, R. D., journal of the American Chemical Society, **2010**, *132*, (20) 6882.

(15) Kanan, M. W.; Yano, J.; Surendranath, Y.; Dinca, M.; Yachandra, V. K.; Nocera, D. G., *Journal of the American Chemical Society*, **2010**, *132*, (39), 13692-13701.

(16) Dinca, M; Surendranath, Y.; Nocera, D. G.; *Proceedings of the National Academy of Sciences of the United states of America*, 2010, *107*, (23), 10337-10341

(17) Esswein, A. J., Surendranath, Y.; Reece, S. Y.; Nocera, D. G., *Energy & Environmental Science*, **2011,** *4* (2) 499-504.

(18) Cook, T. R.; Dogutan, D. K.; Reece, S. Y.; Surendranath, Y.; Teets, T. S.; Nocera, D. G., *Chemical Reviews,* **2010,** *110*, (11) 6474-6502.

(19) Petrykin, V.; Macounova, K.; Shlyakhtin, O. A.; Krtil, P., *Angewandte Chemie International Edition,* **2010**, *49*, (28) 4813-4815.

(20) Yamazaki, H.; Shouji, A.; Kajita, M.; Yagi, M., *Coordination Chemistry Reviews,* 2010, *254,* (21-22) 2483-2491.

(21) Kay, A.; Cesar, I.; Gratzel, M., *Journal of the American Chemical Society*, **2006**, *128,* (49) 15714-15721.

(22) Duret A.; Gratzel, M., *Journal of Physical Chemistry B,* **2005,** *109*, (36), 17184-17191.

(23) Tilley, S. D.; Cornuz, M.; Sivula, K.; Gratzel, M., *Angewandte Chemie International Edition,* **2010**, *49,* (36), 6405-6408.

(24) Thimsen, E.; Le Formal, F.; Gratzel, M.; Warren, S. C., *Nano Letters,* **2011**, *11*, (1), 35-43.

(25) Saremi-Yarahmadi, S.; Vaidhyanathan, B.; Wijayantha, K. G. U., *International Journal of Hydrogen Energy*, **2010** *35,* (19), 10155-10165.

(26) Dau, H.; Limberg, C.; Reier, T.; Risch, M.; Roggan, S.; Strasser, P., C*hemCatChem,* **2010**, *2*, (7), 724-761.

(27) Kok, B.; Forbush, B.; McGloin, M., *Photochem. Photobiol*. **1970**, *11*, 457.

(28) de Jongh, P. E.; Vanmaekelbergh, D., *J. Phys. Chem. B*, **1997**, *101*, 2716-2722.

(29) Macdonald, J. R.; Barsoukov, E., *Impedance Spectroscopy; Impedance Spectroscopy Theory, Experiment, and Applications,* 2nd ed., John Wiley & Sons, Inc., Hoboken, New Jersey, **2005**, 2 and 5.

Chapter 3

Introduction to Experimental Methods

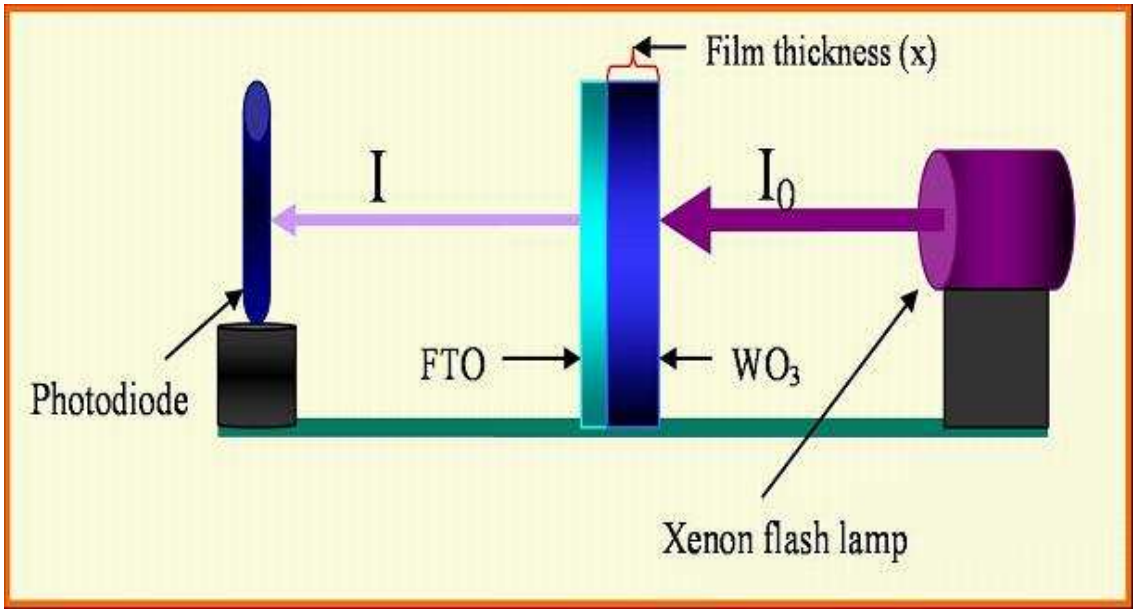

Abstract. In this chapter the key experimental methods are introduced and data analysis methods explained. An overview is given for (i) surface analytical techniques, (ii) spectrometric tools, and (iii) for (photo-) electrochemical methods.

Content

3.1. Surface Analytical Methods

3.1.1. Scanning Electron Microscopy (SEM) and Energy Dispersive X-ray Analysis (EDX)

For understanding the processes which occur at the surface of electrodes, it is important to investigate the surface structure. Scanning electron microscopy (SEM) analysis was performed to provide micro- and nano-scale information on morphology and composition at the electrode surface. The SEM measurements were conducted by using a Jeol 6480 LV scanning electron microscope (Electron Optical Services). Figure 3.1. shows a typical diagram to explain processes in the SEM.

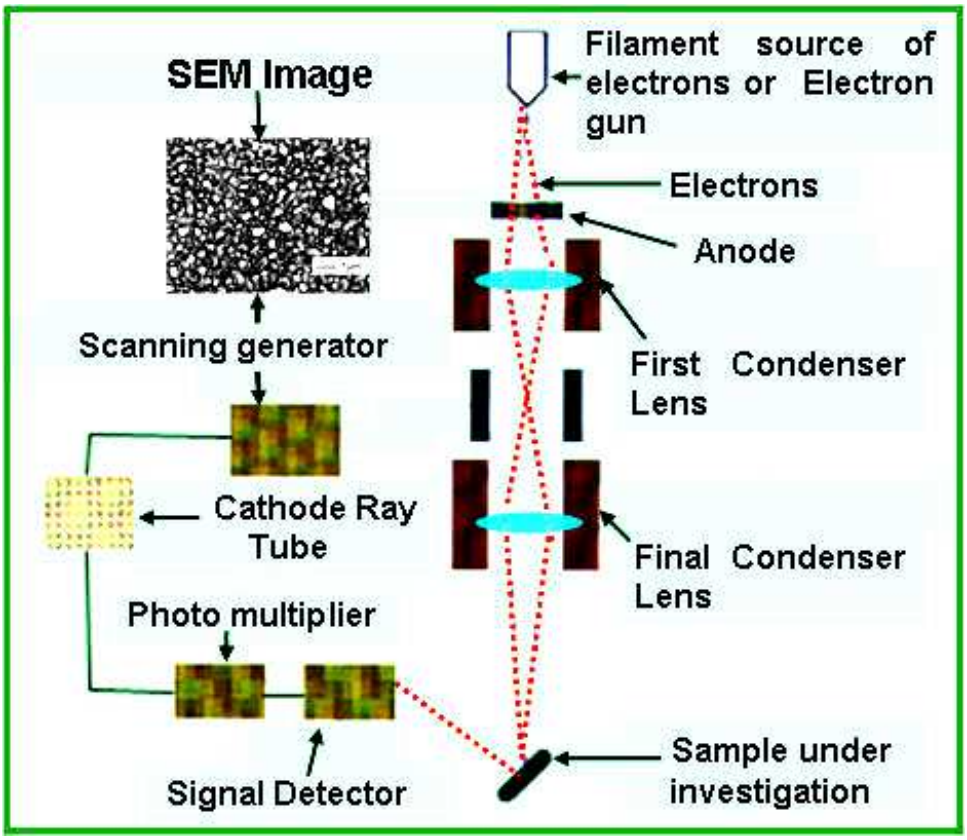

Figure 3.1. Schematic drawing of the processes in scanning electron microscopy (SEM) analysis of surface [(1)].

Electrons with high energy are accelerated towards the sample surface from the filament source. The deflected and scattered electrons provide surface topography information. In addition, X-ray emission from the sample is caused by electron

excitation (inner electrons) after electron impact. Energy dispersive X-ray spectroscopy (EDX)[1] is an analytical technique for surface elemental analysis. EDX can be measured by exposing the material to high energy electrons (20 keV in the present work). This process excites the atoms and consequently some of the core electrons move from the ground state (unexcited state) to a higher energy level or they are emitted leaving an electron hole. Then there are two possibilities: (i) either an electron from an outer, higher-energy shell falls back into this hole causing characteristic X-ray emission lines (EDX) or (ii) a second electron is emitted when the electron drops into the ground state to refill the position (Auger effect, only for light elements). In EDX, the difference in energy between the higher-energy shell and the lower energy shell may be released in the form of characteristic X-rays. The count and energy of the X-rays emitted from a specimen can be measured by an energy dispersive spectrometer. Because of the energy of the X-rays is characteristic for the difference in energy between the two atomic shells, the type of element and the approximate concentration can be determined.

3.1.2. Atomic Force Microscopy (AFM)

A further tool in the analysis of surface topography is atomic force microscopy (AFM). The method is based on a sharp tip in weak mechanical contact to the sample surface. A piezo motor adjusts the tip to surface distance and a piezo translation stage allows surface to be rastered systematically. In a comparison with the scanning electron microscope (SEM), the AFM provides superior topographic resolution and contrast, in addition to direct measurements (without the need for vacuum) of surface features. In the past, AFM was applied for example for the analysis of Fe_2O_3 samples which were prepared by using layer-by-layer surface structuring methods [2].

3.1.3. Profilometry

The thicknesses of most film deposits on electrodes were also measured by using a DEKTAK 6M STYLUS PROFILER system to compare with SEM cross section data of semiconductor films.

3.2. Spectroscopy and Diffraction Methods

3.2.1. UV/Vis Spectroscopy

The UV/Vis absorption measurements of the electrodes were performed on a Varian Cary 50 Probe spectrometer. The background scan was performed using a blank piece of SnO_2(F) conducting glass. Thus, the UV/Vis spectra obtained show the absorbance of the semiconductor film deposits on electrodes only.

Transmittance[3] can be defined as the fraction of incident light at a specified wavelength that passes through a sample as it is shown in equation 3.1.

$$T = \frac{I}{I_0} \tag{3.1}$$

Here, I_0 is the intensity of the incident light and I is the intensity of the light coming out of the sample (see Figure 3.2). The transmittance of a sample is sometimes given as a percentage.

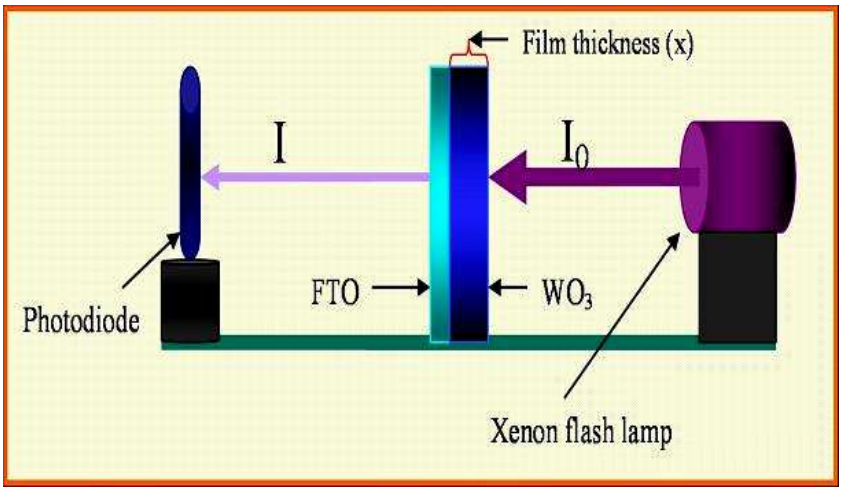

Figure 3.2. Experimental setup for absorption and/or transmittance measurements of semiconductor films on electrodes (here WO_3 on FTO).

The Beer-Lambert law states[4] that there is a logarithmic dependence between the transmittance of light through a substance and the concentration of the substance and path length of the cell through which light travels. In our solid case the film thickness replace the concentration of the substance.

$$\mathcal{T} = e^{-\alpha x} \qquad 3.2$$

Here, α is the attenuation or absorption coefficient and *x* is the film thickness. The expression can be rewritten as eq. 3.3.

$$\ln \frac{I}{I_0} = -\alpha x \qquad 3.3$$

The Beer-Lambert law is also stated that the absorbance of a sample is proportional to the thickness of the sample and the concentration of the absorbing species in the sample. The absorbance is defined as the negative logarithm of transmittance (eq. 3.4).

$$A = -\ln \mathcal{T} = -\ln\left(\frac{I}{I_0}\right) \qquad 3.4$$
$$= \alpha x$$

3.2.2. X-ray Diffraction (XRD) Techniques

The X-ray region is located in the section of the electromagnetic spectrum in the wavelength range between 0.1-100 Å. Like all electromagnetic waves, X-rays can be viewed as both of flow of photon particles and a wave of energy and they can be characterised by their energy. The energy is given by the product of the inverse wavelength (λ), the Planck constant (*h*), and the frequency (υ) (see eq. 3.5).

$$E = h\upsilon \qquad 3.5$$

$$\nu = \frac{c}{\lambda} \qquad 3.6$$

Here *c* is the speed of light, *h* is the Planck constant. From equation 3.5 and 3.6 the photon energy can be calculated (eq. 3.7).

$$E = \frac{hc}{\lambda} \qquad 3.7$$

Thus, X-ray wavelengths are short and they have comparably higher energy. X-rays can be produced when high energy electrons emitted from a hot filament (cathode) strike a metallic target (anode). Usually, the cathode can be maintained at a potential of 30 to 50 kV relative to the anode.

X-rays interact with the material under investigation (more precisely with the electrons around the atom in the material). In regular lattices (for example in crystals) the waves of scattered X-rays reinforce one another in certain direction according to Bragg's law of diffraction (eq. 3.8).

$$n\lambda = 2d \sin \theta \qquad 3.8$$

Here, d is the spacing between lattice planes, n is an integer, and θ is the angle of X-ray incidence and reflection. Figure 3.3 illustrates the interaction of the electromagnetic wave and the crystal planes. Bragg's law is obtained from the condition that the distances AB + BC equal to nλ.

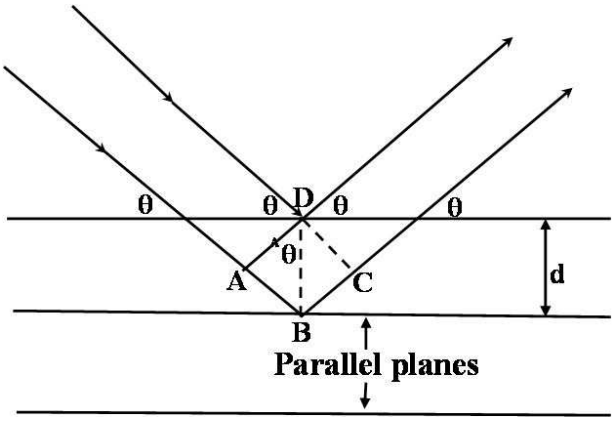

Figure 3.3. Schematic drawing illustrating X-ray diffraction and Bragg's Law.

X-ray diffraction techniques can be used to recognise the atomic structure of materials and is based on the elastic scattering of X-rays from the electron clouds of the individual atoms in the material [5]. As a monochromatic X-ray beam is directed at the sample, which is positioned at a defined plane at an angle θ, reflection of some X-rays occurs, which are detected by a detector as the pattern of reflections. The intensity pattern depends only on the symmetry of the crystal structure and its unit

cell parameters. Powder pattern data and single crystal diffraction pattern data can be used to determine the exact location of atoms within the unit cell of the crystal lattice.

3.3. Electrochemical Methods

3.3.1. Cyclic Voltammetry

Dark cyclic voltammetry was performed with a three-electrode system and controlled with a PGSTAT20 potentiostat (Autolab, Eco Chemie, Netherlands). The experiment is based on scanning the applied potential from an initial potential to a first vertex potential and back. Cycles can be repeated when necessary and combined with the application of pulsed or continuous light.

Cyclic voltammetric measurements in the presence of light were carried out in two different experimental setups:

(A) For the study of WO_3 thin films a PPR1 wavefunction generator was used to control the applied potential with potentiostat (model 3581) and to control the LED driver (Hi-Tek instruments). An X-Y chart recorder (SE 790 XY/XY-YT-COMPACT RECORDER) was used to record the current output during cyclic voltammograms. Figures 3.4 shows the experimental setup of dark cyclic voltammetry. Figure 3.5 shows the illuminated cyclic voltammetry experimental setup using a white LED light source (Farnell 432-5813 nm) set for illumination. An oscilloscope (Tektronix TDS 210, two channel digital real-time oscilloscope, 60MHz/1GS/s) was used in some experiments to record the photocurrent traces upon changing the intensity of the pulsed LED light. Figure 3.6 shows the way in which the LED and oscilloscope were incorporated into the photocurrent response setup shown.

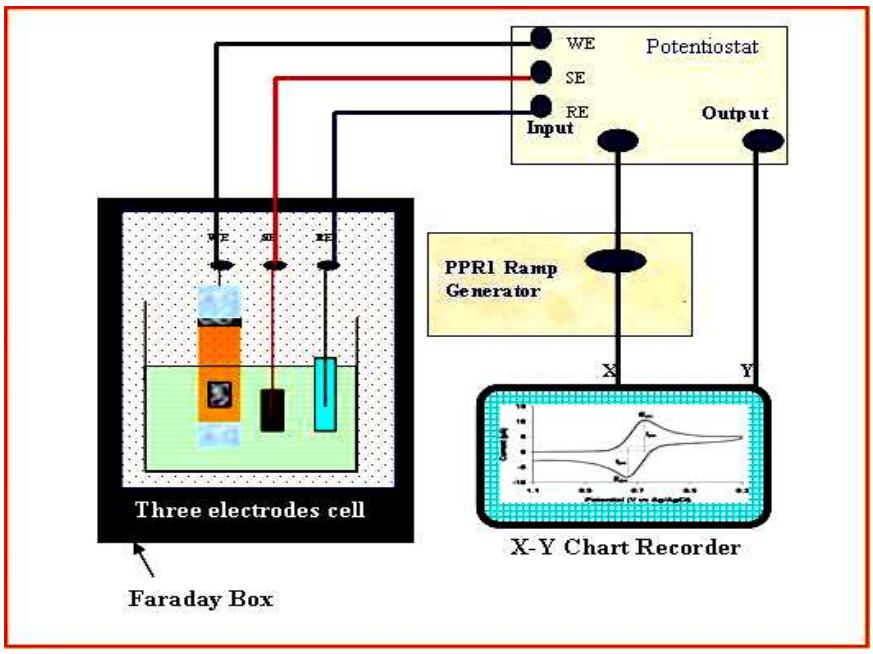

Figure 3.4. Schematic drawing of the experimental setup for dark cyclic voltammetry experiments.

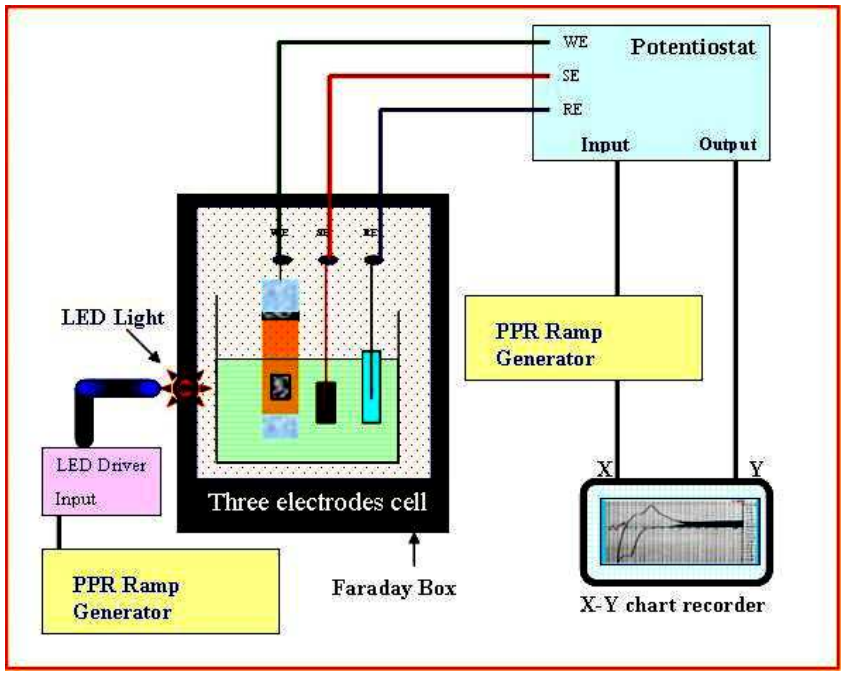

Figure 3.5. Schematic drawing for the experimental setup for illuminated cyclic voltammetry experiments.

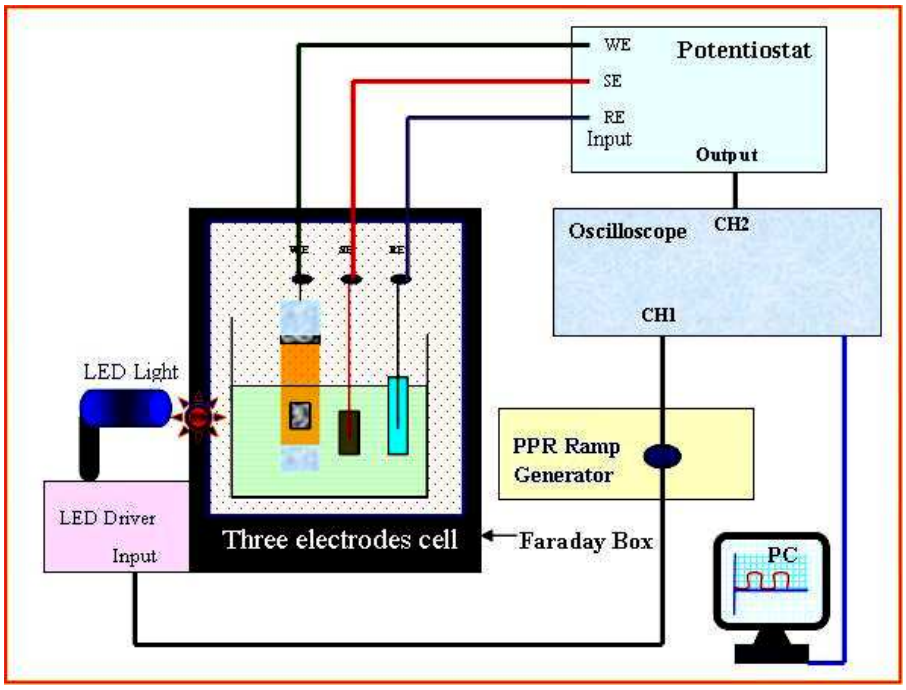

Figure 3.6. Schematic drawing of the experimental setup for photocurrent response experiments.

(B) For cyclic voltammetry measurements of all other samples an Autolab (PGSTAT 12/30) was employed for potential control and for data recording. A blue LED (Farnell, wavelength 455 nm) was used to illuminate samples. The illumination was carried out by pulsing 'On' and 'Off' for different time intervals (typically 0.4 s 'On' and 0.2 s 'Off').

To calibrate the light intensity delivered by the LED light sources at the sample position, a standard photodiode, with known incident photon to current efficiency (IPCE) was used. The light intensities were calculated at different current supplied to the LED (see Table 3.1.).

Table 3.1. The calibration data for the LED light emission intensity (455 nm) as a function of applied current.

.

The current supplied to the LED / mA	LED intensity / mW cm^{-2}
100	7.15
150	8.00
200	9.23
300	10. 9
400	12.13
440	12.52

3.3.2. Electrochemical Impedance Spectroscopy (EIS)

Impedance spectroscopy is considered versatile powerful technique to study of the electrical properties of many materials and their interfaces with electronically conducting electrodes [6]. Impedance is a generalised form of resistance, which takes into account the contributions from resistors, capacitors and inductors. As the ohmic resistance is the DC circuit resistance, impedance can be considered as the AC circuit resistance, which describes the amplitudes of the voltage and current and it describes also the relative phases. Impedance can also be defined as the frequency domain ratio of voltage and current [6]. Resistance is defined in Ohm's law (eq. 3.9) and similarly impedance is defined in eq. 3.10.

Ohm's law states: $$R = \frac{E}{I} \quad (3.9)$$

Impedance Z: $$Z = \frac{\Delta E}{\Delta I} \quad (3.10)$$

Here, ΔE and ΔI are the peak amplitude of an alternating voltage and resultant alternating current, respectively. However, impedance is a vector quantity: it contains both a magnitude (ΔE/ ΔI) and a direction. In this case a phase separation between the

potential and current can be defined. Figure 3.7 shows the relationship between applied AC potential, current response, and their amplitudes as function of time to explain the impedance concept. The diagram also shows the phase shift θ, which arises due to a delay of the current response after application of potential.

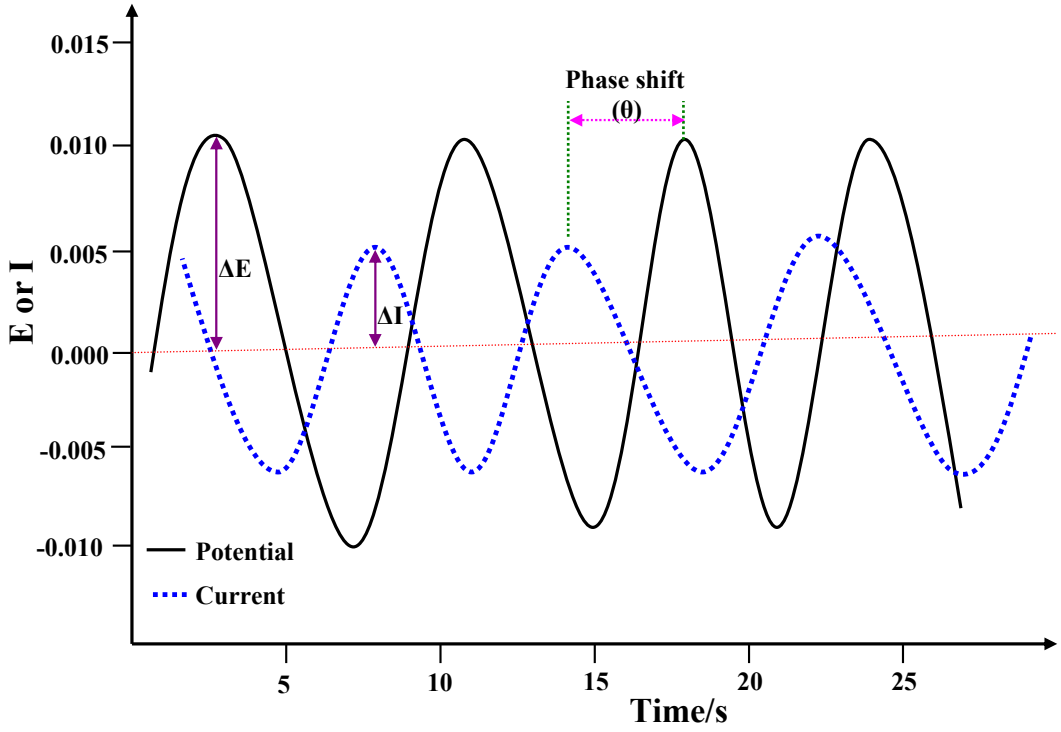

Figure 3.7. Plot of the applied AC potential, the current response, and their amplitudes as functions of time to explain the Impedance concept.

In many cases, impedance depends on the applied frequency. That is for every applied frequency there is a certain value of impedance amplitude |Z| and phase shift θ. Drawing the relationship between the real and imaginary components of impedance in the complex plane (or Nyquist plot) provides a diagnostic tool as it shown in Figure 3.8.

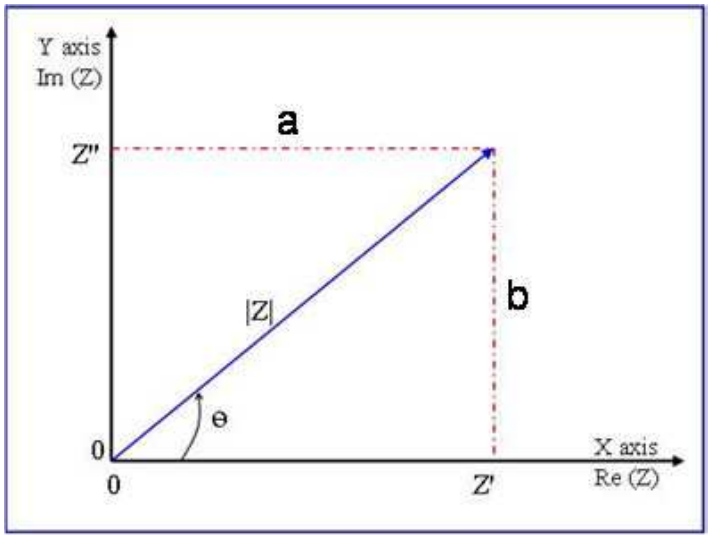

Figure 3.8. The impedance Z plotted as a planar vector using rectangular and polar coordinates.

By connecting the different magnitude points of impedance, as a function of applied frequency, diagnostic elements such as a semicircle for activation controlled processes are observed as shown in Figure 3.9. These elements can be rationalised with mathematical models describing the relationship between real part of impedance (Im or Z``) and the imaginary part of impedance (Re or Z`).

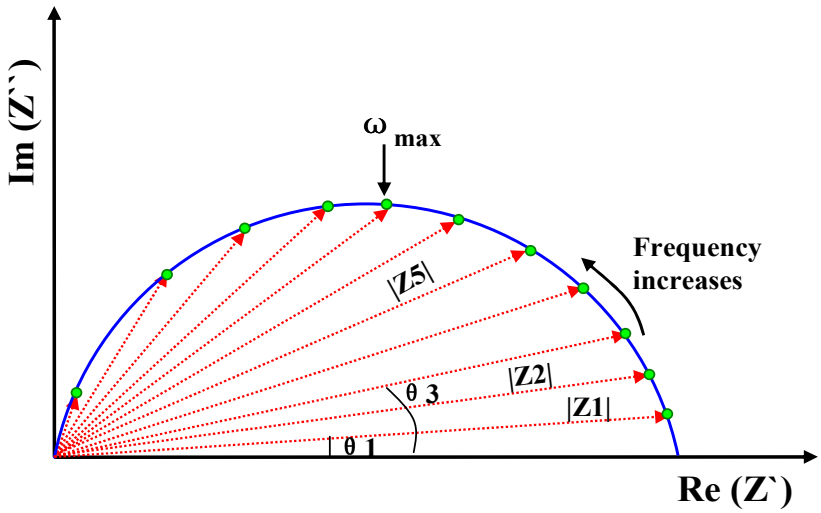

Figure 3.9. The semicircle describes the dependence of the impedance magnitude on the applied frequency for example for an RC parallel circuit in impedance or for a rate limiting process in IMPS (see below).

Impedance can be measured directly in the frequency domain by applying a single-frequency voltage oscillation to the electrode-electrolyte interface and measuring the phase shift (θ) and the amplitude (ΔI) of the resulting current. The magnitude and the direction of a planar vector sum of the components a and b along the axes, that is, by the complex number:

$$Z = a + j\,b \qquad 3.11$$

Here $j = \sqrt{-1}$ is the imaginary number. Thus, in the Nyquist representation (see Figure 3.8), the real part of Z, a, is in the direction of the real axis X, and the imaginary part b is along the Y axis with $Z(\omega) = Z' + jZ''$. The components of the impedance are given in eq. 3.12 to 3.14.

$$\mathrm{Re}\,(Z) = |Z| \cos(\theta) \qquad 3.12$$

$$\mathrm{Im}\,(Z) = Z'' = |Z| \sin(\theta) \qquad 3.13$$

with the phase angle $\theta = \tan^{-1}(Z''/Z')$

$$|Z| = [(Z')^2 + (Z'')^2]^{1/2} \qquad 3.14$$

This defines the Nyquist diagram (or Argand diagram) or complex plane, widely used in both mathematics and electrical engineering. In polar form, Z may now be written as in eq. 3.15.

$$Z(\omega) = |Z| \exp(j\theta) \qquad 3.15$$

This may be converted to rectangular form through the use of the *Euler relation* as in eq. 3.16.

$$\exp(j\theta) = \cos(\theta) + j \sin(\theta) \qquad 3.16$$

It is noticed[7] that the original time variation of the applied voltage and the resulting current have disappeared, and the impedance is time-invariant (provided the system

itself is time-invariant). In general, Z is frequency-dependent, as defined above. Conventional impedance spectroscopy consists of the (nowadays often automated) measurement of Z as a function of ν or ω ($= 2\pi\nu$) over a wide frequency range. In addition to the conventional impedance methods with potential excitation, it is possible to employ for example modulated light sources for external modulation.

To measure EIS, the Z-plot software was used to operate a Solartron SI 1286 electrochemical interface and a Solartron SI 1260 impedance / gain-phase analyser. In light experiments, a blue LED (λ = 455 nm) was used to illuminate the working electrode. Figure 3.10 shows the experimental setup used for EIS measurements.

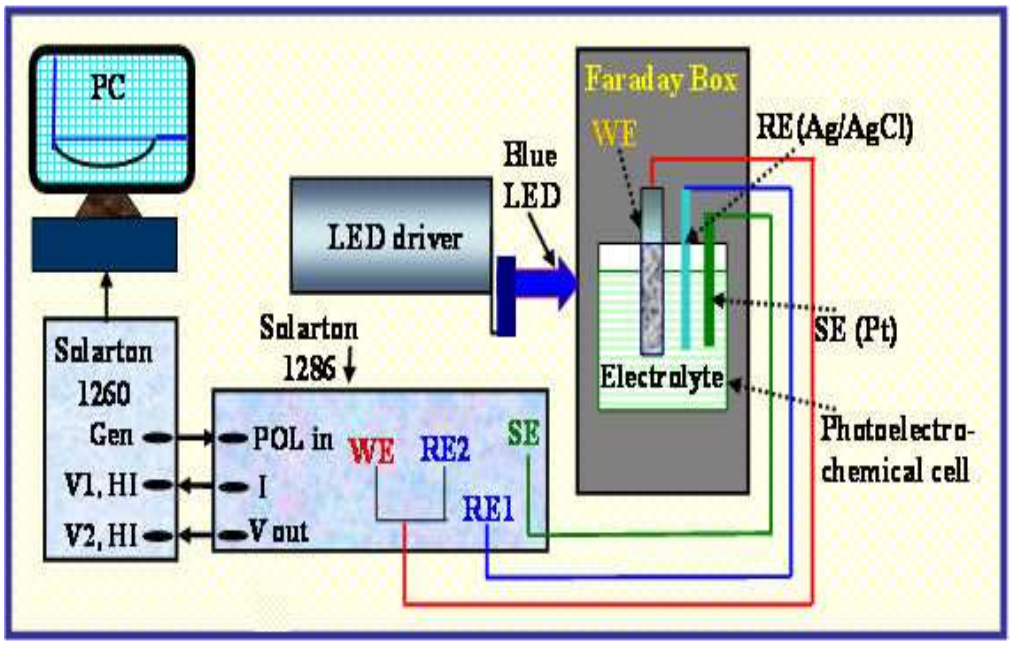

Figure 3.10. Schematic drawing of the experimental setup for electrochemical impedance measurements.

The SI 1286 applied to the cell a dc potential and an ac potential with 10mV amplitude from SI 1260. The frequency was scanned over different frequency ranges according to the investigated films. For example, in measurements of WO_3 film electrodes the frequency was scan from 63 kHz to 0.1 Hz. The dc potential bias was defined to correspond to the open-circuit voltages of the dark or illuminated cell. The SI 1260 detected and measured the impedance of the cell.

3.3.3. Photo-Transients and Incident Photon to Current Efficiency (IPCE)

The IPCE experiments were carried out using the experimental setup shown in Figure 3.11. Output photocurrent from the cell, detected with the aid of chopped light and a lock-in amplifier, was plotted as a function of wavelength of incident light. The applied wavelength was varied from 550 nm to 300 nm in steps of 10 nm. The scan parameters used for all IPCE measurements are given in Table 3.2.

Table 3.2. The scan parameters used in IPCE measurements.

Delay time	Measurement time	Time constant	Chopping frequency
1 s	3 s	1000 ms	73 Hz

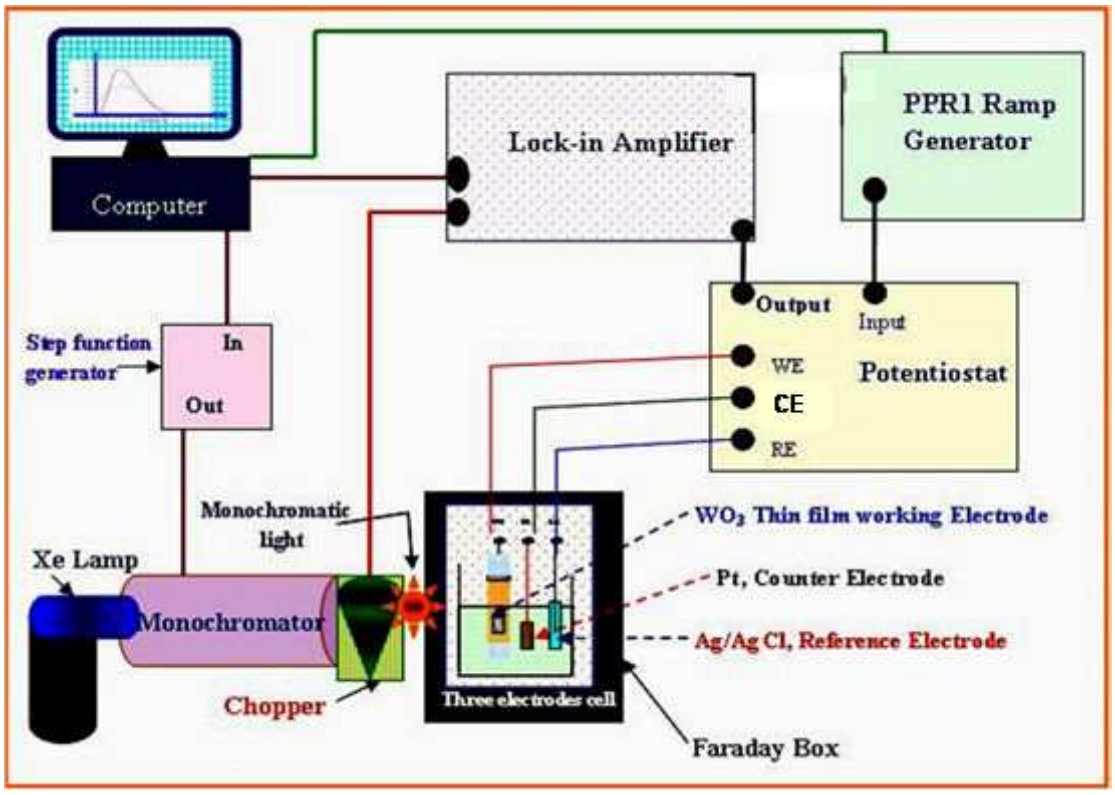

Figure 3.11. Schematic drawing of the experimental setup for incident photon to current efficiency (IPCE) experiments.

The specific apparatus for IPCE measurements was based on a Stanford Research Systems SR830 lock-in amplifier, an Amko SMD 101-M stepping motor control, a home made potentiostat, an Amko A1020 75 W xenon lamp powered by an LPS75X/2 supply, and an Amko monochromator with 10 nm spectral resolution. The PPR1 generator was used to maintain a specific potential in which a strong photocurrent response is observed.

IPCE data were recorded for each sample with both EE (Electrolyte-Electrode or front) and SE (Substrate-Electrode or back) illumination. The wavelength dependence of the current from a silicon photodiode of known IPCE (λ) function was measured to allow the calculation of $IPCE_{cell}$ via equation 3.17. Figure 3.12 shows a diagram of the illumination via EE and SE sides of a WO_3 film, as an example.

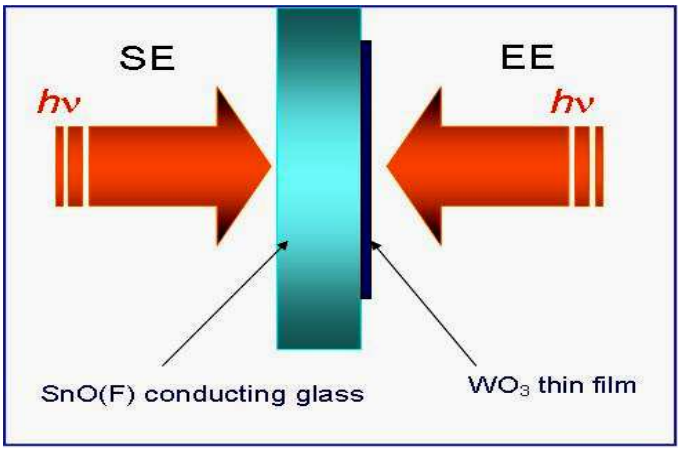

Figure 3.12. Schematic drawing of EE and SE illumination of the semiconductor WO_3 electrode as an example for investigated nanostructured films.

$$IPCE_{cell} = \frac{i_{cell}}{i_{pd}} IPCE_{pd} \qquad 3.17$$

Here i_{cell} is the photocurrent of the electrode under investigation cell and i_{pd} is that for the standard photodiode. The $IPCE_{pd}$ is a standard known value used for calibration and this therefore allows the $IPCE_{cell}$ to be calculated.

3.3.4. Intensity Modulated Photocurrent Spectroscopy (IMPS)

Impedance methods provide powerful tools where measurements are taken in the frequency domain. In conventional impedance experiments the applied potential is employed as the input signal for the system. However, by using the modulated light source and a fixed applied potential, many new experimental details may be revealed. Therefore, the intensity modulated photocurrent spectroscopy or IMPS method is introduced. In IMPS the frequency dependent photocurrent response of the cell based on a modulated illumination is determined in terms of the response function $\Phi(\omega)$ (see eq. 3.18).

$$\Phi(\omega) = \frac{\Delta j_{photo}\ (\omega + \varphi)}{q\,\Delta I_0\ (\omega)} \qquad 3.18$$

Here ω is the radial frequency, ΔI_0 describes a sinusoidal small-amplitude light flux perturbing the cell, q is the mono-electronic charge and Δj_{photo} is the photocurrent response of the cell. The photocurrent response of the cell is given by eq. 3.19 with n the conduction band electron density at the location of the electrode.

$$j_{photo} = qk_{ext}n\big|_{x=0} \qquad 3.19$$

This concentration of charge carriers n can be modelled theoretically when an appropriate kinetic scheme is employed. A continuity equation can be written out for the case of (i) absorption of light, (ii) diffusion of charge carriers, and (iii) chemical or recombination decay of charge carriers. The resulting equation (see 3.20) allows model data to be compared to experimental data and kinetic parameters to be extracted.

$$\frac{\partial n}{\partial t} = \alpha I_0 e^{-\alpha x} + D_n \frac{\partial^2 n}{\partial x^2} - \frac{n - n_0}{\tau_n} \qquad 3.20$$

Here, n is the density of the excess electrons under illumination, n_0 is the equilibrium electron concentration in dark, α is the absorption coefficient, I_0 is the incident photon

flux, D_n is the diffusion coefficient of electrons, τ_n is the electron lifetime. Models can be developed for both front and back illumination.

The photocurrent response of the cell is determined by both the transport and the back reaction (recombination) of electrons, which make the photocurrent lag behind the illumination. If most the injected electrons are collected, the phase lag in the IMPS response is dominated by the delay time arising from electron transport from the injected site to the substrate. The frequency of the minimum of the imaginary component of the IMPS response, f_{min} is related to the value of diffusion coefficient of electrons, D_n as can be seen from the following argument. The approximate relationship between the delay time of electrons and their diffusion coefficient is given by eq. 3.21.

$$\tau_{transit} = \frac{x^2}{D_n} \qquad 3.21$$

Here, x is the average distance travelled by electrons from the excitation position to the back contact and therefore $x = d/2$, where d is the film thickness (see Figure 3.13).

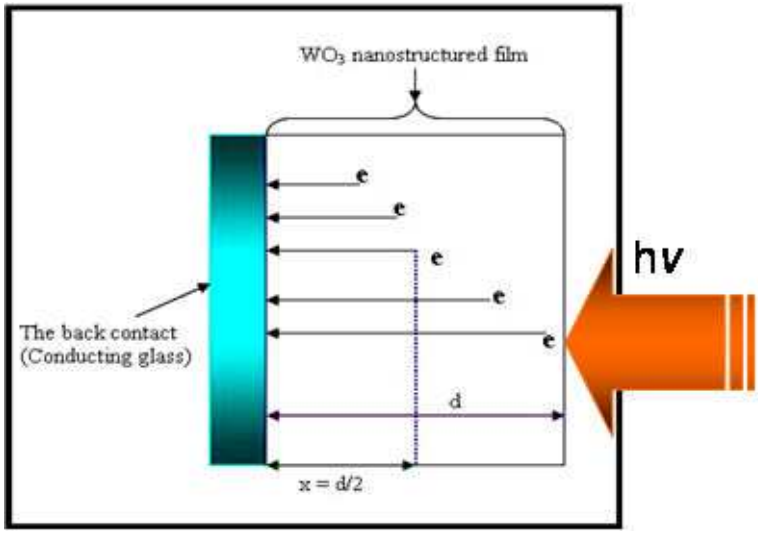

Figure 3.13. The average travelled distance by electrons from the excited position to the back contact in WO_3 electrode as an example.

Based on this the transit time is given by eq. 3.22 and also by eq. 3.23 which links the transit time to the IMPS minima in the Nyquist plot.

$$\tau_{transit} = \frac{d^2}{4 D_n} \quad 3.22$$

$$\tau_{transit} = \frac{1}{\omega_{\min}} = \frac{1}{2\pi f_{\min}} \quad 3.23$$

Here ω_{min} is the angular frequency of the minimum imaginary component in the IMPS response. A more precise value of D_n can be estimated by fitting the IMPS data with the exact analytical solution of equation 3.20. However, if the electron lifetime is so short that most of the injected electrons are lost in transit, the IMPS phase lag is determined by the electron lifetime. The transport of photo-generated electrons through nanocrystalline TiO_2 electrodes has been studied by intensity modulated photocurrent spectroscopy using UV light for electron-hole pair generation. It was found that transport of photo-generated electrons through particulate TiO_2 electrodes is limited by trapping/de-trapping in the band gap states distributed in energy [8].

IMPS measurements were performed with Solarton 1250 frequency response analyser (FRA) which was controlled by the Z-plot software. Figure 3.14 shows the experimental setup for IMPS measurements. A blue LED (λ = 455 nm) was used to illuminate the cell. The modulation of the LED light intensity was driven by the frequency response analyzer (FRA). The applied frequency ranged from 10 kHz to 0.1 Hz. The potentiostat (PSTAT) (model 3581) measured the photocurrent of the cell at short-circuit and fed it to channel 1 of the FRA. The FRA detected and measured the AC components at the same frequency at that of the incident light. The cell signal was divided by the photodiode signal to give IMPS.

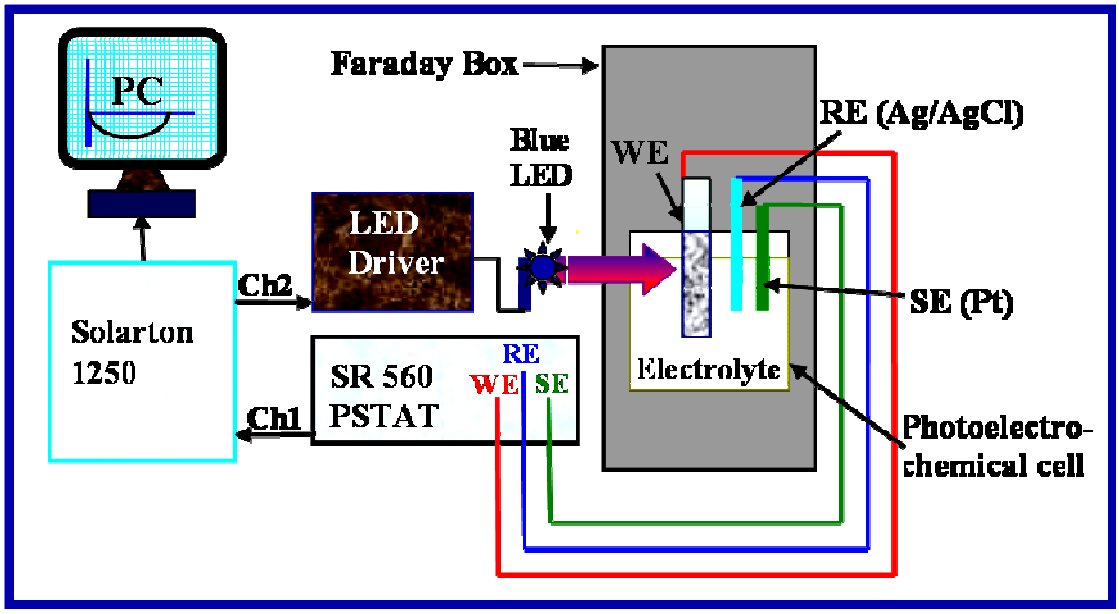

Figure 3.14. Schematic drawing of the experimental setup for IMPS measurements.

3.4. Experimental Setup of Measurement Cells

All the measurements have been performed in specially designed three electrode cells, called photoelectrochemical cell (see Figure 3.15). The photoelectrochemical cell is made from 'PTEF glass filled' material (designed at the University of Bath). The cell consists of two main parts connected together by means of four screws; the body and the lid as shown in Figures 3.16 and 3.17.

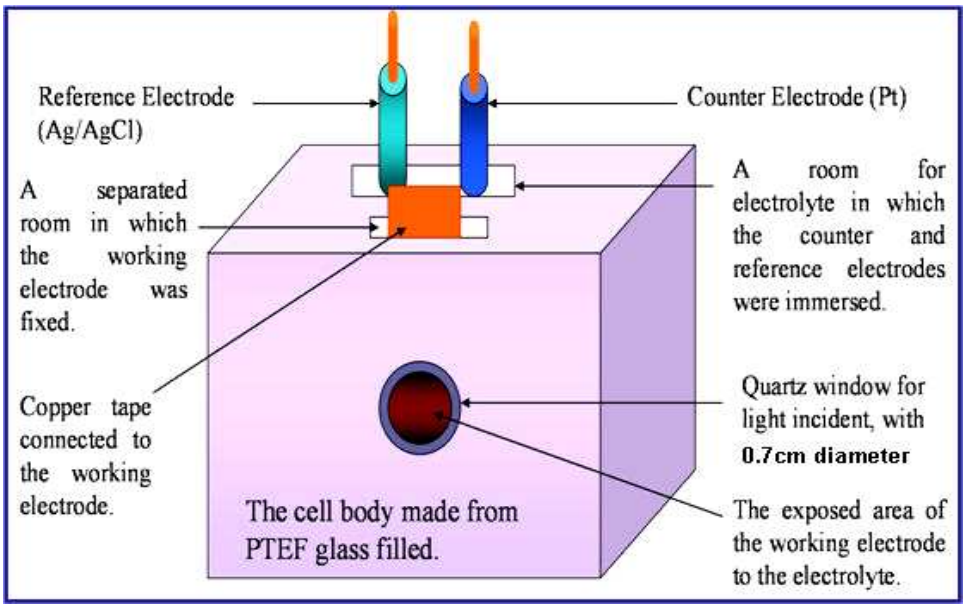

Figure 3.15. Schematic drawing of a specially designed photoelectrochemical cell.

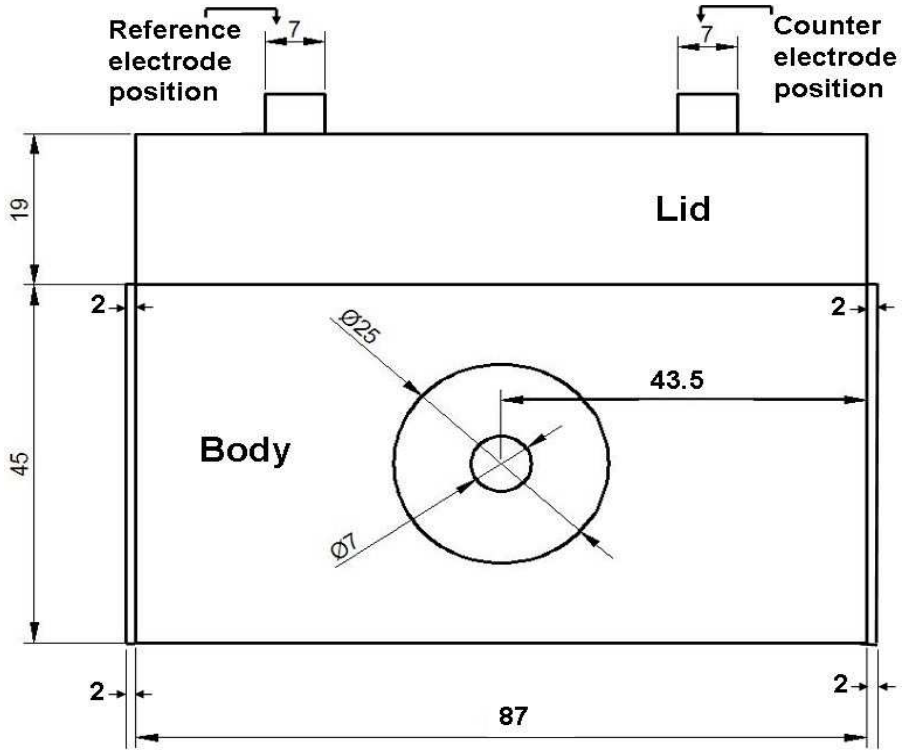

Figure 3.16. Technical drawing of the back side of the body and the lid of the photoelectrochemical cell.

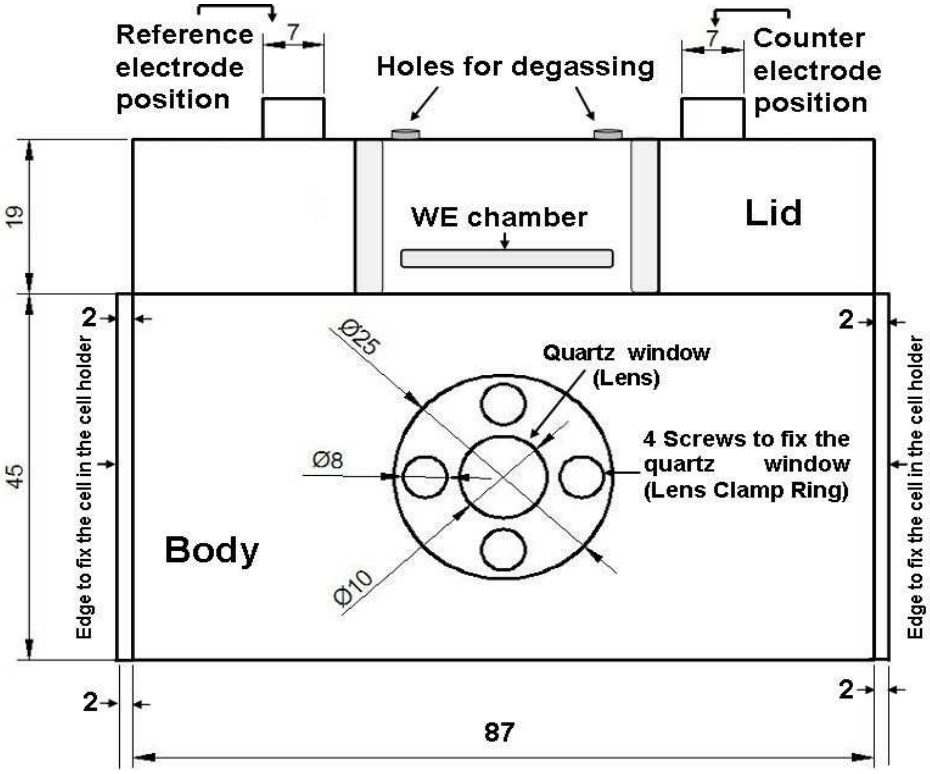

Figure 3.17. Technical drawing of the front side of the body and the lid of the photoelectrochemical cell.

The body of the cell (see Figure 3.18) consists of two separated compartments. The bigger compartment is for the electrolyte in which both the reference electrode (Ag/AgCl) and the counter electrode (Pt) were immersed. The body has a hole in the middle which allows light to go through. Quartz windows were used in order to contain the solution in the cell and be transparent to the light. The lid was designed to hold the reference and counter electrode and also has small holes to let gases out during the reactions. The working electrode was held in the smaller compartment of the cell. A screw was used to fix the working electrode to be in touch with the electrolyte through a specific area of 0.7 cm diameter circular open window between the two compartments of the cell, with an active area of the working electrode of 0.38 cm^2. The light was incident through a quartz window with the same diameter 0.7 cm. There is a window in both of the cell sides for SE and EE illumination. A special designed cell holder has been made from stainless steel (see Figure 3.19) to fix the cell in a Faraday box.

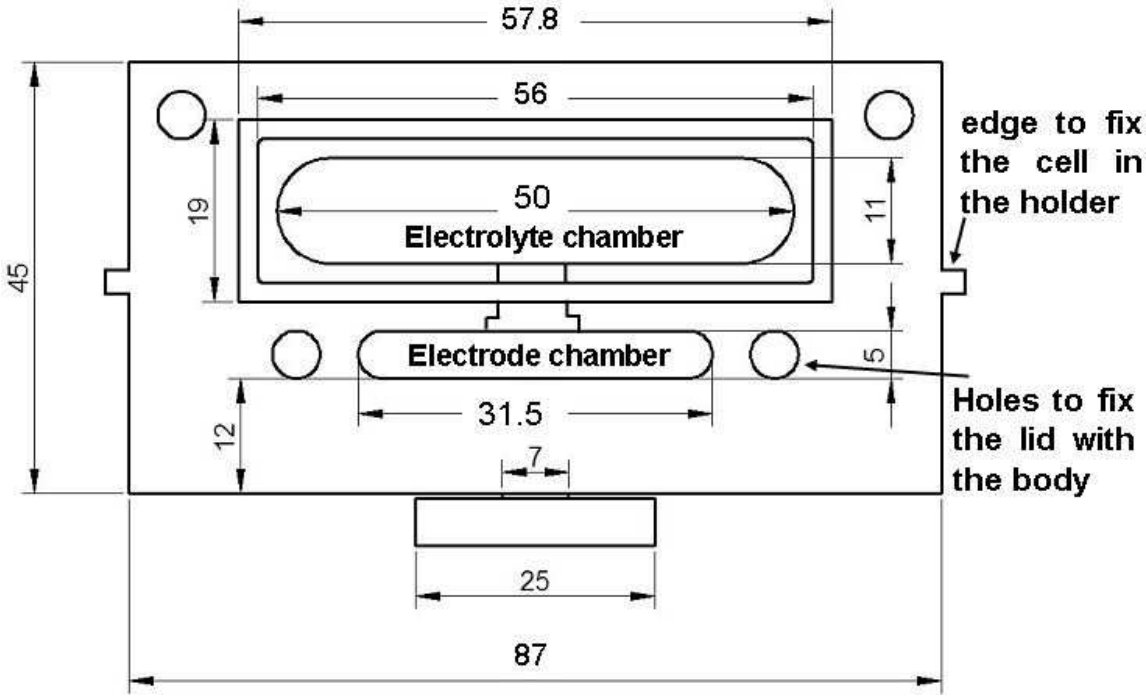

Figure 3.18. Technical drawing of the top view of the body of the photo-electrochemical cell.

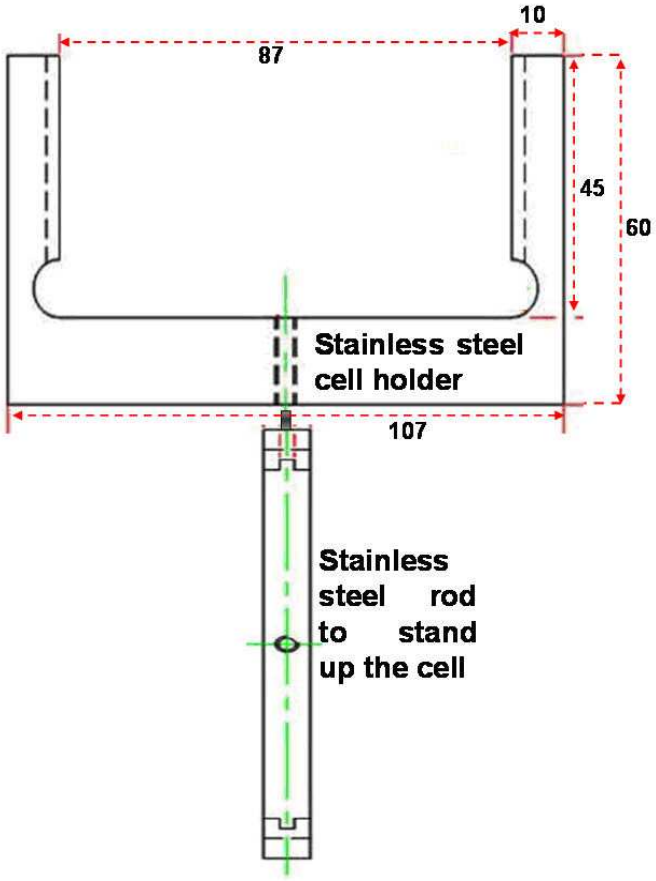

Figure 3.19. Technical drawing of the the stainless steel holder for the photo-electrochemical cell.

Most experiments were conducted in aqueous 1 M NaOH solution electrolyte. Only for the experiments with WO_3 film electrodes 1 M H_2SO_4 has been used. Electrolyte solutions were prepared using filtered and demineralised water. Phosphate buffer solution pH 11 was used as an electrolyte in some Fe_2O_3 film electrode experiments. De-aeration of the electrolyte was achieved by bubbling argon gas for 5 minutes prior to each experiment.

3.5. References

(1) Goldstein, J.; Newbury, D.; Joy, D.; Lyman, C.; Patrick, E.; Lifshin, E.; Sawyer, L.; Michael, J., *Scanning Electron Microscopy and X-Ray Microanalysis*, third edition, New York, **1985.**

(2) Bowen, W. R.; Hilal, N., *Atomic Force Microscopy in Process Engineering; An Introduction to AFM for Improved Processes and Products*, First Edition, Elsevier Ltd, Great Britain **2009.**

(3) Balkose, D.; Oguz, K.; Ozyuzer, L.; Tari, S.; Arkis, E.; Omurlu, F. O., *Journal of Applied Polymer Science*, **2010**, *120*, (3), 1671-1678.

(4) Zitzewitz, P. W., *Glencoe physics*, Glencoe/McGraw-Hill, New York **1999,** 39.

(5) Azároff, L. V.; Kaplow, R.; Kato, N.; Weiss, R. J.; Wilson, A. J. C.; Young, R. A., *X-ray diffraction,* McGraw-Hill, New York **1974**.

(6) Alexander, C.; Sadiku, M., *Fundamentals of Electric Circuits*, 3, revised ed., McGraw-Hill, New York, **2006,** 387-389

(7) Macdonald, J. R., *Impedance Spectroscopy; Emphasizing Solid Materials and Systems*, John Wiley & sons, New York **1987,** 2, 5.

(8) de Jongh, P. E; Vanmaekelbergh, *J. Phys. Chem. B,* **1997**, *101*, 2716-2722.

Chapter 4

Photo-Doping Effects on Spray-Pyrolysed Tungsten Oxide (WO_3) for Water Splitting Catalysts

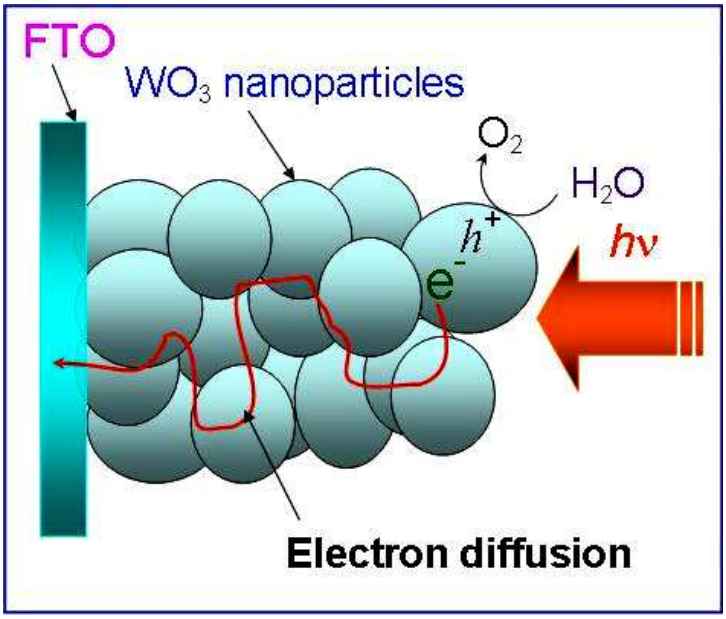

Abstract. In this chapter photo-electrochemically active WO_3 films are prepared and investigated. Thin, nanostructured, WO_3 films are grown onto conducting FTO substrates and shown to act as photo-catalyst for water splitting under positive potential bias. The time dependence of photo-currents is studied by impedance, light pulse, and light modulation techniques, and the time constants for photo-doping and electron transport are dissected. Clear evidence for trapping of diffusing electrons is obtained from intensity modulated photocurrent spectroscopy.

Content:

4.1. Introduction

4.1.1. Formation and Properties of Tungsten Trioxide Films

Water splitting based on solar radiation represents one of the most urgent challenges for humanity to reduce the reliance on fossil fuels[1]. The water splitting process similar to photosynthesis is based on the conversion of solar energy into a versatile fuel, here is hydrogen H_2[2]. Technologies for the widespread application of solar water splitting must be based on sustainable materials[3] and in particular on widely available and chemically robust transition metal oxides. One particularly interesting material for the photo-anode (the formation of oxygen O_2 from water in the presence of sunlight) is tungsten trioxide (WO_3)[4].

Tungsten trioxide (WO_3) is a light yellow powder insoluble in H_2O and acids, but soluble as tungstate in hot alkaline media. It is an intermediary compound in the process of converting tungstates to pure tungsten. Tungstates are treated with alkalis to produce WO_3. By using carbon or hydrogen gas, the compound is reduced to pure metal[5].

$$2\ WO_3 + 3\ C + \text{heat} \rightarrow 2\ W + 3\ CO_2 \quad (4.1)$$

$$WO_3 + 3\ H_2 + \text{heat} \rightarrow W + 3\ H_2O \quad (4.2)$$

Tungsten trioxide is fully transparent in the form of a thin homogeneous layer. Tungsten trioxide can be employed as a typical photochromic material[6]. The conversion from light yellow to dark blue can be driven by light (photo-reduction) or via applied potential (electro-reduction) and occurs as a reversible reaction associated with proton or cation insertion. Tungsten trioxide has also been added to molten glass mixture to improve the corrosion resistance of optical glasses. Additionally, tungsten trioxide has been used in surface acoustic wave sensor devices for the detection of gasses such as hydrogen[7] and ethane[8]. Due to its optical and electrical properties, tungsten trioxide can be a good photoelectrode material in a photoelectrochemical cell for hydrogen production via water splitting [9,10,11].

Since the first report on the photochromic property of WO_3 films by Deb[12] in 1973, the preparation effects on microstructure and photochromic processes for WO_3 films have been extensively studied because of its promising applications in information display devices, high-density memories, and photoelectric sensors[13,14]. In order to obtain good properties, the films need to be nanocrystalline, uniform, stable and compact. However, most of the early WO_3 films, prepared by various physical deposition methods[15,16] were amorphous, and the density, durability, and uniformity are not good enough for industrial applications.

WO_3 film properties for water splitting applications have been reviewed and compared to other oxide photoanode materials[17]. WO_3 is reported to possess a band gap of ca. 2.5 eV (monoclinic) and a photoanodic onset potential of 0.4 V vs. NHE. The light yellow colour is consistent with an absorption maximum at ca. 400 nm. Oxygen evolution during AM1.5 irradiation associated with photocurrents of ca. 3 mA cm^{-2} are possible. For mesostructured films of ca. 2.5 μm thickness (prepared via sol-gel methods) incident photon to current efficiency (IPCE) values of close to 100% and current doubling phenomena have been reported[18].

4.1.2. Applications of Tungsten Trioxide Film Electrodes in Water Splitting

The nano-structure of the WO_3 electrode can play an important role in water splitting. Research into nanostructured tungsten trioxide is relatively new, with only a few papers having been published since the potential use of these structures in the tandem cell was proposed[19]. Most of these papers use the sol-gel method for the preparation of the electrodes[20]. Augustynski et al.[21] demonstrated that a maximum photocurrent response for the nanostructured WO_3 is obtained at a wavelength close to 400 nm with a significant response in the blue part of the solar spectrum. Augustynski observed a conversion efficiency reaching 190 % in the presence of methanol, indicating the occurrence of current doubling. Under simulated solar illumination steady-state photocurrents of the order of several mA/cm^2 were obtained. Prolonged photoelectrolysis studies show that the WO_3 electrodes could act as both an efficient and stable photoanode for the degradation of organic effluents.

Santato et al.[22] have investigated the properties of the nanostructured sol-gel WO_3 electrodes produced based on the key preparation parameters, such as the tungstic acid/PEG ratio, the PEG chain length, and the annealing conditions. They found that a sequential deposition/annealing method allows one to build up smooth, crystallographically orientated WO_3 films in a range of thicknesses from a few hundred nanometres to a few micrometres. The size of the nanoparticles and the film porosity can be tailored by the appropriate tungstic acid/organic additive ratio and the annealing conditions. Santato found that films of 2.5 μm give the best photo-response under solar illumination. In contrast, thinner films (less than 1 μm thick) would be promising candidates for uses in electrochromic devices due to their excellent adherence and mechanical stability, open mesoporous structure, and good transparency.

Initial studies into the electron transport in the WO_3 thin films were performed in water-based electrolytes by Wang et al. in 2000[9]. These investigations were performed in a broad potential range and at different temperatures. Cathodic dark currents below the initial potential were related to the electrochromic process, which is associated with the intercalation of H^+ and/or Na^+ into the WO_3 structure leading to blue colouration. In the dark, oxidation of water started at 1.5 V, which was thought to be due to water leakage (or porosity) at the electrolyte/conductive glass back-contact. Between 0.1 to 1.5 V, photocurrents were shown to increase linearly with light intensity. The photocurrent was saturated above 0.8 V at each light intensity. This shows that the generation of charge carriers within the film, holes and electrons, become the rate limiting factor for the photocurrent as well as the photo-oxidation of water. Linear log |i| - potential behaviour was observed between 0.3 to 0.65 V at all light intensities. Exchange current densities were calculated and were shown to be of the same order as for RuO_2 electrodes (which are good oxygen evolution catalysts) in the dark. Wang[9] showed that both $IPCE_{EE}$ (illumination via the electrolyte) and $IPCE_{SE}$ (illumination via glass substrate) increase with film thickness. Quantum yields (EE and SE) reached a plateau at between 420 and 440 nm wavelength. In this plateau region, the quantum yields for SE illumination for all film thicknesses were close to unity. Quantum yields for EE illumination were shown to be approximately 20 % lower, which decreased with film thickness probably due to recombination losses. Using the quantum yields in

the plateau region and an equation proposed by Södergren et al.[23], the diffusion length of the electron through the film was estimated. Wang conducted an experiment into the temperature dependence of the photoresponse showing that as the temperature increases so the photocurrent increases.

There are many different methods for preparation of metal oxide electrode such as electrodeposition[24], spray pyrolysis[25], thermal oxidation[26], sol-gel[9,22], sputtering[27], and RF sputtering[28]. In this study a pyrolysis process based on a sol-gel mechanism is employed.

4.1.3. Aims of this Study

In this chapter a thin WO_3 film is produced on a fluorine-doped tin oxide (FTO) substrate by spray pyrolysis. The films are shown to be robust and free of cracks or crazing. These films are then investigated by surface analytical techniques and by voltammetry with pulsed light to provide insight into the photo-electrochemical reactivity. The IMPS method (Intensity Modulated Photocurrent Spectroscopy) is employed to study the time dependence of processes within the WO_3 film and to obtain further insight into electron diffusion and the mechanism of photo-electrochemical water splitting at WO_3 films. The effect of photo-doping and light intensity on the mobility of charge carriers is discussed. The main aims of the work are to (i) fabricate robust WO_3 photo-anodes and (ii) reveal the mechanism of the photo-electrochemical oxygen evolution in a quantitative treatment.

4.2. Experimental

4.2.1. Chemical Reagents

Precursor solution was tungsten(VI) chloride, 99.9 % metal basis (WCl6), from Aldrich, dissolved in 1:1 H_2O: ethanol, which was absolute from Fisher Scientific. All these chemicals were obtained commercially and used without any further purification. FTO conducting glass (Asahi) was used as a substrate in all the prepared WO_3 electrodes. Aqueous 1 M sulphuric acid (Fisher Scientific 98.08 %) was used in all experiments as an electrolyte. Water which used in preparation of all solutions was filtered and double de-ionized water (DDW, MilliQ water, from Elga system) with resistivity ca. 18.2 M Ω cm^{-1}.

4.2.2. Instrumentation

A traditional three-electrode system was used consisting of a working electrode, a WO_3 thin film deposited onto an electrically conducting SnO_2(F) coated glass, a reference electrode based on Ag/AgCl (3M KCl), and a Pt auxiliary or counter electrode. The photoelectrochemical measurements were carried out in a custom-build glass cell equipped with a quartz window (see chapter 3).

Direct current-potential (I-V) measurements were carried out with the three-electrode cell using a PPR1 wavefunction generator and a model 3581 potentiostat (Hi-Tek instruments) with a Belmont Instruments Recorderlab. Cyclic voltammetry scans were performed in aqueous 1 M H_2SO_4 from +1.2 V to –0.2 V vs. Ag/AgCl initially in the dark and then illumination was applied with a pulsed white LED (Farnell 432-5813 nm) and Blue LED (Farnell 455nm), which has been used in some experiments. An oscilloscope (Tektronix TDS 210, two channel digital real-time oscilloscope, 60 MHz/1 GS/s) was employed to record individual pulses. For impedance studies, Z-plot software was used to operate a Solartron SI 1286 electrochemical interface and a Solartron SI 1260 impedance / gain-phase analyser. LED driver used to control LED which used to illuminate the working electrode (WO_3 films, 0.6 cm^2). The SI 1286 applied to the cell a dc potential and an ac potential with 10mV amplitude from SI 1260. The frequency was scanned from 63 KHz to 0.1 Hz. The dc potential was varied to correspond to the different open-

circuit voltages of the illuminated cell. The SI 1260 detected and measured the impedance of the cell.

The absorption measurements of the electrodes were performed on a Varian Cary 50 Probe spectrometer. The background scan was performed using a blank piece of SnO_2(F) conducting glass. Photocurrent spectra were recorded for each sample with both EE (Electrolyte entry) and SE (substrate entry) illumination. A silicon photodiode of known IPCE(λ) function allowed calculation of $IPCE_{cell}$. Photocurrent spectroscopy was carried out. Output photocurrent from the cell, detected with the aid of chopped light and a lock-in amplifier, was plotted as a function of wavelength of incident light with λ being varied from 550 nm to 300 nm in steps of 10 nm. The scan parameters used for all IPCE measurements were as follows: delay time = 1 s; measurement time = 3 s; time constant = 1000 ms; chopping frequency = 0.3000 Hz. The specific apparatus were: a Stanford Research Systems SR830 lock-in amplifier; an Amko SMD 101-M stepping motor control; a home made potentiostat; an Amko A1020 75 W xenon lamp powered by an LPS75X/2 supply; an Amko monochromator with 10 nm spectral resolution. The PPR1 was used to maintain a +1 V potential because this is a region where photocurrent response is observed.

IMPS and IMVS measurements were performed with Solartron 1250 frequency response analyser (FRA) which controlled by Z-plot software. The blue LED (λ = 455 nm) was used to illuminate the cell. The modulation of the LED light intensity was driven by the FRA. The applied frequency ranged from 10 kHz to 0.1 Hz. 1 M H_2SO_4 used as an electrolyte in a three-electrode cell which consists of Pt foil as a counter electrode, Ag/AgCl as a reference electrode, and WO_3 as a working electrode. The potentiostat (PSTAT) (model 3581) measured the photocurrent of the cell at short-circuit and fed it to channel 1 of the FRA. The FRA detected and measured the ac components at the same frequency at that of the incident light. The cell signal was divided by the photodiode signal to give IMPS.

4.2.3. Procedure for the Spray Pyrolysis Deposition Method

The preparation of transparent WO_3 nano-structured film by using spray pyrolysis method was performed using the following steps [29]:

(1)- The FTO slide was cleaned by sonication at 40°C for 15 minutes in, sequentially, detergent (5 vol% decon-90), Isopropanol, acetone and in ethanol.

(2)- The FTO substrate was then heated to high temperature (ca. 450° C) for ~15 minutes

(3)- A third of the FTO slide was covered by another microscope slide in order to retain a conducting contact

(4)- Manually, using a spray bottle, the precursor solution (0.01 M WCl_6/ EtOH: H_2O 1:1) was sprayed onto FTO slide on a hot plate at ca. 450 °C. Two sprays along the hot FTO slide per 10 seconds were applied for 5 minutes. The solution was sprayed in fine droplets using air as a carrier gas through a manual-squeezable rubber pump connected to the spray bottle as shown in Figure 1.1

(5)- After completing the spraying process, the sample was left for ca. 5 minutes on the hotplate, and then pushed away from the central hot area to the edge of the hotplate to cool down.

(6)- The sample was then sintered in ELITE furnace for annealing at 450°C for 30 minutes. The film was dark yellowish green before annealing and turned to pale yellow after annealing. The prepared films are reproducible with accuracy 97%.

Figure 1.1. A photograph of the manual spray bottle connected to a squeezable rubber pump.

4.3. Results and Discussion

4.3.1. Formation and Characterisation of WO_3 Films

Films of WO_3 suitable for photochemical water splitting can be formed via a range of deposition methods. Here, spray pyrolysis was chosen as a fast and reproducible approach for making well-defined film electrodes. A WCl6 precursor solution in water-ethanol is sprayed onto a clean FTO substrate at approximately 450^o C (see Experimental). Rapid evaporation of the water/ ethanol and hydrolysis/polymerisation of the tungsten chloride produces finely grained and uniform films of WO_3 similar to literature reports[29].

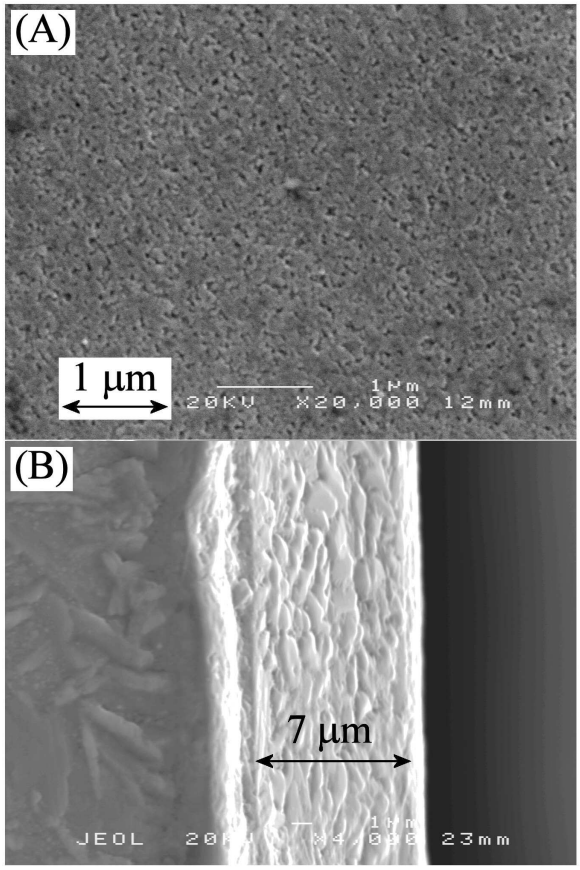

Figure 4.2. SEM images for a spray-pyrolysis film on a FTO substrate. In the surface view (A) a dense film with small pores (<50 nm) is observed. The cross-sectional view (B) shows a uniform film of ca. 7 μm thickness.

Figure 4.2 shows a typical SEM image for the surface topography and the cross sectional view. Films appear dense possibly with small pores up to typically 10-20 nm in diameter. The film thickness is typically 7 μm and the film is visible by eye only as a light yellow colour.

4.3.2. Cyclic Voltammetry Studies of WO_3 Films with and without Illumination

Cyclic voltammetry offers a powerful survey method to explore reactivity of materials as a function of the applied potential. Photocurrents are observed in characteristic potential ranges depending on the mobility and reactivity of photo-generated electrons and holes. WO_3 is a semiconductor material with n-type characteristics[30] where reactive holes (minority charge carriers) are produced locally and electrons (majority charge carriers) can move through the conduction band to the back contact and into the electrode substrate. Films of WO_3 have been demonstrated to be oxygen evolving photo-anodes[31] where the locally generated holes cause oxidation of water or other types of oxidisable reagents[32].

Typical voltammetric responses for spray-pyrolysis WO_3 films on FTO are shown in Figure 4.3. The applied potential was scanned from +1.2 V to –0.2 V and back to +1.2 V vs. Ag/AgCl using scan rates of (i, iii) 10 and (ii) 50 mVs^{-1}.

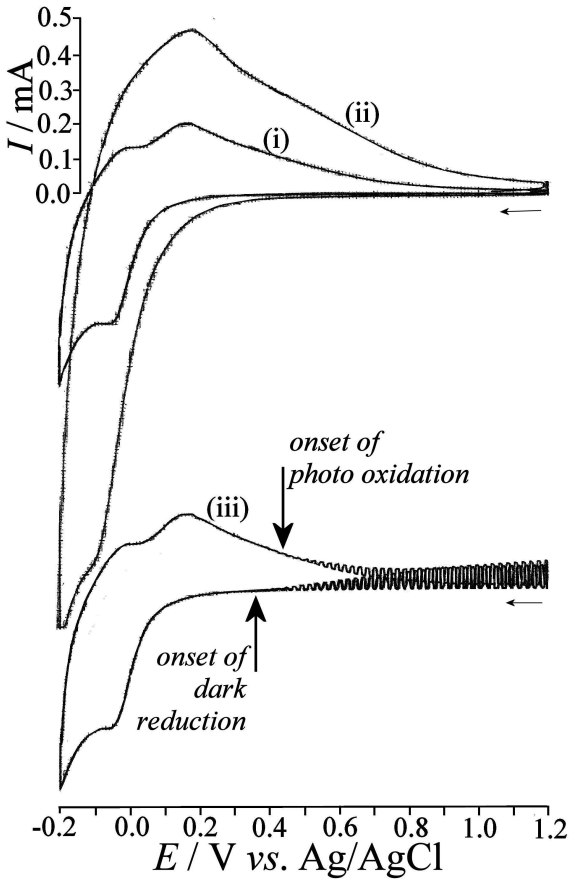

Figure 4.3. Cyclic voltammograms obtained at a 6 mm^2 WO_3 film immersed in aqueous 1 M H_2SO_4 and with a scan rates of (i, iii) 10 and (ii) 50 mVs^{-1}. Voltammograms were obtained (i, ii) without and (iii) with illumination (SE) with a flashing white light LED (10.09 $mW.cm^{-2}$).

In the forward scan without illumination a reduction is observed commencing at ca. 0.37 V vs. Ag/AgCl. A peak for the reduction is observed at ca. -0.05 V vs. Ag/AgCl and the cathodic current continues to increase at more negative potentials. Upon reversing the scan direction an anodic peak is observed at ca. 0.17 V vs. Ag/AgCl. The reduction and re-oxidation process is consistent with the well known reduction of WO_3 to blue "tungsten bronze" or $WO_2(OH)$[33] (see equation 4.3).

$$W(VI)O_3(s) + e^- + H^+(aq) \rightleftharpoons W(V)O_2(OH)(s) \qquad (4.3)$$

Next, cyclic voltammetry was performed in the presence of a flashing white LED at light intensity 10.09 mW/cm^2. The onset of the anodic photo-response is observed at ca. 0.4 V vs. Ag/AgCl. Anodic photocurrents are expected for n-type semiconductor materials and they reflect the formation of electron – hole pairs

upon photon absorption. Electrons are usually mobile due to the availability of the conduction band and they can diffuse towards the electrode. Holes are less mobile and chemically highly reactive, tending to immediately react at the WO_3 | aqueous electrolyte interface to give oxygen (equation 4.4-4.6).

$$2\ W(VI)O_3(s) + h\nu \rightleftharpoons W(V)O_3^-(s) + W(VI)O_2(O\bullet)^+(s) \quad (4.4)$$

$$W(V)O_3^-(s) + H^+(aq) \rightleftharpoons W(V)O_2(OH)(s) \quad (4.5)$$

$$4\ W(VI)O_2(O\bullet)^+(s) + 2\ H_2O \rightleftharpoons 4\ W(VI)O_3(s) + O_2(g) + 4\ H^+(aq) \quad (4.6)$$

Oxygen evolution, in equation 4.6, is a multi-steps process. From these equations it can be seen that simultaneously to the formation of oxygen also the formation of tungsten bronze, $W(V)O_2(OH)$, is possible, but only as a transient intermediate species due to the positive applied potential. At a potential of ca. 0.7 V vs. Ag/AgCl saturation occurs and the anodic photocurrents reach a maximum value (see Figure 4.3.iii). This saturation effect corresponds to a maximum of electrons being harvested from the photo-excited film.

In order to study photocurrent responses in more detail, on-off photo-transients vs. time were recorded (see Figure 4.4.). A comparison of back-lit (SE) versus front-lit (EE) configuration reveals a much improved photo-current response when the light pulse is illuminating the substrate side of the sample. In part this can be attributed to additional losses of light when passing through the electrolyte. But another major factor is believed to be the loss of photo-current due to recombination and the more extended pathway for photo-generated electrons crossing the film after excitation close to the WO_3 | electrolyte interface.

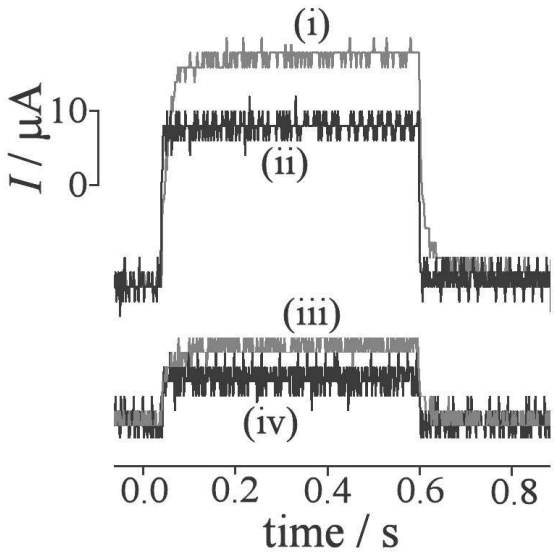

Figure 4.4. Photocurrent responses for WO_3 film electrodes (iii,iv) EE configuration and (i,ii) SE configuration immersed in aqueous 1 M H_2SO_4 and with an applied potential of (i,iii) 1.2 V vs. Ag/AgCl and (ii,iv) 0.8 V vs Ag/AgCl through illumination by using white LED at 10.09 $mW.cm^{-2}$.

It was found also that photocurrent responses increase with increasing illumination intensity. However, the rate of signal rise and decay of the photocurrent appears to be independent of the illumination intensity. The rise and decay of the photocurrents can be attributed to the rate of diffusion of electrons (or ions, vide infra) within the WO_3 film after the holes have been consumed in the generation of oxygen.

A further observation concerns the potential dependence of the transient signal decay. In Figure 4.4. photo-responses obtained at 0.8 V vs. Ag/AgCl and 1.2 V vs. Ag/AgCl are contrasted. Perhaps surprisingly, the signal rise and decay at more positive potential is significantly slower. This effect contradicts the model of a simple diffusion and potential driven charge extraction process. The effect will be discussed in more detail below.

4.3.3. Absorption Spectroscopy and IPCE Studies for Spray-Pyrolysed WO_3 Films

Absorption measurements were carried out in air. It was observed that the WO_3 film electrodes absorb in the 350 nm to 450 nm wavelength range consistent with the UV and Blue colorations. There is significant background absorption throughout the 550 to 350 nm range, probably due to some scattering of light at WO_3 particles. An increase of absorption towards shorter wavelengths without well-defined peak is observed up to ca. 350 nm wavelength consistent with literature reports for similar thin WO_3 films[34].

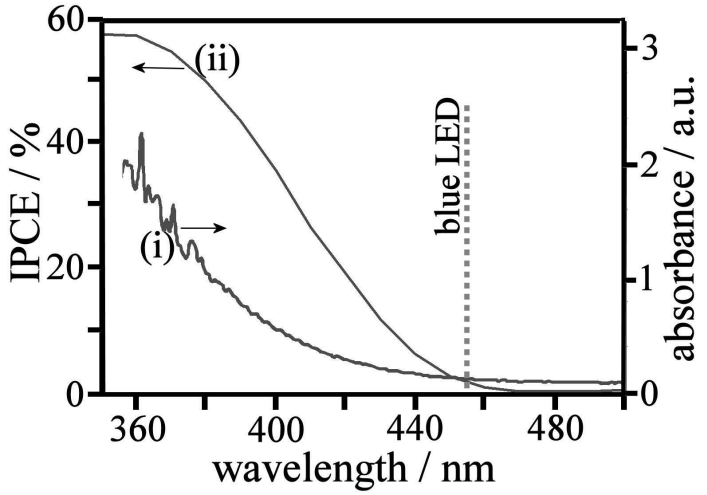

Figure 4.5. (i) Absorption spectrum of WO_3 film electrodes (FTO electrode background substracted). (ii) IPCE measurement for WO_3 film electrode (SE) immersed in 1 M H_2SO_4 and with a +1.0 V vs. Ag/AgCl applied potential.

The absorption coefficient of the WO_3 film can only be estimated. In the wavelength region around 445 nm the onset of the absorption is observed and the absorbance is approximately A = 0.03 (see Figure 4.5i). The extinction coefficient can be estimated based on $\alpha = \frac{A}{2.3\,l} = 1800\,m^{-1}$, where l is the thickness of the WO_3 film. The true absorption coefficient could be considerably lower than this estimate due to additional losses from poor optical coupling and light scattering.

It was observed that the absorption is slightly higher in case of illumination via the EE side compared to that in case of illumination via the SE side. This is likely to be

caused by reflection effects and differences in optical coupling. The efficiency of the cells to photo-activation is the most important component to their use on an industrial scale for example in tandem cell devices. Ideally the cells will absorb as much of the blue region of the spectrum with a high overall incident photon to current efficiency. It has been shown previously that the peak in "Incident Photon Conversion Efficiency" or IPCE (see equation 4.7) is at approximately 400 nm[21]. Therefore a scan range of 500 nm to 300 nm was chosen to investigate the efficiency of the WO_3 cell.

$$IPCE = \frac{i}{J_{photon}\, e} \tag{4.7}$$

In this expression the IPCE is defined as the ratio of current, i, to photon flux, J_{photon}, multiplied with the elementary charge, e. The IPCE has been measured for both EE and SE illumination of all WO_3 samples. It was found that IPCE for the investigated WO_3 samples immersed in aqueous 1 M H_2SO_4 is high and in the range of 20 - 60%. Figure 4.5.ii shows a typical IPCE for a WO_3 film (SE) at +1.0 V vs. Ag/AgCl reaching 58%. The SE configuration gives slightly higher IPCE values up to 60%. The main reason for IPCE values not reaching even higher values could be the considerable thickness of the WO_3 film which may lead to some recombinational losses.

4.3.4. Electrochemical Impedance Spectroscopy (EIS) with and without Illumination

Impedance spectroscopy provides insight into the time dependence of phenomena at a fixed potential. By applying a small amplitude sine wave function to the applied DC potential and changing the frequency over several orders of magnitude often processes at interfaces and in the bulk can be separated[35]. The characterisation of solar cells based on approximate impedance methods is well established[36].

Here thin WO_3 films on FTO electrodes are investigated in aqueous 1 M H_2SO_4. The potential region negative of 0.4 V vs. Ag/AgCl is associated with the direct reduction of WO_3 to tungsten bronzes (see equation 4.3) and no effects of illumination are expected (see Figure 4.3). However, with applied potential positive of 0.4 V illumination affects and photo-currents are observed. Therefore impedance experiments are carried out in this positive potential range and for a range of frequencies from 63 kHz to 0.1 Hz. Typical Bode plots are shown in Figure 4.6.

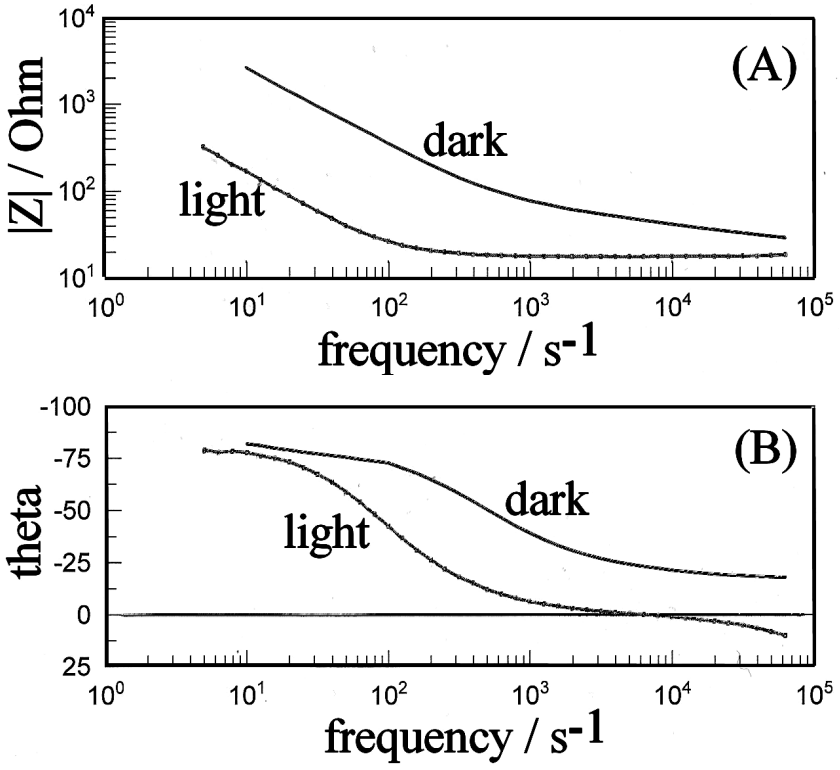

Figure 4.6. Bode plots with (A) absolute impedance versus frequency and (B) phase angle versus frequency for a WO_3 film electrode immersed in 1 M H_2SO_4 with an applied potential of 1.2 V vs. Ag/ACl. Light source blue LED with 455 nm wavelength and with intensity 10.09 $mW.cm^{-2}$.

Impedance spectra for dark conditions are dominated by a serial R (resistor) – C (capacitor) combination resulting in a phase angle of close to zero degree at high frequencies (the capacitor becomes highly conducting) and a phase angle of close to 90 degree at low frequencies (the capacitor becomes highly blocking). The transition from resistive (high frequency) to capacitive (low frequency) behaviour

occurs at a frequency which is characteristic and dependent on applied potential and applied illumination. The Bode plots in Figure 4.6 show typical examples of data sets obtained in the dark and in the presence of light. Data obtained in the dark and in the presence of light are summarised in Table 4.1.

Table 4.1. Impedance data for a spray-pyrolysed WO_3 film on FTO (area 0.38 cm^2) and immersed in aqueous 1 M H_2SO_4 at different applied DC potentials and at 10 mV AC amplitude (light source: blue LED at light intensity 300 mA (10.09 $mW.cm^{-2}$).

***E* / V *vs.* Ag/AgCl**	**Conditions**		***R* /Ω** [a]	***C* / µF** [a]
0.4	**Dark**		21	197
	Light	**EE**	**21**	**155**
		SE	**19**	**222**
0.6	**Dark**		22	74
	Light	**EE**	**21**	**136**
		SE	**18**	**157**
0.8	**Dark**		36	27.7
	Light	**EE**	**20**	**120**
		SE	**18**	**133**
1.0	**Dark**		44	6.8
	Light	**EE**	**19**	**102**
		SE	**18**	**115**
1.2	**Dark**		45	4.77
	Light	**EE**	**19**	**81**
		SE	**18**	**95.1**

[a] parameters obtained by employing the "fit circle" option in Zview.

For impedance data obtained in the dark, a trend of resistance R to higher values and capacitance C to lower values occurs when going from 0.4 V vs. Ag/AgCl to more positive potentials. The FTO film electrode is expected to exhibit a resistance of ca. 20 Ohm with the aqueous electrolyte contributing only a negligible resistance. The resistance in the dark clearly increases and the effect is removed when the electrode is illuminated. It appears likely that the porous WO_3 is contributing a resistance effect which is dependent on the conductivity in pores. A more positive applied potential appears to affect the pore resistance by removing traces of W(V) states. When illuminated (or at lower applied potentials) the presence of mobile W(V) states increases which causes a decrease in WO_3 film resistance. SE illumination is consistently more effective compared to EE illumination. The capacitance in the dark and when illuminated can be understood based on the same model. Removal of mobile charge carriers causes the dark capacitance to fall to very low levels and illumination is causing some of the capacitance to be restored. Illumination causes formation of W(V) sites (see equation 4.4) via photo-doping. The schematic drawing in Figure 4.7 summarises the impedance characteristics.

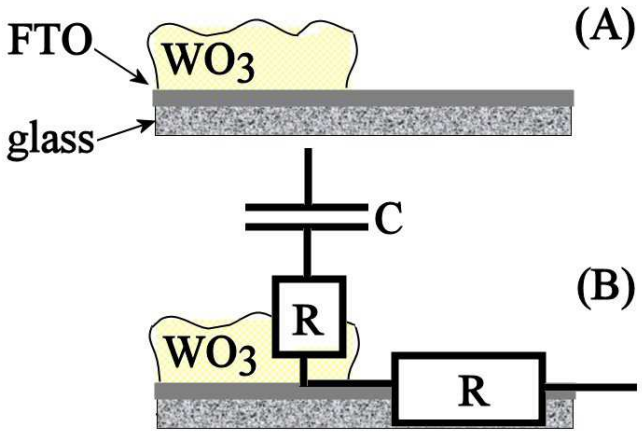

Figure 4.7. Schematic drawing of (A) the FTO electrode with WO_3 film coating and (B) the corresponding oversimplified equivalent circuit based on a serial RC combination.

4.3.5. Intensity-Modulated Photocurrent Spectroscopy (IMPS) and Intensity-Modulated Voltage Spectroscopy (IMVS) for Spray-Pyrolysed WO_3 Films

Photocurrent spectroscopy is a method based on a modulation applied to the light intensity when conducting experiments under potentiostatic or galvanostatic conditions. Transients recorded with potential stimulation are often affected by slow charging of interfaces and important rate information can be obscured. When modulating the light intensity new complementary information is obtained.

Intensity-modulated voltage spectroscopy (IMVS) provides a tool for the investigation of recombination processes at open circuit (zero current). Photo-excitation of WO_3 produces electrons and holes and these may recombine "directly" or "indirectly". Direct recombination will require electrons to diffuse back to the location of the hole. For holes which are very quickly undergo chemical reactions at the semiconductor surface, an indirect recombination pathway is proposed. Oxygen generated from holes at the WO_3 surface in contact with the aqueous electrolyte, can be converted back into water when recombination with electron occurs. This process is known to be very slow[37] (equation 4.8). However, it can be catalysed at the FTO substrate which is in contact with electrolyte solution in the pores of the WO_3 film.

$$4\ W(V)O_2(OH)(s) + 2O_2(aq) + 4\ H^+(aq) \rightleftharpoons 4\ W(VI)O_3(s) + 4\ H_2O \qquad (4.8)$$

In order to establish the recombination rate as a potential loss mechanism for photocurrents, intensity-modulate voltage spectroscopy (IMVS) is employed. In this measurement, the light intensity of a blue LED is modulated around a bias, the electrochemical cell is operated at open circuit, and the resulting modulation of the open circuit voltage is measured as a function of frequency.

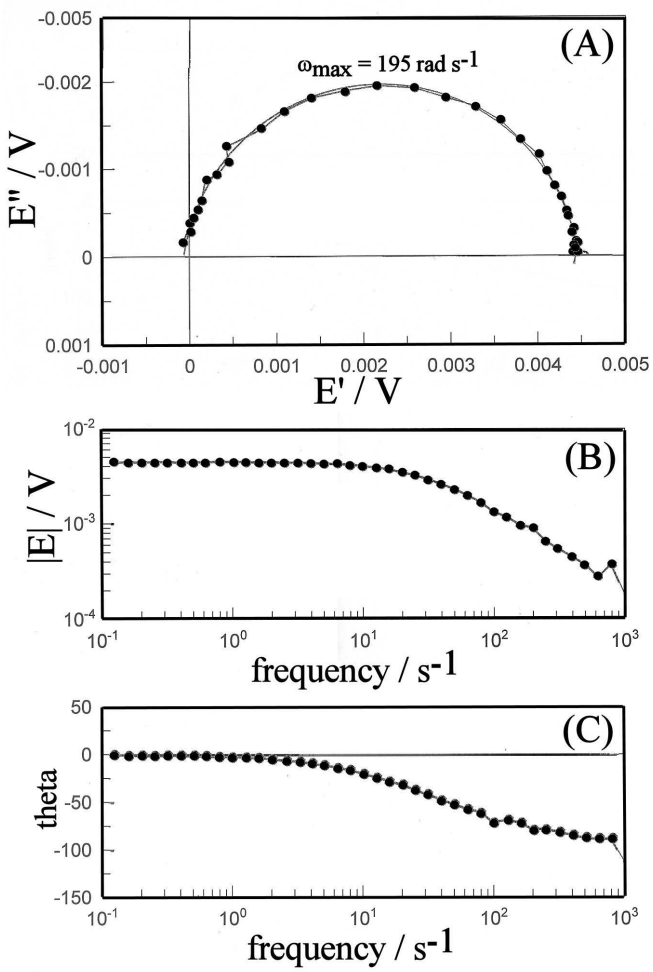

Figure 4.8. IMVS data for a WO_3 film immersed in aqueous 1 M H_2SO_4 illuminated with a blue LED (9.23 mW cm^{-2} bias, 20% modulation).

Figure 4.8 shows typical IMVS data for the WO_3 film electrode in 1 M H_2SO_4. A semi-circular response is obtained in the admittance plane consistent with a serial RC element. The time constant for this RC element provides a good estimate for the "recombination time" when electron in the WO_3 film react with oxygen directly or indirectly. The ω_{max} = 195 rad s^{-1} parameter extracted from the semicircle data suggests that the decay time is ca. $\tau = \frac{1}{\omega_{max}}$ = 5 ms. This value was observed for different illumination intensities and for both EE and SE illumination. The open circuit voltage during measurements was ca. 0.3 V vs. Ag/AgCl, which is in agreement with the onset region for the photocurrent (see Figure 4.3). The data obtained with IMVS will be employed in the analysis of IMPS data.

IMPS is based on the application of a fixed potential and the measurement of the photo-current response when the light intensity is modulated. The analysis of IMPS data can reveal electron mobilities and further insights into electron transfer effects [38]. The overall mechanistic model describing the photo-responses of thin WO_3 films can be based on the generation/collection equation with three important terms (equation 4.9) [39].

$$\frac{\partial n}{\partial t} = D_{app}\frac{\partial^2 n}{\partial x^2} - \frac{n}{\tau} + \alpha I_0 e^{-\alpha x} \tag{4.9}$$

In this equation the rate of formation/loss of electrons $\frac{\partial n}{\partial t}$ is balanced by the diffusion of electrons $D_{app}\frac{\partial^2 n}{\partial x^2}$, the first order decay via recombination processes $\frac{n}{\tau}$, and the photo-generation of electrons $\alpha I_0 e^{-\alpha x}$. This equation has been solved analytically [39] for the case of a sinusoidal modulation of the illumination intensity (equation 4.10).

$$I(t) = I_0 e^{i\omega t} \tag{4.10}$$

The boundary conditions for the process at the substrate and electrolyte interface are given by equations 4.11 and 4.12, respectively.

$$k\, n(0,t) = D_{app}\frac{\partial n}{\partial x}\Big|_{x=0} \tag{4.11}$$

$$\frac{\partial n(x,t)}{\partial x}\Big|_{x=d} = 0 \tag{4.12}$$

The solution for illumination from the solution interface (EE) can be expressed in terms of the photo-current conversion efficiency $\Phi_{EE}(\omega) = \frac{j_{electro}}{q\, I_0}$, which is the ratio of the flux of electrons, $j_{electro}$, and the light intensity I_0 multiplied by the elementary charge q. The expression is given in equation 4.13.

$$\Phi_{EE}(\omega) = \frac{\alpha}{\alpha+\gamma} \frac{e^{(\gamma-\alpha)d} - e^{-(\alpha+\gamma)d} + 2\alpha \dfrac{e^{(\gamma-\alpha)d} - 1}{\gamma-\alpha}}{e^{\gamma d} + e^{-\gamma d} + \dfrac{D_{app}\gamma}{k}(e^{\gamma d} - e^{-\gamma d})} \tag{4.13}$$

In this expression α is the absorption coefficient defined in $A = \alpha x$, d is the film thickness, γ is defined in $\gamma = \sqrt{\left(\frac{1}{D_{app}\tau} + \frac{i\omega}{D_{app}}\right)}$ (with the diffusion coefficient D_{app}, the decay time for recombination τ, the frequency ω, and $i = \sqrt{-1}$), and k (in m s^{-1}), the rate constant for electron transfer at the WO_3 | FTO substrate interface. A similar expression is obtained for the case of illumination from the substrate, SE (see equation 4.14).

$$\Phi_{SE}(\omega) = \frac{\alpha}{\alpha+\gamma} \frac{e^{\gamma d} - e^{-\gamma d} + 2\alpha \dfrac{e^{-\alpha d} - e^{-\gamma d}}{\gamma-\alpha}}{e^{\gamma d} + e^{-\gamma d} + \dfrac{D_{app}\gamma}{k}(e^{\gamma d} - e^{-\gamma d})} \tag{4.14}$$

The photocurrent conversion efficiency Φ is measured as a current response with time. Any resistive elements in the film electrode will therefore produce local potential gradient effects which coupled to the local capacitance of the electrode create an additional attenuation effect. The components R and C are obtained from independent impedance measurements (*vide supra*) and the attenuation effect is given by equation 4.15.

$$\Phi_{total} = \Phi(\omega) \times \frac{1 - i\omega RC}{1 + \omega^2 R^2 C^2} \tag{4.15}$$

Based on these analytical expressions the full data analysis for IMPS data can be based on a fitting process in a spreadsheet programme. However, in order to reduce the number of unknown parameters, first an approximate analysis of IMPS data is discussed.

The generation of a current response at fixed voltage and with modulated light is an illumination intensity dependent process. A typical dataset obtained at a potential of 0.8 V vs. Ag/AgCl with illumination from the solution side (EE) is shown in Figure 4.9.

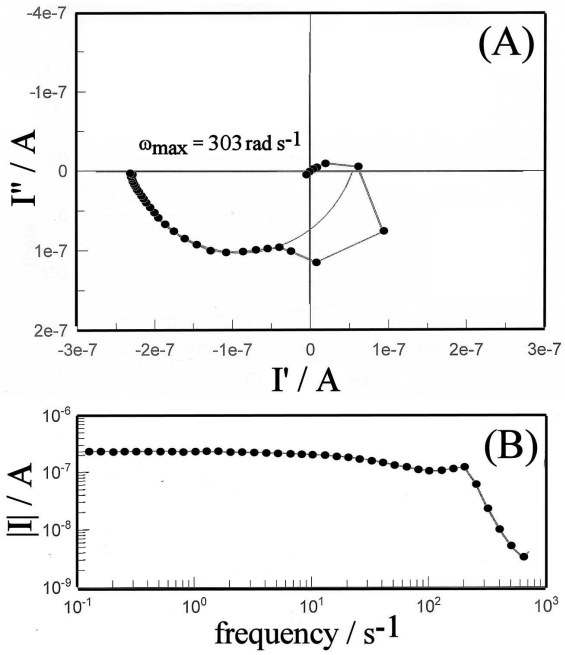

Figure 4.9. IMPS data (potential 0.8 V vs. Ag/AgCl, frequencies 1 kHz to 0.1 Hz) for a WO_3 film electrode immersed in aqueous 1 M H_2SO_4 illuminated with a blue LED (9.23 mW cm^{-2} bias, 10% modulation).

A semicircle observed in the low frequency region represents a relaxation process involving charge transport across the WO_3 film. The characteristic frequency, ω_{max} = 303 rad s^{-1}, can be extracted linked to electron diffusion across the semiconductor film. The transport relaxation time τ_D can be linked to both the frequency ω_{max} and the apparent diffusion coefficient D_{app} (see equation 4.16).

$$\omega_{\max} = \frac{1}{\tau_D} = \frac{4\,D_{app}}{\delta^2} \qquad (4.16)$$

This equation allows the apparent diffusion coefficient D_{app} to be estimated from the semicircle data in Figure 4.9 assuming a WO_3 film thickness of δ = 7 μm. Table 4.2 summarises the frequency and diffusion data as a function of illumination intensity and applied potential. Shown are the data for the EE configuration. A very similar set of data has been obtained for the SE configuration. The main difference

in EE and SE data is the absorption coefficient (see Table 4.2) which is affected by the reflection of light and optical coupling effects in the measurement cell.

The estimated apparent diffusion coefficient can be seen to change only very little with the applied potential (see Table 4.2). An apparent decrease in the diffusion rate occurs at higher potentials and this is consistent with the absence of migration effects. The mobility of electrons in WO_3 is believed to be associated with the presence of trapping states (e.g. $W(V)O_2(OH)$) and a depletion of these states in the vicinity of the FTO substrate could be contributing the lowering of the apparent diffusion coefficient at higher applied potentials.

A significant effect on the apparent diffusion coefficient for electrons in WO_3 is observed when the illumination bias is changed (see Table 4.2). When going from low photon flux to higher photon flux, a one order of magnitude change in D_{app} occurs with faster diffusion at higher levels of illumination. A closer inspection of the dependence of D_{app} on the photon flux I_0 suggests an exponential dependency (equation 4.17).

$$D_{app} = D_{app,0} \times \exp(p \times I_0) \qquad (4.17)$$

In this expression $D_{app,0} = 0.2 \times 10^{-9}$ m^2s^{-1} denotes the apparent diffusion coefficient of electrons in WO_3 in the dark and the parameter $p = 1.4 \times 10^{-16}$ s describes the effect of photon flux on the diffusion coefficient. Similar effects of illumination on charge carrier diffusion have been reported for TiO_2[40], ZnO[41], and for other types of systems[42]. The physical reality of the observed effect can be traced back to the presence of trap states. The apparent diffusion coefficient D_{app} is (in good approximation) inversely proportional to the first order trapping rate constant k_{trap} and this is exponentially dependent on the light intensity (vide infra). Another approach to this intensity dependence of the apparent diffusion coefficient is to consider the trapping states as "photo-doping" states and therefore "photo-doping" (see equation 4.3) the reason for this variability.

Table 4.2. Summary of IMPS data for a WO_3 film electrode immersed in aqueous 1 M H_2SO_4. All measurement in EE configuration with a blue LED (λ = 455 nm).

E_{appl} [a] / V vs. Ag/AgCl	Photon flux I_0 [b] / 10^{16} s^{-1}	ω_{max} [c] / rad s^{-1}	Absorbance [d] α / m^{-1} EE / SE	D_{app} [e] / 10^{-9} m^2s^{-1}	k [f] / m s^{-1}
0.8	0.93	60.6	24 / 37	0.74	0.002
0.8	1.40	124	24 / 39	1.5	0.002
0.8	1.65	210	25 / 39	2.6	0.002
0.8	2.35	303	24 / 38	3.7	0.002
0.8	2.58	628	24 / 38	7.7	0.002
0.8	2.76	810	24 / 38	9.9	0.002
0.4	1.40	128	24 / 39	1.6	0.002
0.5	1.40	127	24 / 39	1.6	0.002
0.6	1.40	127	24 / 39	1.6	0.002
0.7	1.40	124	24 / 39	1.5	0.002
0.8	1.40	124	24 / 39	1.5	0.002
0.9	1.40	122	25 / 39	1.5	0.002
1.0	1.40	120	24 / 39	1.5	0.002
1.1	1.40	119	25 / 39	1.4	0.002
1.2	1.40	111	25 / 39	1.3	0.002

[a] bias voltage applied to the WO_3 film electrode.
[b] photon flux measured with a calibrated photodiode.
[c] the ω_{max} value is obtained by fitting a depressed semicircle into experimental data.
[d] absorbance values estimated by fitting equations 4.13 and 4.14 into experimental data.
[e] apparent diffusion coefficient estimated obtained with $D_{app} = \frac{\delta^2 \omega_{max}}{4}$
[f] rate constant for electron transfer from WO_3 film to FTO substrate not well defined. Similarly good fits are obtained for higher values which suggest diffusion controlled electron transfer rather than rate controlled.

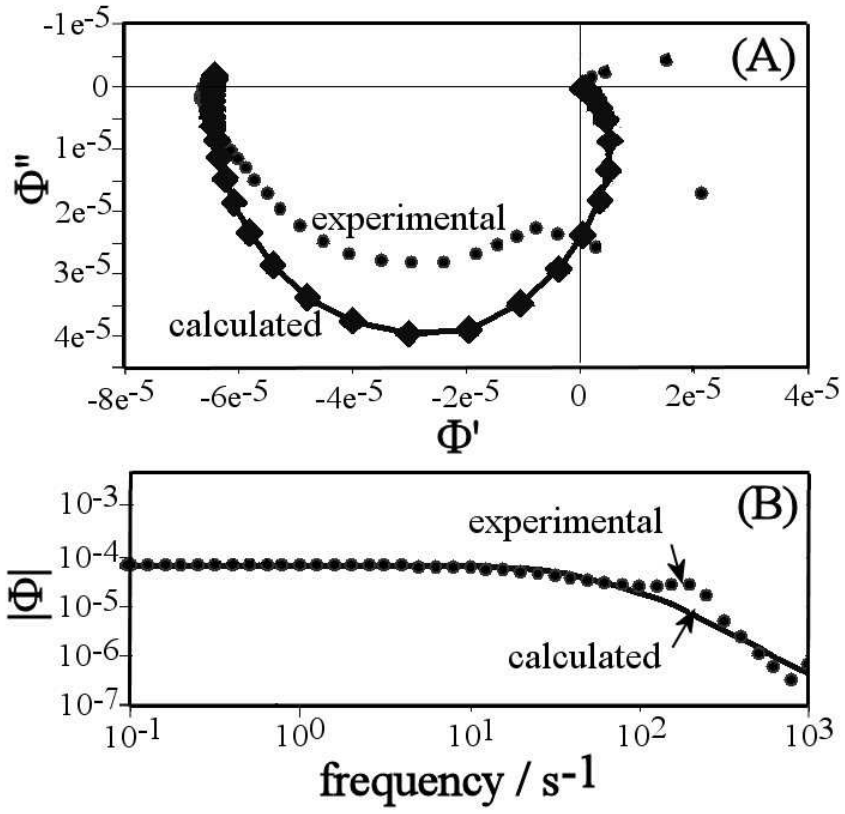

Figure 4.10. Experimental and calculated IMPS data presented as (A) imaginary Φ versus real Φ and (B) absolute Φ versus frequency plots. The data set corresponds to IMPS data (potential 1.2 V vs. Ag/AgCl, frequencies 1 kHz to 0.1 Hz) for a WO_3 film electrode immersed in aqueous 1 M H_2SO_4 illuminated with a blue LED (7.13 mW cm^{-2} bias, 10% modulation).

With many of the parameters required for equations 4.13 and 4.14 determined or estimated in good approximation, it is now possible to attempt a full solution of the IMPS data based on a model of (i) photo-generation of holes and electrons, (ii) holes reacting immediately to give O_2 at the WO_3 | electrolyte interface, (iii) Fickian diffusion of electrons (with trapping), and (iv) recombination via back-reaction of electrons with oxygen (*vide supra*). A schematic drawing of the process is shown in Figure 4.11.

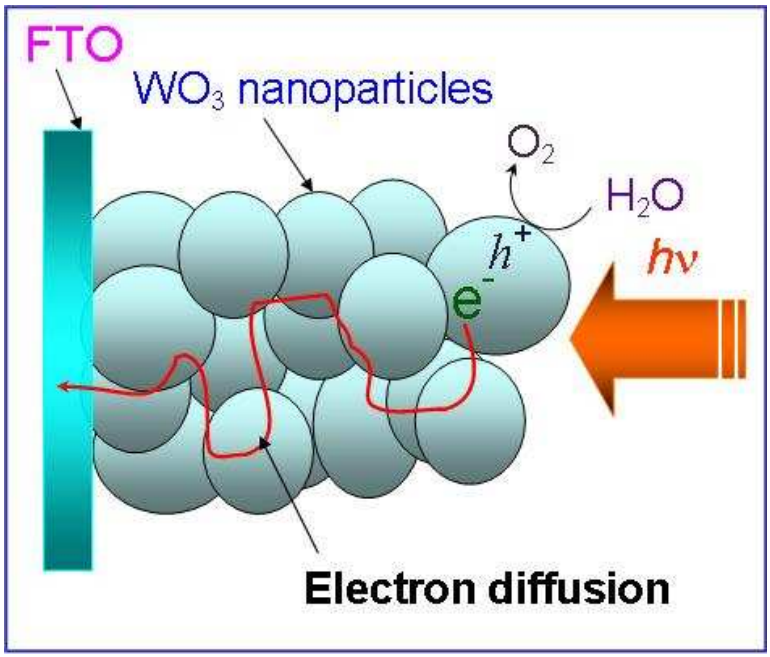

Figure 4.11. The electron diffusion through the thin film WO_3 to the conducting glass substrate, by illumination via EE side.

A typical dataset of experimental and fitted IMPS data is shown in Figure 4.10. The dominant semicircle is readily observed and the slightly depressed nature of the experimental semicircle is apparent. This depression effect is often believed to be associated with a dispersion effect (e.g. a distribution of film thicknesses) but could also be related to trapping effects (*vide infra*). The high frequency region is dominated by more complex behaviour outside of the first simplistic model. The low frequency behaviour is well reproduced with the model. The rate of electron transfer across with WO_3 | FTO interface was observed to be only poorly determined. The value could be increased and the absorbance decreased to give a similar fit. Therefore, the process is believed to be essentially diffusion controlled.

The additional parameters determined via the fitting of IMPS data are the absorbance values. It can be seen (see Table 4.2) that the absorbance for EE illumination is systematically lower compared to the case of SE illumination. This is due to reflection and poor optical coupling of the experimental cell rather than a

real effect. Also, these absorbance values are considerably lower compared to the predicted absorbance $\alpha = 1800\ m^{-1}$ based on the UV/Vis spectrum.

The analysis of IMPS data can be further improved by including the effects of electron trapping kinetics. It is assumed that the mobility of electrons is relatively high, however, intermittent trapping of the electrons slows down the transport and therefore substantially lowers the apparent diffusion coefficient. The trapping transport model can be expressed as in equation 4.18.

$$W(VI)O_2(OH)^+ + e^- \underset{k_{detrap}}{\overset{k_{trap}}{\rightleftharpoons}} W(V)O_2(OH) \qquad (4.18)$$

The trapping and de-trapping of the electron occurs with the (pseudo-) first order rate constants k_{trap} and k_{detrap}, respectively. The trapped electron is assumed to undergo reaction with holes or oxygen with a time constant τ_{trap}. The model assumes that k_{trap} and k_{detrap} are constant throughout the WO_3 film and leads to new expressions for D_{app} and γ as suggested by Peter[38].

$$D_{app} = \frac{D}{1 + \dfrac{k_{trap} k_{\mathrm{detrap}}}{\left(k_{\mathrm{detrap}} + \dfrac{1}{\tau_{trap}}\right)^2}} \qquad (4.19)$$

$$\gamma^2 = \frac{1}{D\tau_{cb}} + \frac{k_{trap}}{D} \frac{\dfrac{1}{\tau_{trap}}\left(k_{\mathrm{detrap}} + \dfrac{1}{\tau_{\mathrm{trap}}}\right) + \omega^2}{\left(\mathrm{k}_{\mathrm{detrap}} + \dfrac{1}{\tau_{\mathrm{trap}}}\right)^2 + \omega^2} + \frac{i\omega}{D}\left(1 + \frac{k_{trap} k_{\mathrm{detrap}}}{\left(k_{\mathrm{detrap}} + \dfrac{1}{\tau_{\mathrm{trap}}}\right)^2 + \omega^2}\right) \qquad (4.20)$$

With this modification of the model, the high frequency IMPS data can suddenly be reproduced and explained. Figure 4.12 shows typical data for three levels of illumination.

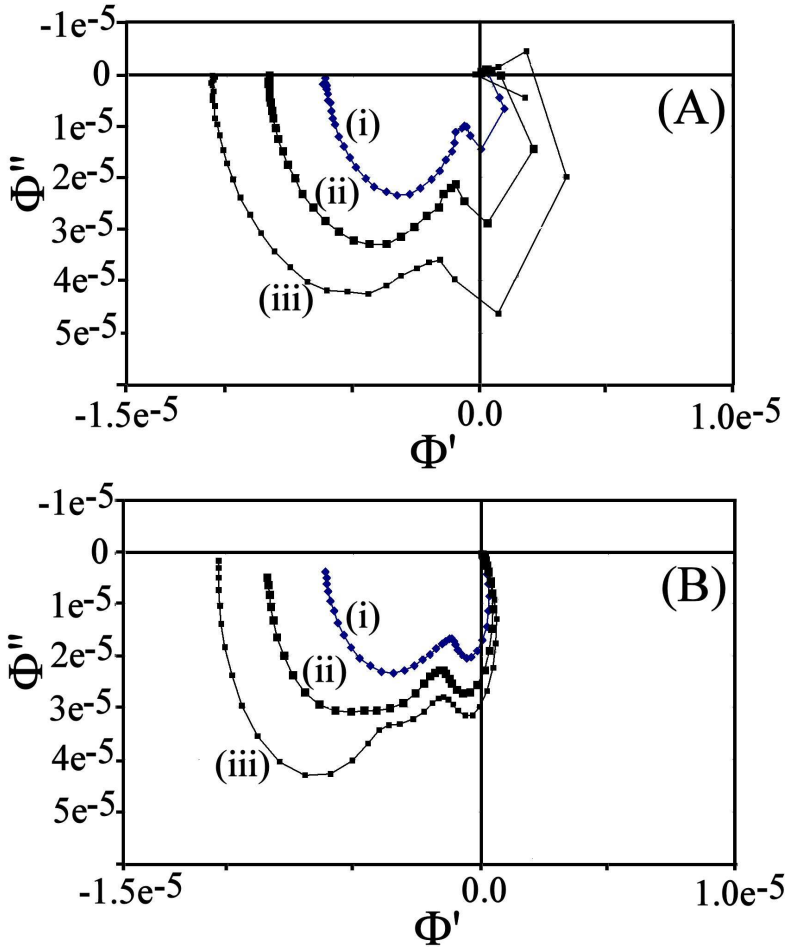

Figure 4.12. (A) IMPS spectra for a WO_3 film electrode immersed in 1 M H_2SO_4 at 0.8 V vs. Ag/AgCl with illumination of I_0 = (i) 0.93 × 10^{16} s^{-1}, (ii) 1.40 × 10^{16} s^{-1}, (iii) 1.65 × 10^{16} s^{-1} and a frequency range of 1000 to 0.1 s^{-1}. (B) Simulated IMPS data based on the trapping model with k = 0.01 m s^{-1}, k_{trap} = 3000 s^{-1}, k_{detrap} = 80 s^{-1}, and D = (i) 2.8 × 10^{-8} m^2s^{-1}, (ii) 5.7 × 10^{-8} m^2s^{-1}, and (iii) 8.0 × 10^{-8} m^2s^{-1}.

The match between experimental and simulation data is only qualitative and in particular in the high frequency range the shape is not fully reproduced. Nevertheless, features appear very similar. An interesting observation is that not k_{trap} but instead D appears illumination dependent. The pseudo first order rate

constant k_{trap} is expected to increase with higher illumination and it does at even higher levels where data becomes even more complex. In contrast, the increase in D is unexpected. Both observations can be understood with a model based on trapping sites close to the WO_3 | aqueous electrolyte interface (e.g. a spatial dependence of k_{trap} and other parameters). With higher light intensity the number of "active trapping sites" may stay relatively constant whereas D increases as the path of electrons penetrates deeper into the WO_3 grains away from the aqueous dielectric.

Interestingly, IMPS data do not show a clear explanation for the slower kinetics observed in photo-transient experiments at +1.2 V vs. Ag/AgCl potential bias. IMPS data are obtained under a small amplitude conditions, which is in agreement with linear response theory. Photo-transient measurements, in contrast, are based on large amplitude responses and additional effects outside the linear response regime are encountered. It is possible that at very positive potential bias a depletion of trapping states near the WO_3 | FTO interface occurs causing a change in time constant at lower electron concentration.

A further aspect missing from the detailed data analysis for IMPS measurements of WO_3 films is the presence of pores and the need for proton conduction into these pores during photo-doping. Photo-doping of the WO_3 film is associated with the formation of $W(V)O_2(OH)$ states and the protons required for these states to form have to be delivered from the aqueous solutions phase. Due to the high proton activity in 1 M H_2SO_4 these effects may be negligible. However, proton depletion in pores could be significant and proton diffusion in pores may also contribute (or even dominate) to the observed apparent diffusion coefficients. Further experimental work and better theoretical models will be required in future to shed more light on these problems.

4.4. Conclusions

Spray-pyrolysis techniques have been applied for the fabrication of thin photo-electrochemically active WO_3 films on FTO substrates. The characterisation of these films revealed good photo-activity for 7 μm thickness and oxygen evolution for bias voltages positive of 0.4 V vs. Ag/AgCl. The effect of illumination on the apparent diffusion coefficient D_{app} for electrons revealed an exponential dependence of D_{app} on light intensity and "photo-doping". Qualitative evidence for the trapping diffusion model has been obtained. Further studies will be required for more quantitative information and to explore the effects of film thickness and pores size.

4.5. References

(1) Currao, A., *Chimia*, **2007,** *61*, (12)**,** 815-819.

(2) Kudoa, A., *International Journal of Hydrogen Energy,* **2007,** *32,* 2673 – 2678.

(3) Murphya, A.B.; Barnesa, P.R.F., Randeniyaa, L.K.; Plumba, I.C.; Greyb, I.E.; Horneb, M.D.; Glasscock, J.A., *International Journal of Hydrogen Energy,* **2006,** *31*, 1999 – 2017.

(4) Darwent, J. R.; Mills, A., *Journal of the Chemical Society Faraday Transactions II,* **1982***, 78*, 359-367.

(5) Patnaik, P., *Handbook of Inorganic Chemical Compounds,* **2003***,* McGraw Hill**,** New York.

(6) Xu, N.; Sun, M.; Cao, Y.W.; Yao, J.N.; Wang, E.G.; *Applied Surface* Science, 2000, 157, 81-84.

(7) Samuel, J. I.; Sasikaran, K.; Kourosh, K.; Adrian, T.; Wojtek, W., *Sensor letters,* **2003***, 1,* 33.

(8) Thiele, J. A.; da Cunha, M. P., *Sensors and Actuators B,* **2006,** *113*, 816

(9) Wang, H.; Lindgren, T.; He, J.; Hagfeldt, A.; Lindquist, S.E., J. *Phys. Chem., B,* **2000,** *104,* 5686.

(10) Georg, A.; Graf, W.; Neumann, R.; Wittwer, V., *Thin Solid Films*, **2001,** *384*, 269.

(11) Jiqiao, L.; Baiyun, H.; Zhiqiang, Z., *Int. J. Refract. Met. Hard Mater.* **2001,** *19,* 79.

(12) Deb, S. K., *Philos. Mag.,* **1973,** *22*, 801.

(13) Oi, T.; Miyauchi, K.; Uehara, K., *J. Appl. Phys.,* **1982,***53,* 1823.

(14) Ohtani, B.; Stsumi, I.; Nishimoto, S.; Kagiya, T., *Chem. Lett.,* **1988**, 295.

(15) Fleisch, T. H.; Mains, G.J., *J. Chem. Phys.* **1982,** *76*, 780.

(16) Loo, B. H.; Yao, J.N.; H. Cobe, D.; Hashimoto, K.; Fujishima, A., *Appl. Surf. Sci.,* **1994,** *81,* 175.

(17) Alexander, B.D.; Kulesza, P.J.; Rutkowska, L.; Solarska, R.; Augustynski, J., *Journal of Materials Chemistry,* **2008,** *18*, (20), 2298-2303.

(18) Solarska, R.; Santato, C.; Jorand-Sartoretti, C.; Ulmann, M.; Augustynski, J., *Journal of Applied Electrochemistry,* **2005,** *35*, (7), 715-721.

(19) Lindgren, T.; Wang, H.; Beermann, N.; Vayssieres, L.; Hagfeldt, A.; Lindquist S., *Solar Energy Materials & Solar Cells,* **2002,** *71,* 231–243.

(20) Yamashev, K.; Malyarevich, A.; Posnov, N., *Chem. Phys. Lett.,* **1998,** *288*, 567.

(21) Santato, C.; Ulmann, M.; Augustynski, J., *J. Phys. Chem. B,* **2001,** *105*, 936.

(22) Santato, C.; Odziemkowski, M.; Ulmann, M.; Augustynski, J., *J. Am. Chem. Soc.,* **2001,** *123,* 10639.

(23) Sodergen, S.; Hagfeldt, A.; Olsson, J.; Lindquist, S., *J. Phys. Chem.,* **1994,** *98,* 5552.

(24) Monk, P.; Chester, S. L., *Electrochim. Acta.,* **1993,** *38*, 1521

(25) Patil, P. S.; Patil, P. R.; Kamble, S. S.; Pawar, S. H., *Sol. Energy Mat. Sol. Cells,* **2000,** *60,* 143.

(26) Reichman, B.; Bard, A.., *J. Electrochem. Soc.,* **1979,** *126,* 583.

(27) Kubo, T.; Nishikitani, Y., *J. Electrochem. Soc.,* **1998,** *145,* 1729-1734.

(28) Orel, B.; Krasovec, U.O.; Stanger, L., *J. Solgel Sci. Technol.,* **1998,** *11*, 87.

(29) Regraguia, M.; Addoua, M.; Outzourhitb, A.; BerneÂdec, J.C., El Idrissia, E.; Benseddikb, E. ; Kachouane, A., *Thin Solid Films,* **2000,** *358,* 40-45.

(30) Sivakumar, R.; Raj, A.M.E.; Subramanian, B.; Jayachandran, M.; Trivedi, D.C.; Sanjeeviraja, C., *Materials Research Bulletin,* **2004,** *39*, 1479-1489.

(31) Enesca, A.; Duta, A.; Schoonman, J., *Thin Solid Films,* **2007,** *515,* 6371–6374.

(32) Sayama, K.; Hayashi, H.; Arai, T.; Yanagida, M.; Gunji, T.; Sugihara, H., *Applied Catalysis B-Environmental,* **2010,** *94,* 150-157.

(33) Miseki, Y.; Kudo, A., *ChemSusChem,* **2011,** *4,* 245 – 251.

(34) Yaacob, M.H.; Breedon, M.; Kalantar-zadeh, K.; Wlodarski, W., *Sensors and Actuators B,* **2009,** *137,* 115–120.

(35) Girault, H.H., *Analytical and Physical Electrochemistry,* **2004,** EPFL Press, Lausanne, 339.

(36) Chang, B.Y.; Park, S.M., *Annual Review of Analytical Chemistry,* **2010,** *3*, 207-229.

(37) Huang, Y. J.; Dai, H. H; Li, W. S.; Li, G. L.; Shu, D.; Chen, H. Y., *Journal of Power Sources,* **2008,** *184*, 2, 348-352.

(38) Dloczik, L.; Ileperuma, O.; Lauermann, I.; Peter, L.M.; Ponomarev, E.A.; Redmond, G.; Shaw, N.J.; Uhlendorf, I., *Journal of Physical Chemistry B,* **1997,** *101,* 10281-10289.

(39) Peter, L.M.; Ponomarev, E.A.; Fermin, D.J., *Journal of Electroanalytical Chemistry,* **1997,** *427,* 79-96.

(40) Peter, L.M.; Wijayantha, K.G.U., *Electrochimica Acta,* **2000,** *45,* 4543-4551.

(41) Oekermann, T.; Yoshida, T.; Minoura, H.; Wijayantha, K.G.U.; Peter, L.M., *Journal of Physical Chemistry B,* **2004,** *108*, 8364-8370.

(42) Kruger, J.; Plass, R., Gratzel, M.; Cameron, P.J.; Peter, L.M., *Journal of Physical Chemistry B,* **2003,** *107,* 7536-7539.

Chapter 5

Layer-by-Layer Formation and Characterisation of Photo-Electro-Chemically Active Films of Nano-Hematite Fe_2O_3

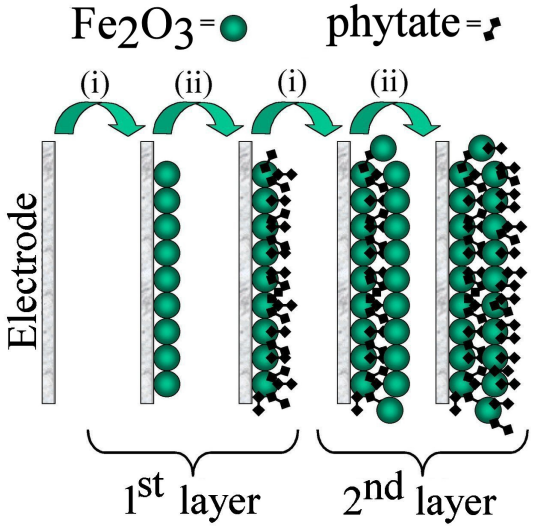

Abstract. In this chapter the layer-by-layer assembly method is employed to form films from hematite nanoparticles and phytate binder molecules. Photo-electrochemical responses are observed as a function of film thickness and applied potential. A model based on differing electron and hole mobility in conjunction with recombination is applied to explain the photo-transient responses.

Acknowledgement. Help and discussion from Charles Y. Cummings (junction experiments) and Frank Marken (digital simulation work) are gratefully acknowledged. Dr. John M. Mitchels is acknowledged for help with SEM and AFM imaging.

Content

5.1. Introduction

5.1.1. Introduction to Layer-by-Layer Assembly

Materials for electrodes often require a high level of optimisation in terms of composition and morphology. In particular in photo-electrochemistry the thickness and composition of mesoporous semiconductor films is important and methods for the controlled design (in contrast to simple spray pyrolysis [1] or growth by sputter coating[2]) of photo-electrochemically active films are required. The electrostatic assembly of colloid particles in layer-by-layer manner could be a useful alternative method and therefore this method is employed in this chapter.

The layer-by-layer assembly process based on colloidal building blocks has been introduced by Hong and Decher [3] and it provides a very good technique for the manufacturing of composite films with nanometer scale. It is a versatile, simple, and easy to use technique, although labour and time intensive. The attractive feature of this approach is the ability to produce complex structures from basic colloidal components, and integration of building blocks into self-assembling constructions for a wide range of applications[4]. Another good feature of self-assembly is hierarchy, where the primary composition blocks adhere with more complex secondary structures that are integrated into the next size-level in a compact structure. These hierarchical constructions may exhibit unique properties that are not found in the individual components [5,6,7]. It is interesting to apply this film design concept to the problem of making optimised photo-active electrodes. Here the focus is on the use of hematite (Fe_2O_3) which is known to be a highly sustainable and promising photo-anode material for water splitting [8,9].

Layer-by-layer (LBL) assembly is based on the electrostatic attraction between charged colloidal species. LBL assembly was used for example to synthesize metal oxide nanostructures for In_2O_3, NiO, SnO_2, Fe_2O_3, and CuO. It has also been widely used to synthesize polymeric multi-composites, inorganic and hybrid hollow-spheres, polymer nanotubes, and core–shell nanostructures [10].

In the past, the layer-by-layer method was used to prepare two types of nanoporous Fe_2O_3 [11]. The first type was a nano-film deposit composed of 4–5 nm sized Fe_2O_3

particles connected by phytic acid as a molecular binder. The second type was a nanoporous film formed after calcination of the first type of deposit in air at 500^o C to give a stable mesoporous hematite film. Scanning electron microscopy (SEM) and atomic force microscopy (AFM) were used to characterize these nano-film deposits. It was found that the average thickness contributed to the film by every layer was ca. 3 nm [11].

5.1.2. Introduction to Photoelectrochemical Processes at Hematite

Hematite films provide a uniquely sustainable technology for water splitting[12] and successful single crystal studies have been reported for example in 1983 by Hamnett and co-workers[13]. This semiconductor material has a band gap of 2.0-2.2 eV (Fe_2O_3 is both an indirect band gap system similar to silicon and a direct band gap system [14] and it allows light absorption up to 550 to 600 nm [15,16] depending on film thickness, particle size, and doping). There is a marked effect of the electrode preparation on the photoelectrochemical performance[2,17,18] and in particular silicon doping has been highlighted as a major factor in improving efficiency [19,20,21,22]. Although the details of the complex photoanodic oxygen evolution process at hematite are not fully resolved [11], it is generally accepted that charge separation upon photon absorption is causing the formation of a mobile conduction band electron and a rather immobile hole. The hole diffusion to the Fe_2O_3 surface is required followed by multi-electron oxidation of water to O_2 in competition to recombination [23]. Catalyst layers based on cobalt and iridium have been suggested to improve the surface reaction and to suppress recombination [21]. The limit for the theoretical current density for (AM1.5) photo-electrochemical oxygen evolution at Fe_2O_3 has been reported as 12 $mAcm^{-2}$ [24]. Reproducible literature values are currently at ca. 3 $mAcm^{-2}$ [25].

5.1.3. Aims of this Study

In this chapter, the layer-by-layer method is employed to make films of nano-hematite, Fe_2O_3 nanoparticles of ca. 5 nm diameter. A negatively charged molecular binder, phytate (see Figure 5.1B), is employed and films are calcined to give purely inorganic mesoporous deposits.

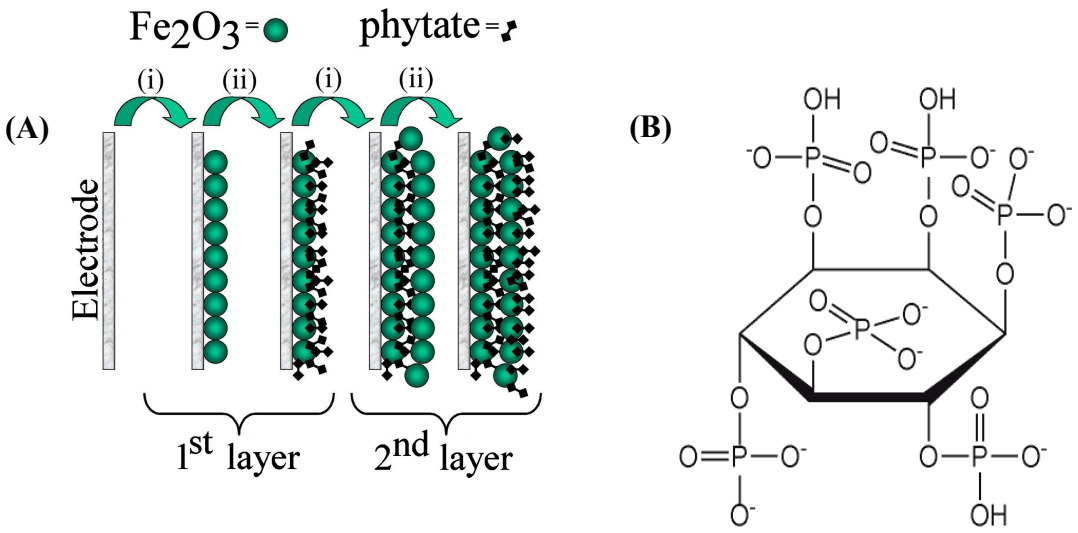

Figure 5.1. (A) Schematic representation of the deposition process based on the alternating film adsorption employing positively charged Fe_2O_3 nanoparticles and negatively charged phytate. The resulting structure is likely to be disordered rather than layered as indicated. (B) Molecular structure of the phytate poly-anion.

Photo-electrochemical experiments are conducted in order to explore the ability of nano-hematite films to undergo photochemical water splitting processes. The nanoparticulate Fe_2O_3 films deposited on FTO are shown to provide dark access to "conduction band" and "valence band" in cyclic voltammetry experiments. Mobility of electrons and holes are investigated as key components in the photo-current transients. Recombination is shown to be the major limiting factor in photoelectrochemical oxygen evolution. A very simple surface conduction model is developed and contrasted to the existing bulk semiconductor models for transient photo-current data interpretation.

The main aims of this chapter are to (i) demonstrate and improve photo-activity for layer-by-layer hematite films and (ii) to develop a new quantitative model for the interpretation of transient and steady state photo-responses.

5.2. Experimental

5.2.1. Chemical Reagents

$FeCl_3$, $NaClO_4$, NaOH, $HClO_4$, phytic acid sodium salt (all Sigma-Aldrich). These chemicals were obtained commercially and used without any further purification. Water for experiments was filtered and double de-ionized water (Elga Filter Systems, Bucks) with a resistivity of 18.2 MΩ cm at 20^{o} C.

5.2.2. Instrumentation

Electrochemical measurements were conducted with an Autolab PGSTAT12 (Ecochemie, NL) potentiostat system. Working electrodes were prepared from tin-doped indium oxide (ITO) coated glass slides (Image Optics, Basildon). ITO used in case of junction experiment and FTO has been used in all the other experiments included in this chapter. These glass slides were sonicated in water and in ethanol and then heat treated at 500 ^{o}C in air to remove all impurities from the surface. The resulting hydrophilic surface was used for dip-coating experiments. An Ag/AgCl (3 M KCl) was used as reference and a platinum wire as counter electrode.

Generator – collector experiments were performed at patterned ITO electrodes. Initially, electrodes were patterned by masking off a "U" pattern (with Kel-F tape). ITO etching was then carried out in 1 wt.% tartaric acid and 3 wt.% oxalic acid solution at 35 ˚C for 20 minuets. The resulting ca. 1 mm wide ITO line was then cut with a focused ion beam (FIB: Ga liquid metal ion source (LMIS), 30 kV, 50 pA ion beam for making a 1 micron deep trench; monitored by SEM: Carl Zeiss XB1540) resulting in a ca. 600 nm wide gap or junction. Prior to electrochemical experiments these junction electrodes were cleaned by rinsing with water and ethanol, drying, 30 minutes heat treated at 500 ^{o}C in air, and re-equilibration to ambient conditions. Dr. Suguo Huo and Dr. Paul Warburton are gratefully acknowledged for allowing access to the EPSRC FIB service at UCL.

5.2.3. Procedures

Preparation of Colloidal Solution of Fe_2O_3 Nanoparticles. A colloidal solution of Fe_2O_3 was prepared following literature procedures [26,27] by drop-wise addition (2 drops per second) of 50 mL aqueous solution of 20 mM $FeCl_3$ into 450 mL boiling distilled water with continuous stirring. After the complete addition the deep orange colour produced was left to cool naturally to room temperature (~22^o C). Then it was transferred into a dialysis tube system. Aqueous 1 mM $HClO_4$ was used as exchange solution for 24 hours and this was repeated for three days. The final solution contained ca. 2 mM Fe(III) in the form of hydrous iron oxide nanoparticles and exhibit a pH of ca. 3. Addition of 5 mM $NaClO_4$ was used to slightly destabilise the colloidal solution for layer-by-layer film deposition.

Preparation of Fe_2O_3 Films at FTO Electrodes. The procedure of preparation of nanoporous Fe_2O_3 was developed elsewhere [11] and consisted of the following steps:

(1)- The FTO (Fluorine-doped tin oxide) slide was cleaned by sonication at 40^{o}C for 15 minutes in, sequentially, detergent (5 vol% decon-90), Isopropanol, acetone and in ethanol.

(2)- A clean and dry FTO was immersed into Fe_2O_3 colloidal solution for 1 minute, and then rinsed with distilled water and dried using warm air.

(3)- The electrode was immersed into a binder solution (40 mM phytate solution for 1 minute followed by rinsing and drying with warm air.

(4) Steps 1 and 2 were repeated as many times as required to deposit the desired number of layers

(5) The film was then calcined at 500^o C in air for 2 hours to remove the binder and to produce a completely inorganic hematite film consisting of 5-6 nm diameter nanoparticles

Numerical Simulation Progam and Procdure. Two cases of numerical simulation are employed to interpret voltammetric data. (i) Results from junction studies are modelled to give approximate diffusion coefficients for electron mobility in mesoporous hematite films. (ii) Photo-current transient for hematite films are modelled to allow shape analysis. One dimensional diffusion models was coded in Fortran (using Matlab on a PC). Mathematical details are provided in the text and the programs are shown in the appendix.

5.3. Results and Discussion

5.3.1. Formation and Characterisation of Nano-Hematite Films

Hematite film samples on FTO substrates were prepared using the layer-by-layer method. Samples were obtained with different numbers of layers varying from 10 to 60 layers following a literature procedure [11]. After deposition, samples were calcined at 500 ^{o}C in air for 30 minutes. This ensured removal of organic components from the film and conversion of the colloidal ferric hydroxide to hematite [28].

Consistent with literature reports, nano-hematite films on FTO substrates are uniform and smooth. In order to obtain height information, atomic force microscopy (AFM) images were obtained for a scratched sample. Figure 5.2 shows a typical film image with cross-sectional information. A scratch was applied to probe the thickness. The height is typically 40 nm for a 10-layer deposit and the thickness varies approximately linearly with the number of layers applied to the FTO substrate. This suggests approximately 4 nm thickness increase in each deposition cycle. This is consistent with a typical particle size of 5-6 nm after calcination.

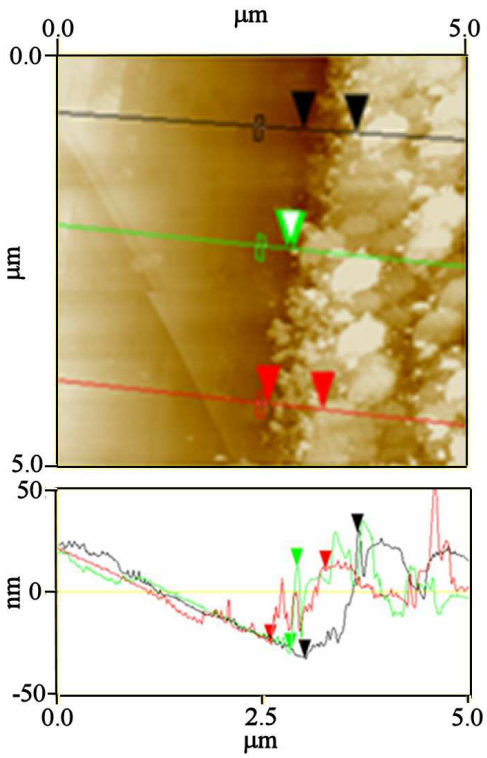

Figure 5.2. An AFM image for a scratched 10-layer (calcined for 30 minuets at 500^{o}C) nano-hematite film. The height profiles suggest ca. 40 nm thickness for a 10-layer film.

The brownish-yellow coloration of the Fe_2O_3 film can be clearly observed for 30- and 60-layer films. UV/Vis absorbance measurements were carried out. It was found that the absorbance increases with increasing the number of layers (the thickness). Figure 5.3 shows the absorbance of different samples with different numbers of layers ranging from 10 to 60 layers. The onset of the absorption occurs at about 550 nm and towards shorter wavelengths an increase absorbance is recorded. Note that the non-linearity for thicker films originates from the non-Lambert-Beer conditions for absorption in dense media.

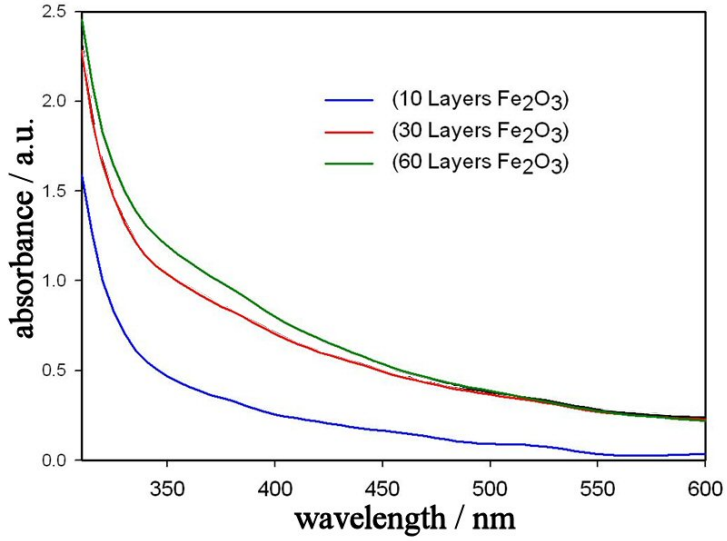

Figure 5.3. The absorbance of Fe_2O_3 film electrodes in air as a function of thickness.

5.3.2. Cyclic Voltammetry of Nano-Hematite Films

Dark Cyclic Voltammetry. Cyclic voltammetry experiments were carried out on the samples prepared by using the layer-by-layer method. Figure 5.4 shows typical cyclic voltammograms for a 60-layer sample at different scan rates immersed in aqueous 1 M NaOH. A specially designed cell was used in the measurements and the solution-exposed area of the Fe_2O_3 film was well-defined as 0.38 cm^2 through a circular quartz window with 0.7cm diameter.

Figure 5.4A shows that both a reduction and an oxidation of Fe_2O_3 are observed. The reduction (see P1) is chemically reversible and it leads to the formation of Fe(II). A chemical reaction proposed for this process (consistent with literature reports [29]) is shown in equation 5.1.

$$Fe(III)_2O_3 + e^- + H^+ \rightleftharpoons Fe(II)Fe(III)O_2(OH) \quad (5.1)$$

This reaction shown in equation (5.1) is a concerted reaction. The reduction of Fe(III) leads to Fe(II) surface sites and the charge balance requires the uptake of a cation, tentatively assigned here to H^+. The electron can be assumed to be mobile at the surface of the mesoporous Fe_2O_3 film with an apparent diffusion coefficient which may depend on the concentration of Fe(II) sites. A pre-wave observed in phosphate containing electrolyte media is likely to be associated with a surface layer of iron phosphate.

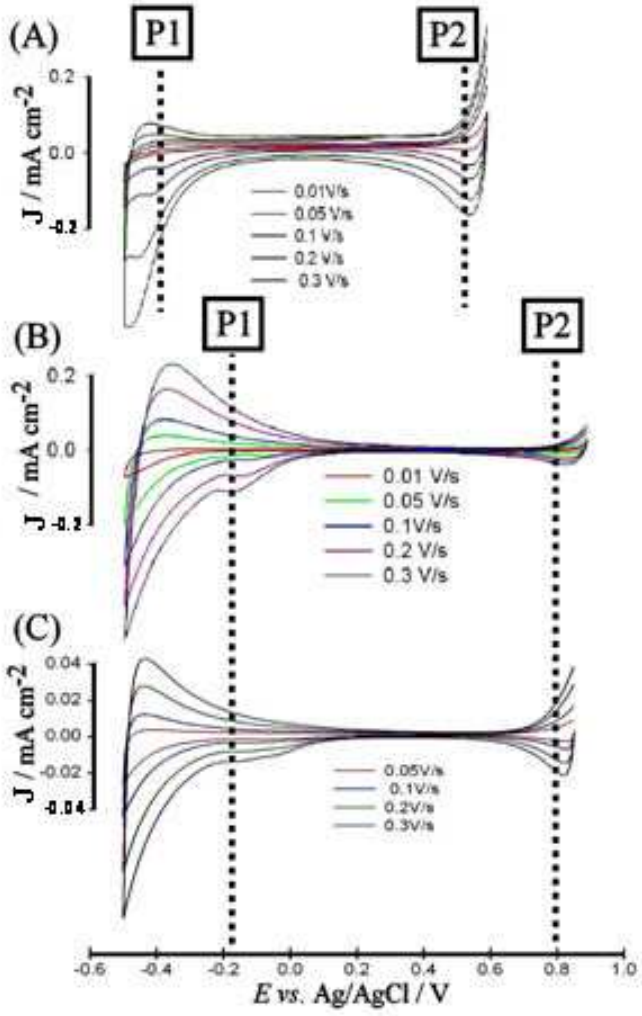

Figure 5.4. (A) Dark cyclic voltammograms for a 60-layer hematite film immersed in 1 M NaOH at different scan rates. (B) Dark cyclic voltammograms for the same electrode in 1 M phosphate buffer solution pH 11 at different scan rates. (C) Dark cyclic voltammograms for a 10-layer hematite film in 1 M phosphate buffer solution pH 11 at different scan rates.

The oxidation of Fe_2O_3 (see process P2) giving rise to a characteristic chemically reversible voltammetric response at ca. 0.6 V vs. Ag/AgCl in aqueous 1 M NaOH has been reported previously in the literature [29]. This process is formally associated with the formation of Fe(IV) sites (see equation 5.2).

$$Fe(III)_2O_3 + OH^- \rightleftharpoons Fe(IV)Fe(III)O_3(OH) + e^- \qquad (5.2)$$

The formation of Fe(IV) can be understood formally as "hole" formation and transport across the Fe_2O_3 surface. This oxidation process produces highly reactive surface states and at slower scan rates of ca. 0.01 V s^{-1} the process becomes chemically irreversible (see Figure 5.4.A, and B). It is known that the oxidized hematite surface in contact to aqueous 1 M NaOH solution leads to the slow evolution of oxygen [30]. The first order rate constant for this oxygen evolution process (based on a very much oversimplified mechanistic model, see below) can therefore be estimated for dark conditions based on $k_c = \frac{\nu F}{RT} = 0.4\ s^{-1}$ (for the 60-layer film).

For both, reduction and oxidation, the voltammetric current response increases approximately linearly with scan rate indicating an immobilised redox system. However, the shape of the voltammetric response is complex and charge transport phenomena are likely to affect the shape. A similar series of experiments was conducted in aqueous 1 M NaOH (pH 14) and in 1 M phosphate buffer at pH 11. The comparison of data in Figure 5.4A and B clearly demonstrates the resulting shift in the voltammetric responses. For a pH change of ca. 3 units the onset potentials for both oxidation and reduction shift by ca. 0.2 V consistent with the proposed equation 5.1 and 5.2.

The thickness of the Fe_2O_3 film electrode affected the magnitude of voltammetric current responses. In Figure 5.4C it can be seen that for the reduction (process P1) a 10-layer film exhibits approximately 6-times lower currents compared to a 60-layer film. Therefore voltammetric response is approximately proportional to the film thickness, which suggests that most of the film is electrochemically active (for sufficiently thin films). For the oxidation (process P2) the response seems less

dependent on thickness indicating perhaps a lower apparent diffusion coefficient for holes.

Illuminated Cyclic Voltammetry. When applying a pulsed light signal to the Fe_2O_3 film electrodes during cyclic voltammetry, it is possible to explore potential dependent photo-electrochemical phenomena. Figure 5.5 shows typical voltammetry traces obtained under pulsed illumination with a blue LED light source (λ = 455 nm). It was found that the photocurrent onset starts at different potentials depending on the electrolyte (according to the pH values). In 1 M NaOH (Figure 5.5A) it starts at ca. -0.3 V vs. Ag/AgCl, while by using phosphate buffer pH 11 the photocurrent onset commenced at ca. -0.1 V vs. Ag/AgCl. This shift is in agreement with the pH dependent shift observed in dark voltammetry.

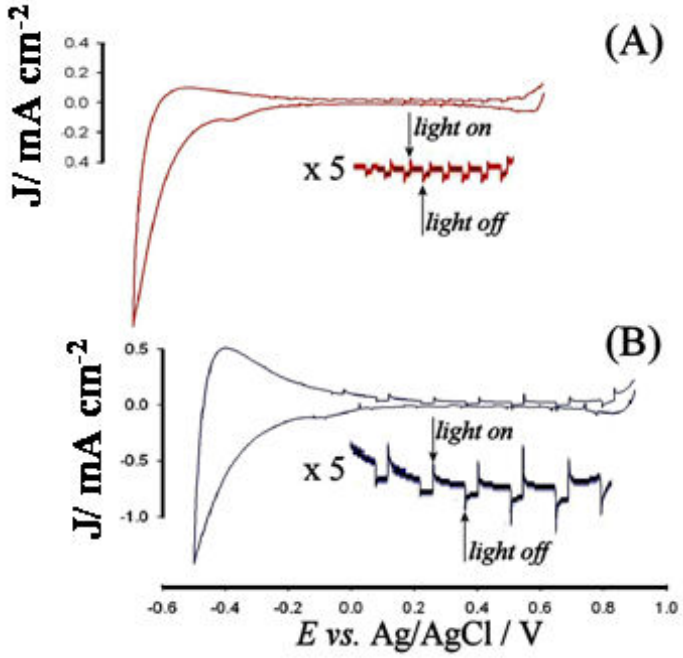

Figure 5.5. (A) Illuminated cyclic voltammetry for a 60-layer hematite film electrode SE in 1 M NaOH with a scan rate of 0.1 Vs^{-1}. (B) Illuminated cyclic voltammograms SE in 1 M phosphate buffer pH 11 with a scan rate of 0.1 Vs^{-1}. Insets show photocurrent with expanded current scale.

When cycling the potential over a wide potential window, it was found that the backward photocurrent response (going from negative to positive potentials) is higher than that of the forward photocurrent (going from positive to negative potentials) for the same electrode under the same conditions. This effect might be due to the

temporary de-activation of the electrode by the initial oxidation (hole formation) process. Magnified in Figure 5.5 insets, the dominating photo-electrochemical responses for the potential scan in positive direction are shown. It can be seen that anodic photo-currents are produced in the presence of light. The overall mechanism for this process is summerised in equations 5.3 and 5.4.

$$Fe(III)_2O_3 + h\nu \rightarrow Fe(III)_2O_3^* \quad (5.3)$$

$$Fe(III)_2O_3^* + Fe(III)_2O_3 + H_2O \rightarrow Fe(II)Fe(III)O_2(OH) + Fe(IV)Fe(III)O_3(OH) \quad (5.4)$$

The formation of an "electron" (or $Fe(II)Fe(III)O_2(OH)$) and a "hole" (or $Fe(IV)Fe(III)O_3(OH)$) leads to two oppositely charge and freely diffusing charge carriers. These are very likely to undergo recombination and only a small fraction of electrons are able to diffuse into the FTO substrate electrode. The "hole" states are likely to diffuse to the surface of the hematite film to undergo slow reaction with the aqueous solution (see equation 5.5) or recombination.

$$4\ Fe(IV)Fe(III)O_3(OH) + 2\ H_2O \rightarrow 4\ Fe(III)_2O_3 + 3O_2 + 8\ H^+ + 8\ e^- \quad (5.5)$$

The shape and further features associated with the photo-current transients will be investigated in more detail below.

5.3.3. Electrochemical Impedance Spectroscopy of Nano-Hematite Films

Impedance methods can be employed to provide time scale (or frequency domain) dependent information about reactions and processes. Here, the impedance measurements were taken for the samples prepared by using the layer-by-layer method. Figure 5.6 shows data for the dark impedance for a 60-layer Fe_2O_3 film obtained at a range of applied potentials (0.0 to 0.7 V vs. Ag/AgCl) in aqueous 1 M NaOH.

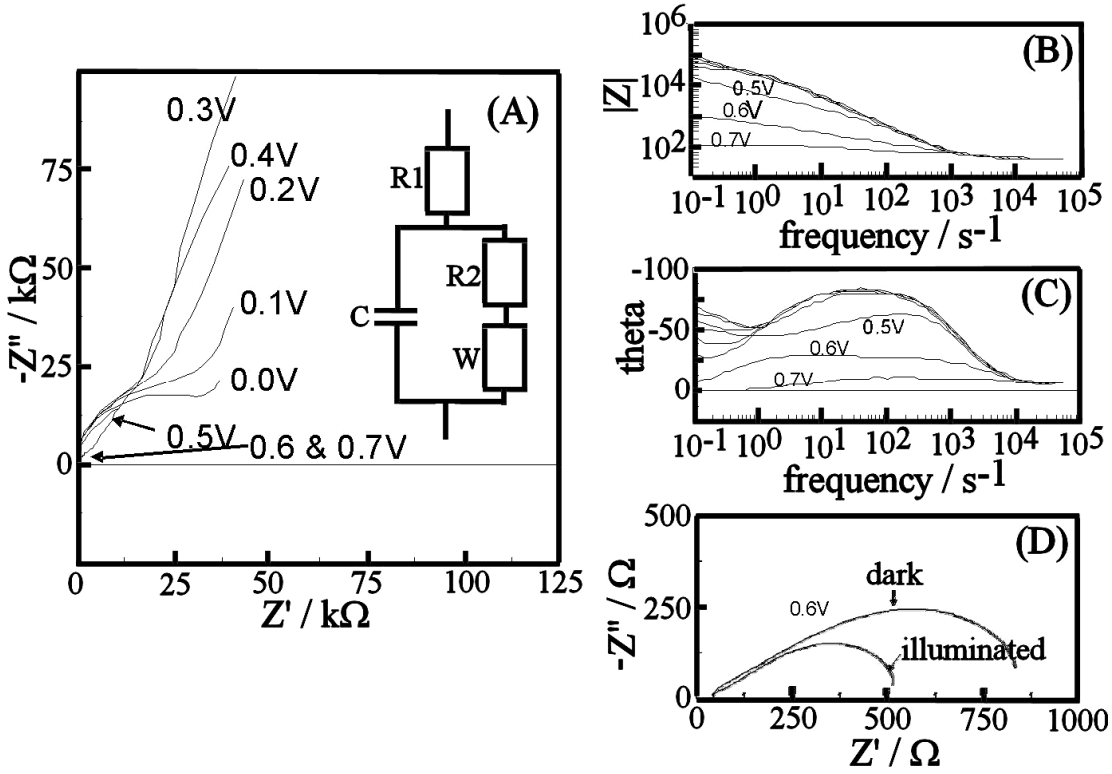

Figure 5.6. (A,D) Nyquist plots and (B, C) Bode plots for the effect of different applied (DC) potentials on the dark impedance for a 60-layer Fe_2O_3 film electrode in 1 M NaOH (potentials in V *vs*. Ag/AgCl. (D) The effect of illumination on impedance spectra for a 60-layer Fe_2O_3 film electrode at an applied potential of 0.6 V vs. Ag/AgCl in 1 M NaOH.

In the intermediate potential range from 0.3 to 0.4 V vs. Ag/AgCl the impedance data remain relatively simple and consistent with a simple RC element model. The resistance, R1 ≈ 44 Ohm, is dominated by the electrolyte solution (probably insignificant) and the FTO film electrode (dominating). The capacitance, C ≈ 3 μF, is representative of the double layer capacitance for the exposed FTO film electrode. The resulting time constant $R \times C = \tau_{RC} = 0.13$ ms is responsible for the major feature at ca. 5 kHz in the Bode plots.

When changing the applied potential to more negative values a semi-circle feature is beginning to emerge (see Figure 5.6A) consistent with interfacial electron transfer. Impedance data can be modelled based on the Randles circuit (see Figure 5.6A inset)

with a "short" Warburg element to represent a thin film of redox active material. In contrast, when changing the applied potential to more positive values, a decrease in impedance is observed. The impedance data can be approximately modelled when assuming the Randles circuit with "open" Warburg element. The physical significance of this observation is associated with the electron transfer at the film – electrode interface, formation of Fe(IV), and the water spitting reaction causing higher or "catalytic" currents. In the presence of light, additional currents cause a further decrease of the impedance (see Figure 5.6D) consistent with a faster light energy driven water splitting reaction.

Although very informative, impedance data for this system are difficult to further quantify in terms of diffusion processes and reaction rates. In order to progress and to obtain more information about the photo-electrochemical processes at the surface of the Fe_2O_3 film, voltamemtry in an ITO junction is employed and then the transient photo-current responses are analysed quantitatively.

5.3.4. Junction Voltammetry for Nano-Hematite Films

Electrochemical junctions [31] can be employed with bipotentiostatic control to measure transport phenomena in thin films and deposits. Here, a tin-doped indium oxide (ITO) electrode is employed. A focussed ion beam mill has been used to cut a thin junction (ca. 600 nm width) into the transparent ITO film (see Figure 5.7).

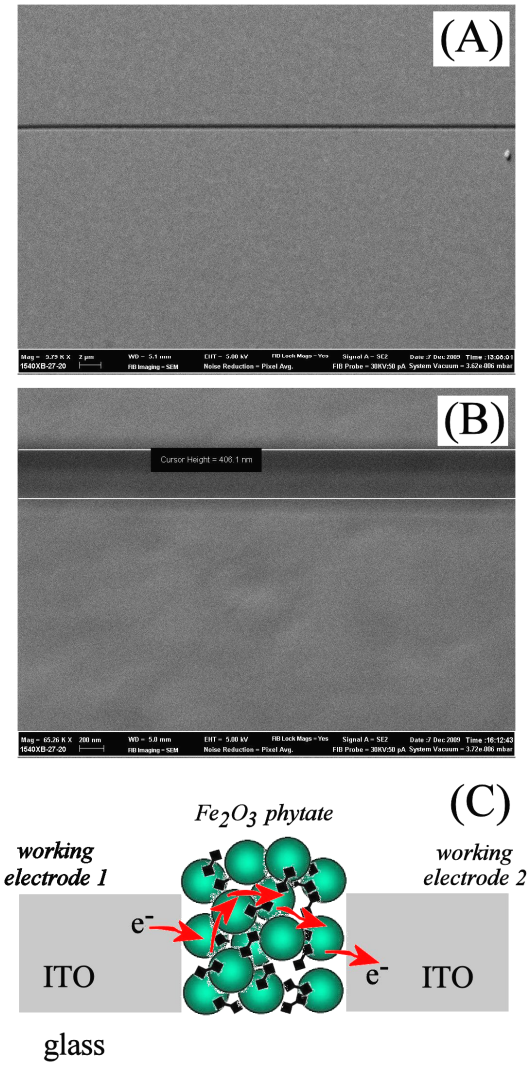

Figure 5.7. (A) SEM image of a tin-doped indium oxide (ITO) thin film electrode with a "cut" applied by ion beam milling. The cut in the conducting film is approximately 600 nm wide (B) and this allows films to be deposited into the gap for electron diffusion measurements (C).

A film composed of phytate and of Fe_2O_3 nanoparticles is then deposited into the ITO junction to provide a potential dependent path for electron and hole diffusion. Voltammetric data are summarised in Figure 5.8.

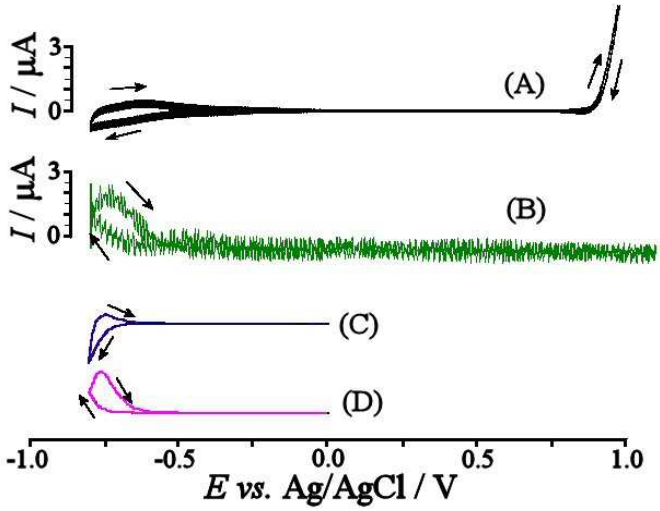

Figure 5.8. Cyclic voltammogram (scan rate 0.01 V s^{-1}) for Fe_2O_3-phytate deposited into a symmetric 600 nm ITO junction electrode, immersed into aqueous 1.0 M NaOH, scanning the generator potential from 0.0 to -0.8 to +1.1 V vs. Ag/AgCl, and holding the collector potential at 0.3 V vs. Ag/AgCl. (A) generator current response. (B) Collector current response. (C) Simulation of generator current. (D) Simulation of collector current assuming $D_e = 5 \times 10^{-15}$ m^2s^{-1}.

The generator current response is characteristic for the formation of Fe(II) at potential negative of -0.2 V vs. Ag/AgCl and the formation of Fe(IV) at potentials positive of 0.6 V vs. Ag/AgCl. The collector responses give clear evidence for the diffusion of "electrons" across the ITO gap (see Figure 5.8B). However, under all conditions employed in this study (different scan rates, different electrolyte media) no evidence for hole diffusion in the positive potential range is observed. The effect of light on the generator-collector current response was insignificant.

A finite element diffusion model (one dimensional between generator and collector with a 600 nm gap) was employed to recreate the electron diffusion effect and data shown in Figure 5.8C and D show the resulting current transients. From the shape analysis (and assuming a simple model of only one diffusing species) it can be concluded that under electrochemical conditions and in the absence of light the electron diffusion in Fe_2O_3 nanoparticle films can be very approximately given as $D_e = 5 \times 10^{-15}$ m^2s^{-1}. The corresponding hole diffusion coefficient appears to be lower and not measurable with this gap size.

5.3.5. Incident Photon to Current Efficiency (IPCE) and Transient Photocurrent Responses for Nano-Hematite Films

The photo-current efficiency of the prepared film electrodes using layer-by-layer deposition was found to be small and the highest efficiency obtained was that for a 60-layer Fe_2O_3 in 1 M NaOH, ca. 4.3% as shown in Figure 5.9A.

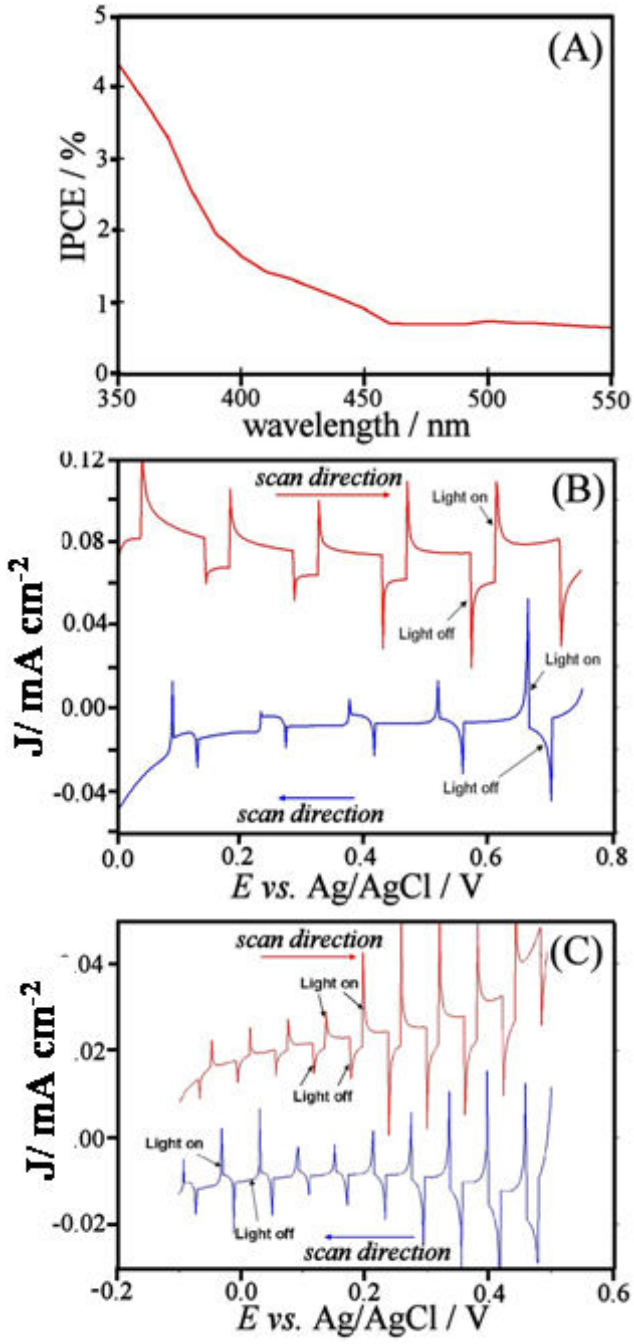

Figure 5.9. (A) The efficiency (% IPCE) for a 60-layer Fe_2O_3 film electrode immersed in 1 M NaOH obtained at 0.1 V *vs*. Ag/AgCl with illumination through the SE side. (B) Pulse-illuminated cyclic voltammogram for SE in phosphate pH 11 at 0.1 Vs^{-1}. (C) Pulse-illuminated cyclic voltammogram for SE in 1 M NaOH at 0.1 Vs^{-1}.

Usually, SE illumination results in better efficiency compared to EE illumination. Thinner deposits show significantly lower IPCE and samples immersed into phosphate buffer pH 11 also exhibit a lower IPCE. Although the level of conversion of photon energy into electrical energy is low, it is interesting to further explore the mechanism and reasons for low efficiency.

The light-on light-off phototransients shown in Figure 5.9B and C are typical for Fe_2O_3 film deposits [32]. Peak-shaped transients of this type have been attributed to band bending transients at the semiconductor | liquid interface. Salvador et al. [33] developed a general model which applies to flat semiconductor surfaces. Here the peak-shaped transient responses are re-examined in the context of a layer-by-layer deposited mesoporous Fe_2O_3 film deposit. A very approximate model based on a finite element simulation approach is employed to explore the effect of relevant physical parameters in the appearance of the peak transients.

Theory. The finite difference simulation model is based on a very approximate description of the processes and concentration gradients in the mesoporous Fe_2O_3 film. The formation of electrons and holes after absorption of light (with intensity I_0 = 10^{-3} mol photons s^{-1} and absorption coefficient $\alpha = 1$) is assumed and both electrons and holes are treated as a freely diffusing "particle" with a concentration and a well defined diffusion coefficients D_e and D_h. A first order chemical reaction of holes to give oxygen at the solid | liquid interface is introduced with a rate constant k_c (assumed to be light intensity independent). The recombination of holes and electrons is described by a second order reaction with rate constant k_{rec} which is dominated by pseudo first order behaviour in the presence of excess electrons. Expressions 5.6 and 5.7 allow the spatial and temporal behaviour of electrons and holes to be investigated.

$$\frac{\partial n_e}{\partial t} = D_e \frac{\partial^2 n_e}{\partial x^2} - k_{rec} \times n_e \times n_h + \alpha I_0 e^{-\alpha x} \tag{5.6}$$

$$\frac{\partial n_h}{\partial t} = D_h \frac{\partial^2 n_h}{\partial x^2} - k_{rec} \times n_e \times n_h - k_c \times n_h + \alpha I_0 e^{-\alpha x} \tag{5.7}$$

In these equations n_e and n_h denote the concentration of electrons and holes, respectively, and x is the space variable. The current for electrons and holes is evaluated separately and assumed to be additive (recombination may occur in the electrode) to give a final current response (see equation 5.8) which reflects the combined mobility and reactivity of both electrons and holes.

$$I_{total}(t) = FD_h A\frac{\partial n_h}{\partial x} - FD_e A\frac{\partial n_e}{\partial x} \quad (5.8)$$

First the effect of the diffusion coefficients is highlighted in the absence of hole reactivity (k_c = 0 s^{-1}). Transient photo-responses are calculated for the case of one second light pulses and for SE illumination.

For calculations the light intensity I_0 = 10^{-3} mol photons s^{-1} and the absorption coefficient α = 1 are assumed. The calculations are performed for a relatively "thick" 400 nm film (corresponding to ca. 100 layers) in order to provide information about different reaction zones in the mesoporous film. The rate for recombination k_{rec} = 1 mol^{-1} dm^3 is assumed (*vide infra*). The diffusion coefficient for electrons has been determined approximately with the junction voltammetry experiment (*vide supra*) and is therefore fixed at $D_e = 5 \times 10^{-15}$ m^2s^{-1}.

The effect of varying the diffusion coefficient for holes (over three light-on light-off cycles) is shown in Figure 5.10B. It can be seen that the difference in diffusion coefficients D_e and D_h has a significant effect on the magnitude of the current transient during light-on and light-off experiments. Interestingly, the shape of transients (the decay rate) is not due to a simple diffusion process of one charge carrier, but rather it is due to the coupled diffusion of electrons and holes and the formation of a diffusion/reaction zone in the hematite film (see zone 2). However, the net effect can be interpreted in terms of the mobility of electrons. It can be seen that the active film is reaching ca. 160 nm after 0.9 s light-on time (see Figure 5.10C). Both light-on and light-off transients decay to zero current due to the absence of oxygen evolution.

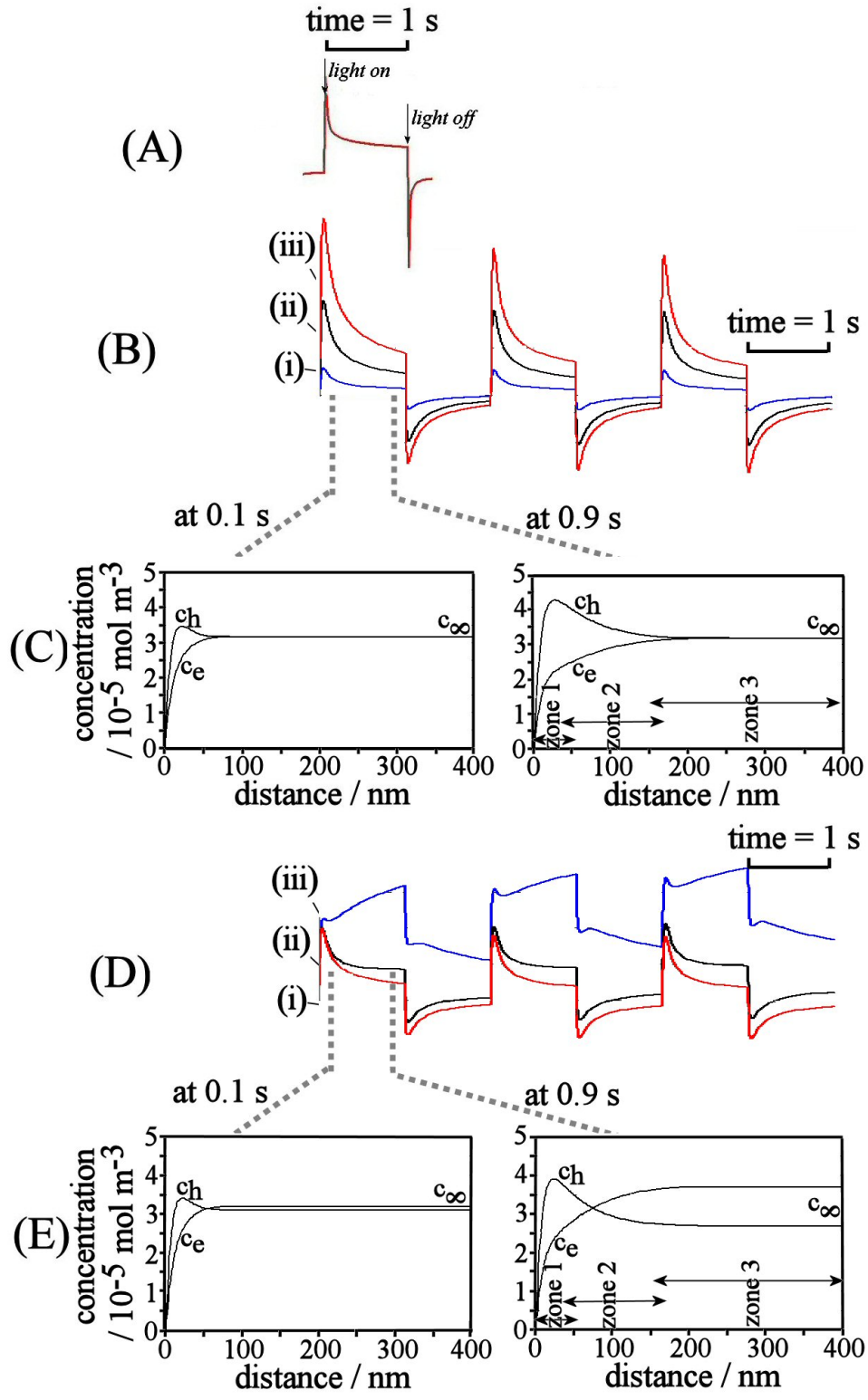

Figure 5.10. (A) Experimental photo-current transient from Figure 5.9. (B) Simulation photo-current for D_h = (i) 4×10^{-15} m^2s^{-1}, (ii) 2×10^{-15} m^2s^{-1}, and (iii) 0.5×10^{-15} m^2s^{-1} ($D_e = 5 \times 10^{-15}$ m^2s^{-1}). (C) Concentration profile in the Fe_2O_3 film at 0.1 s and at 0.9 s time. (D) Simulation photo-currents for $D_h = 2 \times 10^{-15}$ m^2s^{-1}, $D_e = 5 \times 10^{-15}$ m^2s^{-1}, and k_c = (i) 0 s^{-1}, (ii) 0.4 s^{-1}, and (iii) 4 s^{-1}.

When the oxygen evolution process is taken into account (see Figure 5.10D and E) an additional current component is observed. In cyclic voltammetry experiments in the dark the rate constant k = 0.4 s^{-1} (assumed first order rate constant for oxygen evolution, *vide supra*) was estimated and when applied in the numerical simulation reasonable transient shapes in comparison with the experimental data are generated. The additional anodic current increases with every light pulse due to the build up of electrons in the bulk film (see zone 3). A further increase of the rate constant for oxygen evolution increases the anodic current response but this produces calculated transient which disagree with the experimental results (see Figure 5.10Diii).

From this qualitative simulation experiment, characteristic photo-current transients are obtained and, more importantly, the concentration gradients for electrons and holes within the photo-active film can be plotted and studied. The following key conclusions can be drawn:

- The diffusion coefficients D_e and D_h need to be different in order to give transient photo-current responses. The diffusion coefficient for holes D_h needs to be smaller compared to the diffusion coefficient for electrons D_e to result in anodic light-on photo-current transients. Both of these observations agree with experimental results in junction experiments.
- The photo-current decay follows closely that expect for a Cottrell decay but the apparent diffusion coefficient extracted from the Cottrell plot is different to those selected for D_e and D_h due to the effects of two coupled diffusion layers.
- The concentration profiles can be dissected into three regions indicated as zone 1, zone 2, and zone 3. Zone 3 is the electrochemically inactive part of the film which can be termed "recombination layer". In this zone holes and electrons are continuously generated and recombined. The resulting concentration of holes or electrons is $n_e = n_h = \sqrt{\frac{I_0 \alpha}{k_{rec}}} = 3.16 \times 10^{-5}\ mol\, m^{-3}$.

  Zone1 with an extent of ca. 50 nm can be assigned as "reaction zone" where photo-generated holes and electrons are directly consumed by the electrode. The thickness of the reaction zone 1 is governed by the competition of

diffusion, photo-generation, and recombination and can be estimated based on the reaction layer thickness $\delta_{zone1} = \sqrt{\frac{D_e}{k_{rec} \times n_e}} \approx 13\,nm$. Zone 2 reflects the diffusion process and the corresponding thickness is obtained for example at 0.1 s as $\delta_{zone2} = \sqrt{6D_e t} = 55\,nm$ or at 0.9 s as $\delta_{zone2} = \sqrt{6D_e t} = 164\,nm$ consistent with the numerical simulation data.

- Due to the very thin reaction zone 1 the finite element simulation needs to be conducted with a box size of typically 10^{-9} m to give reliable current data.
- The effect of the chemical rate constant k_c is to cause a build-up of electrons in the film and this then causes an overall rising current transient. The rate constant where the switch from falling to rising current transient occurs is approximately $k_c \approx \frac{1}{\tau}$ where τ is the time of the pulse. In the example above the pulse time is 1 s and the switch occurs at $k_c \approx 1\ s^{-1}$.
- The presence of anodic and cathodic photo-current transients can be explained based on this model when the effect of applied potential (not considered in the simple simulation model) is taken into consideration. At potentials negative of ca. 0.0 V vs. Ag/AgCl (see Figure 5.9) in particular when first accumulating Fe(IV) in the more positive potential range, light-on transient appear to result in cathodic current responses as expected when the flow of electron into the substrate electrode is slowed down. This phenomenon will require further study.

Overall, the simulation model does provide a successful qualitative model for electrochemical and photo-electrochemical processes in the mesoporous Fe_2O_3 film deposits. The resulting water splitting processes are of low efficiency but the model clearly suggests that (i) the low rate k_c and (ii) fast recombination are responsible for this observation. The model also predicts a distinct reaction zone (zone 2) where oxygen evolution is most effective. These findings will be of interest in future water splitting device development.

5.4. Conclusions

It has been shown that well-defined mesoporous hematite films are formed in a layer-by-layer deposition process. Films of this type allow thickness variation and the development of a new reaction model based not on a bulk semiconductor, but on a quasi-homogeneous porous material where electrons and holes can freely diffuse, recombine, or react. A simplistic numerical simulation tool has been developed and tested successfully providing new insights into reaction and diffusion zones at the hematite | aqueous electrolyte interface. In future, this model needs to be refined further and applied to a wider range of experimental data.

5.5. Appendix

The numerical simulation model is based on a one dimensional diffusion process (finite) and employing the finite difference method [34] to describe diffusion, light absorption, recombination, and chemical reaction. The corresponding differential equations for electrons and holes are given in 5.9 and 5.10, respectively.

$$\frac{\partial n_e}{\partial t} = D_e \frac{\partial^2 n_e}{\partial x^2} - \frac{n_h}{\tau_{rec}} + \alpha I_0 e^{-\alpha x} \qquad (5.9)$$

$$\frac{\partial n_h}{\partial t} = D_h \frac{\partial^2 n_h}{\partial x^2} - \frac{n_h}{\tau_{rec}} - \frac{n_h}{\tau_c} + \alpha I_0 e^{-\alpha x} \qquad (5.10)$$

The current for electrons and holes is evaluated separated and assumed to be additive to give a final current response (see equation 5.11) reflecting the mobility and reactivity of both electrons and holes.

$$I_{total}(t) = FD_h A \frac{\partial n_h}{\partial x} - FD_e A \frac{\partial n_e}{\partial x} \qquad (5.11)$$

Discretization of the diffusion equations and expression for the current result in equation 5.12 and 5.13.

$$c(x,t+\Delta t) = c(x,t) + \frac{D\Delta t}{\Delta x^2}[c(x+\Delta x,t) - 2c(x,t) + c(x-\Delta x,t)] \qquad (5.12)$$

$$I(t) = nFDA\frac{c(\Delta x,t) - c(0,t)}{\Delta x} \qquad (5.13)$$

The Fortran code (executed in Matlab on a PC) is given below.

```
% EE light-on light-off Cottrell transient in absorption - recombination films 2010 %%%%%%%

clear;
L = 600e-9;
nbox = 600;
dt = 0.5e-6;
time = 1;
ntime = time/dt;
npoints = 1000;
nskip = round(ntime/npoints);
dx = L/nbox;
De = 5e-15;
Dh = 2e-15;
lambdae = De*dt/dx/dx;
lambdah = Dh*dt/dx/dx;
alpha = 1;
J = 1e-3;
k = 1e6;
kc = 0.4;
F = 96487;
A = 1e-4;
current(1:npoints,1:3) = 0;
counter = 0;

for jx=1:nbox
   ce(jx) = 0;
   ceo(jx) = 0;
   ch(jx) = 0;
   cho(jx) = 0;
   ce1(jx) = 0;
   ch1(jx) = 0;
end

% Light on transient %%%%%%%%%%%%%%%%%%%%%%%%%%%%%%%%%%%%%%%%%%%%%%%%%%%%%%%%%%%%%%%%%%%%

for jt=1:ntime
   ceo = ce;
   cho = ch;
   if jt == 200000
      ce1 = ce;
      ch1 = ch;
   end
   if jt == 1800000
      ce9 = ce;
      ch9 = ch;
```

```
    end
    ce(1) = 0;
    ch(1) = 0;
    for jx=2:nbox-1
      ce(jx) = ceo(jx) + lambdae*(ceo(jx+1)-2*ceo(jx)+ ceo(jx-1)) + dt*J*alpha*exp(-alpha*jx*dx) -
       dt*k*ceo(jx)*cho(jx);
      ch(jx) = cho(jx) + lambdah*(cho(jx+1)-2*cho(jx)+ cho(jx-1)) + dt*J*alpha*exp(-alpha*jx*dx)
       - dt*k*ceo(jx)*cho(jx) - dt*kc*cho(jx);
    end
    ce(nbox) = ceo(nbox) + lambdae*(ceo(nbox-1) -ceo(nbox)) + dt*J*alpha*exp(-alpha*nbox*dx) -
     dt*k*ceo(nbox)*cho(nbox);
    ch(nbox) = cho(nbox) + lambdah*(cho(nbox-1) -cho(nbox)) + dt*J*alpha*exp(-alpha*nbox*dx) -
     dt*k*ceo(nbox)*cho(nbox) - dt*kc*cho(nbox);
    if rem(jt,nskip) == 0
      counter = counter + 1;
      current(counter,1) = jt*dt;
      current(counter,2) = F*A*De*(ce(2)-ce(1))/dx;
      current(counter,3) = -F*A*Dh*(ch(2)-ch(1))/dx;
    end
  end

% Light off transient %%%%%%%%%%%%%%%%%%%%%%%%%%%%%%%%%%%%%%%%%%%%%%%%%%%%%%%%%%%%

  for jt=ntime:2*ntime
    ceo = ce;
    cho = ch;
    ce(1) = 0;
    ch(1) = 0;
    for jx=2:nbox-1
      ce(jx) = ceo(jx) + lambdae*(ceo(jx+1)-2*ceo(jx)+ ceo(jx-1)) - dt*k*ceo(jx)*cho(jx);
      ch(jx) = cho(jx) + lambdah*(cho(jx+1)-2*cho(jx)+ cho(jx-1)) - dt*k*ceo(jx)*cho(jx) -
      dt*kc*cho(jx);
    end
    ce(nbox) = ceo(nbox) + lambdae*(ceo(nbox-1) -ceo(nbox)) - dt*k*ceo(nbox)*cho(nbox);
    ch(nbox) = cho(nbox) + lambdah*(cho(nbox-1) -cho(nbox)) - dt*k*ceo(nbox)*cho(nbox) -
     dt*kc*cho(nbox);
    if rem(jt,nskip) == 0
      counter = counter + 1;
      current(counter,1) = jt*dt;
      current(counter,2) = F*A*De*(ce(2)-ce(1))/dx;
      current(counter,3) = -F*A*Dh*(ch(2)-ch(1))/dx;
    end
  end
```

5.6. References

(1) Inukai, A.; Sakamoto, N.; Aono, H.; Sakurai, O.; Shinozaki, K.; Suzuki, H.; Wakiya, N., *Journal of Magnetism and Magnetic Materials,* **2011,** *323*, 965–969

(2) Glasscock, J. A.; Barnes, P. R. F.; Plumb, I. C.; Savvides, N., *J Phys Chem C* **2007,** *111,* 6477-16488.

(3) Decher, G.; Hong, J. D. *European patent, 0472 990 A2*, **1992**

(4) Ling, X.Y.; Reinhoudt, D.N.; Huskens, J., *Pure and Applied Chemistry,* **2009**, *81*, 2225-2233.

(5) Decher, G., *"Fuzzy Nanoassemblies: Toward Layered Polymeric Multi composites,"* Science, **1997,** *277*, 1232-1237

(6) McShane, M.; Lvov, Y., *"Layer-by-Layer Electrostatic Self-Assembly," in book: "Dekker Encyclopedia of Nanoscience & Nanotechnology,"* v. 4, Ed. J. Schwartz, C. Contescu, M. Dekker Publ., NY, **2005**, 1-21

(7) Nohria, R.; Khillan, R.; Su, Y.; Kikshit, D., Lvov, Y.; Varahramyan, K., *"Humidity Sensor Based on Ultrathin Polyaniniline Film Deposited by Layer-by-Layer Nanoassembly," Sensors and Actuators B*, **2005,** 119.

(8) Zhong, D. K.; Sun, J..; Inumaru, H.; Gamelin, D. R., *J. Am. Chem. Soc*. **2009**, *131*, 6086–6087

(9) Lindgren, T.; Wang, H.; Beermann, N.; Vayssieres L., Hagfeldt, A.; Lindquist S., *Solar Energy Materials & Solar Cells,* **2002,** *71*, 231–243

(10) Du, N.; Zhang, H.; Chen, B. D.; Ma, X. Y.; Liu, Z. H.; Wu, J. B.; Yang, D. R., *Advanced Materials*, **2007,** *19*, (12), 1641-1642

(11) McKenzie, K. J.; Marken, F.; Hydeb, M.; Compton, R. G., *New J. Chem.*, **2002,** *26*, 625–629

(12) Cornuz, M.; Grätzel, M.; Sivula, K., *Chemical Vapor Deposition*, **2010,** *16* (10-12) 291.

(13) Hamnett Dare-Edwards, M. P., Goodenough, J. B., Hamnett, A.; Trevellick, P. R., *J. Chem. Soc., Faraday Trans. I,* **1983***, 79,* 2027.

(14) Wang, H.L.; Turner, J.A., *Journal of the Electrochemical Society*, **2010**, *157*, F173-F178.

(15) Alexander, B.D.; Kulesza, P.J.; Rutkowska, I.; Solarska, R.; Augustynski, J., *J. Mater. Chem.* **2008,** *18*, 2298.

(16) Wang, Y.; Yu, T.; Chen, X.; Zhang, H.; Ouyang, S.; Li, Z.; Ye, J.; and Zou, Z., *J. Phys. D: Appl. Phys*. **2007,** *40*, 3925–3930

(17) Jorand-Sartoretti, C.; Ulmann, M.; Alexander, B.D.; Augustynski, J.; Weidenkaff, A., *Chem. Phys. Lett*. **2003,** *376*, 194.

(18) Jorand-Sartoretti, C.; Alexander, B.D., Solarska, R., Rutkowska, I.A.; Augustynski, J.; Cerny, R., *J. Phys. Chem*. *B*, **2005,***109*, 13685.

(19) Cesar, I.; Kay, A., Gonzalez-Martinez, J. A., Grätzel, M., *J. Am. Chem. Soc.*, **2006,** *128*, 4582.

(20) Kay, A.; Cesar, I.; Grätzel, M., *J. Am. Chem. Soc.*, **2006,** *128*, 15714.

(21) Saremi-Yarahmadi, S; Vaidhyanathan, B; Wijayantha, K. G. U., *international Journal of Hydrogen Energy*, **2010,***35* (19), 10155-10165.

(22) Saremi-Yarahmadi, S.; Wijayantha, K. G. U.; Tahir, A. A.; Vaidhyanathan, B., *Journal of Physical Chemistry C*, **2009***, 113*, (12), 4768-4778

(23) Eggleston, C. M.; Shankle, A. J. A.; Moyer, A. J.; Cesar, I.; Graetzel, M., *Aquatic Sciences*, **2009,** *71*, (2), 151-159

(24) Brillet, J.; Grätzel, M.; Sivula, K., *Nano Letters*, **2010,** *10*, (10), 4155-4160

(25) Tilley, S.D.; Cornuz, M.; Sivula, K.; Grätzel, M., *Angewandte Chemie*, *International Edition*, **2010**, *49*, 6405–6408.

(26) Sorum, H.; *J. Am. Chem. Soc.*, **1928,** *50,* 1263.

(27) Mulvaney, P.; Cooper, R; Grieser, F; Meisel, D., *Langmuir*, **1988**, *4* (5), 1206-1207

(28) Kwon, S. K. ; Kimijima, K.; Kanie, K.; Muramatsu, A.; Suzuki, S.; Matsubara, E., *High Temperature Materials and Processes*, **2005**, *24* (5), 275-287.

(29) Cummings, C.Y.; Bonne, M.J,; Edler, K.J.; Helton, M.; McKee, A.; Marken, F., *Electrochemistry Communications*, **2008**, *10*, 1773-1776

(30) Duret, A.; Grätzel, M., *J. Phys. Chem. B,* **2005**, *109,* 17184-17191.

(31) French, R.W.; Gordeev, S.N.; Raithby, P.R.; Marken, F., *Journal of Electro-analytical Chemistry*, **2009**, *632*, 206-210

(32) Herrera, F.V.; Grez, P.; Schrebler, R.; Ballesteros, L.A.; Munoz, E.; Cordova, R.; Altamirano, H.; Dalchiele, E.A., J. Electrochem. Soc. *D,* **2010**, *157*, 302.

(33) Salvador, P.; Garcia-Gonzalez, M.L.; Munoz, F., *J. Phys. Chem*., **1992**, *96*, 10349.

(34) Bard, A.J.; Faulkner, L.R., *Electrochemical Methods*, 2nd ed.,Wiley, New York, **2001**, 785.

Chapter 6

Chemical Vapour Deposition Formation of Porous Films of Photoelectrochemically Active Nano-Hematite Fe_2O_3

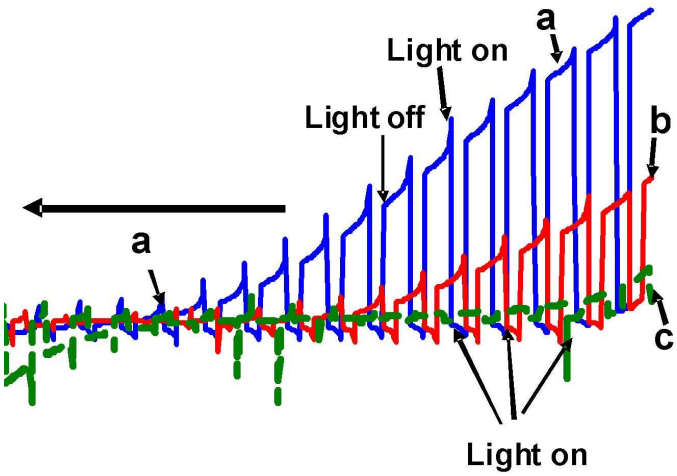

Abstract. In this chapter hematite films are formed in a chemical vapour deposition (CVD) growth process from a ferrocene precursor. Films are formed in variable thickness on FTO (fluorine-doped tin oxide) and ITO (tin-doped indium oxide) substrates. Photo-electrochemical experiments are conducted and the effect of thickness and illumination direction discussed in the context of a water splitting process in a mesoporous Fe_2O_3 film. In contrast to the thin mesoporous films investigated in the previous chapter, here thicker and denser films are studied. The photo-catalytic efficiency is improved by a factor of 4 due to higher density and potential gradient effects.

Acknowledgement. Film growth experiments were carried out by Prof. Kieran Molloy and Dr. Steven Richards. Dr. John M. Mitchels is gratefully acknowledged for help with electron optic experiments.

Content

6.1. Introduction

There are many ways of preparing photo-active films of iron oxide and in particular Chemical Vapour Deposition (CVD) methods have attracted attention as cheap and reliable techniques [1]. Iron oxide thin films have been prepared, for example, by using the Metal-Organic Chemical Vapour Deposition (MOCVD) method at temperature of typically ca. 400-600 ^oC and with the precursor iron acetylacetonate $Fe(acac)_3$ [2]. Nitrogen gas has been used as the carrier gas while oxygen has been introduced as an oxidant for oxide formation and redox state adjustment. At 400 ^oC β-Fe_2O_3 was deposited even without flowing O_2. Whereas at 500 and 600 ^oC spinel–type Fe_3O_{4+x} was formed as a single phase for a low rate of O_2 flowing. By increasing the O_2 flow rate a mixture of β-Fe_2O_3 and Fe_3O_{4+x} were formed, and finally with further increasing the O_2 flow rate β-Fe_2O_3 was formed as a single phase. In this way compositional control could be achieved by varying the reagents. Other parameters for the compositional control are temperature and substrate material or morphology.

In a similar study, the gas phase decomposition of the iron complex $[Fe(O^tBu)_3]_2$ was used to prepare α-Fe_2O_3 and Fe_3O_4 [3]. Films were formed homogeneously and with a nanometer thickness range. The iron oxide phase and its morphology were controlled by varying the temperature of the substrate. The influence of microstructure and phase on the optical properties has been studied for both α-Fe_2O_3 and Fe_3O_4. Mathur et al. [3] found that the substrate affects the crystallisation process. For example, Fe_3O_4 was obtained at 450 ^oC on a copper substrate while it needed a higher temperature of 600 ^oC on quartz. In contrast, the pure hematite phase was found to deposit on quartz in a temperature range of 450-475 ^oC. At 500 ^oC a mix of hematite (needle shaped) and magnetite (faceted grains) were found on the quartz substrate. Therefore substrate effects can be essential in controlling the type and crystallinity of the growing oxide phase.

The effect of the precursor material on iron oxide formation has been investigated. A comparison of nanostructured α-Fe_2O_3 produced from iron pentacarbonyl and from ferrocene as vapour precursors has been reported based on Atmospheric Pressure Chemical Vapour Deposition (APCVD) [4]. Ferrocene was found to be a much better

precursor for the preparation of α-Fe_2O_3 with products showing improved optical absorption and two orders of magnitude higher photocurrent densities (0.54 mA cm^{-2} at 1.23 V_{RHE}). Further benefits of ferrocene are lower costs, less toxicity, and safer handling.

Un-doped nanostructured α-Fe_2O_3 films have been prepared by aerosol-assisted chemical vapour deposition (AACVD) [5] using the iron cluster precursor $[Fe_6(PhCOO)_{10}(acac)_2(O)_2(OH)_2]3C_7H_8$ (where PhCOO = benzoate and acac = acetyl acetonate). XRD, XPS and Raman spectroscopy showed that iron oxide films in the prepared films formed highly crystalline α-Fe_2O_3 without contamination from other phases of iron oxide. Scanning Electron Microscopy (SEM) showed that α-Fe_2O_3 had a needle-like shape with length ~ 100-160 nm and diameter 30-50nm. The band gap was found to be 2.13eV and the flat band potential ~-0.86V vs. Ag/AgCl reference electrode. The photocurrent density was optimised to 0.6 mA cm^{-2} at 1.23 V vs. RHE.

Qiao et al.[6] compared substrate effects on iron oxide growth for flourine-doped tin oxide (FTO) and tin-doped indium oxide (ITO) as substrates for a photo-active layer of P3OT/TiO_2. They found that FTO is performing better than ITO in this solar cell application. P3OT-TiO_2/FTO gave an open circuit voltage (V_{OC} = 0.65 V) and short circuit current density (J_{SC}=100 μA/cm^2) which was 0.15 V and 20 μA cm^{-2} higher than those for P3OT-TiO_2/ITO. A further comparative study between FTO and ITO as transparent substrates prepared by a spray pyrolysis method has been reported [7]. At 400^o C deposition temperature, both of FTO and ITO showed a single phase. FTO was found to be tetragonal structure. ITO shows a cubic structure with a preferred orientation (4 0 0). The particle size for FTO was found to be ca. 190 nm, while that for ITO was found to be ca. 257 nm. In the visible light region, the typical transmittance is lower for FTO than for ITO substrates. Reflectance in the infrared was found to be lower in FTO than in ITO. From electrical measurements, it was found that the best electrical resistivity values are 8 x 10^{-4} Ωcm and 6 x 10^{-4} Ωcm for ITO (6% Sn) and FTO(2.5 % F), respectively.

Spray pyrolyzed antimony-doped tin oxide (ATO), FTO, and ITO films have been prepared by Bitht et al. at 500-550^{o}C [8]. Optical and electrical properties have been investigated. It was found that the resistivity of ITO decreases with increasing the

film thickness down to 3 x 10^{-4} Ωcm (thickness = 300 nm). The thicker ITO samples (thickness >300 nm) showed optical transmission 80% in the visible light and 96% reflection in the near IR region. FTO films (thickness >350nm) showed higher resistivity of ~5 x 10^{-3} Ωcm. Bitht et al. concluded that ITO films, especially after an optimized reduction treatment under forming gas, showed the best properties in terms of the lowest electrical resistivity and the highest optical transmission for applications in solar and water splitting cells.

In the present work, iron oxide films are prepared by the Atmospheric Pressure Chemical Vapour Deposition (APCVD) method employing a ferrocene precursor. Iron oxide films are deposited onto two different substrates: Flourine-doped Tin Oxide (FTO) and Tin-doped Indium Oxide (ITO). Varying deposition times have been applied (10-35 minutes) to produce films as a function of thickness and to systematically study the photoactivity of Fe_2O_3 on those two substrates as a function of thickness. The photo-current data and transients are compared to data obtained with layer-by-layer Fe_2O_3 nanoparticle films. The effect of going from a mesoporous iron oxide to a more dense iron oxide in photo-electrochemical oxygen evolution is discussed.

6.2. Experimental

6.2.1. Chemical Reagents

Ferrocene $Fe(C_5H_5)_2$ was used as precursor in Chemical vapour deposition method. Nitrogen gas has been used as carrier gas. FTO and ITO electrodes are sourced from Asahi. Oxygen gas has been used as an oxidised gas.

6.2.2. Instrumentation

An Electro Gas Systems Ltd apparatus has been used to prepare the samples with CVD method. Sonicator has been used for cleaning the ITO and FTO samples. SEM, XRD CV, IPCE, Impedance, techniques are applied here as it was described in chapter 3.

6.2.3. Chemical Vapor Deposition Experimental Procedure

Chemical vapour deposition runs were carried out using an Electro Gas Systems Ltd apparatus in reduced pressure thermal chemical vapour deposition configuration. The precursor was volatilised in a heated precursor tube at 120 ºC and delivered to the quartz reactor chamber in a stream of N_2 carrier gas (at a rate of 100 ml/min) through heated stainless steel tubing maintained at 120 ºC. The substrate was supported on a graphite wedge heated to 450 ºC through the reactor chamber wall by an external halogen lamp. The precursor stream (100 ml/min) was mixed with the O_2 oxidant stream (100 ml/min) at the entrance to the reactor chamber. The precursor and oxidant were transported to the heated substrate and the volatile decomposition products removed from the chamber at a rate of 500 ml/min by means of the main N_2 carrier gas stream. The apparatus was maintained at a pressure of 150 Torr by an Edwards XDS5 dry vacuum pump for the duration of the deposition run.

In the present work, many films of iron oxide (Fe_2O_3) have been prepared by atmospheric pressure chemical vapour deposition (APCVD) on two substrate; Florine-doped Tin Oxide (FTO) and Indium-doped Tin Oxide (ITO). The main purpose of that was to make a comparison between the effect of FTO and ITO on the photoactivity of Fe_2O_3. Higher deposition times have been chosen (10-35 minutes) because most of iron oxide films prepared by CVD method have been deposited at shorter deposition times.

6.3. Results and Discussion

6.3.1. Film Deposition, Structure, Morphology, and Optical Properties

Films of iron oxide from CVD deposition from ferrocene precursor appear uniformly brown and dense. A summary of the types of films investigated here (different thicknesses and two different substrates) is given in Table 6.1. The average thickness of these films is estimated based on cross-sectional SEM images (see Figure 6.1.) and consistent with a growth of typically 30 nm per minute.

Table 6.1. Summary of Fe_2O_3 samples prepared by the CVD method from ferrocene precursors at 450^{o}C and varying the deposition times

Sample number	Substrate type	Deposition time / minutes	Approximate thickness / nm
FTO10	**FTO**	**10**	**300**
FTO15	**FTO**	**15**	**450**
FTO20	**FTO**	**20**	**600**
FTO25	**FTO**	**25**	**750**
FTO30	**FTO**	**30**	**900**
FTO35	**FTO**	**35**	**1050**
ITO10	**ITO**	**10**	**300**
ITO15	**ITO**	**15**	**450**
ITO20	**ITO**	**20**	**600**
ITO25	**ITO**	**25**	**750**
ITO30	**ITO**	**30**	**900**
ITO35	**ITO**	**35**	**1050**

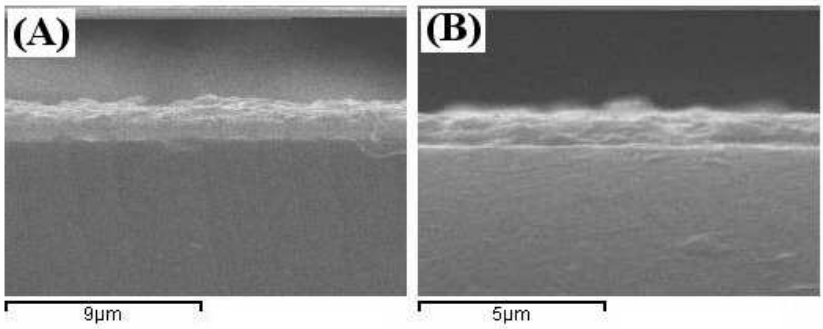

Figure 6.1. Cross-sectional SEM images for (A) sample FTO25 and (B) sample ITO25.

During cross-sectional SEM imaging also an EDX profile for the films was obtained. Figure 6.2. shows that a film of typically 1 μm is formed at the glass surface (for sample FTO35) as expected for the estimated film thickness. Cross-sectional EDX data for Fe and Si are consistent with the film structure.

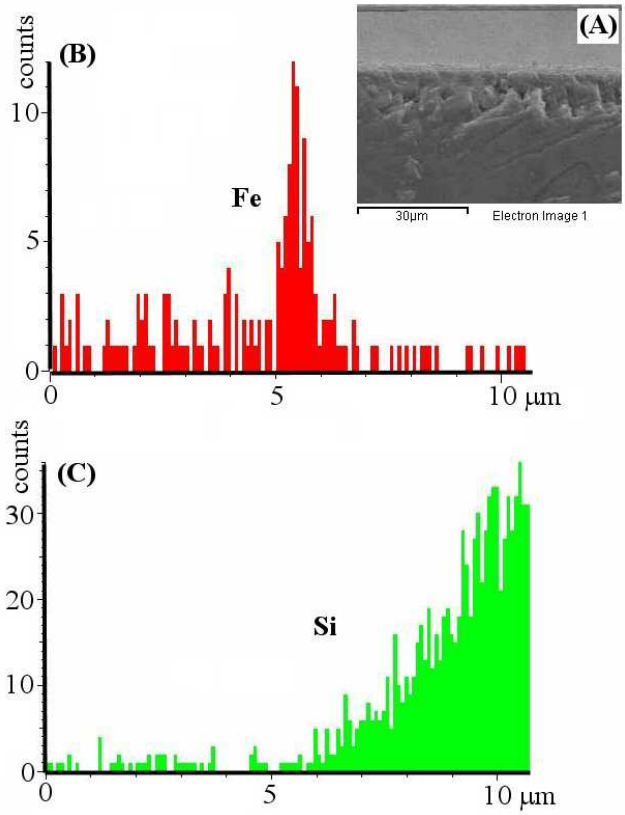

Figure 6.2. (A) SEM cross-sectional image for sample FTO35. (B) EDX scan across the sample cross section with Fe counts. (C) EDX scan with Si counts, which contained in the conducting glass.

Next, XRD measurements were carried out. Evidence for hematite formation was obtained in particular for the thicker film samples. Figures 6.3. and 6.4. summarise the XRD data. Samples grown by the CVD method on FTO substrates are dominated by Fe_2O_3 (**110**) orientation (peaks at 27, 38, and 52 degree are FTO substrate peaks). With increasing deposition time peaks for (**104**) (**012**) and (**116**) also emerge. It is likely that the initially dominating (**110**) peak is due to a preferential growth direction caused by the underlying FTO substrate.

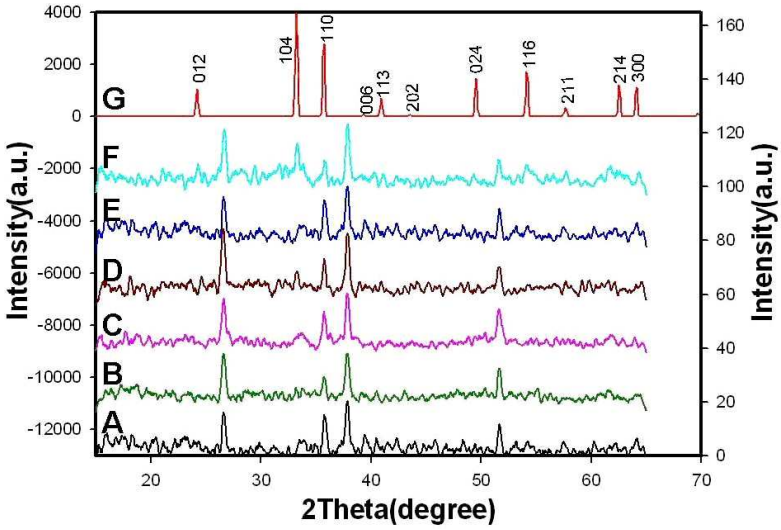

Figure 6.3. XRD data for Fe_2O_3 thin film samples on **FTO** substrate (A = FTO10, B = FTO15, C = FTO20, D = FTO25, E = FTO30, F = FTO35, G = literature reference by Shin et al. [9].

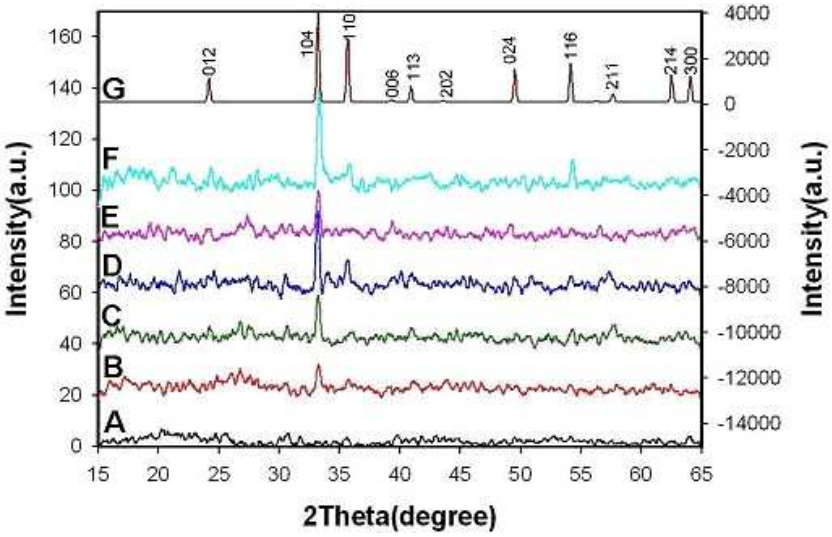

Figure 6.4. XRD data for Fe_2O_3 thin film samples on **ITO** substrate (A = ITO10, B = ITO15, C = ITO20, D = ITO25, E = ITO30, F = ITO35, G = literature reference by Shin et al. [9].

In case of Fe_2O_3 films deposited on ITO (see Figure 6.4.) it was found that the orientation is mainly dominated by the **(104)** diffraction peak. This peak increases strongly with deposition time and (**012**) (**110**) (**116**) peaks appear only for films of approximately 1 μm thickness (see ITO35). The change in crystal orientation is a clear substrate effect.

$$B_{FWHH}(2\theta) = \frac{K\lambda}{L\cos\theta} \qquad (6.1)$$

In order to obtain an estimate for the average crystallite size in CVD films of hematite, the Scherrer method [10,11] has been used. The Scherrer constant is assumed here approximately $K = 0.9$, and the wavelength of radiation is $\lambda(\text{Cu-K}_\alpha) = 1.5406$ Å. With a typical width at half height of $B_{FWHH} = 0.4$ degrees (for the (**104**) line in Figure 6.4.) the estimated grain or crystallite size (L) is approximately 0.4 nm, which is very small. This value is an estimate, and the real value for grain size may be somewhat higher due to instrumentation effects in the measurement of the peak broadening. For the film deposit on ITO (see Figure 6.3.) and based on the (**110**) diffraction peak essentially the same value is obtained. SEM images suggest that these films of hematite are dense, but voltammetry data suggest that some aqueous electrolyte can penetrate through these films to the substrate electrode (*vide infra*) and therefore some porosity has to be assumed.

Fe_2O_3 film samples either those deposited on FTO or those deposited on ITO showed high light absorption ability and UV/Vis spectra were obtained. Figure 6.5. shows absorbance data for films of typically 300 nm, 450 nm, and 600 nm thickness. The onset point for the absorbance is at ca. 580 nm which is consistent with the photon energy of 2.15 eV. The band gap energy for hematite films deposits is frequently reported as ca. 2.15 eV [12] (for the direct transition) in excellent agreement with this measurement. Non-linearity and non-ideality in the absorbance data preclude further in depth analysis.

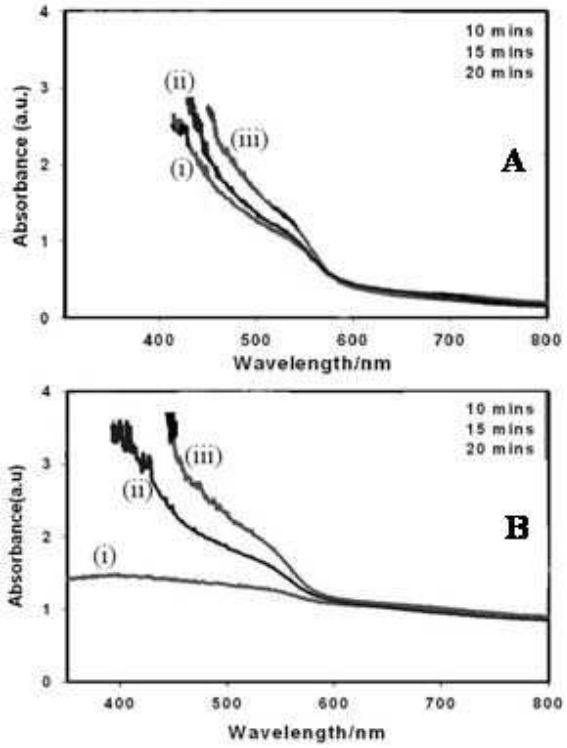

Figure 6.5. (A) UV/Vis absorbance spectra for dry CVD Fe_2O_3 film electrodes (samples FTO10, FTO 15, and FTO 20) on **FTO** as a function of film thickness. (B) UV/Vis absorbance spectra for dry CVD Fe_2O_3 film electrodes (samples ITO10, ITO 15, and ITO 20) on **ITO** as a function of film thickness.

In the following section the electrochemical properties of the CVD hematite films will be investigated under dark and illuminated conditions. The effect of the substrate electrode will be investigated and a comparison to the much thinner layer-by-layer film electrodes will be made.

6.3.2. Dark and Pulse-Illuminated Cyclic Voltammetry for CVD Deposited Hematite Film Electrodes: Experiment

Processes at ITO Substrates. Voltammetric data for CVD hematite films were obtained in aqueous 1.0 M NaOH. Features very similar to those observed for layer-by-layer Fe_2O_3 films are observed, although the higher density of CVD films causes characteristic changes. Figure 6.6 shows typical cyclic voltammograms for samples ITO15, ITO20, and ITO25. In the negative potential range a cathodic process

consistent with the reduction of Fe(III) is observed. The process is denoted P1 and tentatively assigned here to the formation of a surface Fe(II) (see equation 6.2).

$$Fe(III)_2O_3 + e^- + H^+ \rightleftharpoons Fe(II)Fe(III)O_2(OH) \qquad (6.2)$$

When scanning the potential into a more positive potential range an oxidation is observed. This oxidation denoted P2 occurs at ca. 0.7 V vs. Ag/AgCl and the presence of a back-reduction peak is highly likely to indicate the dark formation of Fe(IV) (see equation 6.3).

$$Fe(III)_2O_3 + OH^- \rightleftharpoons Fe(IV)Fe(III)O_3(OH) + e^- \qquad (6.3)$$

When compared to typical cyclic voltammograms for layer-by-layer hematite (see chapter 5), the shape of reversible processes appears to have become more complicated presumably due to smaller pores and "membrane effects" in small pores where potential gradients can appear causing migration and more drawn out voltammetric responses.

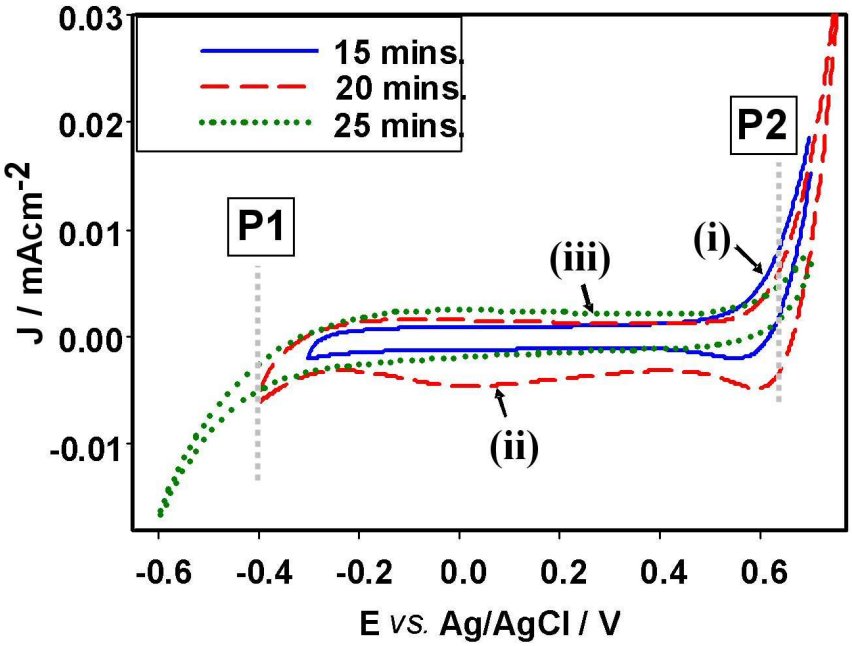

Figure 6.6. Cyclic voltammograms (scan rate 0.1 V s^{-1}) in aqueous 1.0 M NaOH. Effect of deposition time (thickness) on the dark cyclic voltammograme for Fe_2O_3 film samples (i) ITO15, (ii) ITO20, and (iii) ITO25 on **ITO** substrates.

Further inspection of the cyclic voltammetry data suggests that the thicker films of hematite are resulting in slightly more long-lived Fe(IV) surface states. The transition scan rate (compare chapter 5) of 0.1 Vs^{-1} is observed here and this suggests an apparent chemical rate constant for oxygen evolution of $k_c = \frac{vF}{RT} = 4\ s^{-1}$ (for CVD hematite films in 1.0 M NaOH), which is faster when compared to data from films prepared by the layer-by-layer methodology. The magnitude of this apparent rate constant may be affected by the porosity and pore size in the CVD film. Importantly, the fact that these voltammetric responses are observed at all suggests that aqueous electrolyte is able to penetrate into the porous CVD hematite films and to directly contact the substrate surface where the interfacial electron transfer for this oxidation process occurs. The extent of the contact between aqueous phase and substrate may depend on the CVD film thickness.

Next, the CVD deposited films of hematite on ITO substrates are investigated in the presence of pulsed illumination. A flashing blue LED light with 8 $mWcm^{-2}$ was used to measure the photocurrents of the iron oxide samples as a function of thickness and illumination direction. Experiments were conducted with a scan rate 0.01 Vs^{-1} and with 4 second on-pulses and 2 second off-pulses.

Voltammetry data in Figure 6.7A shows photocurrent responses for samples ITO15, ITO20, and ITO25 under SE illumination (substrate exposure). The anodic photocurrent responses seem to decrease with increasing deposition time (film thickness). An additional cathodic photocurrent is seen to increase with thickness in the negative potential range. The cathodic photocurrent for these samples is likely to be associated with Fe(II) formation and photo-corrosion and therefore not discussed in any detail. However, the anodic photocurrent is associated with the formation of Fe(IV) and subsequently the formation of oxygen, which is important in the water splitting process. The decrease in photocurrent for thicker hematite films is likely to be due to absorption of light in a zone of the film with poor electrolyte contact and therefore limited oxygen evolution reactivity.

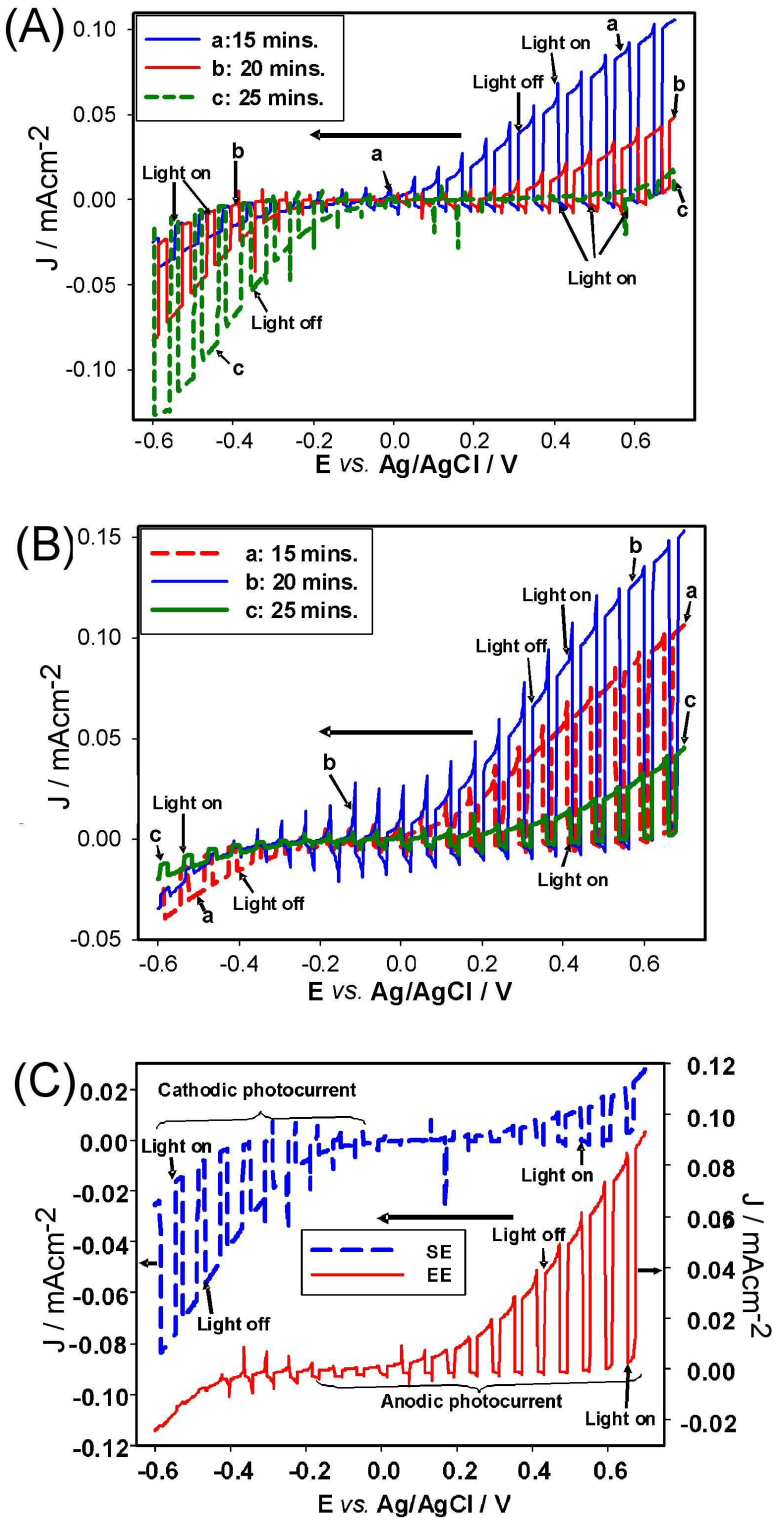

Figure 6.7. (A) Effect of deposition time (thickness) on the pulse-illuminated (**SE**) cyclic voltammogram (scan rate 10 mVs^{-1}) for Fe_2O_3 samples ITO15, ITO20, and ITO25 immersed in 1M NaOH using a blue LED with 8 $mWcm^{-2}$. **SE**. (B) Data for the same experiment for (**EE**) illumination. (C) Comparison between the forward photocurrent response of sample ITO35 for illumination through **SE** and **EE** sides using a blue LED with 8$mWcm^{-2}$.

In contrast to the SE case, in the case of illumination through the electrolyte (EE), initially an increase and then a decrease for thicker films is observed (see Figure 6.7B). Good photo-current generation is observed for sample ITO20 with an approximate thickness of 600 nm. This behaviour can be rationalised by considering (i) the diffusion of charge carriers through the film and (ii) the recombinative losses for thicker films. The optimum film thickness of ca. 600 nm (sample ITO20) reflects the ability of electrons to diffuse across the film and the competing loss during recombination. This will be considered in more detail below in an overall reaction model. In a comparison of data for SE and EE illumination (see Figure 6.7C) it can be seen that EE illumination is more effective even for a very thick film (sample ITO35). This can be explained as in case of EE (Electrolyte-Electrode) illumination, the majority of holes are produced from the first front layers of Fe_2O_3 which can readily diffuse to the hematite/electrolyte interface where the oxidation of water occurs which is resulting in a relatively high anodic photocurrent (see in Figure 6.7.C). In case of SE (Substrate-Electrode) illumination, the majority of holes are produced on the Fe_2O_3 layers which are adjacent to the substrate. Hole diffusion is ineffective and the intensity reaching the Fe_2O_3-electrolyte interface is lower. Therefore, SE photocurrents are lower.

Processes at FTO Substrates. Figure 6.8 shows typical voltammetric responses for the CVD-hematite films deposited onto FTO substrates and immersed into 1 M NaOH. In Figure 6.8A the effect of thickness on cyclic voltammetry responses for samples FTO15, FTO20, and FTO30 is shown. Both the cathodic process P1 and the anodic process P2 are observed and a distinct peak feature at ca. 0.5 V suggests some reversibility (corresponding to a significant lifetime of Fe(IV) states in these samples). Figure 6.8B demonstrates the effect of scan rate on the degree of reversibility and the magnitude of the peak feature. Even at a lower scan rate of 0.01 Vs^{-1} is the peak for the reduction of Fe(IV) (process 2) observed. The more defined peak responses observed on FTO samples as compared to ITO samples suggest a more open pore structure probably due to a different crystal orientation (see XRD data above).

Comparison of the dark cyclic voltammetry data for ITO substrates (see Figure 6.6) and for FTO substrates (see Figure 6.8) suggests that only small changes due to the substrate material occur. The lifetime of Fe(IV) states could be slightly longer for

FTO samples and this may be related to the crystal orientation and pore structure of the hematite (see XRD data). However, difference between ITO and FTO substrates are probably insignificant in the overall behaviour of these films.

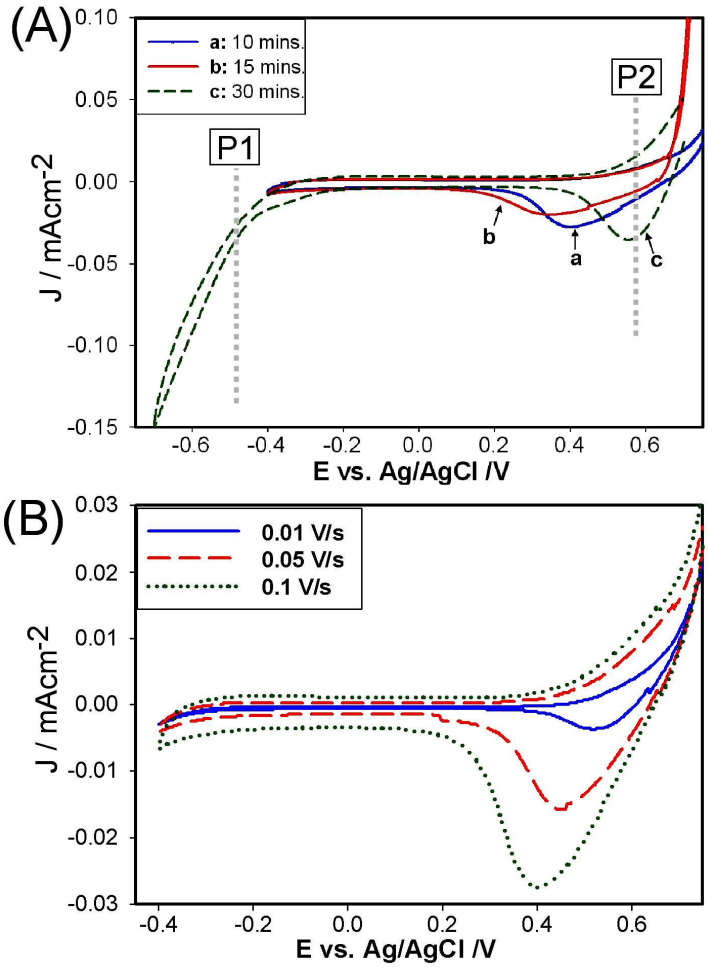

Figure 6.8. (A) Effect of deposition time (thickness) on the dark cyclic voltammograms (scan rate 0.1 Vs^{-1}) for Fe_2O_3 samples FTO10, FTO15, and FTO30 prepared by the CVD method. (B) Effect of scan rate on the dark cyclic voltammogram for Fe_2O_3 (FTO10 sample) in 1M NaOH.

Data recorded for the FTO substrate electrodes with hematite thin film deposits confirm trends observed for ITO substrates. Figure 6.9A shows pulse-illuminated cyclic voltammograms measured by exposing the samples to a flashing blue LED (455 nm) with a power 8 $mWcm^{-2}$. For thin films the photocurrent response for iron oxide is significant but it decreases with increasing the deposition time (or film thickness).

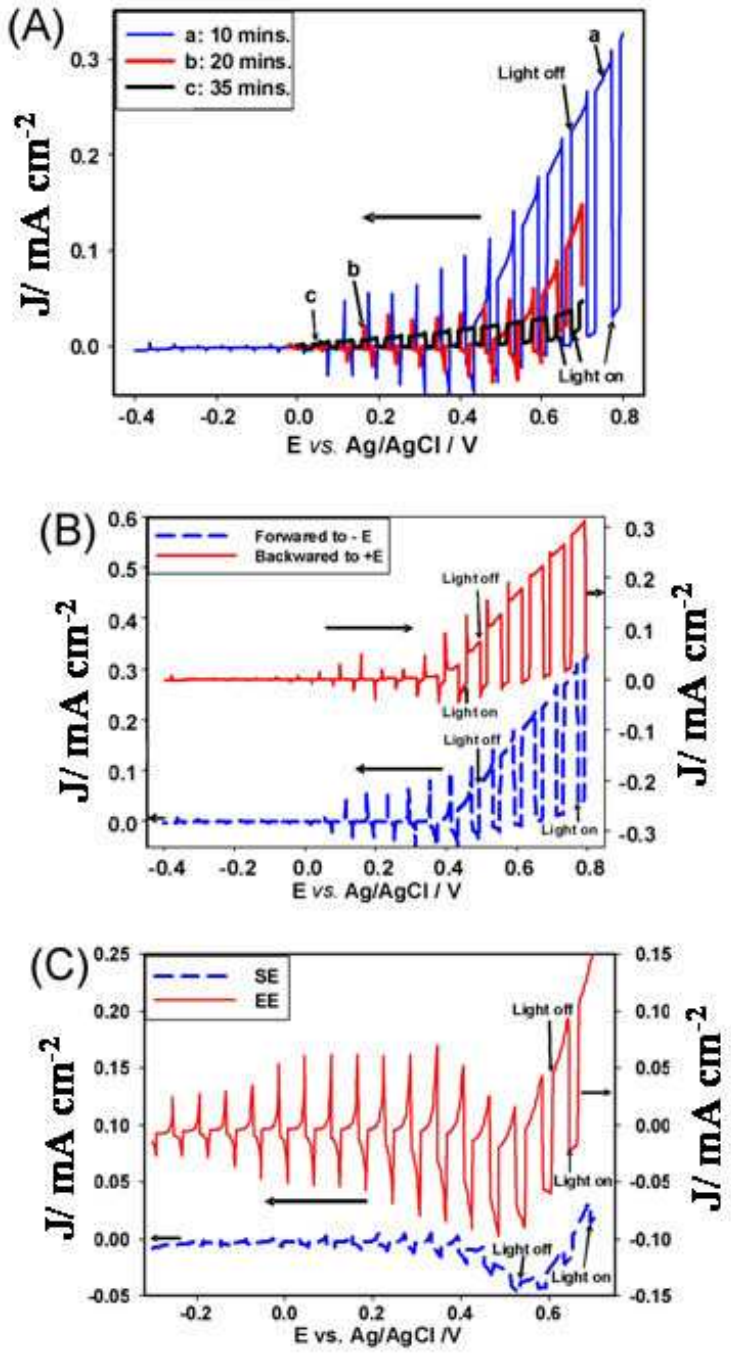

Figure 6.9. (A) Effect of deposition time (thickness) on the pulse-illuminated (**SE**) cyclic voltammogram (scan rate 0.1 Vs^{-1}) for Fe_2O_3 samples FTO10, FTO20, and FTO30 immersed in 1 M NaOH using a blue LED with 8 $mWcm^{-2}$. (B) Voltammograms (scan rate 10 mVs^{-1}) for forward and backward photocurrents (**SE**) for Fe_2O_3 FTO10 immersed in 1 M NaOH using blue LED with 8 $mWcm^{-2}$. (C) Comparison of the forward photocurrent voltammetric responses (scan rate 10 mVs^{-1}) for sample FTO30 with illumination through **(SE)** and **(EE)** sides using a blue LED with 8 mW cm^{-2}.

Measurements for the forward and backward scan direction are shown in Figure 6.9B. It can be seen that no significant effects due to the scan direction are observed. The

comparison of substrate exposure (SE) and electrolyte exposure (EE) for a thick FTO30 sample is shown in Figure 6.9C. The onset of photocurrents appears very positive and additional cathodic photocurrents may be attributed to the photo-conductivity effect. Excess Fe(IV) states produced at positive potential and under illumination can reach the electrode more quickly under illumination and this causes apparent cathodic peaks which are however, likely to be associated with the conversion of Fe(IV) back to Fe(III). The photocurrents for the EE illumination are significantly better in good agreement with findings for the ITO substrate samples.

Comparison of Processes at ITO and FTO Substrates. A comparison between the forward photocurrents for Fe_2O_3 samples deposited on ITO and on FTO are shown in Figure 6.10A and B. With SE illumination and for thin samples ITO15 and FTO15 significant photocurrents are observed with onset potentials of ca. 0.0 and 0.2 V vs. Ag/AgCl, respectively. This difference in onset potential appears to be significant and linked to film structure. The earlier onset for photo-oxidation of water on ITO suggests that the more porous FTO film under these conditions is less effective. One major effect of the porosity is the change in the potential gradients within the semiconductor film. A dense film of low porosity is likely to behave more like a "true semiconductor" film whereas a highly porous film will behave more like the layer-by-layer film samples discussed in chapter 5. The presence of aqueous electrolyte in bigger pores eliminates potential gradients within the semiconductor material and allows charge hopping conduction on the hematite surface. In contrast, in a bulk semiconductor potential-driven electron transport with higher speed (with less trapping states in the bulk) could improve efficiency. It is possible that for the films with approximately 750 nm thickness (see Figure 6.10A) this film structure effect is dominating the behaviour. In addition to the earlier onset of the anodic photo-current there is also an increase in cathodic photocurrent.

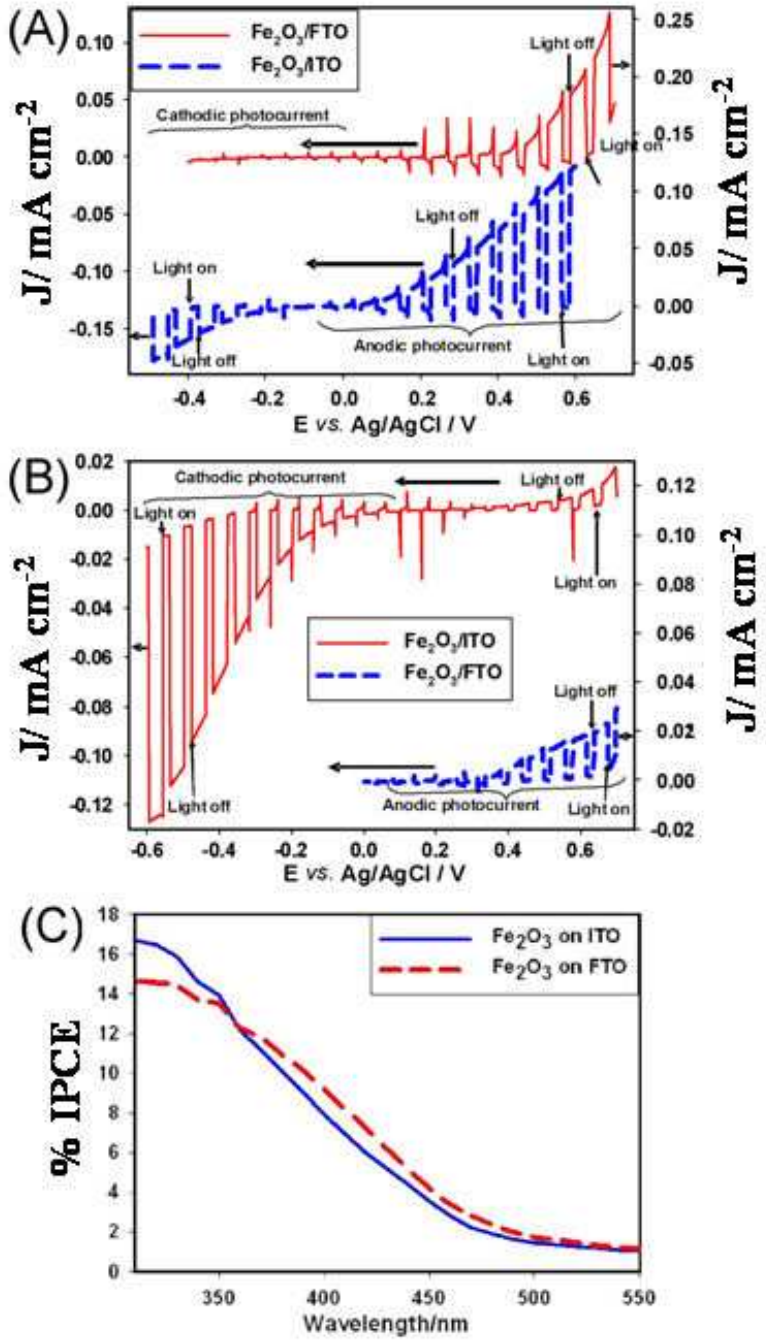

Figure 6.10. (A) Comparison between the forward photocurrent responses for Fe_2O_3 samples FTO15 and ITO15 with SE illumination using a blue LED 8 $mWcm^{-2}$ immersed in 1 M NaOH and with a scan rate 0.01 Vs^{-1}.(B) Comparison between the forward photocurrent responses for Fe_2O_3 samples FTO25 and ITO25 with SE illumination and a scan rate 0.01 Vs^{-1}. (C) Comparison of the %IPCE for Fe_2O_3 samples FTO30 and ITO30 immersed in 1 M NaOH at applied potential 0.8V vs. Ag/AgCl EE illuminated with a xenon lamp.

In spite of the differences in onset potential and the improved photocurrent production at lower potential, both FTO and ITO samples show good photocurrent

generation at ca. 0.8 V vs. Ag/AgCl. Figure 6.10C shows typical IPCE data sets obtained for FTO30 and ITO30 samples. For both materials typically 14% to 16% incident photon to current conversion occurs suggesting that under these conditions both films (both substrates) behave very similar.

In order to unravel the effects of sample thickness and sample porosity in some more detail, the finite element simulation method is applied in the next section. In particular the effect of EE versus SE illumination will be investigated.

6.3.3. Dark and Pulse-Illuminated Cyclic Voltammetry for CVD Deposited Hematite Film Electrodes: Finite Element Simulation

In this section the finite element simulation method introduced in chapter 5 will be used to uncover and rationalise further details of the photo-oxidation process at CVD hematite films. This method is highly oversimplified and appropriate only for highly porous films. However, the simulation is insightful in particular when contrasted to the more common semiconductor models used in the literature [13]. The key variables will be chosen (see chapter 5) as the apparent electron diffusion rate $D_e = 5 \times 10^{-15}$ m^2s^{-1}, the apparent hole diffusion rate $D_h = 2 \times 10^{-15}$ m^2s^{-1}, the recombination rate constant $k = 1 \times 10^6$ $mol^{-1}m^3s^{-1}$, the apparent chemical oxygen evolution rate constant $k_c = 0.4$ s^{-1}, and the thickness of the film 600 nm (or as specified in the text). The absorption of light is treated based on the Lambert-Beer law with an extinction coefficient α concentration combined parameter of 2.68×10^6 m^{-1} giving ca. 80% light absorption through a 600 nm thick film. The effect of electrolyte exposure (EE) and substrate exposure (SE) are investigated.

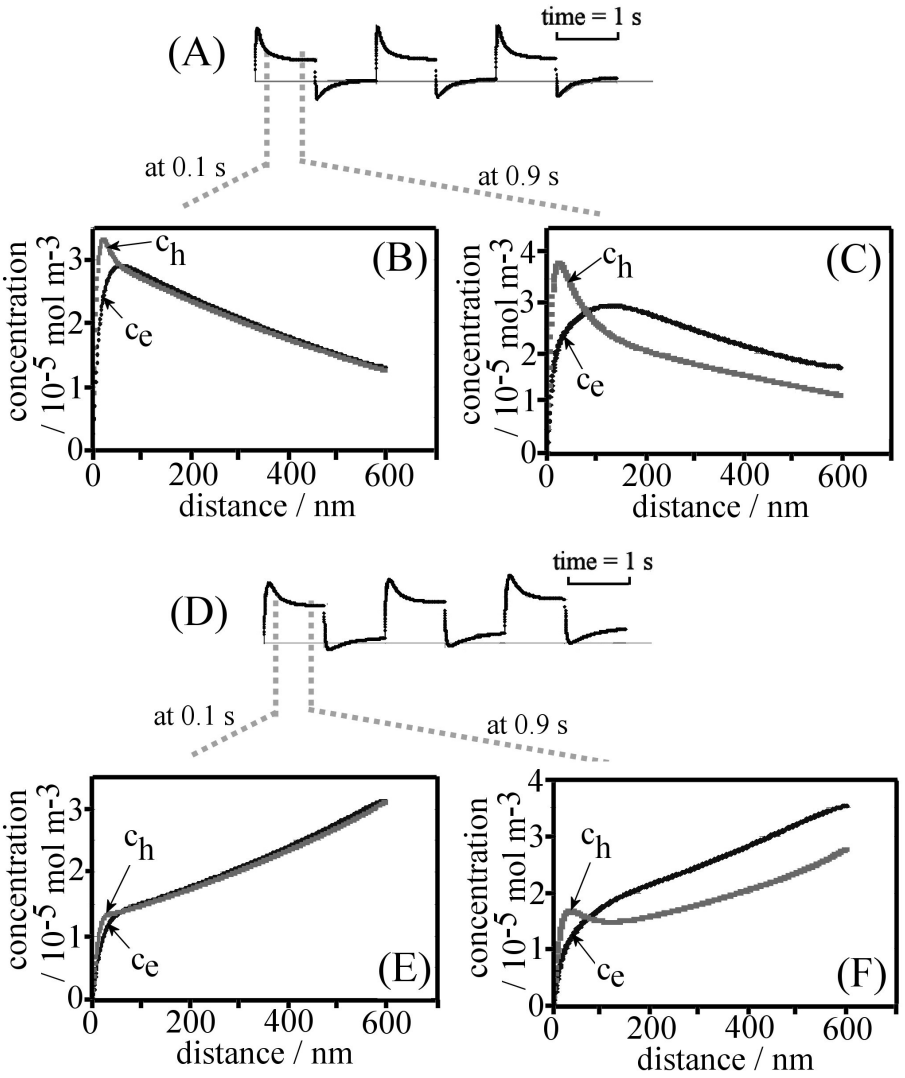

Figure 6.11. Numerical simulation data for a photo-active thin film assuming photo-excitation to give mobile electrons ($D_e = 5 \times 10^{-15}$ m^2s^{-1}) and holes ($D_h = 2 \times 10^{-15}$ m^2s^{-1}), with holes reacting to give oxygen ($k_c = 0.4$ s^{-1}), and with recombination within the film ($k = 1 \times 10^6$ $mol^{-1}m^3s^{-1}$) or within the substrate electrode. (A) Simulated photo-current transient (SE) for a 600 nm film. (B) Plot of the electron and hole concentration profile after 0.1 s. (C) Plot of the electron and hole concentration profile after 0.9 s. (D) Simulated photo-current transient (EE) for a 600 nm film. (E) Plot of the electron and hole concentration profile after 0.1 s. (F) Plot of the electron and hole concentration profile after 0.9 s.

Figure 6.11A shows a calculated current transient for light-on and light-off transients (three consecutive pulses) for substrate exposure (SE). Sharp peaks are observed followed by decay due to recombination and gradual formation of a diffusion zone throughout the film. Figure 6.11B and C show the diffusion profiles for electrons and for holes at 0.1s and at 0.9s. The gradient in the concentration profile clearly shows

the effect of light absorption (here arbitrarily chosen to be 20% transmission for 600nm) with a higher concentration of charge carriers being generated at the substrate – film interface in Figure 6.11B and C. In contrast, in Figure 6.11E and F electrolyte exposure causes the opposite concentration gradient to form. The photo-current transients for EE illumination are shown in Figure 6.11D. One significant difference can be seen in the shape of the initial peak which is sharp for SE (process close to the electrode) and broader for EE (process occurs further away from the electrode). The build-up of hole concentration close to the substrate surface is characteristic for the mechanism in the mesoporous film (see chapter 5) and caused by the lower concentration of electrons in this zone (the electrons have an extended diffusion zone due to a higher diffusion coefficient). The rate of oxygen formation should scale with the hole concentration and therefore a higher oxygen evolution activity close to the substrate seems likely. However, the model is inappropriate for films of low porosity (vide infra).

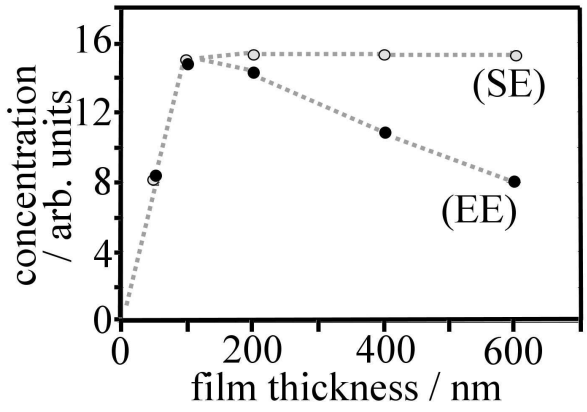

Figure 6.12. Plot of the simulation data for the photo-current after 1s for the first light-on transient as a function of thickness and direction of illumination.

In the photo-current transient after ca. 1s almost photo-stationary state conditions are reached and it is interesting to compare the simulated relative magnitude of the photo-currents after 1s illumination as a function of thickness. Figure 6.12 shows a plot of these photo-currents for both EE and SE illumination. It is interesting to see that for both cases, SE or EE, the same photo-currents are predicted for very thin films (ca. 100 nm). This can be explained based on the insignificant effect of the

absorption coefficient under these conditions. For EE illumination a clear maximum is observed and for thicker films the simulated photo-currents decay with thickness. This effects is due to the lower charge carrier concentration at the substrate side for thicker films. Experimental data shown above did show a maximum in the photo-transient data, but this is only in very qualitative agreement. For SE illumination initially an increase for thinner films is observed and after this a constant photo-current (at 1 s) is observed. In real electrodes an additional effect introduced with thickness is lower ionic conductivity and this is not considered in the simulation model. For the limit of a highly porous film an optimum photo-current response is predicted for thicker films.

6.3.4. Rationalisation of Electrochemical Data for Substrate and Thickness Effects in Mesoporous Hematite Film Electrodes

The comparison of the experimental data and the numerical simulation data demonstrate that CVD hematite films are more complex and the model is probably inappropriate. Compared to the layer-by-layer hematite films (chapter 5) much more dense iron oxide is produced by CVD and aqueous electrolyte is less able to penetrate into the pores. This leads to potential gradients within the iron oxide films and additional effects on transport and concentration profiles. It is interesting to consider two extreme cases for the mechanism:

(A) A single crystal semiconductor surface exposed to the electrolyte solution where the applied potential bias (positive for n-type semiconductor such as Fe_2O_3) creates a deletion zone at the interface to the electrolyte. Light absorption results in hole generation close to the electrode surface and electron capture in the substrate electrode (see Figure 6.13A).

(B) A highly mesoporous electrode with electrolyte solution throughout the porous membrane. Here the classical semiconductor model can be replaced with a model of diffusing holes and electrons without potential gradients through the film. The hole concentration will be highest at the interface to the electrolyte (assuming EE illumination) and recombination is strongly affected

by the presence of oxygen evolution catalysts at the iron oxide surface (see Figure 6.13B).

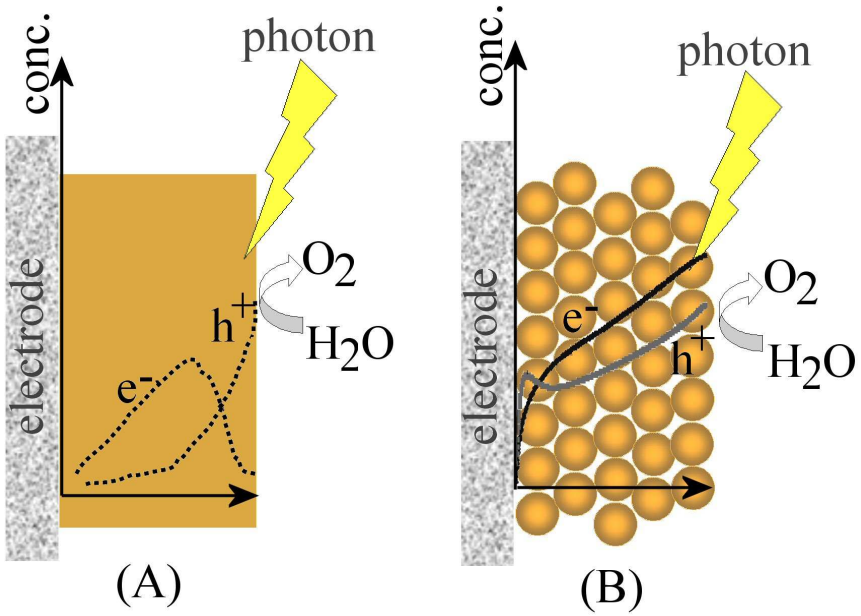

Figure 6.13. Schematic representation of photo-stationary states for (A) the bulk semiconductor model with depletion layer and higher hole concentration at the interface to the liquid and (B) the mesoporous film model with hole reactivity throughout the film.

The photo-electrochemical processes observed in this chapter for the CVD iron oxide films are likely to be best considered intermediate between the two cases of models. Due to the higher density of the CVD hematite the pores provide less space for electrolyte to penetrate to the substrate electrode and therefore potential gradients within the films are likely to contribute to the overall characteristics. Subtle changes in the growth conditions (e.g. ITO versus FTO substrate) can result in significant changes in the grain orientation and porosity of films and this is the reason why significant changes in reactivity are observed.

6.4. Conclusions

It has been shown that high quality CVD hematite films can be grown from ferrocene precursors onto both ITO and FTO substrates. Both types of films give complex photo-current responses with anodic and cathodic regions. When focusing on the anodic photo-currents associated with oxygen evolution from aqueous electrolyte characteristic effects of thickness and illumination direction were observed. Difference between ITO and FTO substrates were significant in the morphology of films but less dramatic in photo-electrochemical behaviour. Photo-electrochemical transient were discussed in the light of the mesoporous film model and it was concluded that the complex behaviour observed in these films is based on a mixed behaviour with contributions from both semiconductor and mesoporous film models.

6.5. References

(1) Satsangia, V. R.; Kumaria, S.; Singha, A. P.; Shrivastavb, R.; Dassb, S., *International Journal of Hydrogen Energy,* **2008** , *33,* 312-318.

(2) Ueyama, R.; Kuribayashi, K.; Itoh, N., *Journal of the Ceramic Socity of Japan* **1996,** *104* (10) 949-952.

(3) Mathur, S.; Sivakov, V.; Shen, H.; Barth, S.; Cavelius, C; Nilsson A.; Kuhn, P., *Thin Solid Films,* **2006,** *502,* 88-93

(4) Saremi-Yarahmadi, S.; Tahir, A. A.; Vaidhyanathan, B.; Wijayantha, K.G.U., *Material Letters,* **2009**, *63,* 523-526

(5) Tahir, A. A.; Wijayantha, K.G.U.; Saremi-Yarahmadi, S.; Mazhar M.; McKee, V., *Chem. Mater.* **2009,** *21*, 3763-3772

(6) Qiao, Q.; Beck, J.; Lumpkin, R.; Pretko, J.; Mcleskey Jr, J. T., *Solar Energy Materials & Solar Cells,* **2006,** *90,* 1034-1040.

(7) Aouaj, M. A.; Diaz, R.; Belayachi, A.; Rueda, F., Abd-Lefdil, M., *Materials Research Bulltin,* **2009,** *44,* 1458-1461.

(8) Bitht, H.; Eun, H.-T.; Mehrtens, A.; Aegerter, M. A., *Thin Solid Films,* **1999** *351*, 109-114

(9) Shin, H. -S.; Kwon, S. -J., *Yoop Hakoechi (Journal of the Korean Ceramic Society)*, **1993**, 30, 499-509.

(10) Langford, J.I.; Wilson, A.J.C*, J. Appl. Cryst., 1978 11*, 102-113.

(11) Krishnan, R. R.; Vinodkumar, R.; Rajan, G.; Gopchandran, K. G.; Pillai, V. P. M., *Materials Science and Engineering b-Advanced Functional Solid-state Materials*, **2010**, *174,* (1-3), 150-158.

(12) Beermann, N.; Vayssieres, L.; Lindquist, S.E.; Hagfeldt, A., *J. Electrochem. Soc.*, **2000**, *147*, 2456

(13) Peter, L. M., Walker, A. B., Boschloo, G., Hagfeldt, A., *J. Phys. Chem. B*, **2006**, *110*, (28), 13695.

Chapter 7

Spray Pyrolysis Growth and Photoelectrochemistry of Silica-Doped Nano-Hematite Fe_2O_3

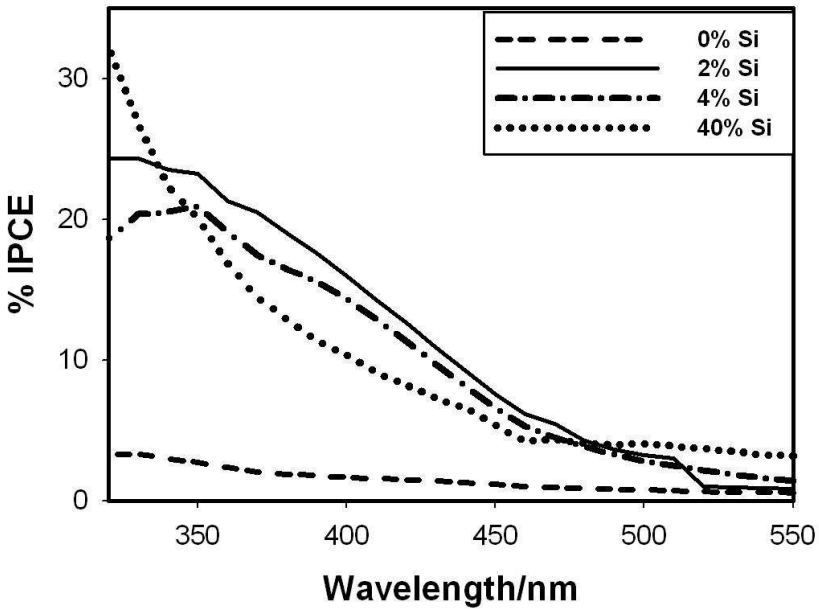

Abstract. The spray-pyrolysis formation of photo-electrochemically active films is versatile and it allows additives to be introduced in order to affect morphology and structure of deposits. Here, addition of tetramethoxysilane (TMS) in varying amounts to iron oxide precursor systems for spray pyrolysis is investigated and the dramatic effect on the photo-electrochemical water splitting current in aqueous 1 M NaOH is discussed.

Content

7.1. Introduction

Hematite (α-Fe_2O_3) was found to be a good film component for photo-electrochemical electrodes for water splitting because it is abundant, cheap, and effective [1]. Even more promising are modified hematite films, especially those obtained after doping with effective dopants such as silicon [2]. The potential effects of the dopants in photo-electrochemistry are complex and may be based on (i) altering the hematite band gap, (ii) changing morphology, (iii) altering the crystal shape and orientation, (iv) blocking or enhancing recombination or catalysitc sites, and (v) affecting charge carrier mobility.

Atmospheric pressure chemical vapour deposition (APCVD) methods have been used previously for preparation of pure and Si-doped α-Fe_2O_3 [3] to investigate and improve the photo-electrochemical efficiency for splitting of water. It was found that some Si incorporated into Fe_2O_3 lattice as Si^{4+} and this led to some disordering in the iron oxide films [4]. Meanwhile Saremi-Yarahmadi et al. [2] found also that the optical band gap of Si-doped Fe_2O_3 increases with increasing of TEOS (tetraethoxysilane) incorporation rate. It was observed that the incorporation of silicon into the hematite lattice reduced its particle size and increased the donor densities.

Reactive magnetron sputtering [4] was used to prepare un-doped hematite as well as Si and Ti-doped Fe_2O_3. From this study it was found that doping of hematite with silicon and titanium enhanced the photochemical reaction of the film while decreasing the onset potential. Doping with titanium was found to be more effective than doping with silicon. Glasscock et al. [3] explained that dopants lead to passivity of the grain boundaries with improvements due to decreasing the recombination rate.

Tetraethoxysilane (TEOS) has been used to modify hematite with silicon, which affected beneficially the photochemical reaction of hematite in an aqueous electrolyte as Cesar et al. found [5]. They used atmospheric pressure vapour deposition (APCVD) to prepare the nanostructured silicon-doped hematite and pure hematite from $Fe(CO)_5$. Through this study, it was found that the substrate temperature has a considerable influence on the grain size and morphology. It was found also that the growth rate of

films is slower at high temperatures. The feature size of the film was found to depend on the silicon content in iron oxide film. Silicon-hematite doping increases the electron density (10^{20} cm^{-3}), which can lead to formation of a space charge region inside the nano-structured hematite and this can help separating photo-generated electron-hole pairs. Cesar et al. also found that the recombination rate is much higher on the tin oxide-fluorine substrate in comparison to that in the bulk part of the hematite film.

The donor density in hematite was found to be between 10^{17} to 10^{20} cm^{-3} after doping with silicon using the spray pyrolysis method with a $Fe(acac)_3$ precursor. Liang et al.[6] deposited a 5 nm SnO_2 film as an interfacial buffer-layer between Fe_2O_3 and the conducting substrate and they found that the highest photocurrent response was obtained for hematite doped with 0.2 % Si (it gave 0.37 $mA.cm^{-2}$ at 1.23 V (RHE) in 1 M KOH electrolyte under 80 mW cm^{-2} (AM 1.5 illumination).

Zhang et al. [7] found that because of the trend in cation radius of $Si^{4+}<Fe^{3+}<Ti^{4+}$, both of Si and Ti co-doping can be used to balance the ion radius difference between Fe^{3+} and Si^{4+} (or Ti^{4+}) and to increase the donor concentration in the films prepared by ultrasonic spray pyrolysis. By calculation the slope of Mott-Schottky plots for α-Fe_2O_3, Si- Fe_2O_3, Ti- Fe_2O_3, and for co-doped-Fe_2O_3 it was found that charge carrier densities are 9.10 x 10^{18} cm^{-3}, 1.89 x 10^{20} cm^{-3}, 2.04 x 10^{20} cm^{-3}, and 7.06 x 10^{20} cm^{-3}, respectively. IPCE data for these films obtained at 365 nm and at 0.6 V vs. Ag/AgCl were found to be 10%, 20%, 22%, and 34%, respectively. These levels of efficiency are very high and very promising for applications.

In this part of the study the effect of silicon doping is investigated as a tool for improving photo-electrochemical activity in hematite films. The spray pyrolysis method is employed as a commercially viable and highly versatile technique. A range of different precursor systems and doping levels are investigated. Silicon doping is shown to be the most promising approach for enhancing photo-electrochemical yields in water splitting.

7.2. Experimental

7.2.1 Chemical Reagents

Iron acetylacetonate $(C_5H_8O_2)_3Fe$ (99.9%), Ferrocene carboxlic acid and tetramethoxysilane (TMS, $Si(OCH_3)_4$), 99%) were obtained from Aldrich, while absolute methanol was from Fisher Scientific, and ferrocenecarboxlic acid 98% was from Alfa Aeser. These chemicals were bought commercially and used without further purification. Water used in preparation of some solutions was filtered and double de-ionized water (DDW, MilliQ water, from Elga system) with resistivity of ca. 18.2 M Ω cm.

7.2.2 Spray Pyrolysis Formation of Iron Oxide Films

Two different precursor solutions with different concentrations of either $Fe(acac)_3$ or ferrocenecarboxlic acid were used for spray pyrolysis. The solvent was DDW (double deionised water) mixed with either methanol or other organic solvents, as shown in Table 7.1. Different "apparent" dopant concentrations were obtained by adjusting the tetramethoxysilane (TMS) $Si(OCH_3)_4$) concentration.

The FTO (Fluorine-doped tin oxide, (Asahi Tech 15), conducting glass was put onto three microscope glasses. One third of the electrode was covered with another microscope glass to leave a conducting part of the electrode uncovered with the film. All the glass slides and the FTO were heated on a hotplate (ca. 500^o C) for ca.15 minutes until they were all at the same temperature. Then the precursor solution (at room temperature) was sprayed manually onto FTO conducting glass in cycles (each cycle contains 5 seconds spray on and 5 seconds spray off) for 2 minutes, or more according to the required thickness. After completing the spraying, the slides were left for ca. 5 minutes on the hotplate, and then pushed away from the central hot area to the edge of the hotplate to cool down. The sample was then annealed in ELITE furnace for annealing at 500 ^{o}C for 2 hours. A manual spray bottle (DESAGA, SARSTEDT GRUPPE, NS 18.8/26) **(**Figure 7.1**)** was used to spray the precursor solutions.

Figure 7.1. Photograph of the manual spray bottle filled with precursor solution.

Un-doped Fe_2O_3 have been prepared from 50 mL of 0.5 M $Fe(acac)_3$ / 1:1 MeOH: H_2O sprayed onto a FTO film, at 500^o C, as described above, for 12.10 minutes. Then the sample left on a hotplate for ~10 minutes, and then it was annealed at 500 ^{o}C for 2 hours. The same method has been applied in doping Fe_2O_3 with TMS (bulk doping) in concentrations; 0 at.%, 0.5 at.%, 1 at.%, 2 at.%, 4 at.%, and 40 at.% Si, to get the samples 2F0Si, 6SiF, 7SiF, 8SiF, 4SiF, and 3SiF, respectively. Silicon doping of iron oxide was achieved by bulk doping through mixing the calculated amount of TMS into the iron salt precursor solution. Then they were sprayed together by using the same manual spray bottle. Ferrocenecarboxlic acid in different solvents has also been used to prepare some un-doped and Si-doped Fe_2O_3 as it is shown in Table 7.1.

Table 7.1. Summary of doped and un-doped-iron precursor solutions used for spray pyrolysis at 500 ^oC.

Sample	Chemical composition	Precursor solution	Si content
1F0Si	Fe_2O_3	0.5 M ferrocenecarboxlic acid/ 3:1 methanol : butanol	0 %
3F0Si	Fe_2O_3	0.05 M ferrocenecarboxlic acid/ 1:3 methanol : butanol	0 %
5SiF	Si-Fe_2O_3	50 mL 0.05 M ferrocenecarboxlic acid + 15 µL TMS conc. soln. was sprayed on FTO, tech 15 for 13 mins. Annealed at 500^o C for 2 hrs.	4 %
2SiF	Si-Fe_2O_3	25 mL 0.169 M ferrocenecarboxlic acid + 2 µL TMS conc. soln. then 18 mL 0.05 M $Fe(acac)_3$ was sprayed on top. Annealed at 500^o C for 2 hrs.	4 %
2F0Si	Fe_2O_3	0.5 M $Fe(acac)_3$ / 1:1 Methanol:DDW	0 %
3SiF	Si-Fe_2O_3	0.05 M $Fe(acac)_3$ + 300µL TMS conc. soln. was sprayed on FTO, tech 15 for 12 mins. Annealed at 500^o C for 2 hrs.	40 %
4SiF	Si-Fe_2O_3	50 mL 0.05 M $Fe(acac)_3$ + 15 µL TMS conc. soln. was sprayed on FTO, tech 15 for 12 mins. Annealed at 500^o C for 2 hrs.	4 %
6SiF	Si-Fe_2O_3	50 mL 0.05 M $Fe(acac)_3$ + 1.875 µL TMS conc. soln. was sprayed on FTO, tech 15 for 13.4 mins. Annealed at 500^o C for 2 hrs.	0.5 %
7SiF	Si-Fe_2O_3	50 mL 0.05 M $Fe(acac)_3$ + 3.75 µL TMS conc. soln. was sprayed on FTO, tech 15 for 12.5 mins. Annealed at 500^o C for 2 hrs.	1 %
8SiF	Si-Fe_2O_3	50 mL 0.05 M $Fe(acac)_3$ + 7.5 µL TMS conc. soln. was sprayed on FTO, tech 15 for 12.50 mins. Annealed at 500^o C for 2 hrs.	2 %

7.3. Results and Discussion

7.3.1. Effects of Doping Fe_2O_3 with Si on Morphology

Figure 7.2 shows the SEM front pictures of un-doped and Si-doped Fe_2O_3, as a comparison between un-doped Fe_2O_3 prepared by using Ferrocenecarboxlic acid precursor solution (A), and that of 4% Si-doped Fe_2O_3 prepared from the same precursor after adding 4% atomic weight of (TMS) into the Ferrocenecarboxlic acid precursor solution (C). From this comparison it was found that the insertion of Si^{4+}, as it was estimated elsewhere [1, 5], affects the particle size and shape.

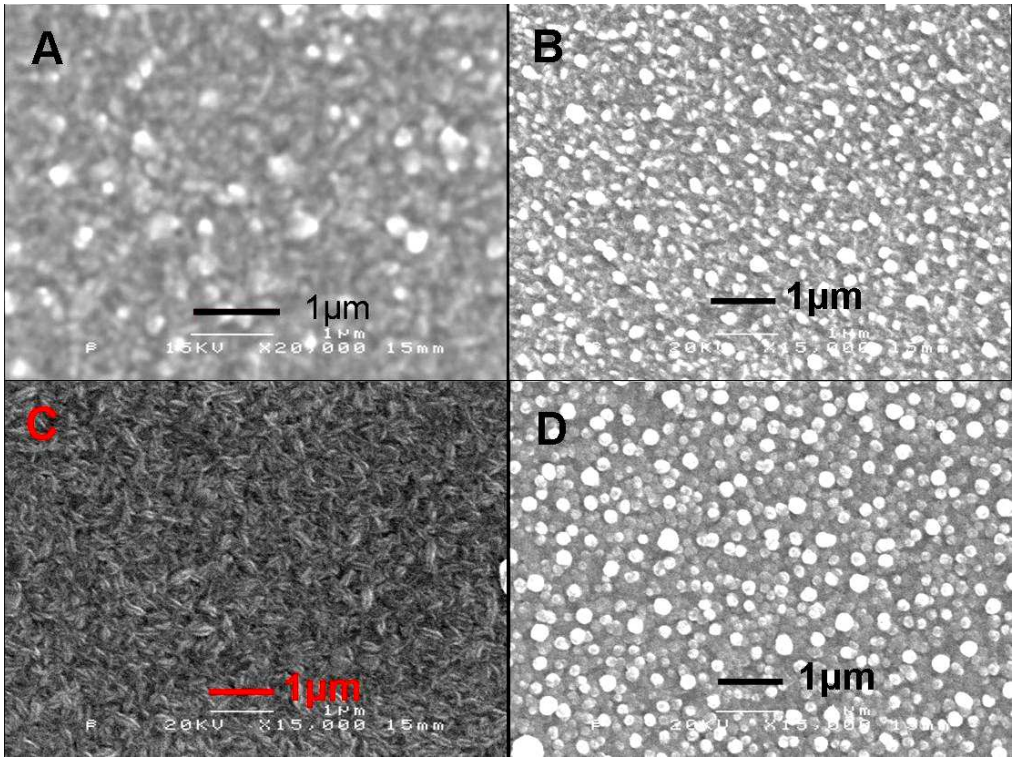

Figure 7.2. SEM images of; **A**: 0% Si-Fe_2O_3 (1F0Si), **B**: 4% Si-Fe_2O_3 (4SiF1) **C**: 4% Si-Fe_2O_3 (5SiF4), and **D**: 40% Si-Fe_2O_3 (3SiF3).

Particles in image A are almost circular and bigger while in image C, they are coffee bean shaped and much smaller. Images B and D are for 4% and 40% Si-Fe_2O_3 doped using $Fe(acac)_3$ precursor solution containing the above ratios of atomic weight

contents. Although, the samples in image A and those in images B and D were prepared from different precursor solutions (from ferrocenecarboxlic and $Fe(acac)_3$) precursor solutions), it can be noticed that they are similar in the shape, which is almost circular with a particle size slightly smaller in B and D than in A. However, in a comparison between image B (4% Si-Fe_2O_3) and that of D (40% Si-Fe_2O_3), it can be noticed that there is no a big difference in either shape or in the particles size.

Figure 7.3 shows clearer images of the effect of silicon doping on the shape and particle size of Fe_2O_3 film. It can be noticed that the particle size of hematite decrease up to 7 times after bulk doping with silicon.

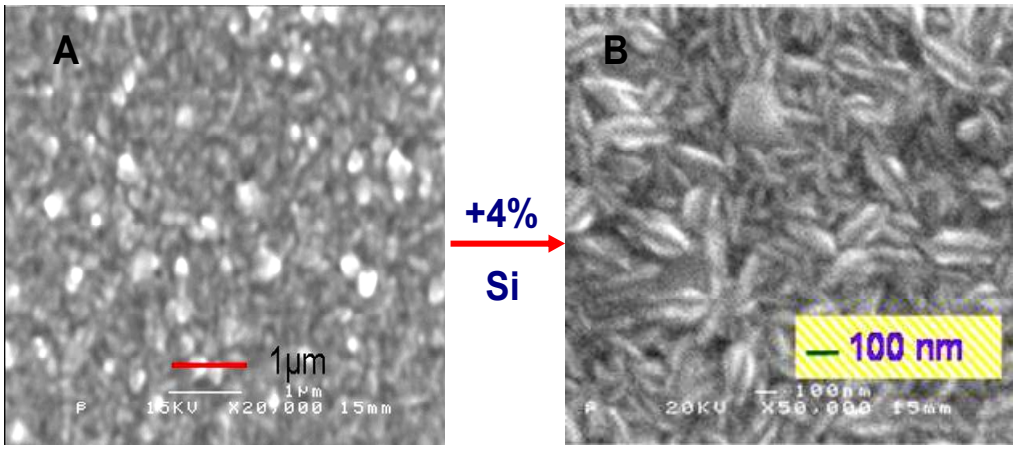

Figure 7.3. Effect of Si-doping on the particle size of Fe_2O_3. **A:** un-doped Fe_2O_3, **B:** 4% Si-doped Fe_2O_3.

It can be noticed from the photographic film images in Figures 7.4 and 7.5 that the iron oxide colour is slightly darker with increasing the silicon content.

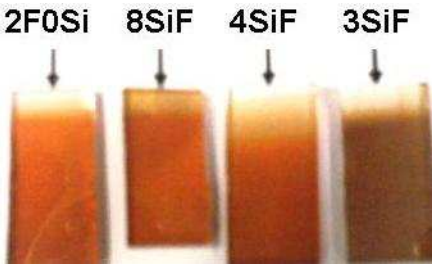

Figure 7.4. Photographic images of 2F0Si: Un-doped Fe_2O_3, 8SiF: 2% Si-doped-Fe_2O_3, 4SiF: 4% Si-doped-Fe_2O_3 and 3SiF: 40% Si-doped-Fe_2O_3

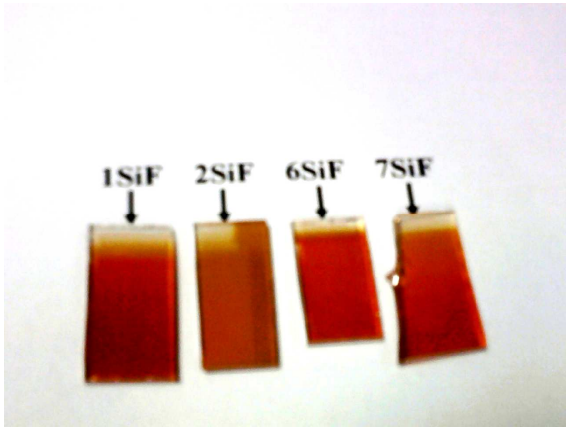

Figure 7.5. Photographic images of 1SiF: 0.3% Si-doped Fe_2O_3, 2SiF: 4% Si-doped-Fe_2O_3, 6SiF: 0.5% Si-doped-Fe_2O_3 and 7SiF: 1% Si-doped-Fe_2O_3.

7.3.2. Effects of Doping Fe_2O_3 with Si on XRD Data

XRD for un-doped hematite and Si-doped Fe_2O_3 are shown in Figure 7.6. Unfortunately, these data are dominated by the main FTO diffraction peaks and only very weak (104) and (110) lines indicate the presence of the hematite film. Comparison with literature data shows that an increase in silicon doping level does change the ratio of (104) to (110) intensities. Similar observation have been reported by Wijayantha et al. [8] and attributed to morphological changes with an associated change in the type of hematite surface exposed to the solutions phase.

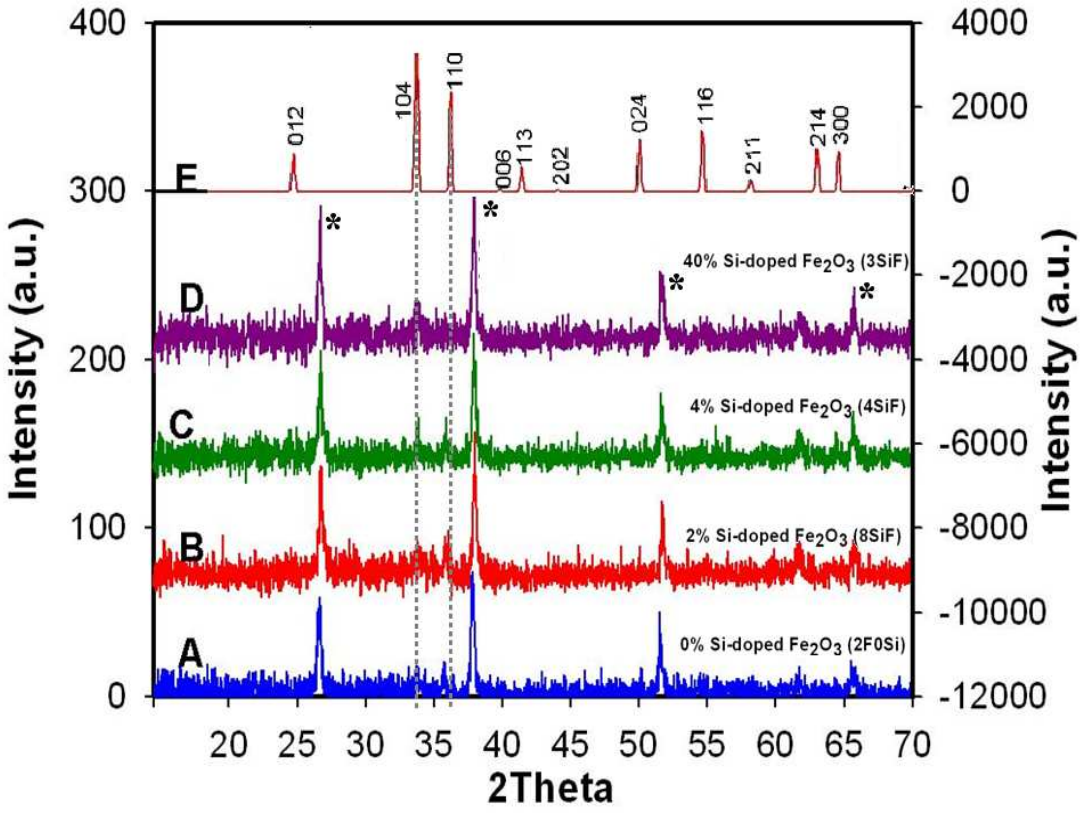

Figure 7.6. XRD patterns of un-doped α-Fe_2O_3 (hematite) and Si-doped Fe_2O_3 films (A: 2F0Si, B: 8SiF, C: 4SiF, D: 3SiF) in comparison with a standard XRD for powder Fe_2O_3 (E: literature data from Shin et al.[9]. The asterisk denotes FTO diffraction lines.

7.3.3. Pulse-Illuminated Voltammetry Studies

Dark and illuminated cyclic voltammetry measurements were carried out on the samples prepared by using spray pyrolysis. Dark cyclic voltammetry results show similar behaviour to the samples prepared by using layer by layer method. It was also found that the oxidation and reduction peaks increase with increasing of the scan rate as expected for an immobilised redox system.

Silicon-doping strongly increases photocurrent responses for Fe_2O_3 film electrodes. Figure 7.7 shows typical current transient responses as a function of potential and scan direction. A 4% silicon doping causes a one order of magnitude increase in the resulting photo-currents associated with oxygen evolution. This may be explained because silicon atom acts as an electron donor due to substitution of Fe^{3+} by Si^{4+} in the Fe_2O_3 lattice and this could improve its electrical conductivity. In addition, and as

it was noticed from the morphology studies that doping of Fe_2O_3 with silicon decreases the particle size to up to 7 times, an increase in the surface area and porosity of the photoanode could also increase the light harvesting. The same effect of Si-doping was noticed on the photocurrent responses for forward and backward scans. Higher doping levels did not further increase the effect.

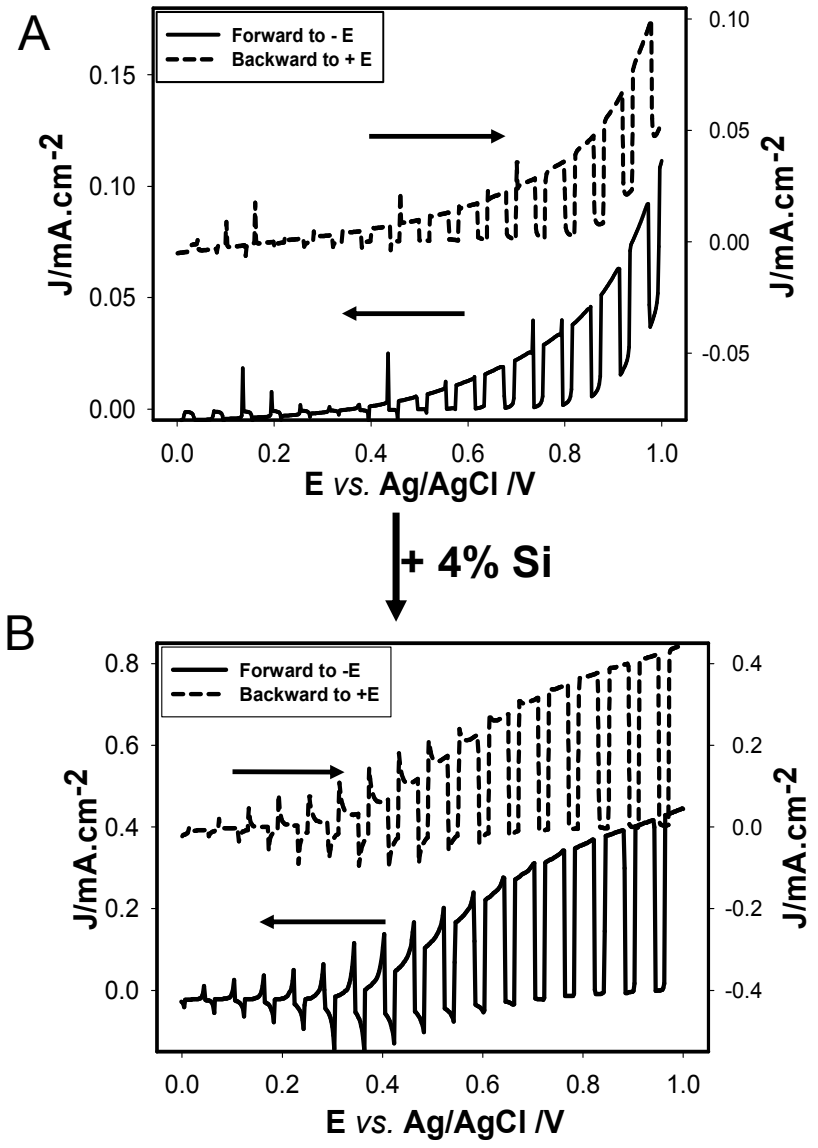

Figure 7.7. Effect for Si-doping on Illuminated CV of Fe_2O_3 A: undoped Fe_2O_3 and B: 4% Si-doped Fe_2O_3 (prepared by spray pyrolysis of $Fe(acac)_3$ precursor solution), in 1 M NaOH, using blue LED 7.15 mW cm^{-2}.

7.3.4. Incident Photon to Current Efficiency (IPCE) Studies

It was found that silicon doping strongly increases the efficiency of Fe_2O_3 electrodes possibly because it acts as an electron donor due to substitution of Fe^{3+} by Si^{4+} in the Fe_2O_3 lattice. This is believed to improve electrical conductivity, the charge transfer, and consequently decrease the recombination rate of the photo-generated pairs. The trend in photo-activity is confirmed in IPCE measurements (see Figure 7.8).

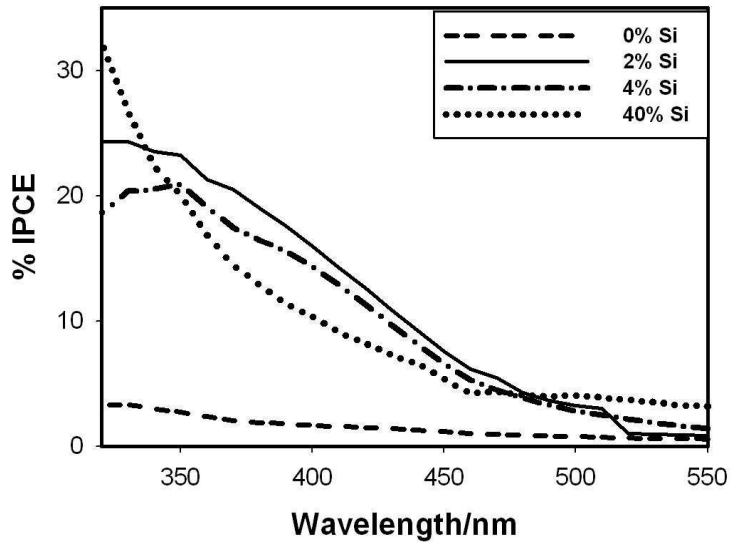

Figure 7.8. IPCE data showing the effect of doping Fe_2O_3 with different concentrations of Si using the spray pyrolysis method (0%= 2F0Si, 2%=8SiF, 4%=4SiF, 40%=3SiF). Data obtained in 1 M NaOH, at applied potential 0.7 V vs. Ag/AgCl and by illuminating by 75W Xenon lamp

An increase in the doping level from 0% to 2% causes a significant increase in photo-electrochemical activity. Any further increase is not detrimental but also not beneficial. It is likely that even lower levels of silicon doping may suffice. Excess silicon may simply be present as trace silicate impurity. The smaller grain size caused by silicon doping increases the surface area and porosity of the photo-anode and consequently this may increase the light harvesting effect.

7.4. Conclusions

It has been shown that spray pyrolysis offers a simple methodology for the formation of highly active hematite photo-absorber layers. In particular when used in conjunction with silicon doping high efficiencies (IPCE up to 20%) can be achieved. The choice of hematite precursor appears to be not very important and tetramethoxysilane offers good doping effects.

In future, film efficiency can be improved further by (i) systematically changing the film thickness, (ii) further decreasing the doping level, and (iii) developing layer structures with morphology/structural gradients from the substrate to the hematite solution interface to aid charge separation and to restrict recombination.

7.5. References

(1) Sivula, K.; Le Formal, F.; Grratzel, M., *ChemSusChem*, **2011**, *4*, (4) 432 – 449.

(2) Saremi-Yarahmadi, S.; Wijayantha, K. G. U.; Tahir, A. A.; Vaidhyanathan, B., *J Phys Chem C,* **2009,** *113* (12), 4768-4778.

(3) Glasscock, J. A.; Barnes, P. R. F.; Plumb, I. C.; Savvides, N., *J Phys Chem C* , **2007**, 111, 16477-16488.

(4) Zhu, Y.; Li, C., *Mrrreriuls Chetnisiry and Physics,* **1997,** *51*, 169-l 73.

(5) Cesar, I.; Sivula, K.; Kay, A.; Zboril, R.; Graetzel, M., *J Phys Chem C***, 2009**, 113 (2), 772-782.

(6) Liang, Y. Q.; Enache, C. S.; van de Krol, R., Int. J. Photoenergy, 2008.

(7) Zhang, M. L.; Luo, W. J.; Li, Z. S.; Yu, T.; Zou, Z. G., *Appl Phys Lett* **2010,** *97* (4).

(8) Wijayantha, K. G. Upul; Saremi-Yarahmadi, Sina; Peter, L. M., *Phys. Chem. Chem. Phys.*, **2011**, *13*, 5264–5270.

(9) Shin, H. -S.; Kwon, S. -J., *Yoop Hakoechi (Journal of the Korean Ceramic Society)*, **1993**, *30*, 499-509

Chapter 8

Spray Pyrolysis Growth and Photoelectrochemistry of Strontium Titanate Ferrate

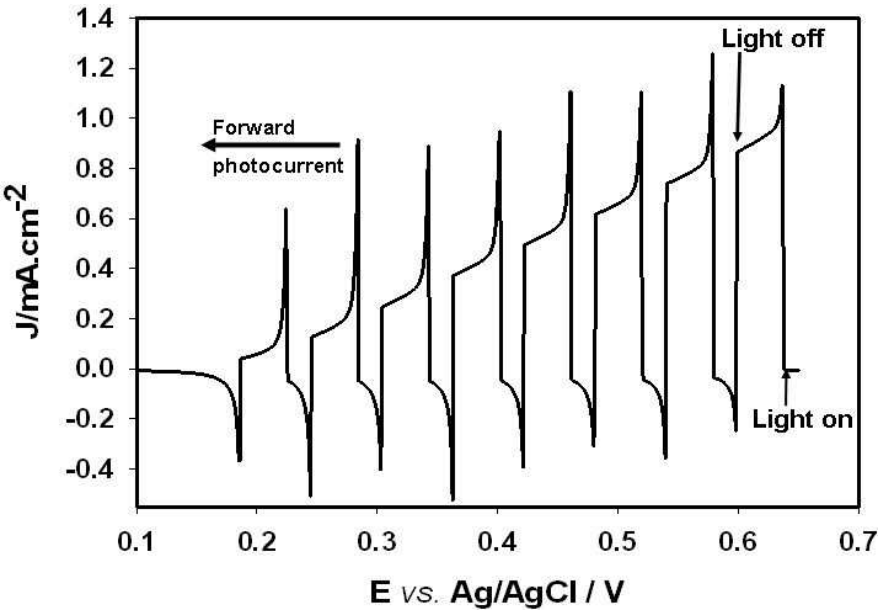

Abstract. Iron oxides with substitution of metal sites give rise to a family of materials $SrTi_{1-x}Fe_xO_{3-y}$ or strontium titanate ferrate (STF) with solid solution character. In this chapter a spray pyrolysis approach to prepare STF films on ITO substrates is employed. In preliminary data, the nanostructured films show good photoactivity with IPCEs of up to 11%.

Content

8.1. Introduction

Mixed metal oxides can be employed to control and improve physical properties, for example for photo-electrochemical films. For the case of iron oxides it has been shown that strontium ferrites and strontium titanates can form solid solutions to provide control over ionic and electronic conductivity [1]. Mixed ionic electronic conductors (MIEC) play a core role in the manufacturing of solid-state electrochemical devices, which can be designed for energy conversion and for gas sensor applications [2]. There are many important applications for MIEC such as solid oxide fuel cell (SOFC) electrodes, oxygen separation membranes, insertion electrodes, electrochromic windows, oxygen and gas sensors, and as catalysts [3]. The strontium titanate ferrate (STF) family ($SrTi_{1-x}Fe_xO_{3-y}$) forms a continuous solid solution between strontium titanate ($SrTiO_3$) and strontium ferrite ($SrFeO_3$) over the entire composition range $0 < x < 1$. $SrTi_{1-x}Fe_xO_{3-y}$ (STF) solid solution materials have been prepared [3] by conventional mixed-oxide techniques and by calcination of $SrCO_3$, Ti, Fe mixed oxide in air at 1200 ^oC. The electronic structure, defect chemistry and transport properties of its members have been studied [3].

The related titania-doped Ruddlesden-popper ferrite ($Sr_3Fe_{2-x}Ti_xO_{6+\delta}$) where; $0 < x < 2$, have been prepared and characterized [4]. This material has been prepared by conventional solid-state reaction method starting with Sr, Ti, and Fe pure oxides. After pressing the metal oxides mixture into discs under high pressure, high temperatures up to 1350^oC have been used to prepare these materials. The characterization has been reported by XRD and theromgravimetry measurements. The effect of oxygen content and titania- doping have been studied. The oxygen ion conductivity was found to decrease with increasing the titania content.

In the present work, STF-like films are prepared and investigated for photo-electrochemical applications. After failing to keep the conducting part of ITO quartz slides without damage by the effect of the very high calcination temperature 1200 ^oC, a low temperature approach has been investigated. STF films are prepared on ITO conducting glass by normal spray pyrolysis technique at 500 ^oC and via annealing in air at the same temperature for 2 hours in a furnace. Structural studies are preliminary

and in-conclusive, but initial photoelectrochemical studies have revealed very promising photo-activity for water splitting.

8.2 Experimental

8.2.1 Chemical Reagents

0.2 M $Fe(NO_3)_3.9H_2O$ 99.999% (Sigma-Aldrich) / MeOH, 0.1 M $Sr(NO_3)_2$ 99.995% (Aldrich) / H_2O, diisopropxytitanium-bis-(acetylacetonate) (C_{16} H_{28} O_6 Ti) solution, 75% wt.% (Aldrich) / isopropanol precursors have been prepared. All chemicals were obtained commercially and used without any further purification.

8.2.2 Instrumentation

An Auto-lab potentiostat (Ecochemie) was employed in three-electrode configuration. Incident photon-to-current efficiency (IPCE), UV-vis absorption spectroscopy, electrochemical impedance spectroscopy (EIS), scanning electron microscopy (SEM), X-ray diffraction (XRD), and energy dispersive X-ray spectroscopy (EDX) were performed as described in chapter 3. A hotplate, a sonicator, and a furnace instrument were used for film preparation (see chapter 3 of the general experimental).

8.2.3 Procedure for Spray Pyrolysis Method

The indium-doped tin oxide (ITO) slide was cleaned by sonication at 40 ^oC for 15 minutes in, sequentially, detergent (5 vol% decon-90), isopropanol, acetone and finally in ethanol, in which the slides were kept. A mixture of the above precursors, with the concentrations as shown in the chemical reagents, has been prepared to contain 50 wt.% Fe, 25 wt.% Sr, and 25 wt.% Ti. So it was taken 93.36 mL of 0.1 M $Sr(NO_3)_2/H_2O$, 31.77 mL of 0.2 M $Fe(NO_3)_3.9H_2O$/MeOH and 8.33 mL of diisopropxytitanium-bis-(acetylacetonate) (C_{16} H_{28} O_6 Ti) solution and they are mixed together. Stirring of the mixed precursor has been carried out for 10 minutes, on an electric stirrer, to ensure of completely mixing the precursors as a dark violet solution. The ITO slide has been dried with nitrogen gas and then preheated to ~ 500^oC on a hotplate and then 50 mL of the mixed precursor (at room temperature ~22^o C) has been sprayed by using a manual spray bottle (see chapter 7) and by spraying two sprays on three different spots along the slide every 10 seconds. Different spraying

times have been used to obtain different thicknesses. The slide left on the hotplate for 10 minutes and then annealed in the furnace at 500 ^{o}C for further 2 hours.

8.3. Results and Discussion

8.3.1 Morphology and Structural Studies

Samples of strontium titanate ferrate (STF) have been prepared by the spray pyrolysis method on ITO conducting glass slides at 500 ^{o}C followed by 2 hour annealing in air at 500 ^{o}C. Table 1 shows types of samples produced at different spraying times. The average thickness has been estimated based on profilometry and SEM measurements.

Table 1. STF samples prepared by spray pyrolysis method at 500^{o}C for different spraying times

Sample	Substrate	Spraying time (mins.)	Approx. average thickness
2STF	**ITO**	**4**	**1.1 (+/-0.2) μm**
3STF	**ITO**	**3**	**1.0 (+/-0.2) μm**
4STF	**ITO**	**5**	**1.2 (+/-0.2) μm**

SEM and EDX. SEM images show that the films are not completely homogenous when studied over a wider area (see in case of samples 2STF and 3STF, Figure 8.1a,b) while being more homogenous with grains of ca. 20 nm to 200 nm (see in case of sample 4STF, Figure 8.1c). Additional EDX measurement have been performed for sample 2STF (Figure 8.1d) and it shows that the sample contains Sr, Ti, and Fe. The accuracy of EDX in this case is not sufficient to confirm the elemental composition, but based on the ratio of starting materials a composition Sr:Ti:Fe of 1:1:2 is expected.

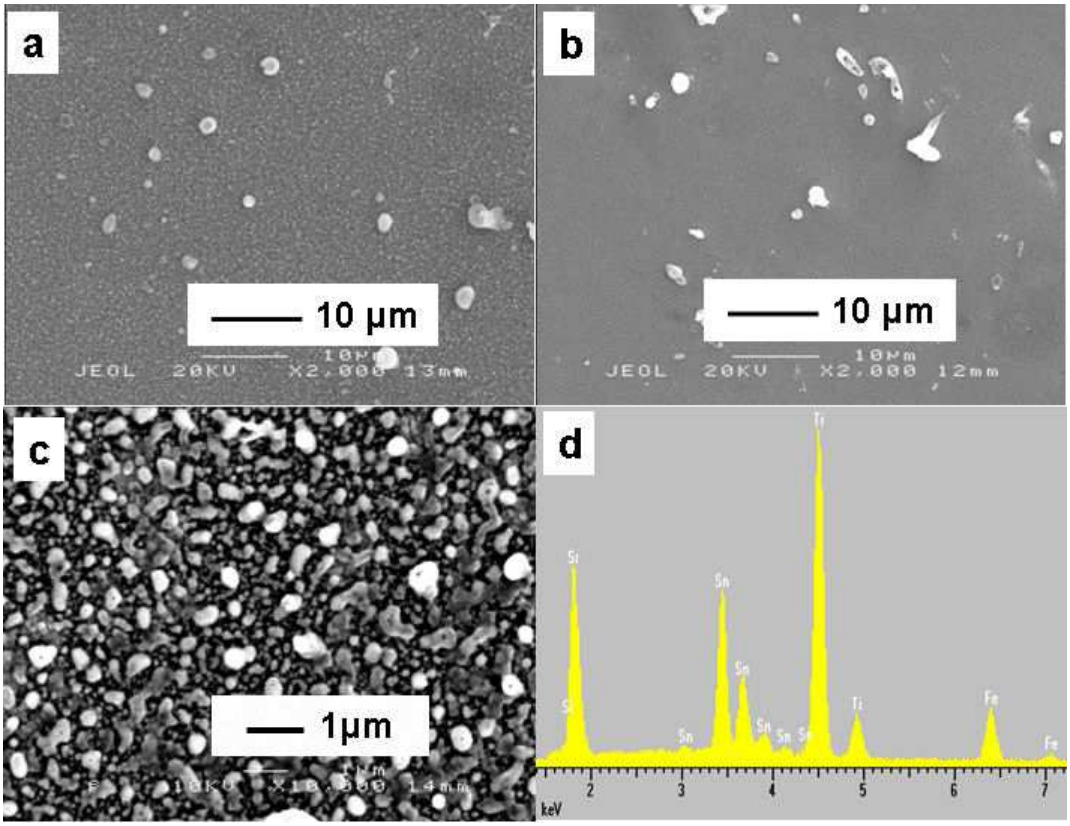

Figure 8.1. Typical SEM images of samples **a**: 2STF, **b**: 3STF, and **c**: 4STF. **d**: EDX of sample 2STF showing the presence of Sr, Ti, and Fe.

Figure 8.2 shows the cross section of sample 2STF and that of 4STF which indicates that the thickness of these films is about 1.1 µm in average, but an error of at least +/- 0.2 µm has to be assumed. The films are visible by eye as a dark reddish-brown colour.

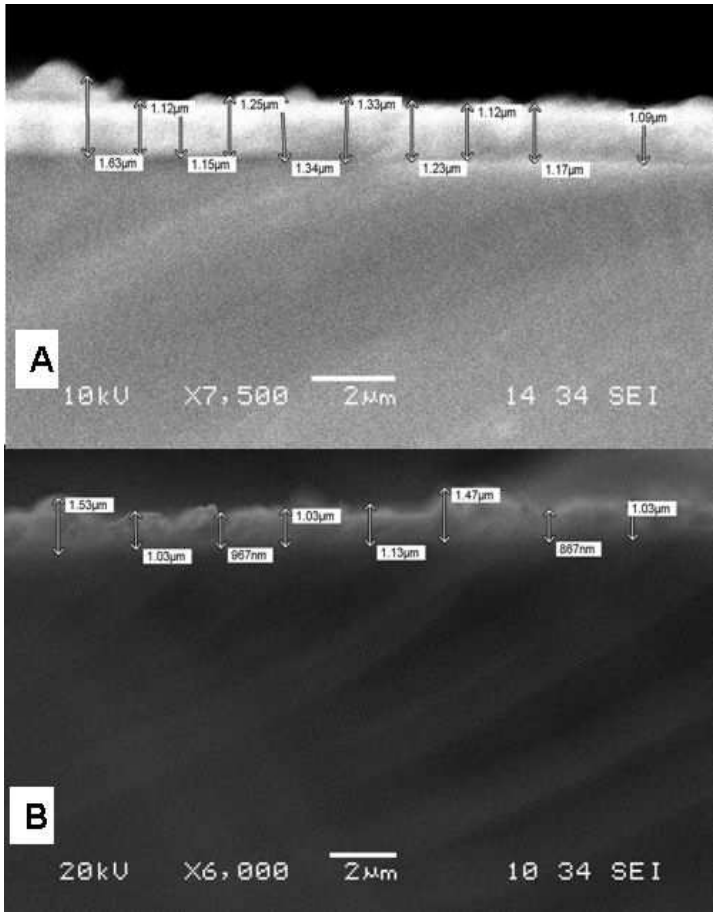

Figure 8.2. SEM cross section images of **A**: 2STF, and **B**: 4STF.

X-Ray Diffraction (XRD). XRD results showed that the main peak in STF films could be explained as due to the orientation (**112)** which is the main peak in the related structure of Sr ($Fe_{0.9}$ $Ti_{0.1}$) $O_{2.95}$ according to published literature data by Adler et al. [(5)]. This result indicates that the STF film compound may contain some material belonging to the perovskite[a] family AMO_3, where A and M are metals. The peaks of the ITO substrate are described with (*) symbols (see Figure 8.3). According to the preparation procedures it was expected that the overall chemical composition is given by $(SrFe)(TiFe)O_6$ which could result in the formation of a perovskite-type structure. However, evidence for this structure is currently weak and in future additional experiments confirming the type of structure and structural homogeneity are required.

[a]A perovskite[(6)] is the material with the crystal structure like calcium titanium oxide ($CaTiO_3$), or $A^{2+}B^{4+}X^{2-}{}_3$.

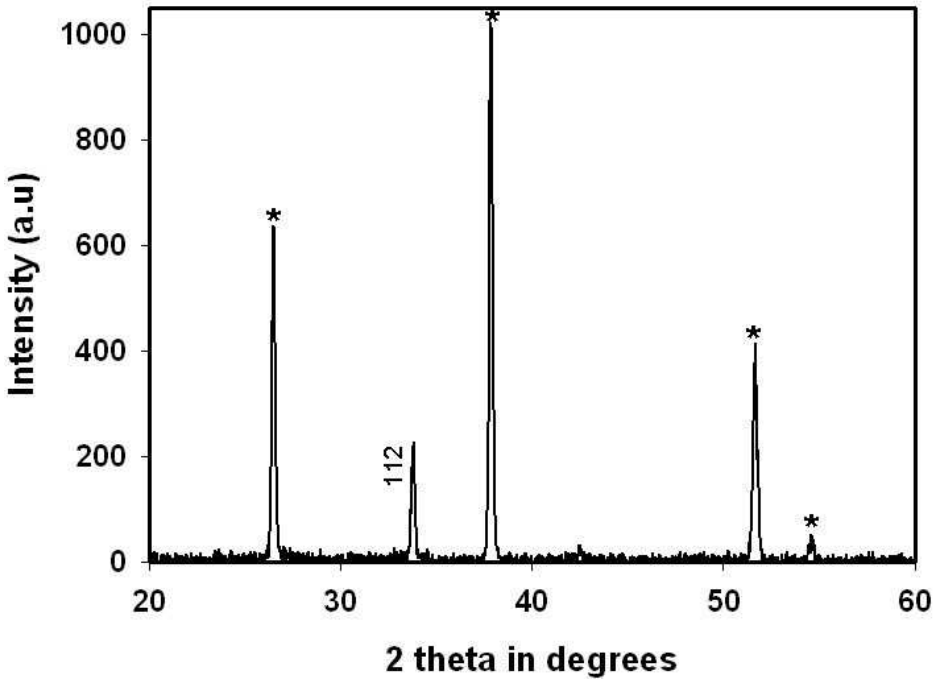

Figure 8.3. XRD for sample 2STF (* denotes ITO diffraction peaks).

In order to obtain a better estimate for the average crystallite size in STF films, the Scherrer method [7,8] has been used (see Scherrer equation 8.1)

$$B_{FWHM}(2\theta) = \frac{K\lambda}{L\cos\theta} \qquad (8.1)$$

According to the conventional Full Width at Half Maximum method (FWHM), the Scherrer constant is assumed here approximately $K = 0.94$. The wavelength of X-ray radiation is $\lambda(\text{Cu-K}_\alpha) = 1.5406$ Å. With a typical width at half height of $B_{FWHH} = 0.15$ degrees (for the (**112**) peak in Figure 8.3.). The estimated grain or crystal size is approximately 1 nm, which is very small. This estimate could be affected by instrumental parameters and should be seen as a very rough estimate, but it shows that the low calcination temperature may have resulted in very small grains. The fact that only one dominant peak is observed is promising and in agreement with a reasonably homogeneous material.

8.3.2 Dark and Illuminated Cyclic Voltammetry Studies

Cyclic voltammograms have been measured first without illumination for samples immersed in aqueous 1 M NaOH. From the voltammograms (see Figure 8.4) it was found that there are strong reduction peaks at applied potential -0.9 V. In contrast, the oxidation peaks are relatively small and observed at an applied positive potential of 0.7 V. The additional reduction is likely to be associated with the Ti(IV/III) rather than the Fe(III/II) process. The oxidation or reduction peaks were found to be relatively independent of the film thickness (see Figure 8.4).

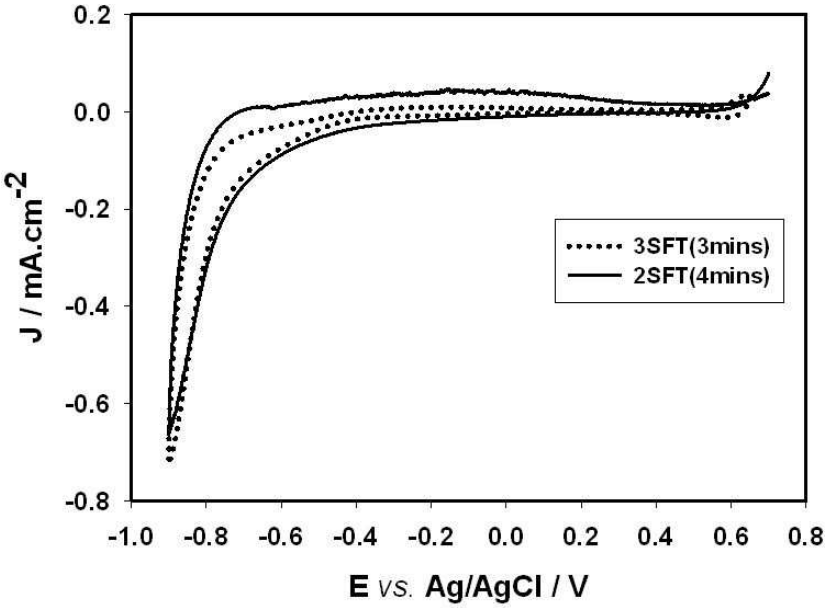

Figure 8.4. Comparison between dark cyclic voltammograms for samples 3STF (sprayed for 3 minutes) and 2STF (sprayed for 4 minutes) immersed in 1 M NaOH recorded with a scan rate $0.1Vs^{-1}$ vs. Ag/Agcl.

Next voltammetric measurements were performed with illumination. Flashing blue LED (λ = 455 nm) light was used in illuminating the STF samples to measure the characteristic photocurrents. Light has been controlled through a LED driver and PPR1 wave generator and gives pulses as 0.4 seconds 'On' and 0.2 seconds 'Off'. Figure 8.5 shows the typical photocurrent response obtained by illumination of the SE side of sample 3STF. It was found that the photocurrent reaches about 1 mA/cm^2 at

applied potential 650 mV under illumination by blue LED at 10.9 mW Cm^{-2}. Similar results were obtained with samples 2STF and 4STF. This indicates that these materials are promising photochemically active and they can be used for example in the tandem cell for water splitting purposes. It was also found that for these materials the SE photocurrent is higher than that of EE one, which can due to the relatively high porosity of these film materials with sufficient electrolyte contacting the substrate electrode. The SE photocurrent increases with increasing the spraying time with sample 2STF giving slightly higher currents.

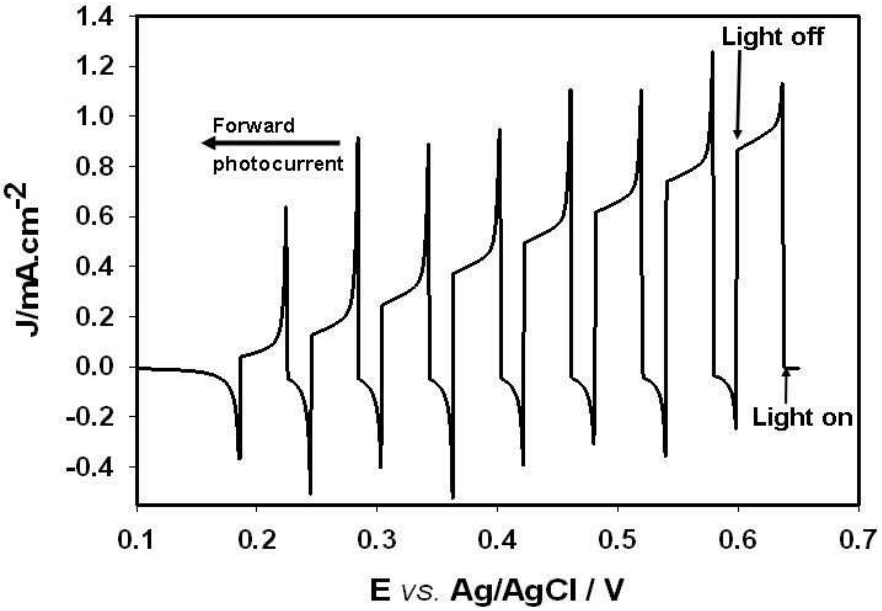

Figure 8.5. Pulse-illuminated voltammogram for sample 3STF (sprayed for 3 minutes) **SE** immersed in 1 M NaOH at a scan rate $0.1Vs^{-1}$, using a blue LED with 10.9 mW/cm^2.

It can be noticed from the transient peaks (Figure 8.5) that there are still high recombination rates destroying the generated hole-electrons pairs. Sharp peak transients can be seen especially at lower applied potentials. This high recombination might due to the presence of the trapping sites between the particles of different oxides components.

8.3.3. Absorption Spectroscopy and IPCE Studies

STF samples showed high absorption of UV-visable light in air, in the wavelength range 300 to 400 nm (see Figure 8.6). As expected, it was found that absorption increases with increasing the spraying time.

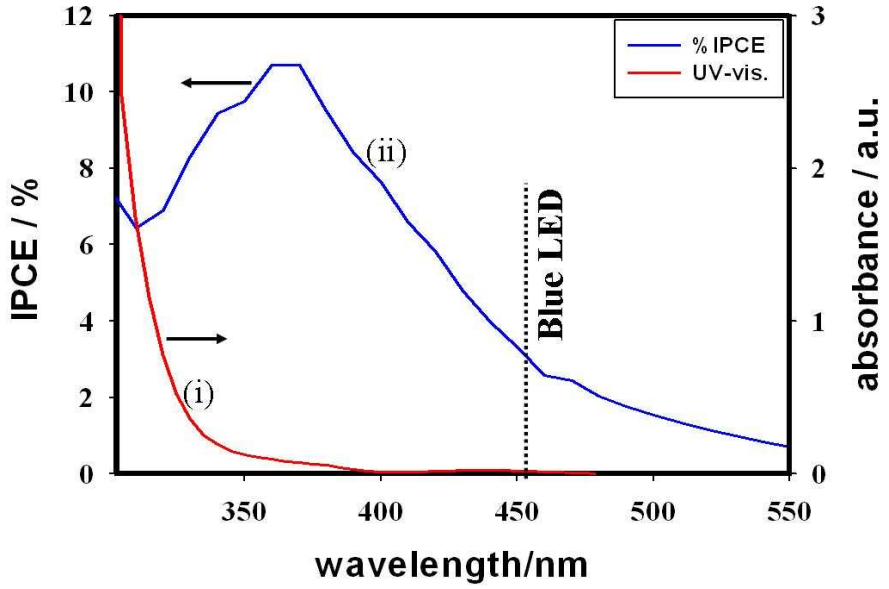

Figure 8.6. (i) Absorption spectrum (in air) of 3STF film electrodes (ITO electrode background subtracted). (ii) IPCE measurement for 3STF (EE) film electrode immersed in 1 M NaOH and with a +0.7 V vs. Ag/AgCl applied potential. Illuminated using xenon lamp.

The absorption coefficient of the STF film can only be estimated. In the wavelength region around 380 nm the onset of the absorption is observed and the absorbance is approximately A = 0.058 (see Figure 8.5i). The extinction coefficient can be estimated based on $\alpha = \frac{A}{2.3\,l} = 21928\,m^{-1}$, where l is the thickness of the STF film (ca. 1.15 μm). The real absorption coefficient could be considerably lower than this estimated value due to additional losses from poor optical coupling and light scattering.

It was observed that the absorption is slightly higher in case of illumination via the EE side compared to that in case of illumination via the SE side as it was discussed in the previous chapters. Ideally, the cells will absorb as much of the blue region of the

spectrum with a high overall incident photon to current efficiency. It has been found that the peak in "Incident Photon Conversion Efficiency" or IPCE (see Figure 8.6) is at approximately 380 nm. Therefore a scan range of 550 nm to 300 nm was chosen to investigate the efficiency of the STF cell.

A comparison between the efficiency of SE illumination and that on EE shows that the difference between the IPCE of EE side and that if SE side are not that high. This might be due to the fact that the films are not thick. It was found also that the efficiency increases slightly with increasing the film thickness as it is shown in Figure 8.7.

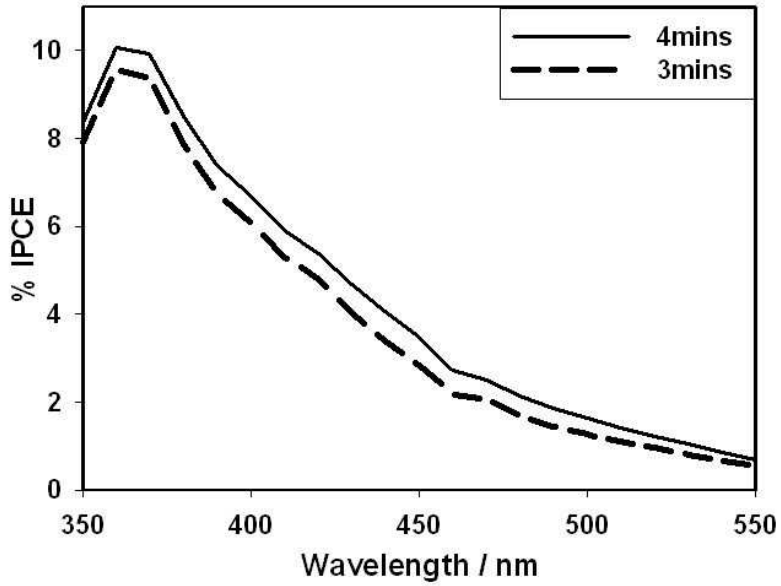

Figure 8.7. Comparison of %IPCE of samples 3STF and 2 STF deposited by spray pyrolysis on ITO for 3 and 4 minutes, respectively, immersed in 1 M NaOH at applied potential **0.7V** vs. Ag/AgCl, illuminated by xenon lamp through **SE** side.

IPCE data suggest good photoelectrochemical activity (although not quite as good as the silica-doped materials, chapter 7). Further improvements are likely when the effects of thickness and calcination temperature are studied in more detail.

8.3.4. Electrochemical Impedance Spectroscopy

Impedance methods can be employed to provide time scale (or frequency domain) dependent information about reactions and processes. Here, the impedance measurements were taken for STF samples prepared by using the spray pyrolysis

method. Figure 8.8 shows data for the dark impedance for a STF film (3STF) obtained at a range of applied potentials (0.0 to 0.7 V vs. Ag/AgCl) in aqueous 1 M NaOH. In zeroth approximation, impedance data can be modelled based on the Randles circuit or equivalent circuit (see Figure 8.8 up left inset) with a "short" Warburg element to represent a thin film of redox active material. R1 and C represent the dominating cell resistance and interfacial capacitance. It was found, as expected, that by increasing the applied positive potential, a decrease in impedance is observed (more current can flow). The impedance data can be approximately modelled when assuming the Randles circuit with "open" Warburg element. The physical significance of this observation is associated with the electron transfer at the film|electrode interface, which may lead to formation of higher oxidation states of Fe(IV/V/VI) and the resulting water spitting reaction causing higher or "catalytic" currents.

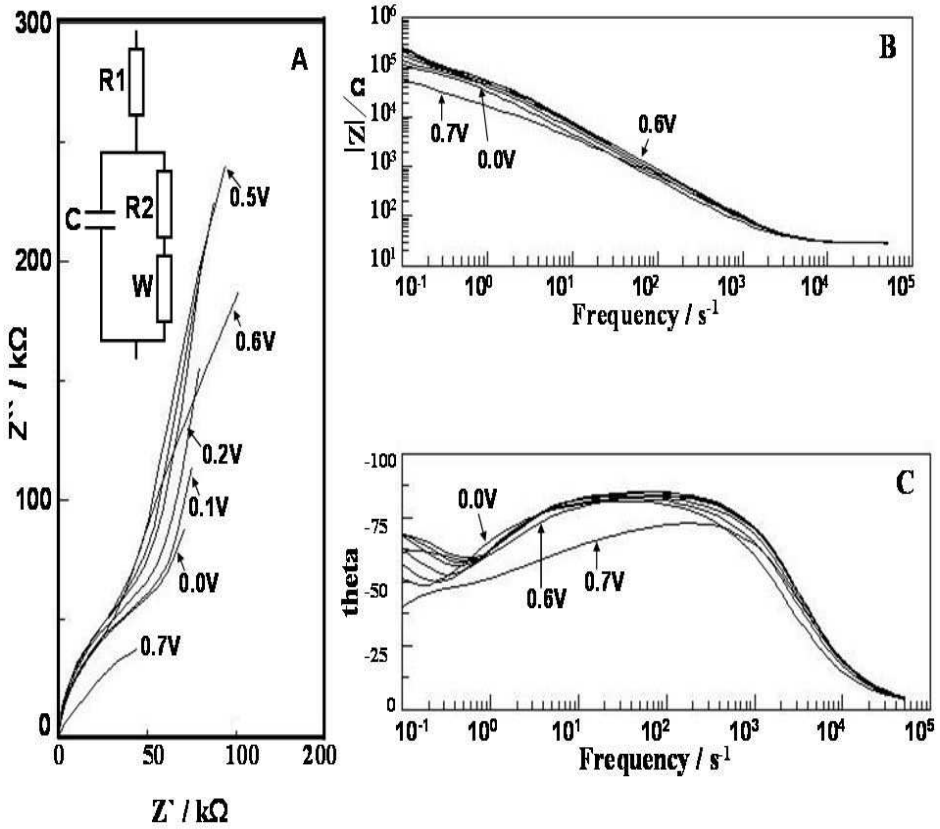

Figure 8.8. (A) Nyquist plots and (B, C) Bode plots for the effect of different applied (DC) potentials on the dark impedance for 3STF film electrode in 1 M NaOH (potentials in V *vs.* Ag/AgCl. The inset (up left) shows the equivalent circuit which has been used.

It was also found that, in the presence of light, additional currents cause a further decrease of the impedance consistent with a faster light energy driven water splitting reaction. Figure 8.9 represents the Nyquist plots (A) and Bode plots (B, C as inset) of impedance results under illumination of sample 3STF (spraying time 3 mins.) through SE side by using blue LED (455 nm) at light intensity corresponding to 300 mA (10.09 mW cm^{-2}). By increasing the applied positive potential the impedance dramatically decreases as at potentials 0.4 V to 0.7 V in comparison to data at lower positive potentials 0.0 V to 0.3 V (see Figure 8.9 A). This confirms the results of high photocurrent transients at higher applied positive potentials (see Figure 8.5).

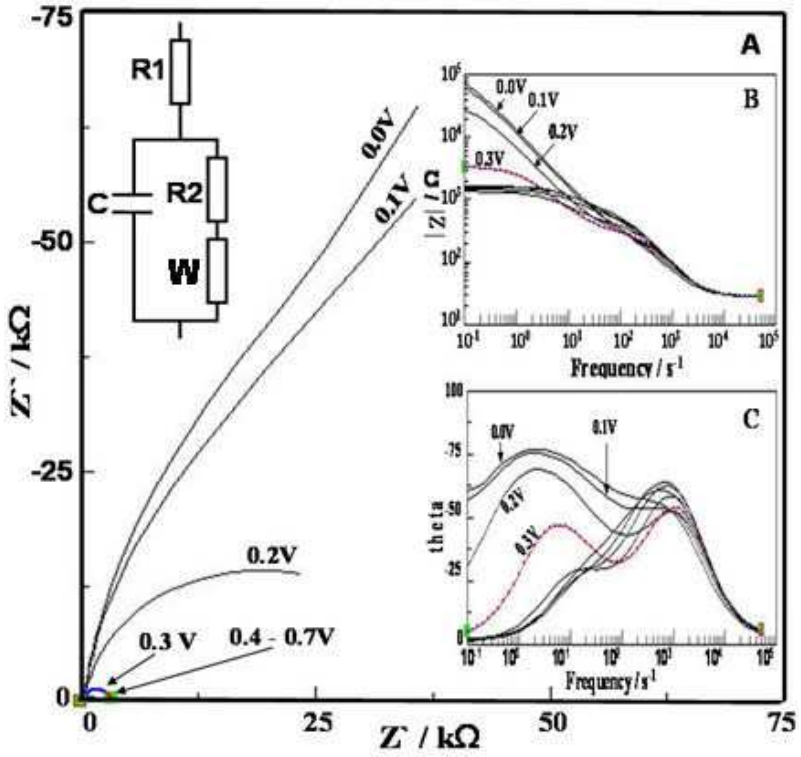

Figure 8.9. (A) Nyquist plots and (B, C as inset) Bode plots for the effect of SE illumination at different applied (DC) potentials (0.0 - 0.7V) on the impedance for 3STF film (3 minutes spraying time) electrode in 1 M NaOH (potentials in V *vs*. Ag/AgCl). The inset (up left) shows the equivalent circuit which has been used. The impedance resulted after application of potentials 0.4- 0.7 V are hidden in the left bottom corner because they are very small in comparison to the impedance resulted by application of lower potentials 0.0 - 0.3 V.

For more illustration for the effect of illumination on the obtained impedance results, a comparison between the impedance of 3STF at dark and under illumination through SE side using blue LED at 10.09 $mWcm^{-2}$ light intensity is shown in Figure 8.10.

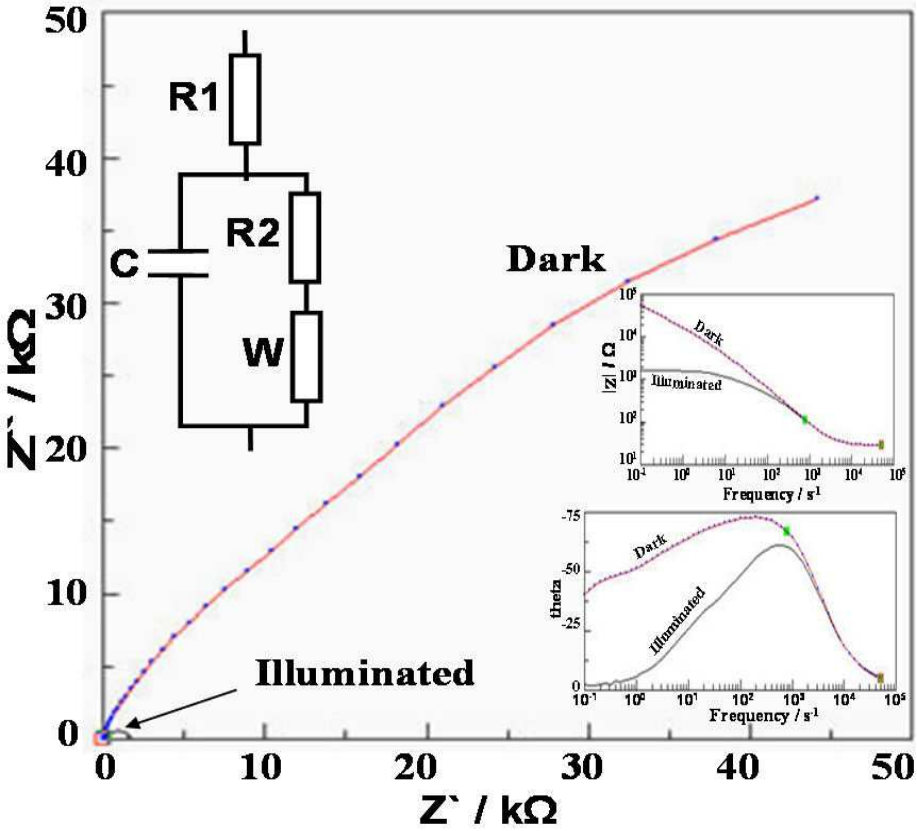

Figure 8.10. A: Nyquist plots and (B, C as inset) Bode plots for the effect of SE illumination at 0.7 V applied (DC) potentials on the impedance for 3STF film (3 minutes spraying time) electrode in 1 M NaOH (potentials in V *vs*. Ag/AgCl. The inset (up left) shows the equivalent circuit which has been used.

All impedance data obtained from the application of the Randles circuit, as it is shown in the above Figures, for dark and illuminated impedance for sample 3STF (spraying time 3 mins.) and that of dark and illuminated impedance of sample 2STF (spraying time 4 mins.) are shown in tables 8.2 and 8.3.

In dark impedance both of resistance and capacitance are slightly decreasing with increasing the applied potential from 0.0 to 0.7 V vs. Ag/AgCl. The same behaviour has been noticed by illuminations through EE side, in case of sample 2STF and on both SE and EE sides in case of sample 3STF (see Tables 8.2 and 8.3). The resistance reported in the tables 8.2 and 8.3 are mainly the ITO substrate resistance in addition to that of the electrolyte (which is tiny in comparison to that of the substrate).

Table 8.2 Impedance data for a spray-pyrolysed 3STF film (3 minutes spraying time) on ITO (area 0.38 cm^2) and immersed in aqueous 1 M NaOH at different applied DC potentials and at 10 mV AC amplitude (light source: blue LED at light intensity 300 mA (10.09 mW cm^{-2}).

E **/ V *vs.* Ag/AgCl**	**Conditions**		***R*** **/Ω** [a]	***C*** **/ µF** [a]
0.0	**Dark**		30.3	2.68
	Light	**EE**	**27.56**	**1.96**
		SE		
0.1	**Dark**		29.8	2.14
	Light	**EE**	**38.31**	**4.33**
		SE		
0.2	**Dark**		29.35	1.87
	Light	**EE**	**38.31**	**4.33**
		SE		
0.3	**Dark**		29.02	1.72
	Light	**EE**	**35.61**	**3.28**
		SE		
0.4	**Dark**		29.13	1.81
	Light	**EE**	**35.44**	**3.21**
		SE	**27.42**	**1.72**
0.5	**Dark**		28.95	1.78
	Light	**EE**	**35.23**	**3.17**
		SE	**27.92**	**1.79**
0.6	**Dark**		28.39	1.65
	Light	**EE**	**35.39**	**3.21**
		SE	**28.28**	**1.83**
0.7	**Dark**		28.68	1.73
	Light	**EE**		
		SE	**29.03**	**2.10**

[a] parameters obtained by employing the "fit circle" option in Zview.

Table 8.3. Impedance data for a spray-pyrolysed 2STF film (4 minutes spraying time) on ITO (area 0.38 cm^2) and immersed in aqueous 1 M NaOH at different applied DC potentials and at 10 mV AC amplitude (light source: blue LED at light intensity 300 mA (10.09 $mW.cm^{-2}$).

***E* / V *vs.* Ag/AgCl**	**Conditions**		***R* /Ω** [a]	***C* / µF** [a]
0.0	**Dark**		65.42	1.94
	Light	**EE**	**63.42**	**9.57**
		SE	**64.03**	**5.40**
0.1	**Dark**		64.28	1.47
	Light	**EE**	**63.09**	**8.66**
		SE	**56**	**2.57**
0.2	**Dark**		63.64	1.30
	Light	**EE**	**62.79**	**7.71**
		SE	**56.04**	**2.85×10^{-8}**
0.3	**Dark**		63.46	1.24
	Light	**EE**	**62.83**	**7.63**
		SE	**59.57**	**8.85×10^{-3}**
0.4	**Dark**		63.38	1.21
	Light	**EE**	**62.82**	**7.56**
		SE	**63.94**	**4.70**
0.5	**Dark**		63.81	1.26
	Light	**EE**	**63.10**	**8.64**
		SE	**64.28**	**4.78**
0.6	**Dark**		63.55	1.23
	Light	**EE**	**62.48**	**8.24**
		SE	**64.38**	**4.95**
0.7	**Dark**		66.3	1.62
	Light	**EE**	**72.83**	**5.94**
		SE	**62.34**	**4.15**
0.8	**Dark**		70.96	2.34
		EE		
		SE		

[a] parameters obtained by employing the "fit circle" option in Zview.

Figure 8.11 represents the comparison between the dark impedance of sample 3STF (spraying time 3 mins.) and that of sample 2STF (spraying time 4 mins.) in 1 M NaOH at applied potential 0.7V vs. Ag/AgCl. It was found that by increasing the spraying time (thickness) the impedance decreases (see Figure 8.10) and that found at all applied potentials.

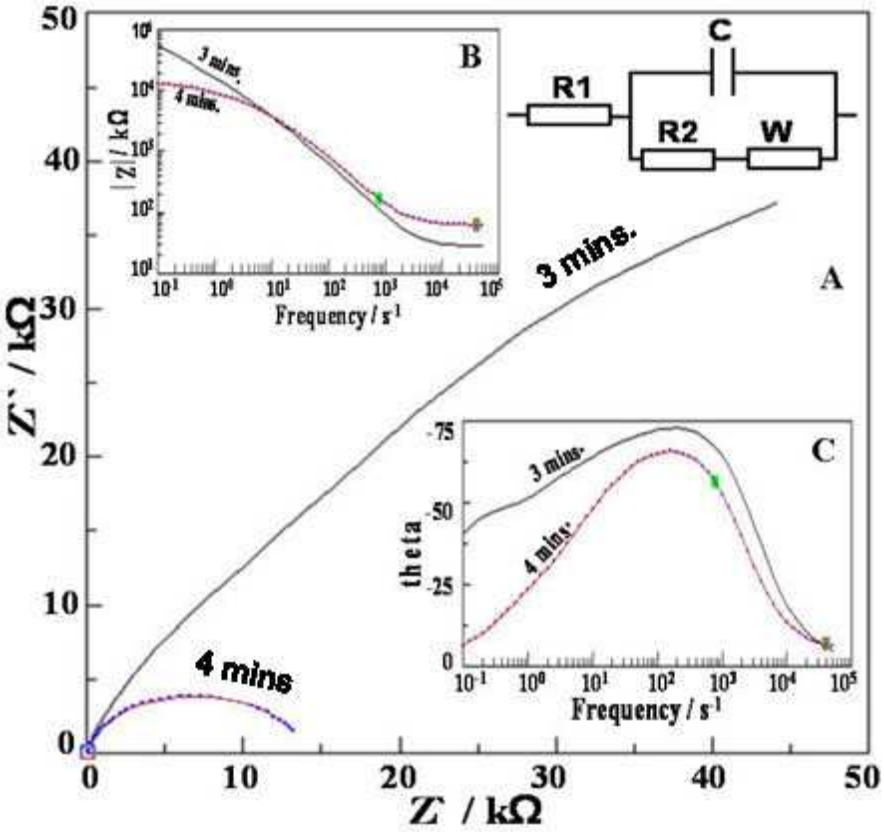

Figure 8.11. (A) Nyquist plots and (B, C as inset) Bode plots for the effect of sample thickness or spraying time (3 and 4 minutes spraying time for samples 3STF and 2 STF films respectively) on dark impedance of STF samples at 0.7 V applied (DC) potential vs. Ag/AgCl in 1 M NaOH (potentials in V *vs*. Ag/AgCl. The inset (top right) shows the equivalent circuit which has been used.

The impedance method provides some additional insight via parametrization in terms of resistances and capacitances. However, for further insight in to the mechanism and potential applicability of STF films in photo-electrochemical devices a wider range of thicknesses and a wider range of compositions needs to be studied.

8.4. Conclusions

The spray pyrolysis method has been applied in an attempt to prepare low temperature solid solution substance of strontium titanate ferrate (STF). According to XRD results it was found that the film material is consistent with Sr ($Fe_{0.9}$ $Ti_{0.1}$) $O_{2.95}$, which indicates that this compound may be from the perovskite family AMO_3. The material has been prepared in a nano-scale form on ITO conducting glass substrates. Photo-electrochemical investigations have been carried on the prepared films and they show that these films are highly photoactive as they show efficiency up to 11 % even without further optimisation. This opens up new opportunities for solid solutions as "tunable" photoanodes, which can be used as a main photosystem for example in the tandem cell to split water by using solar radiations. A lot more work will be necessary to develop these types of material in the future.

8.5. References

(1) Brixner, L. H., *Materials Research Bulletin*, **1968**, *3,* (4) 299-308.

(2) Rothschild, A; Tuller, H. L., *Journal of Electroceramics*, **2006,** *17*, (2-4)1005-1012.

(3) Rothschild, A.; Menesklou, W.; Tuller, H. L.; Ivers-Tiffee, E.; *Chem. Matter.,* **2006,** *18***,** 3651-3659.

(4) Shilova, Y. A.; Patrakeev, M. V.; Mitberg, E. B.; Leonidov, I. A.; Kozhevnikov, V. L.; Poeppelmeier, K. R., *Journal of Solid State Chemistry,* **2002,** *168,* 275-283.

(5) Adler, P.; Eriksson, S.; *Structural properties, Moessbauer spectra and magnetism of perovskite-type oxides Sr* Fe_{1-x} Ti_x O_{3-y}*, (PM3-M),* **2000**, WILEY-VCH Verlag GmbH, Weinheim, Germany.

(6) Wenk, Hans-Rudolf; Bulakh, Andrei, *Minerals: Their Constitution and Origin*, **2004, New** York, NY: Cambridge University Press, 413.

(7) Langford, J.I.; Wilson, A.J.C*, J. Appl. Cryst.,* **1978** *11*, 102-113.

(8) Krishnan, R. R.; Vinodkumar, R.; Rajan, G.; Gopchandran, K. G.; Pillai, V. P. M., *Materials Science and Engineering b-Advanced Functional Solid-state Materials*, **2010**, *174,* (1-3), 150-158.